Detangling climate and topographic history from Cenozoic proxy records: Examples from western North America and the Andes

by

Ran Feng

A dissertation submitted in partial fulfillment
of the requirements for the degree of
Doctor of Philosophy
(Earth and Environmental Sciences)
in the University of Michigan
2015

Doctoral Committee:

Professor Christopher J. Poulsen, Chair
Associate Professor Brian K. Arbic
Associate Professor Mark G. Flanner
Associate Professor Nathan A. Niemi
Associate Professor Nathan D. Sheldon

Acknowledgements

First, I would like to thank my advisor Dr. Chris Poulsen for opening the door of paleoclimate modeling for me and guiding me through the PhD journey. I am truly grateful for Chris's support and insightful suggestions for this research and for his patience in helping to improve my writing. Chris, with his passion for science, strong work ethic, and high efficiency, sets a role model for me to follow in the years to come.

I am also grateful to my other committee members, Mark Flanner, Nathan Sheldon, Nathan Niemi, and Brian Arbic. Their constructive comments and suggestions constantly push me to gain deeper understandings of the proxy data and climate models.

I would like to thank my collaborators, Martin Werner from AWI and Hari Mix from Stanford University. Martin is generous enough to share his code with me and help me port and set up the models. Hari has provided me with insights about proxy data that inspired the research idea of Chapter 4.

I am very lucky to be a member of the supportive and productive Climate Change Research lab. My labmates, including former members, Jing Zhou, Dan Horton, Louise Jeffery, Nadja Insel, Brian Yanites, Allison Yanites, and Alex Thompson, and current members, Clay Tabor, Rich Fiorella, Chana Tilevitz, Chris Skinner, Sierra Peterson, and Dora Shen, have all been tremendously helpful with manuscript preparation and life in general.

I am indebted to the kindness of our technician Mike Messina and graduate coordinator Anne Hudon as well as many other faculty and staff members of the Department of Earth and Environmental Sciences. Their generous help has greatly facilitated the completion of this dissertation work.

Finally, I would like to thank my family for being supportive and always being there for me.

Table of Contents

List of Figures

List of Tables

Chapter 1

Introduction

1.1 Overview and motivation

The eastern circum-Pacific orogenic belt, located along the western boundary of the North and South American continents, is one of the most magnificent mountain belts on Earth's surface. This orogenic belt was uplifted primarily by diachronous subduction of the Farallon and Kula Plates beneath the North American continent during the middle Mesozoic and early Cenozoic (~155 to ~50 Ma ago, e.g., DeCelles, 2004) and the subduction of the Nazca Plate beneath the South American continent starting at the beginning of the Cenozoic (~66 Ma ago) (Isacks, 1988). Concomitant with uplift of the American Cordilleras, Cenozoic climate has evolved from a "greenhouse" to an "icehouse" climate. However, the mechanisms of how these mountain belts were uplifted and how surface uplift affected Cenozoic climate evolution are not well understood.

The timing and rate of the Andean uplift is strongly debated. One hypothesis suggests that uplift was gradual throughout the late Cenozoic (since ~15 Ma ago) (Poulsen et al., 2010; Insel et al., 2012). A competing hypothesis, however, suggests an abrupt elevation pulse during the late Miocene (between 10 – 6 Ma ago) (Garzione, 2008). For western North America, there is agreement that an Andean-type plateau existed over the present-day Basin and Range Province prior to the Neogene (since ~20 Ma ago) extension (Dickinson, 2004). However, the timing of uplift and peak elevation of this high plateau, as well as the amount and distribution of its elevation loss during the Neogene extension, are highly uncertain (DeCelles, 2004; Clark, 2007).

The reconstruction of paleoelevations is complicated by the complex patterns of co-evolving Cenozoic climate and tectonic history of the Andes and the North American Cordillera. Reconstructing paleoelevations often relies on quantifiable estimates of regional climate responses to elevation increase using either modern observations or theoretical calculations of decreasing rates of certain climate variables with elevation (lapse rates). This approach does not account for climate variations that are independent of elevation changes, such as variations due

to changing CO_2 level and geographic configuration, or variations that are only marginally dependent on elevation changes, such as uplift induced rapid precipitation and circulation shifts that do not scale linearly with elevation increases. In the case of the Andes, for example, evidence for abrupt surface uplift comes from interpretations of geochemical (Ghosh et al., 2006; Garzione et al., 2008) and geomorphological proxies (Whipple and Gasparini, 2014) that assume that a rapid, regional climate transition during the late Miocene was a direct result of an elevation pulse. However, more recent studies have questioned this interpretation by showing that the rapid climate transitions can occur as a threshold response to gradual uplift of the Andes above a critical height (~3 km) (Poulsen et al., 2010; Insel et al., 2012).

Orogenic-scale topography has a first-order influence on regional climate. For instance, the Rockies cool and dry the climate over Western North America by 1) enhancing snow and ice formation and increasing the associated albedo and diabatic cooling (Ruddiman and Kutzbach, 1989), 2) creating a rain shadow in the leeward eastern side of the mountains (e.g., Kutzbach et al., 1997), and 3) inducing winter cold weather outbreaks through strengthening of the winter trough east of the mountains (Ruddiman and Kutzbach, 1989; Broccoli and Manabe, 1997; Rind, 1997). At seasonal time scales, the presence of the Rockies enhances monsoonal circulation in the vicinity of the Gulf of Mexico due to enhanced differences in the summer heating rate between the continent and the ocean (Ruddiman and Kutzbach, 1989; Sewall and Sloan, 2006). Likewise, the surface elevation of the Andes is closely associated with the strength of the monsoonal circulation eastward of the central Andes. During austral summer, the high-elevation Andes divert the low-level airflow (Ehlers and Poulsen, 2009; Insel et al., 2009; Saurral et al., 2014; Fiorella et al., 2015) and enhances moisture convergence towards the eastern side of the central Andes (Lenter and Cook, 1995), resulting in strong summer moist convection and cloud formation (Insel et al., 2009). Andean uplift is also thought to influence the position and geometry of the Intertropical Convergence Zone (ITCZ). As shown by numeric modeling studies, elevating the Andes strengthens the present-day asymmetric pattern of the ITCZ (double ITCZ in the western equatorial Pacific, but single ITCZ in the eastern equatorial Pacific) through enhancement of the low cloud formation and diffusion of the southern ITCZ in the eastern tropical Pacific (Xu et al., 2004; Takahashi and Battisti, 2007a; 2007b).

1.1.1 New climate insights from paleoelevation reconstructions of the Andes

The uplift history of the Andes may have important implications for Cenozoic tropical climate. The gradual 2 km uplift of the Andes during the late Cenozoic corresponds with the transition of the tropical Pacific climate from a more zonally symmetric state to the present-day, zonally asymmetric state. The present-day state is distinguished by quite different climate patterns in the eastern tropical Pacific (15 °S – 15 °N, 150 ° – 80 °W) versus the western tropical Pacific (15 °S – 15 °N, 120 °E – 180 °). In the east, the SSTs are ~7–8 °C cooler (Hadley Center SST data, Rayner et al., 2002), the upwelling is significantly stronger, and the thermocline is shallower than in the west. This east-west contrast in SSTs and the subsurface ocean state is coupled with a zonally asymmetric Walker circulation, characterized by rising air in the western equatorial Pacific and subsidence in the eastern equatorial Pacific. The Walker circulation is connected with equatorial surface easterlies and coastal southerlies, which further strengthen the equatorial and coastal upwelling of subsurface cold water and shoaling of the thermocline in the eastern tropical Pacific.

Proxy reconstructions suggest that prior to the late Cenozoic, the asymmetric climate state of the tropical Pacific was weaker. During the late Miocene (12 – 8 Ma) and early Pliocene (~5 – 4 Ma), SSTs were about ~5 – 6 °C warmer in the eastern equatorial Pacific (e.g., Fedorov et al., 2013; Zhang et al., 2014) and ~4 °C warmer along the Peruvian coast (Dekens et al., 2007) associated with weaker upwelling and a deeper thermocline in the eastern equatorial Pacific (e.g., Ford et al., 2015). Yet, SST reconstructions show similar or only mildly warmer conditions (up to ~ 4 °C) in the western tropical Pacific (Zhang et al., 2014). These records display long-term trends evolving towards modern conditions during the late Cenozoic (since ~12 Ma), suggesting long-term enhancement of tropical Pacific climate asymmetry.

The mechanisms behind this climate transition are not well understood, but Andean uplift may have played a role. Andean uplift has been shown to enhance the zonal asymmetry of the rain band, atmospheric circulation patterns, and cloud formation across the eastern tropical Pacific (Xu et al., 2004; Takahashi and Battisti, 2007a, b; Insel et al., 2009). However, it is unclear how uplift influences the tropical ocean and whether it has contributed to the development of the modern asymmetric ocean state. These questions motivate the research reported in **Chapter 5**.

1.1.2 Paleoelevation estimates of the Cenozoic western North America Cordillera

The Cenozoic elevation and climate history of the western North American Cordillera is also unclear, as it is for the Andes. The North American Cordillera consists of four major tectonic units from the west to the east: the coastal accretionary terrains, hinterland metamorphic belt, Sevier fold and thrust belt, and Laramide foreland province (Figure 1) (Decelles, 2004). The timing and magnitude of uplift over this region are debated. It has been proposed that the Cordilleran hinterland, east of the Thrust belt and Laramide foreland province, was uplifted prior to the early Eocene (e.g. Chase et al, 1998; Sewall et al., 2013; Snell et al., 2014). In contrast, recent studies suggest the hinterland elevations are only moderate (≤ 2 km) prior to the Eocene (~55 – 34 Ma) (Chamberlain et al., 2012; Lechler et al., 2013), and uplift occurred from the early Eocene to Oligocene (~55 – 28 Ma) and migrated from north to south (Mix et al., 2011; Chamberlain et al., 2012). Estimates of maximum hinterland elevations differ between ~2 – 3 km (Chase et al., 1998; Wolfe et al., 1998) and ~3 – 4 km (Mix et al., 2011).

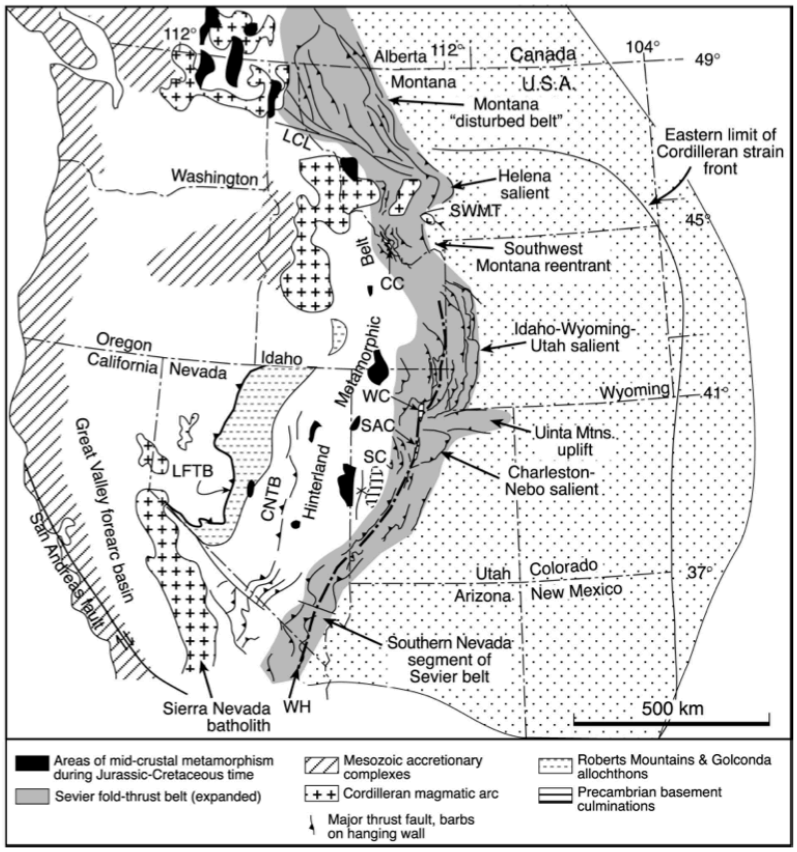

Figure 1 Tectonic map of the western US.
The major tectonic provinces mentioned in this dissertation from the west to the east are the coastal accretionary terrains, hinterland metamorphic belt, Sevier fold and thrust belt (gray shading), and Laramide foreland province (stippled). Figure is from DeCelles (2004).

Additionally, estimates of the foreland elevations differ between moderate elevations similar to today (≤ 2 km) (Fan and Dettman, 2009) and elevations (~ 4 km) higher than the hinterland high plateau (Chase et al., 1998). Uncertainties in pre-extensional elevations of these regions preclude accurate estimates of the amount and distribution of elevation loss during the Neogene (~23 Ma to present) extension. Across the central Rockies, estimates of Neogene elevation loss range from kilometers (based on early Cenozoic reconstructions by Chase et al., (1998)) to near negligible amounts (since ~40 Ma) (Fan et al., 2014a; 2014b).

1.1.3 Climate and tectonic importance of understanding Cenozoic elevation history of the North American Cordillera

The uncertainty in paleo-elevations of the North American Cordillera limits our understanding of the climate history over this region. Paleoclimate reconstructions from the Laramide foreland basins suggest a warm and humid environment during the early Cenozoic. Regional climate has since evolved towards arid conditions with widespread eolian deposition in Wyoming (Fan et al., 2015, personal communication), New Mexico, and Arizona (Cather et al., 2008) during the early Oligocene (33.5 – 27 Ma). This long-term aridification could result from large-scale climate drying during the Oligocene (Cather et al., 2008) or the local rain shadow effect associated with weakening of the paleo-North American Monsoon in response to Cordilleran uplift (Chamberlain et al., 2012). Uncertainties in paleoelevation estimates of the Cordillera and understanding of monsoon responses to the uplift preclude rigorous evaluation of these hypotheses. More importantly, interpretations of climate trends and patterns from proxy records of western North America require an understanding of the regional elevation history. The same proxy values could indicate different climate conditions under different elevation scenarios. For example, a reconstructed cooling trend from proxies could indicate either a climate cooling without elevation changes or a steady climate state with significant uplift. Paleoelevation reconstructions, therefore, are a key to detangling climate information from terrestrial archives of the western U.S.

Besides climate, the pre-extension topography and patterns of elevation loss during the extension can be used to test tectonic hypotheses of the North American Cordillera. A pre-extension high plateau over the extended region would indicate conservation of the crustal mass during the extension. Alternatively, the absence of a pre-extension high plateau would violate mass conservation over the extensional region, indicating redistribution or generation of crustal

materials through lateral influx of lower crustal materials or mantle processes. The pattern of elevation loss during the extension is also useful for testing whether the mantle lithosphere is involved in the extension. Given that thinning of the mantle lithosphere may happen at different wavelengths than the crust, tectonic models proposing lithospheric thinning also indicate heterogeneous elevation loss and even pulses of uplift due to replacement of the thinned mantle lithosphere with more buoyant asthenosphere (Clark, 2007; Chamberlain et al., 2012).

1.1.4 Paleoaltimetry of the North American Cordillera

Paleoaltimetry estimates for the North American Cordillera mainly come from two methods: fossil leaf paleoaltimetry and stable isotope paleoaltimetry. Other proxies for paleoaltimetry, including basalt vesicularity, leaf stomatal frequency, cosmogenic nuclides, and clumped isotope paleoaltimetry, have also been used but are not common, and therefore, are not discussed in this dissertation. Fossil leaf altimetry uses reconstructed temperature, and moist enthalpy (an atmospheric thermo-dynamic quantity that combines internal and latent heat), both taken from quantitative measurements of leaf physiognomy, to estimate paleoelevations. Stable isotope altimetry estimates paleoelevations using oxygen and hydrogen stable isotopic compositions of authigenic minerals and organic materials ($\delta^{18}O$ and δD). In this dissertation, $\delta^{18}O$ is used to refer to both $\delta^{18}O$ and δD, given that δD is convertible to $\delta^{18}O$ in most paleoaltimetry applications. The $\delta^{18}O$ compositions of proxy materials are assumed to be in equilibrium with compositions of soil water, which are further assumed to be equivalent to compositions of meteoric water. The principle underlying both fossil leaf and stable isotope paleoaltimetry assumes that climate responses to surface uplift, including temperature, moist enthalpy, and rainout rate of heavier isotopes, are steady and follow quantifiable lapse rates.

Applications of these paleoaltimetry methods require known lapse rates of temperature, moist enthalpy, and $\delta^{18}O$. These lapse rates are either chosen to match modern values (Chase et al., 1998; Poage and Chamberlain, 2002; Meyer, 2007), or determined through theoretical calculations (Wolfe et al., 1998; Forest et al., 2007; Rowley et al., 2007). Usage of modern lapse rates assumes that the lower tropospheric stratification has been invariant from the past to present, while usage of theoretical calculations in previous studies assumes that changes in temperature, humidity, and ^{18}O-rainout rate with elevations strictly follow the conservation of moist static energy (the measure of the energy state of stationary moist air parcels) with no influences from advection or radiative fluxes. At a regional scale, these assumptions are rarely met (see a review

discussing mid-latitude tropospheric thermostructure by Schneider and O'Gorman, 2008), rendering paleoaltimetry estimates prone to large errors.

This dissertation quantifies paleoelevation biases due to using modern or theoretical lapse rates and updates paleoelevation estimates for the uplift and subsidence of the western North American Cordillera. More specifically, it addresses the following questions: 1) How does Eocene $\delta^{18}O_p$ respond to changes in regional atmospheric circulation and precipitation under different elevation scenarios of the North American Cordillera? What are the implications for $\delta^{18}O_p$ based paleoaltimetry? (**Chapter 2**) 2) How do changes in temperature and moist enthalpy between modern and Eocene climate states and amongst different uplift scenarios affect fossil leaf paleoaltimetry estimates of the North American Cordillera? (**Chapter 3**) And how do large-scale changes in climate structure and surface conditions affect estimates of the western U.S. elevation loss during the Neogene? (**Chapter 4**)

1.1.5 Methods

Two modeling approaches are carried out in this dissertation. For the paleoaltimetry studies (Chapter 2, 3, and 4), a multi-disciplinary approach of incorporating climate simulations into hypsometric estimates is used to detangle the climate and elevation signals from the Cenozoic proxy $\delta^{18}O$ and fossil leaf records of western North America. This approach differs from previous methods in its treatment of both regional climate and paleoelevation as unknowns. Using simulations with a range of topographic scenarios, this method provides a range of estimates of altimeters ($\delta^{18}O$, δD, temperature, and moist enthalpy) at the proxy sites. Through comparison of the simulations with reconstructions, optimal solutions for paleoelevations can be approximated based on the match between the climate model and proxy. Apart from paleoaltimetry, a slightly different modeling approach is used for investigating tropical Pacific responses to surface uplift (Chapter 5). A coupled ocean-atmosphere model is applied to quantify the oceanic responses to a suite of elevation scenarios mimicking the gradual uplift of the Andes. This approach provides estimates for the coevolving ocean dynamics, which is entirely absent in previous studies using either fixed SSTs or a mixed layer ocean model. All these methods provide unique insights toward understanding the tectonic-climate interactions across the North and South American Cordillera from the viewpoint of co-evolving elevation and climate, and will ultimately guide us towards more accurate paleoelevation estimates and understandings of tectonics and climate dynamics.

1.2 Dissertation outline

This dissertation contains four chapters (2 through 5), followed by a summary and discussion chapter (6). Chapters 2 and 3 elucidate the dominant lower tropospheric (below 500 hPa) physics and dynamics that control the alpine distributions of $\delta^{18}O$ (δD) in precipitation, temperature, and moist enthalpy across the Eocene (~55 to 40 Ma) North American Cordillera. These two chapters provide new paleo-elevation estimates based on comparisons between the simulations and proxy records. Chapter 4 extends this approach to the Neogene (since ~23 Ma) and incorporates a sophisticated land model component. This new version of the climate model is capable of simulating the soil water $\delta^{18}O$ and δD, and therefore, allows direct comparisons to proxy values. The model results provide estimates of Neogene large-scale environmental changes (including cooling, aridification, grassland expansion, and continental drift and shoreline migration) on proxy $\delta^{18}O$ and δD from the western U.S., which is then incorporated into estimating the amount and pattern of elevation loss during the Neogene extension. In Chapter 5, the responses of tropical Pacific climate to Cenozoic surface uplift, focusing on the Andes-eastern tropical Pacific system are investigated. The results provide a better understanding of the contributions and mechanisms of Andean uplift to the late Cenozoic climate transition across the tropical Pacific.

1.3 Publications associated with this dissertation

Feng, R., Poulsen, C.J., Werner, M., Chamberlain, C.P., Mix, H.T., Mulch, A., 2013. Early Cenozoic evolution of topography, climate, and stable isotopes in precipitation in the North American Cordillera. American Journal Science (Chapter 2), front page story.

Feng, R. Poulsen, C.J., 2015. Refinement of Eocene lapse rates, fossil-leaf altimetry, and North American Cordilleran surface elevation estimates. Earth and Planetary Science Letters (under review) (Chapter 3).

Feng, R. Poulsen, C.J., 2015. Imprints of Neogene strengthening of the Hadley circulation and tectonic extension on the terrestrial $\delta^{18}O$ records of the western U.S. (in prep for Geology) (Chapter 4).

Feng, R., Poulsen, C.J., 2014. Andean elevation control on tropical Pacific climate and ENSO. Paleoceanography (Chapter 5), highlighted in EOS research spotlight: "Peruvian Andes helped to cool eastern equatorial Pacific".

Bibliography

Broccoli, A. J., and Manabe S., 1992: The effects of orography on midlatitude Northern Hemisphere dry climates. J. Climate, 5, 1181-1201.

Cather, S.M., Connell, S.D., Chamberlin, R.M., McIntosh, W.C., Jones, G.E., Potochnik, A.R., Lucas, S.G., Johnson, P.S., 2008. The Chuska erg: Paleogeomorphic and paleoclimatic implications of an Oligocene sand sea on the Colorado Plateau. Geol Soc America Bull 120, 13–33. doi:10.1130/B26081.1

Chamberlain, C.P., Mix, H.T., Mulch, A., Hren, M.T., Kent-Corson, M.L., Davis, S.J., Horton, T.W., Graham, S.A., 2012. The Cenozoic climatic and topographic evolution of the western North American Cordillera. American Journal of Science 312, 213–262. doi:10.2475/02.2012.05

Chase, C. G., Gregory-Wodzicki, K. M., Parrish-Jones, J. T., and DeCelles, P. G., 1998. Topographic history of the western Cordillera of North America and controls on climate, in: Crowley, T.J., and Burke, K., eds., Tectonic boundary conditions for climate model simulations, New York, Oxford University Press, 73-99.

Clark, M.K., 2007. The Significance of Paleotopography. Reviews in Mineralogy and Geochemistry 66, 1–21. doi:10.2138/rmg.2007.66.1

DeCelles, P.G., 2004. Late Jurassic to Eocene evolution of the Cordilleran thrust belt and foreland basin system, western USA. American Journal of Science 304, 105–168.

Dickinson, W.R., 2004. Evolution of the North American Cordillera. Annu. Rev. Earth Planet. Sci. 32, 13–45. doi:10.1146/annurev.earth.32.101802.120257

Ehlers, T.A., Poulsen, C.J., 2009. Influence of Andean uplift on climate and paleoaltimetry estimates. Earth and Planetary Science Letters 281, 238–248.

Fan, M., Dettman, D.L., 2009. Late Paleocene high Laramide ranges in northeast Wyoming: Oxygen isotope study of ancient river water. Earth and Planetary Science Letters 286, 110–121. doi:10.1016/j.epsl.2009.06.024

Fan, M., Heller, P., Allen, S.D., Hough, B.G., 2014a. Middle Cenozoic uplift and concomitant drying in the central Rocky Mountains and adjacent Great Plains. Geol 42, 547–550. doi:10.1130/G35444.1

Fan, M., Hough, B.G., Passey, B.H., 2014b. Middle to late Cenozoic cooling and high topography in the central Rocky Mountains: Constraints from clumped isotope geochemistry.

Earth and Planetary Science Letters 408, 35–47. doi:10.1016/j.epsl.2014.09.050

Feng, R., Poulsen, C.J., 2014. Andean elevation control on tropical Pacific climate and ENSO. Paleoceanography 29, 795–809. doi:10.1002/2014PA002640

Feng, R., Poulsen, C.J., Werner, M., Chamberlain, C.P., Mix, H.T., Mulch, A., 2013. Early Cenozoic evolution of topography, climate, and stable isotopes in precipitation in the North American Cordillera. American Journal of Science 313, 613–648. doi:10.2475/07.2013.01

Feng, R. Poulsen, C.J., 2015. Refinement of Eocene lapse rates, fossil-leaf altimetry, and North American Cordilleran surface elevation estimates. Earth and Planetary Science Letters (under review).

Feng, R. Poulsen, C.J., 2015. Imprints of Neogene strengthening of the Hadley circulation and tectonic extension on the terrestrial $\delta^{18}O$ records of the western U.S. Geology (in prep).

Fiorella, R.P., Poulsen, C.J., Pillco Zolá, R.S., Barnes, J.B., Tabor, C.R., Ehlers, T.A., 2015. Spatiotemporal variability of modern precipitation δ18O in the central Andes and implications for paleoclimate and paleoaltimetry estimates. Journal of Geophysical Research: Atmospheres 120, 4630–4656. doi:10.1002/2014JD022893

Forest, C.E., 2007. Paleoaltimetry: A Review of Thermodynamic Methods 66, 173–193. doi:10.2138/rmg.2007.66.7

Garzione, G.N., Gregory D.H., Libarkin J.C. et al., 2008. Rise of the Andes (vol 320, pg 1304, 2008). Science 321, 1295–1295.

Ghosh, P., Garzione, G.N., and Eiler J.M., 2006. Rapid Uplift of the Altiplano Revealed Through 13C-18O Bonds in Paleosol Carbonates. Science 311, 511–515. doi:10.1126/science.1119365

Insel, N., Poulsen, C.J., Ehlers, T.A., 2009. Influence of the Andes Mountains on South American moisture transport, convection, and precipitation. Clim Dyn 35, 1477–1492. doi:10.1007/s00382-009-0637-1

Insel, N., Poulsen, C.J., Ehlers, T.A., Sturm, C., 2012. Response of meteoric δ18O to surface uplift — Implications for Cenozoic Andean Plateau growth. Earth and Planetary Science Letters 317-318, 262–272. doi:10.1016/j.epsl.2011.11.039

Isacks, B.L., 1988. Uplift of the Central Andean Plateau and bending of the Bolivian Orocline. Journal of Geophysical Research: Solid Earth 93, 3211–3231. doi:10.1029/JB093iB04p03211

Kutzbach, J.E., Ruddiman W.F., and Prell W.L., 1997. Possible effects of Cenozoic uplift and CO_2 lowering on global and regional hydrology. In "Tectonic Uplift and Climate Change" (W.F. Ruddiman, ed.), Plenum Publishing Corporation, New York, pp. 149-170.

Lenters, J. D. and Cook K. H., 1995: Simulation and Diagnosis of the Regional Summertime Precipitation Climatology of South America. J. Climate, 8, 2988–3005. doi: http://dx.doi.org/10.1175/1520-0442(1995)008<2988:SADOTR>2.0.CO;2

Lechler, A. R., Niemi, N. A., Hren, M. T., et al., 2013. Paleoelevation estimates for the northern and central proto–Basin and Range from carbonate clumped isotope thermometry. Tectonics, 32(3), 295-316. doi: 10.1002/tect.20016

Meyer, H.W., 2007. A Review of Paleotemperature Lapse Rate Methods for Estimating Paleoelevation from Fossil Floras. Reviews in Mineralogy and Geochemistry 66, 155–171. doi:10.2138/rmg.2007.66.6

Mix, H.T., Mulch, A., Kent-Corson, M.L., Chamberlain, C.P., 2011. Cenozoic migration of topography in the North American Cordillera. Geol 39, 87–90. doi:10.1130/G31450.1

Poage, M.A., Chamberlain, C.P., 2001. Stable isotopic evidence for a Pre–Middle Miocene rain shadow in the western Basin and Range: Implications for the paleotopography of the Sierra Nevada. Tectonics 21. doi:10.1029/2001TC001303

Poulsen, C.J., Ehlers, T.A., Insel, N., 2010. Onset of convective rainfall during gradual late Miocene rise of the central Andes. Science 328, 490–493.

Prell, W.L., and Kutzbach J. E., 1997. The impact of Tibet-Himalayan elevation on the sensitivity of the monsoon climate system to changes in solar radiation. In "Tectonic Uplift and Climate Change" (W.F. Ruddiman, ed.), Plenum Publishing Corporation, New York, pp. 171-201.

Rind, D., Russell G., and Ruddiman W.F., 1997. The effects of uplift on ocean-atmosphere circulation. In Tectonic Uplift and Climate. W.F. Ruddiman, Ed. Plenum Press, 123-147.

Rowley, D. B. and Garzione, C., 2007. Stable isotope-based Paleoaltimetry, Annual Reviews of Earth and Planetary Sciences, Volume 35, 463-508.

Ruddiman, W.F., Kutzbach, J.E., 1989. Forcing of late Cenozoic northern hemisphere climate by plateau uplift in southern Asia and the American west. Journal of Geophysical Research: Solid Earth 94, 18409–18427. doi:10.1029/JD094iD15p18409

Saurral, R.I., Camilloni, I.A., Ambrizzi, T., et al., 2014. Links between topography, moisture

fluxes pathways and precipitation over South America. Clim Dyn 45, 777–789. doi:10.1007/s00382-014-2309-z

Sewall, J.O., Sloan, L.C., 2006. Come a little bit closer: A high-resolution climate study of the early Paleogene Laramide foreland. Geol 34, 81. doi:10.1130/G22177.1

Sewall, J.O., Fricke, H.C., 2013. Andean-scale highlands in the Late Cretaceous Cordillera of the North American western margin. Earth and Planetary Science Letters 362, 88–98. doi:10.1016/j.epsl.2012.12.002

Schneider T. and O'Gorman P.A., 2008. Moist Convection and the Thermal Stratification of the Extratropical Troposphere. J. Atmos. Sci., 65, 3571–3583. doi: http://dx.doi.org/10.1175/2008JAS2652.1

Snell, K. E., Koch, P. L., Druschke, P., et al., 2014. High elevation of the 'Nevadaplano'during the Late Cretaceous. Earth and Planetary Science Letters, 386, 52-63. doi:10.1016/j.epsl.2013.10.046

Takahashi, K., Battisti, D.S., 2007a. Processes controlling the mean tropical pacific precipitation pattern. Part I: The Andes and the eastern Pacific ITCZ. J. Climate 20, 3434–3451. doi:10.1175/JCLI4198.1

Takahashi, K., Battisti, D.S., 2007b. Processes controlling the mean tropical pacific precipitation pattern. Part II: The SPCZ and the southeast pacific dry zone. J. Climate 20, 5696–5706. doi:10.1175/2007JCLI1656.1

Whipple, K.X., Gasparini, N.M., 2014. Tectonic control of topography, rainfall patterns, and erosion during rapid post-12 Ma uplift of the Bolivian Andes. Lithosphere 6, 251–268. doi:10.1130/L325.1

Wolfe, J.A., Forest, C.E., Molnar, P., 1998. Paleobotanical evidence of Eocene and Oligocene paleoaltitudes in midlatitude western North America. Geol Soc America Bull 110, 664–678. doi:10.1130/0016-7606(1998)110<0664:PEOEAO>2.3.CO;2

Xu, H., Wang, Y., Xie, S.P., 2004. Effects of the andes on eastern pacific climate: A regional atmospheric model study*. J. Climate.

Chapter 2

Early Cenozoic evolution of topography, climate, and stable isotopes in precipitation in the North American Cordillera

2.1 Abstract

Paleoelevation reconstructions of the North American Cordillera inferred from the oxygen ($\delta^{18}O$) and hydrogen (δD) isotope ratios of terrestrial paleoclimate proxy materials (soils, ashes, lake sediments) suggest rapid north-to-south migration of topography in the early Cenozoic (pre-49 Ma to 28 Ma). The validation of this reconstruction relies on an accurate understanding of the $\delta^{18}O_p$ and the associated regional climate change in response to the uplift of the western North America. Here we study this response using a global climate model (GCM) with explicit $\delta^{18}O_p$ diagnostics (ECHAM5-wiso) focusing on the isotopic effects of different types of precipitation, vapor mixing, recycling and moisture source and compare the response against estimates made using a Rayleigh distillation models of moist adiabatic condensation (RDM). Four experiments are performed with Eocene topography inferred from terrestrial stable isotope paleoaltimetry records to investigate how southward propagation of topography affects regional climate (temperature, precipitation and circulation pattern) and $\delta^{18}O_p$ over North America. Our experiments predict $\delta^{18}O_p$ patterns that are broadly consistent with maps of temporally binned proxy $\delta^{18}O$ and generally support an early Cenozoic north-to-south propagation of high topography in the North American Cordillera. They do not support the commonly made assumption that isotopic fractionation occurs primarily through rainout following Rayleigh distillation nor the application of modern empirical $\delta^{18}O_p$ lapse rates to past environments.

In our GCM simulations, precipitation processes and climate changes that are not captured by RDMs substantially affect $\delta^{18}O_p$. These processes include shifts in local precipitation type between convective and large-scale rain and between rain and snow; intensification of low-level vapor recycling particularly on leeward slopes; development of air mass mixing and changes in wind direction and moisture source. Each of these processes can have significant

(≥2‰) influences on $\delta^{18}O_p$ that are comparable in magnitude to surface uplift of hundreds or even thousands of meters. In many regions, these processes fortuitously compensate each other, explaining the apparent agreement between ECHAM5-wiso and proxy $\delta^{18}O$ and, more broadly, between RDM estimates and observed $\delta^{18}O$-elevation relationships. In some regions, compensation is incomplete, and as a result, ECHAM5-wiso $\delta^{18}O_p$ does not agree with estimates from the RDM. In these regions, including the interior of the northern cordillera and the eastern flank of the southern Cordillera, moderate adjustments of paleoelevations may be in order.

2.2 Introduction

A wealth of geophysical, tectonic, structural and sedimentological data suggests that prior to Basin and Range extension (~23-2 Ma) crustal conditions necessary to support a high plateau existed across western North America (DeCelles, 2004; Dickinson, 2004; Chamberlain et al., 2012). When and how this plateau topography developed is an open question. Two popular tectonic models have been proposed. The first suggests that a high plateau existed early, by the Late Cretaceous, over-thickened, and then collapsed due to internal extension or frontal propagation to form a lower elevation mountainous region (see review by DeCelles, 2004). The second suggests that the plateau developed through early Cenozoic north-to-south propagation of topography as asthenosphere replaced denser mantle lithosphere due to piecemeal removal of mantle lithosphere and/or adjustment of the Farallon slab geometry (Humphreys, 1995; Forte et al., 2010; Schmandt and Humphreys, 2011). These two models call for disparate surface topography histories (Humphreys, 1995; Clark, 2007) that can potentially be distinguished through the reconstruction of past surface elevations.

To this end, Mix et al. (2011) analyzed a record of over 3000 mineral samples and created temporal snapshots of the distribution of oxygen stable isotope values ($\delta^{18}O$) over western North America. These $\delta^{18}O$ snapshots show a systematic southward decrease in mineral $\delta^{18}O$ and were interpreted, following a Rayleigh condensation model, to represent rapid southward propagation of high topography (the *SWEEP* model of Chamberlain et al., 2012) from southern British Columbia to the central Great Basin of Nevada and Colorado between 50 and 28 Ma (Mix et al., 2011; Chamberlain et al., 2012).

Using mineral oxygen stable isotopic values to infer past surface elevations has become a common technique founded on modern observations that demonstrate a decrease in stable isotopic composition of precipitation ($\delta^{18}O_p$ and δD_p) with elevation at a global-average rate of

approximately −2.8‰ km^{-1} (Poage and Chamberlain, 2001). This relationship is commonly attributed to Rayleigh distillation of the heavy isotopes (^{18}O, D) as an ascending air parcel adiabatically cools, water vapor condenses, and precipitation forms (for example, Blisniuk and Stern, 2005). Following this theory, Rayleigh distillation models have been developed and applied to interpret stable isotope chronostratigraphies (Rowley, 2007; Rowley and Garzione, 2007). However, in some orogenic regions, Rayleigh distillation models may be inappropriate due to air parcel deflection around topography (for example, Galewsky, 2009), air mixing (for example, Gedzelman, 1988; Sherwood and Dessler, 2001) and recycling (for example, Salati et al., 1979), and the development of moist convection (for example, Risi and Vimeux, 2008; Poulsen et al., 2010). In these regions, stable isotope-elevation relationships deviate substantially from those predicted by Rayleigh distillation (Blisniuk and Stern, 2005). Examples in western North America include the Basin and Range province, which is characterized by particularly low $\delta^{18}O_p$-elevation lapse rates due to mixing and recycling of moisture from multiple sources (Lechler and Niemi, 2011), and the Sierra Nevada, which is characterized by isotopic enrichment of leeside precipitation due to orographic blocking and flow around the range (Lechler and Galewsky, 2013).

Moreover, stable isotope-elevation relationships may change as surface topography and climate evolve in concert, complicating paleoelevation reconstructions (Ehlers and Poulsen, 2009; Poulsen et al., 2010; Poulsen and Jeffery, 2011). In the Andes of northern and central South America, for example, Cenozoic surface uplift has been demonstrated to (1) block zonal winds, leading to a shift in position of South American low-level jet to more southerly latitudes (Insel et al., 2009; Poulsen et al., 2010) and a shift in moisture source from the South Pacific Ocean to the equatorial Atlantic (Ehlers and Poulsen, 2009; Poulsen et al., 2010); (2) induce convective precipitation on the windward side flanks, enhancing isotopic fractionation through rainout (Poulsen et al., 2010; Insel et al., 2012); and (3) strengthen atmospheric subsidence and vertical mixing on the top and leeward flanks of the mountains (Poulsen and Jeffery, 2011). These effects were shown to leave strong imprints on Andean $\delta^{18}O_p$, complicating paleoelevation reconstructions. It is likely that similar phenomena affected Cenozoic $\delta^{18}O_p$ during the development of Cordilleran topography in western North America.

The purpose of this study is twofold, (i) to quantify the influence of non-Rayleigh processes on the stable isotopic composition of precipitation in and around orogenic regions and

(ii) to evaluate the *SWEEP* hypothesis inferred from mineral $\delta^{18}O$ and δD. The first objective is a test of the traditional stable isotope paleoaltimetry method. If non-Rayleigh processes have a substantial influence on stable isotopic compositions, then this method is unlikely to be robust for estimating past elevations of Eocene western North America. The second objective is a test of the *SWEEP* hypothesis. Simulations of precipitation $\delta^{18}O_p$ using *SWEEP* topography should be broadly consistent with proxy $\delta^{18}O_p$. Inconsistencies between model and proxy values would bring into question the *SWEEP* reconstruction. To achieve these goals, a series of Eocene simulations have been developed using ECHAM5-wiso, a global climate model (GCM) capable of tracking water isotopologues through the hydrological cycle, to simulate the evolution of climate and $\delta^{18}O_p$ to the migration of topography described by the *SWEEP* hypothesis. These simulations are compared with both proxy $\delta^{18}O$ and estimates of $\delta^{18}O_p$ from a Rayleigh distillation model.

2.3 Methods

2.3.1 Description of the climate model and boundary conditions

ECHAM5-wiso, a global three-dimensional atmospheric GCM with isotope-tracking capability (Werner et al., 2011), permits simulation of both early Cenozoic climate and isotopologue distribution ($H_2{}^{18}O$ and HDO) of vapor and precipitation over western North America. ECHAM5 has been widely used to study both past and future climate change and has been included in the Intergovernmental Panel on Climate Change (IPCC) assessment reports. Simulated temperature and precipitation means and extremes under IPCC emission scenarios fall well within the range of other GCMs, indicating reasonable model skill for projecting future climate (for example, Kharin et al., 2007). ECHAM5 also successfully simulates many aspects of modern North American climate, including the distribution of precipitation over western North America (Salathé, 2006; Cook et al., 2008). In comparison to other GCMs, ECHAM5 produces a more realistic simulation of the Aleutian low and the storm track over the Pacific Northwest (Salathé, 2006). ECHAM5, coupled to the ocean model MPI-OM, also does a better job of simulating zonal precipitation gradients across central and western North America than many other GCMs (Cook et al., 2008). Finally, in comparison to many GCMs, ECHAM5_MPI-OM simulates an Eocene climate with a lower equator-to-pole temperature gradient and ice-free Arctic at low CO_2 level of 560 ppmv (Heinemann et al., 2009).

In ECHAM5-wiso, water isotopologues are treated as independent tracers that undergo equilibrium and kinetic fractionation during phase transitions in the atmosphere. Vapor fluxes from the sea surface and lakes undergo non-equilibrium fractionation as a function of temperature, seawater $\delta^{18}O$ ($\delta^{18}O_{sw}$), relative humidity and $\delta^{18}O$ of vapor at the bottom of the atmosphere. Vapor fluxes from the land surface are not fractionated (Hoffmann et al. 1998), since root uptake and transpiration have minimal effect on the isotopic composition (Zimmermann et al., 1967). Seawater $\delta^{18}O$ ($\delta^{18}O_{sw}$) is prescribed at each grid cell as described below. Lake water $\delta^{18}O$ is set to a constant value of 0.5‰. Surface runoff and drainage are based on a single bucket scheme (Roeckner et al., 2003). Water isotopologues that infiltrate the surface are treated as passive tracers (Hoffmann et al., 1998). The $\delta^{18}O$ of runoff is assumed to be the same as soil water. The water isotope-tracking module of ECHAM has been used to investigate modern (Hoffmann et al. 1998; Werner et al. 2011) and past hydrological cycles (Hoffmann et al. 2000). For North America, the simulations have been shown to be in good agreement with observed $\delta^{18}O_p$ from the Global Network of Isotopes in Precipitation (GNIP) and vapor δD by Scanning Imaging Absorption Spectrometer for Atmospheric Cartography (SCIAMACHY) (Frankenberg et al., 2009) (figs. 1 and 10 in the paper by Werner et al., 2011).

ECHAM5-wiso can be coupled to a 50-m mixed-layer ocean model with prescribed ocean heat flux (Roeckner et al., 2003). However, in the absence of knowledge about Eocene ocean heat fluxes, monthly-varying sea-surface temperatures (SSTs) were prescribed in all experiments. The Eocene SST dataset was calculated (i) using ECHAM5 with a mixed-layer ocean model and modern ocean heat fluxes to estimate the zonal distribution of SST, and (ii) then modifying the resulting SST distribution to replicate the Eocene meridional temperature gradient reconstructed from multiple proxies (Figure 2c). As a result of this procedure, the SST distribution has zonal features reminiscent of modern including a west-east equatorial temperature gradient, poleward warming in the vicinity of subtropical western boundaries, and equatorward cooling along subtropical eastern boundaries (Figure 2a), yet a meridional gradient that is appropriate for the Eocene (Figure 2c).

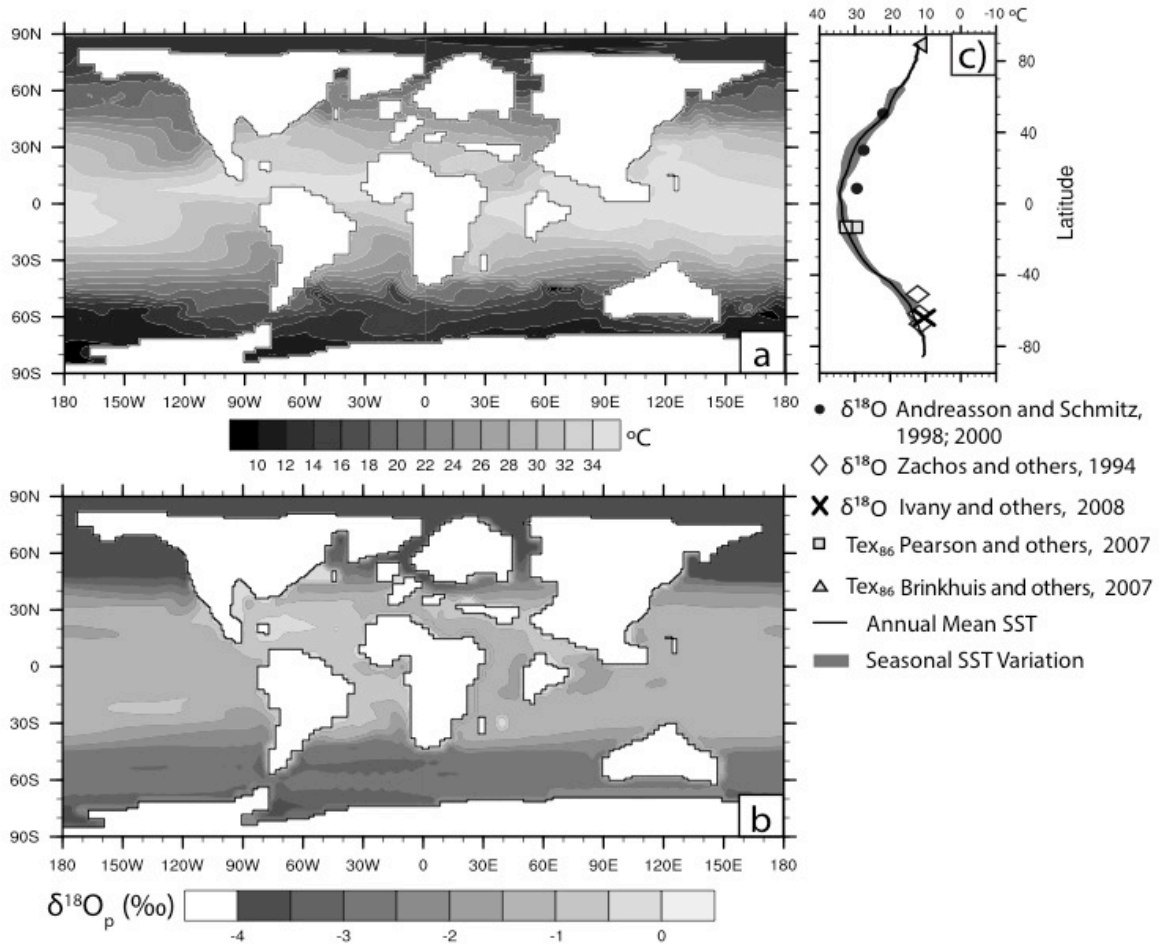

Figure 2 Annual mean Eocene a) sea surface temperature (SST, °C), b) seawater $\delta^{18}O$ ($\delta^{18}O_{sw}$, ‰) and c) meridional SST gradient (line) and its seasonal variation (gray shading) versus proxy reconstructions (markers).
SST and $\delta^{18}O_{sw}$ are fixed boundary conditions in this study.

ECHAM5-wiso requires the input of seawater $\delta^{18}O$ values. We estimated these values from a lower resolution (spectral T31, ~3.75° in latitude and longitude) Eocene simulation using a coupled ocean-atmosphere model with isotope-tracking capability (GENMOM, Zhou et al., 2008). Our Eocene simulation was run with boundary conditions (that is geometry, topography, CO_2) similar to those used in our ECHAM5-wiso experiments, and a flat ocean with a depth of 5600 m. The simulation was initialized with uniform $\delta^{18}O_{sw}$ of −1.2‰, the average $\delta^{18}O_{sw}$ in an ice-free world, and was integrated for 2020 model years, until the time rates of change of upper-ocean temperature and salinity were <0.1 °C 100 yrs^{-1} and 0.1 ‰ 100 yrs^{-1}. Northward of 75° N, the $\delta^{18}O_{sw}$ simulated by GENMOM is less than −7‰, due to insufficient seawater exchange across the Bering Straight in this low resolution simulation (Zhou et al., 2008). To correct for

this bias, we set the minimum Arctic $\delta^{18}O_{sw}$ to −4‰, about the value of the modern Arctic (Clementz and Sewall, 2011). The average of the last 40 years of $\delta^{18}O_{sw}$ and δD from the GENMOM Eocene simulation were used as boundary conditions in the ECHAM5-wiso simulations. The meridional $\delta^{18}O_{sw}$ gradient is roughly similar to the modern gradient with a low gradient at low latitudes and a higher gradient (0.06‰ °latitude^{-1}) at middle to high latitudes (between 30° N to 70° N and 30° S to 60° S).

In all experiments, ECHAM5-wiso is configured with 19 vertical levels and a spectral triangular truncation of 106 horizontal waves (~100 km horizontal grid spacing). In comparison to most paleoclimate simulations, with horizontal grid spacing of 200 – 300 km, our resolution is finer in order to better capture orographic processes. We use the Eocene paleogeography and paleotopography from Bice et al. (2000) but modify the geography over western North America to include foreland basins with mean elevations of 500 m and interior lakes. Both basins and lakes are inferred from the stratigraphic analysis of Eocene sedimentary successions by Dickinson et al. (1988).

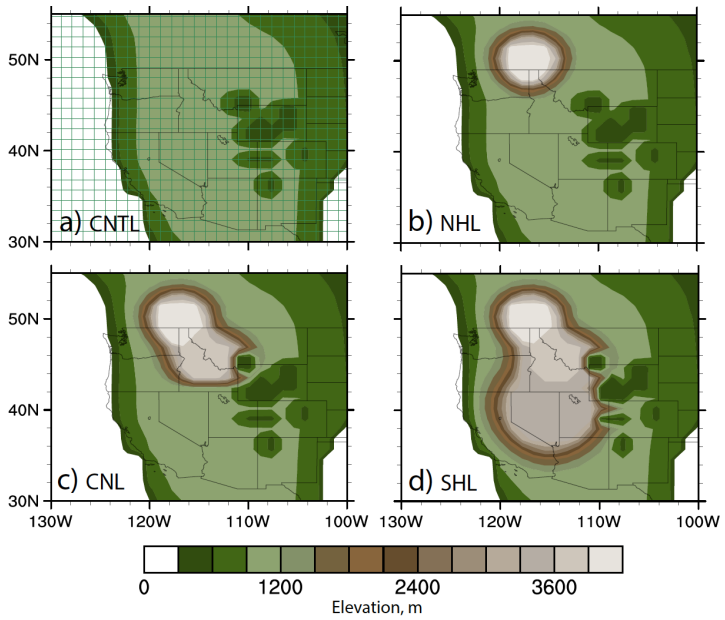

Figure 3 Topography of western North America for the (a) control (CNTL), (b) northern highland (NHL), (c) central highland (CHL) and (d) southern highland (SHL) experiments.
NHL, CHL, and SHL are modified after Mix et al. (2011) and represent the southern propagation of an Eocene highland through the early Cenozoic. The grid lines in (a) represent the computational grid used in our ECHAM5-wiso experiments. U.S. state borders are shown to simplify the referencing of sample locations. The borders have been modified to account for Neogene Basin and Range extension by narrowing Nevada by ~2° longitude.

Table 1. Boundary conditions for ECHAM5-wiso Eocene experiments.

Parameter	Model input
Topography	55 Ma (Bice et al., 2001)
Vegetation	The Eocene vegetation distribution is based on Sewall et al., (2000). Surface parameters including albedo, roughness length, field capacity of soil, and forest ratio, are prescribed according to Hagemann (2002) based upon vegetation type.
pN_2O and pCH_4	306 ppb and 1.65 ppm (modern values)
pCO_2	1120 ppm (Beerling et al., 2011)
Sea ice and glacial ice	None
Sea water $\delta^{18}O$ ($\delta^{18}O_{sw}$)	Prescribed from GENMOM Eocene simulation
SST	Prescribed SSTs with mean and meridional distribution to fit Eocene proxy

We have developed a series of experiments to investigate the influence of Cenozoic paleotopographic evolution on regional $\delta^{18}O_p$ and climate. The only parameter that varies between experiments is the land-surface topography; all other boundary conditions remain the same between experiments (table 1). Four scenarios are simulated including a control case with no significant highlands (CNTL) and a series of three cases that portray progressive Cenozoic uplift of the North American Cordillera from north to south following the reconstructions of Mix et al. (2011). These cases are referred to as northern highlands (NHL), central highlands (CHL), and southern highlands (SHL) (Figure 3). All experiments were run until the time rate of change of the global surface temperature was $\leq 0.01°C\ yr^{-1}$. The simulations were then integrated an additional ten years. All results in this study are reported as averages of the final ten years.

2.3.2 Rayleigh Distillation Model of adiabatic condensation (RDM)

We have constructed a Rayleigh distillation model of adiabatic condensation (RDM), similar in concept to that outlined in Rowley and Garzione (2007), as a diagnostic tool to (i) evaluate the extent to which local $\delta^{18}O_p$ in our ECHAM5-wiso simulations can be described by Rayleigh distillation and (ii) quantify the biases associated with assuming a fixed moisture source in paleoaltimetry estimates. The RDM, described in detail in Appendix A1, is a one-dimensional (altitude dependent) model that tracks the isotopic composition of a single near-surface air parcel as it ascends, becomes saturated, and condenses. The model assumes that as an air parcel attains saturation, the resulting condensate is immediately removed from the system.

The RDM requires knowledge of the initial vapor temperature (T_s), specific humidity (q_s), and $\delta^{18}O_v$ of the ascending air mass. In applications of RDMs for paleoaltimetry purposes, $\delta^{18}O_v$ is often prescribed from proxy data assuming a known moisture source. For example, in their use of an RDM to estimate paleoelevations, Mix et al. (2011) used mineral $\delta^{18}O$ from an Eocene coastal site based on the assumption that, as today, these sites received most of their moisture from the western Pacific Ocean.

In our application of the RDM, we run two types of experiments: those with *fixed-moisture* sources and those with *GCM-moisture* sources. *Fixed-moisture* source experiments are intended to quantify the bias introduced by a uniform western Pacific source and a constant initial $\delta^{18}O_v$ (inferred from mineral $\delta^{18}O_p$). In these experiments, initial vapor temperature and specific humidity are specified from GCM mean-annual surface temperature and low-level (1000 hPa) specific humidity from the western side of each highland (values are shown in Figure 4). In our *GCM-moisture* source experiments, initial vapor $\delta^{18}O_p$, in addition to temperature and specific humidity, are specified from mean-annual GCM output. We use the RDM to track air masses from both the western and eastern sides of the range. Though it is typically assumed that all moisture sources from the west, our GCM simulations and simulations by Sewall and Sloan (2006) indicate that this is not the case. Initial T_s, q_s and $\delta^{18}O_v$ values of *GCM-moistures source*s (GCM-derived $\delta^{18}O_v$ and moisture source) for each side of the highlands (dash line square) and the $\delta^{18}O_v$ values of *fixed-moisture source*s (solid line square) are shown in Figure 4a-c.

The RDM describes an open isotopic system, in which the condensation is continuously removed. Yet, in our GCM simulations, recycling through evaporation of surface water can account for up to ~70% to 76% of precipitation on the leeside of the Cordillera. To account for this process, we have developed a modified RDM that incorporates vapor recycling. At each time

step, a portion of any condensate, equal to the condensate mass times the recycling potential, is added back to the air mass. The recycling potential is defined as the local ratio of surface evaporation to precipitation from GCM output averaged over the leeside of the mountain and neglects vapor integrated through mixing and transport aloft. The vapor temperature and isotopic ratio are unchanged by assuming isothermal expansion and that recycled vapor has the same isotopic ratio as existing vapor (details see Appendix A2).

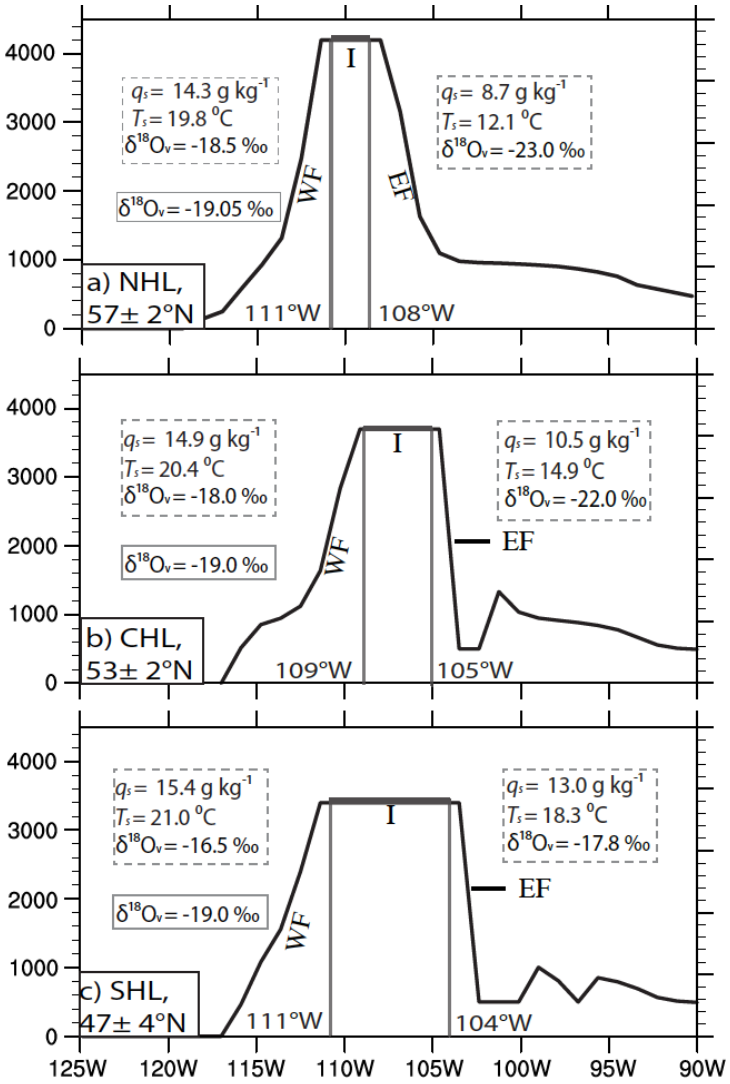

Figure 4 Topographic cross-section across northern (NHL), central (CHL) and southern (SHL) highlands.

The different topographic regimes (western flank, WF; eastern flank, EF; and interior, I) discussed in the text are labeled. The specific humidity (q_s), temperature (T_s) and ^{18}O composition of vapor ($\delta^{18}O_v$) of GCM-moisture source (dashed box) and $\delta^{18}O_v$ (solid box) are show. The q_s and T_s of fixed-moisture source are the same as the GCM-moisture source at the western flank (dashed box at the western flank).

2.3.3 Analysis of $\delta^{18}O_l$ Mixing

In contrast to the scenario depicted in RDMs, an air parcel is not isolated and may interact with its environment through mixing, which can change both its isotopic composition and humidity. At the local scale, mixing between a parcel and its environment happens primarily through turbulence. On regional and continental scales, mixing can also occur through large-scale circulation (Pierrehumbert and Yang, 1993). This type of mixing includes vapor entrainment through moist convection and lateral mixing of dry air and moist plumes through advection. The former is of primary importance in the tropics (Pierrehumbert and Yang, 1993), while the latter is most important in subtropical regions (Pierrehumbert, 1998). As evidenced by global observations of mid-troposphere δD (Worden et al., 2007) and demonstrated in GCM simulations (Poulsen and Jeffery, 2011), large-scale mixing through subsidence and convection can significantly affect the isotopic composition of vapor. Mixing can change vapor isotopic composition by changing (i) the isotopic composition of the air parcel; (ii) the fractionation temperature of condensate; and (iii) the relative humidity, and thus condensation potential, of the air parcel (for example, Sherwood and Dessler, 2001).

To estimate the effect of vapor mixing on the $\delta^{18}O_p$, we calculate the $\delta^{18}O$ of equilibrium condensate ($\delta^{18}O_c$) from the advection potential of $\delta^{18}O_v$ using the GCM output of $\delta^{18}O_v$ and three-dimensional wind velocities. The temporal change of $\delta^{18}O_c$ due to flow in the s-direction (either zonal, meridional or vertical direction), $\frac{\partial \delta^{18}O_c}{\partial t}$, can be approximated using the advection equation:

$$\frac{\partial \delta^{18}O_c}{\partial t} \sim -V_s \frac{\partial \delta^{18}O_c}{\partial s} \qquad (1),$$

where $\frac{\partial \delta^{18}O_c}{\partial s}$ and V_s are the $\delta^{18}O_c$ gradient and flow velocity.

The $\frac{\partial \delta^{18}O_c}{\partial s}$ is estimated by assuming immediate condensation of advected vapor:

$$\delta^{18}O_c \approx \delta^{18}O_v + 1000 \ln \alpha \qquad (2),$$

where α is the fractionation factor. 1000lnα describes isotopic fractionation due to condensation and is expanded as in Majoube (1971):

$$1000\ln\alpha = -7.685 + \frac{6.7123\times10^3}{T} - \frac{1.6664\times10^3}{T^2} + \frac{0.35041\times10^9}{T^3} \quad (3).$$

Computing the $\delta^{18}O$ gradient on both side of equation (2) gives:

$$\frac{\partial\delta^{18}O_c}{\partial s} = \frac{\partial\delta^{18}O_v}{\partial s} + \frac{\partial T}{\partial s}\left(-\frac{6.7123\times10^3}{T^2} + \frac{3.3328\times10^6}{T^3} - \frac{1.05123\times10^9}{T^4}\right) (4),$$

where $\frac{\partial T}{\partial s}$ is the temperature gradient along the s-direction. Calculating the inner dot product of the velocity and gradients in the s-direction on both sides of equation (4) yields:

$$V_s\frac{\partial\delta^{18}O_c}{\partial s} = V_s\frac{\partial\delta^{18}O_v}{\partial s} + V_s\frac{\partial T}{\partial s}\left(-\frac{6.7123\times10^3}{T^2} + \frac{3.3328\times10^6}{T^3} - \frac{1.05123\times10^9}{T^4}\right) (5).$$

V_s, T and $\delta^{18}O_v$ are then rewritten as the sum of the annual mean and its perturbation, following the form $x = \bar{x} + x'$. Expanding the right-hand side, neglecting the high-order term ($\frac{\overline{T'^2}}{\overline{T^2}}$, $\frac{\overline{T'^4}}{\overline{T^4}}$ and $(\delta^{18}O_v)'$), and taking the annual average yields:

$$\overline{V_s\frac{\partial\delta^{18}O_c}{\partial s}} \approx \overline{V}_s\overline{\frac{\partial\delta^{18}O_v}{\partial s}} + \left(\overline{V}_s\frac{\partial\overline{T}}{\partial s} + \overline{V_s'\frac{\partial T'}{\partial s}}\right)\left[-\frac{6.7123\times10^3}{\overline{T}^2} + \frac{3.3328\times10^6}{\overline{T}^3} - \frac{1.05123\times10^9}{\overline{T}^4}\right] (6).$$

The mean annual advection of $\delta^{18}O_c$ is determined by the mean-annual advection of $\delta^{18}O_v$ and T, and the annual average of sub-annual scale advection of T'. As a first order approximation, this part of advection is estimated with monthly climatology. Advection terms are estimated using center differencing and are averaged to the mid-point of each grid cell in the vertical direction.

The $\frac{\partial\delta^{18}O_c}{\partial t}$ is then estimated using equation (1). The calculation assumes that vapor advected into a grid cell immediately mixes with the existing vapor following the equilibrium liquid condensation. This approximation has several sources of potential error. First, not all of the vapor advected into a grid cell will condense to form precipitation. Second, condensate may form solid precipitation (snow, hail), particularly in updrafts, which undergoes kinetic fractionation and diffusive processes, leading to a smaller fractionation factor. As a result of these errors, our estimate of $\delta^{18}O_c$ changes due to advection likely represent an upper bound.

2.3.4 Analysis of moisture source through back trajectory

To locate the source of orographic moisture in our experiments, we calculate horizontal back trajectories of high-humidity, low-level air parcels originating from positions on the highlands. Back trajectories are calculated from 10-year daily climatologies of humidity-weighted (averaged between 1000 and 850 hPa) winds from our ECHAM5-wiso experiments. Each back trajectory is calculated for 7 prior days with a 1-hour time step. Wind speeds at each time step are calculated by linearly interpolating between daily values. The use of daily climatologies filters the velocity field, eliminating the influence of transient eddies. Additional details about our back trajectory method are described in Appendix A3.

For the NHL, CHL, and SHL cases, back trajectories are performed for the following locations on the western flank and eastern flank: 57° N, 125° W and 115° W (NHL case); 53° N, 122° W and 102° W (CHL case); and 47° N, 125° W and 102° W (SHL case). For comparison, back trajectories from the same locations are also calculated for the CNTL case. For each location, 365 back trajectories are calculated beginning on the 1st of January and extending through the 31st of December. Air parcel relative humidity is also recorded along the trajectory path. Trajectories are only reported in Figure 12 and Figure 13 for air parcels at starting location with relative humidity ≥ 60%.

2.4 Results

2.4.1 Simulated early Eocene temperature of western North America

Mean annual temperature (MAT) in the CNTL experiment is largely zonal over North America ranging from a minimum of 9.2 °C at high latitudes to a maximum of 27.5 °C over southwestern North America (Figure 5a). The simulated latitudinal MAT gradient is ~0.5 °C latitude^{-1} between 40° N and 70° N at 100° W, slightly higher than the Early Eocene *equable climate* gradient reconstructed from paleofloras (~0.4 °C °latitude^{-1}, Greenwood and Wing, 1995). The cold month mean temperature has a similar zonal distribution with minimum of 2.6 °C and maximum of 15 °C. The inclusion of highlands disrupts the zonal distribution of MATs, depressing temperatures in their vicinity (Figure 5b-d). The minimum MAT of all three sensitivity experiments drops to −7.6 °C on the highland top with sharp zonal gradients on the western and eastern flanks with average magnitudes of ~2.7 and ~1.8 °C °longitude^{-1}. The smaller MAT gradient along the eastern flanks is partly due to the development with highlands of both stationary and mountain gravity waves, which promote cold air mass intrusion from the north and from the mountain top.

In general, surface temperatures in our CNTL experiment agree with western North American paleotemperature based on early Eocene floras (>49 Ma) from lower elevation basins and valleys (Figure 6). Simulated surface temperatures are systematically warmer than paleofloral temperatures estimated using the Climate Leaf-Analysis Multivariate Program (CLAMP), but are generally within 3 °C. Some of the disagreement may be due to an underestimate of surface temperatures by CLAMP, which tends to produce temperature estimates that are ~2 °C lower than those from the Leaf Margin Analysis method (Wing and Greenwood, 1993). A systematic underestimate of leaf size by CLAMP may cause the paleotemperatures to be too cool by an additional 1 °C (Peppe et al., 2010).

The dating of most Middle and Late Eocene floras is not precise enough to unambiguously assign them to a specific uplift scenario. Nevertheless, an apparent cooling trend inferred from the Late Eocene floras may be consistent with regional surface uplift. Paleofloras from Florissant (central Colorado), Salmon (central Idaho) and Copper Basin formations (upper northeast of Nevada) have temperature estimates ranging from 7.6 to 12.4 °C (Wolfe, 1994) much cooler than the nearby sites of early Eocene age such as Kisinger Lake (15.–16.8 °C) and Green River Formation (14.3–16.7 °C) (Figure 6). Although some of this cooling is undoubtedly associated with Late Eocene global climate cooling (Wolfe, 1994), it may also reflect the development of high elevations through topographic migration (Figure 5b-d).

2.4.2 Simulated early Eocene precipitation of western North America

Mean annual precipitation (MAP) in the CNTL experiment exhibits a northwest-southeast trend with maximum of 393.4 cm yr^{-1} in the Pacific Northwest region and minimum of 10.9 cm yr^{-1} over southwestern North America (Figure 5e). The inclusion of the highlands leads to formation of orographic precipitation on both sides of the mountains and precipitation minima on the eastern side of the highland interior (Figure 5f-h).

Windward precipitation occurs mainly during winter (December – February, Figure 5i-l) and results from forced ascent of westerly air masses over the mountain barrier. Diabatic cooling occurs on and around the top of the high Cordillera and facilitates condensation and snow formation. The southward propagation of the highlands significantly increases the amount of winter windward precipitation (Figure 5i-l) and the portion of precipitation falling as snow (from 10% in CNTL to 28%, 38%, and 54% in NHL, CHL, and SHL experiments averaged over 40 – 60° N, 120° – 110° W). In summer, warming of the mountain flank and weakening of the

Westerlies reduces relative humidity and moisture transport, decreasing precipitation along the higher latitude coast (50° – 60° N, 120° – 115° W, Figure 5m-p). On the western side of the highland peaks, localized increases of summer precipitation occur in the NHL and CHL experiments, likely due to cooling and condensation induced by high elevation.

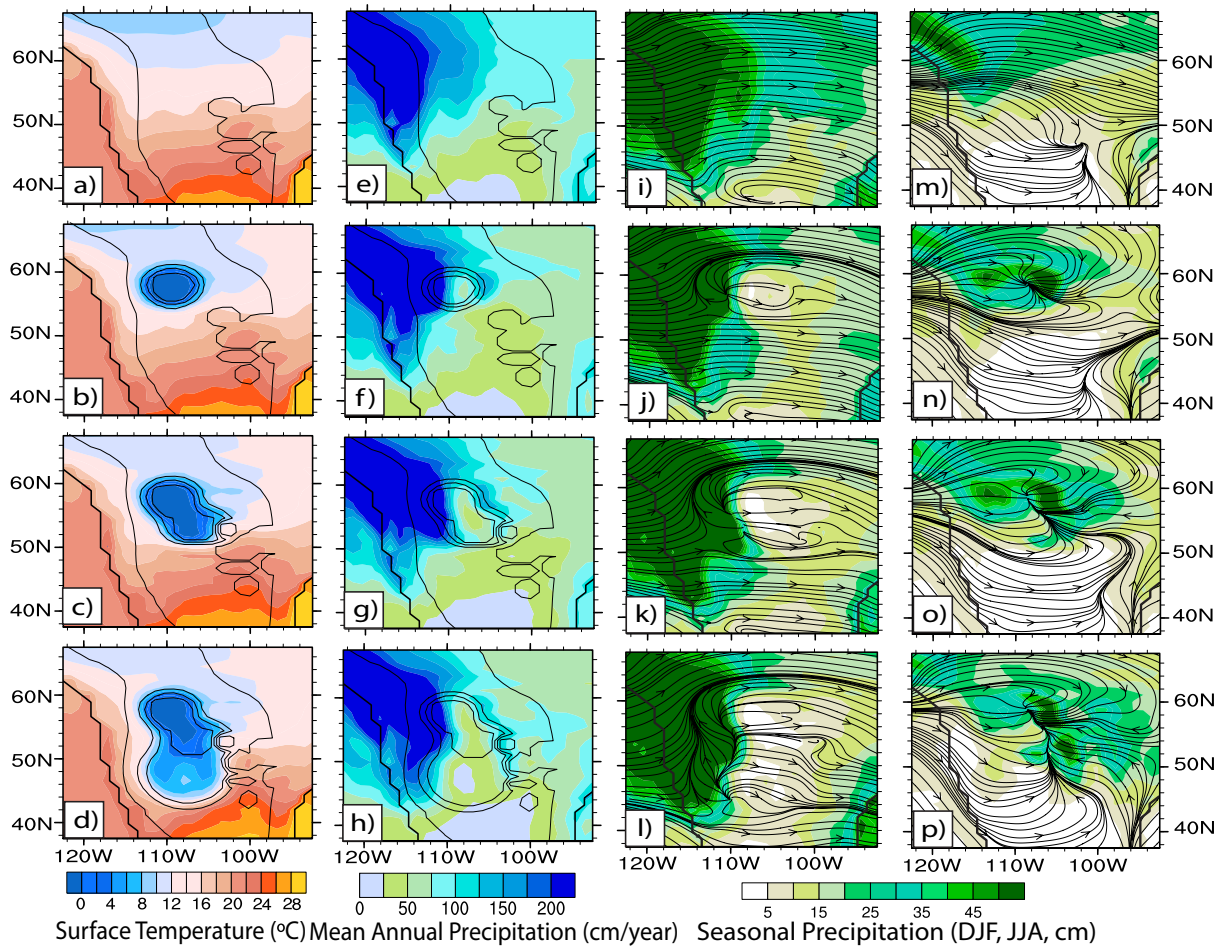

Figure 5 Simulated western North American climate for CNTL (first row), NHL (second row), CHL (third row), and SHL (fourth row) scenarios.
(a-d) Mean annual surface temperature (°C); (e-h) mean annual precipitation rate (cm yr^{-1}); (i-l) winter (December, January and February, DJF) precipitation (cm) and 850 hPa circulation (i-l); and (m-p) summer (June, July and August, JJA) precipitation (cm) and 850 hPa circulation. Thick black contours indicate the continental shoreline. Thin black lines in a-h represent elevation from 900 to 3600 m with 900 m interval. Notice the development of the paleo-North American Monsoon in o-p as indicated by summertime airflow from the paleo-Gulf of Mexico.

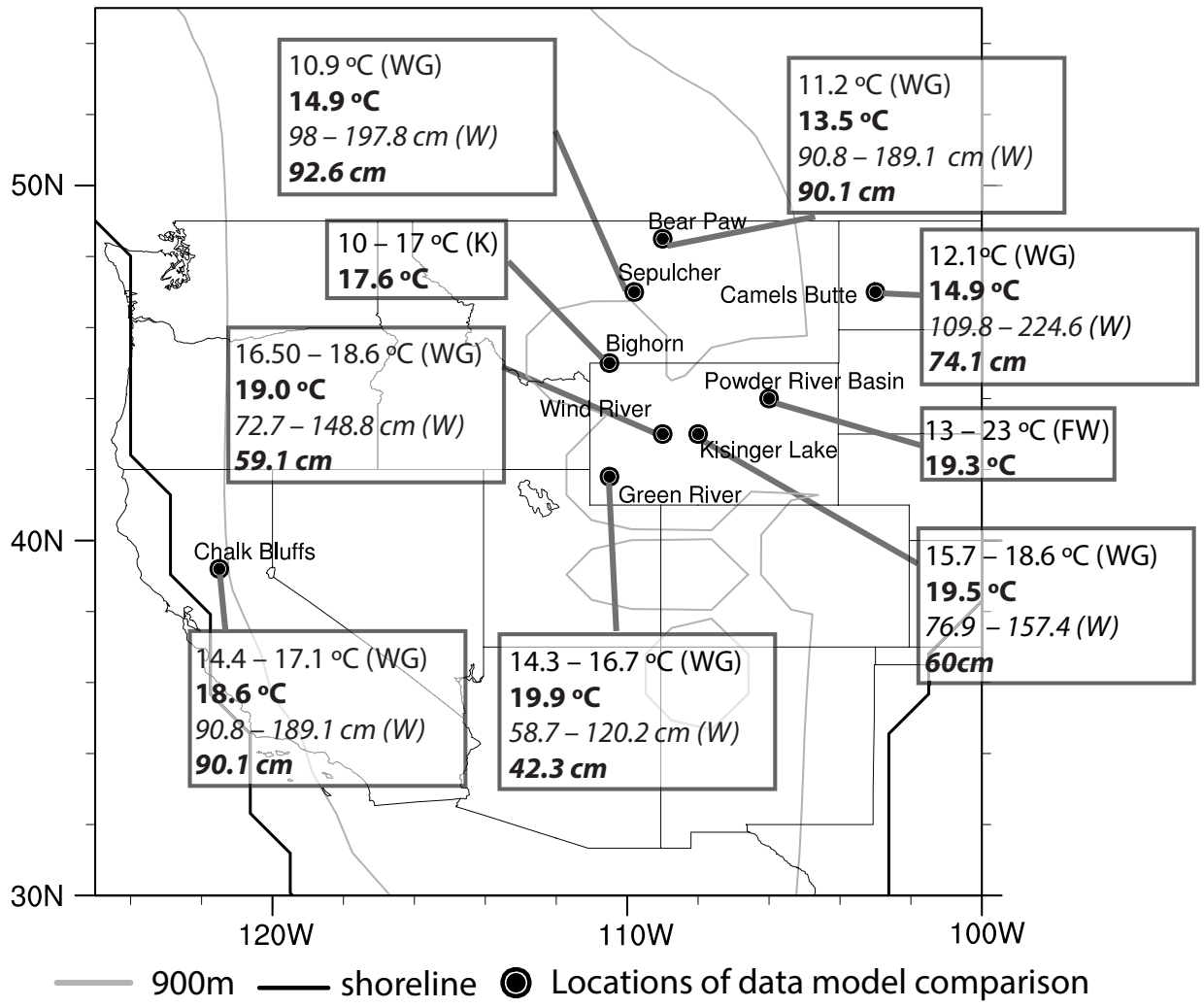

Figure 6. Comparison between simulated (bold font) and proxy (regular font) surface temperature and precipitation (in italics) reconstructed from paleoflora of western North America (black dots).
WG: Wing and Greenwood, (1993); W: Wilf et al. (1998); K: Koch et al. (1995); FW: Fricke and Wing (2004). The ranges of proxy temperatures are reported from the individual studies. The ranges of proxy precipitation are reported as the averages added with the uncertainties of estimations of precipitation.

Leeward precipitation falls mostly in summer (June – August, Figure 5m-p) with a substantial portion occurring as convective precipitation. The moisture source of leeward precipitation is generally thought to come from below cloud-base evaporation and/or mixing with moisture-bearing air masses other than those traveling directly across the mountains (Gat and Rietti-Shatti, 1999). Consistent with this interpretation, simulated middle-to-low atmosphere water vapor has high deuterium excess (14 – 16 ‰) over this region, indicating the likely

contribution of moisture from both surface and below cloud-base evaporation. The migrating topography induces north-to-south propagation of summer wetness in the lee of the highlands. As a result of surface uplift and topographic blocking, westerly flow is split into northern and southern branches (note streamlines in Figure 5m-p). These two branches converge in the lee of the highland, promoting frontal development between cold, dry air from the north and warm, moist air from the south and high precipitation rates in NHL and CHL (Figure 5m-p). The transport of Pacific moisture through the southern branch of the Westerlies is weaker in SHL due to blocking (compare streamline densities at 56° N, 120° W to 52° N, 110° W in Figure 5n-p). The southward propagation of high topography promotes southeasterly moisture transport from the Gulf of Mexico. This summer southeasterly flow, which emerges in the CHL case (Figure 5o) but is most strongly expressed in SHL, represents a seasonal wind reversal and, as such, signifies the development of the paleo-North American Monsoon system.

The annual mean precipitation in the CNTL simulation is within 30% of estimates based on early Eocene paleofloral reconstructions by Wilf et al. (1998). We speculate that the mismatch results from uncertainties related to taphonomical biases, leaf area analysis of fossil leaves and the possible underrepresentation in our simulation of local water bodies, such as small lakes and rivers. The pattern of precipitation is comparable to that simulated for the Paleogene using a higher resolution limited-domain model (Sewall and Sloan, 2006).

2.4.3 $\delta^{18}O_p$ response to surface uplift

In the absence of significant topography, simulated western North American $\delta^{18}O_p$ is mainly a function of latitude and continentality (Figure 7a). In the interior of the continent (between 115° and 90° W), $\delta^{18}O_p$ is zonal and decreases with latitude. Along the coastlines, $\delta^{18}O_p$ is high due to the proximity of ^{18}O- and D-enriched moisture sources.

In ECHAM5-wiso, $\delta^{18}O_p$ strongly decreases with surface uplift of the Western Cordillera (Figure 7b-d). Along the crest of the highlands, $\delta^{18}O_p$ drops by ~10‰ to values less than −18‰ forming sharp isotopic gradients on the flanks. With southward propagation of the highlands, precipitation in foreland areas east of 100° W become enriched in ^{18}O due to the contribution of moisture from the paleo-Gulf of Mexico (Figure 7d).

Proxy estimates of $\delta^{18}O_p$ derived from authigenic minerals require knowledge of the isotope exchange temperature, the temperature of the water from which the mineral precipitated. In the absence of this information, Mix et al. (2011) and Chamberlain et al. (2012) use

temperatures from paleofloral assemblages as the isotope exchange temperature. To compare simulated and proxy $\delta^{18}O_p$ directly and to eliminate differences due to surface temperature assumptions, we recalculate mineral-derived $\delta^{18}O_p$ using simulated surface temperatures (**Appendix A4**). Because isotopic fractionation has only a small temperature dependence (~0.2‰ $°C^{-1}$ at 25 °C for carbonate), most proxy $\delta^{18}O_p$ estimates change by ≤2‰. The exceptions are two samples from the Galisteo Basin of New Mexico (Davis et al. 2009), with ages of 39–49 (3.6‰) and 28–39 Ma (5.2‰), and two samples (2.1‰), with ages of 39–49 Ma, from eastern Wyoming (Sjostrom et al. 2006). These samples, all from low altitude basins, were originally assigned isotope exchange temperatures of 7.5 °C, 0 °C and 10.9 °C, much lower values than the simulated temperatures of 24.5 °C and 24.1 °C for the Galisteo Basin and 20.8 °C for eastern Wyoming. For comparison, modern mean-annual temperatures in the Galisteo Basin and eastern (Casper) Wyoming are ~11 and ~9 °C. Early Eocene paleotemperatures for the Wind River, Kisinger Lake and Powder River basin, located in central and eastern Wyoming, are 16.5 – 23 °C (Figure 6).

In Figure 7b-d, we compare simulated $\delta^{18}O_p$ from our three topography scenarios with temperature-adjusted proxy $\delta^{18}O_p$. Co-located simulated and proxy $\delta^{18}O_p$ agree within 2 ‰ at 60 % of sites (Figure 7b-d). Differences within this group have an average of 0 ‰ with a 1σ value of 1.1 ‰, indicating no systematic offset. More importantly, there is good correspondence in all three scenarios between very low values (<−16 ‰) of simulated and proxy $\delta^{18}O_p$. Mix et al. (2011) use mineral $\delta^{18}O_p$ from four sites (Princeton Basin, Sage Creek Basin, Copper Basin, and Elko Basin) to estimate maximum highland elevations (Figure 7, values in black). Our simulated $\delta^{18}O_p$ at these sites is the same or slightly lower (with magnitude < 2‰) than the mineral $\delta^{18}O_p$ (Figure 7, values in red). The good match indicates that surface uplift is a reasonable hypothesis for explaining temporal trends in the mineral proxies.

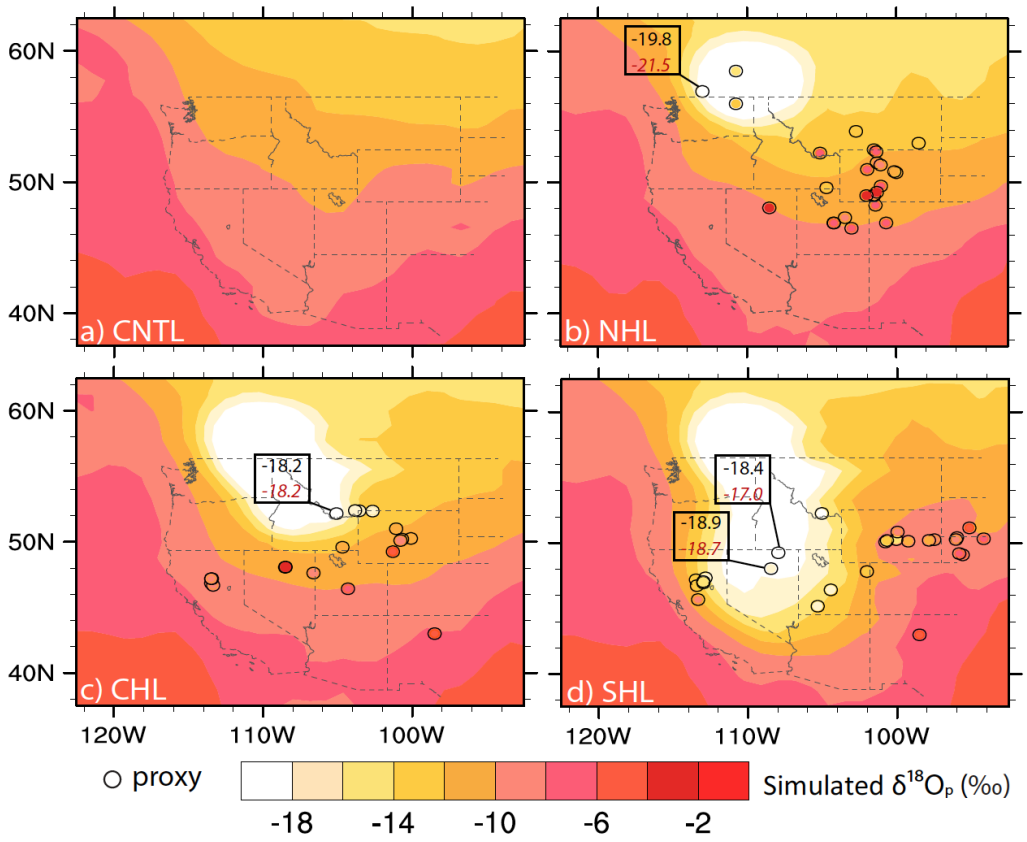

Figure 7 Comparison of proxy and simulated $\delta^{18}O_p$. Simulated values of $\delta^{18}O_p$ are shown for the (a) CNTL, (b) NHL, (c) CHL, and (d) SHL experiments.
Following Mix et al. (2011) and Chamberlain et al. (2012), the NHL, CHL, and SHL scenarios represent topographic conditions in western North America ranges across approximately pre-49 Ma of Eocene, 48 – 39 Ma, and 38 – 28 Ma. Proxy δ18Op from authigenic minerals corresponding in age to these time intervals are overlain as filled circles. Simulated (black font) and mineral (red font) $\delta^{18}O_p$ are shown for the Princeton Basin (b), Sage Creek Basin (c), and Copper (north) and Elko (south) Basins (d). U.S. state borders are shown to simplify the referencing of sample locations. The borders have been modified to account for Neogene Basin and Range extension by narrowing Nevada by ~2° longitude as in Figure 3.

$\delta^{18}O_p$ difference for the remaining 40% of sites averages −2‰ with a 1σ value of 4.5‰. Many of the points of disagreement occur in the NHL case and are located in the Laramide foreland basins east of 102° W and in the Elko Basin in northeast Nevada, regions of low elevation. The mismatch at these lowlands may be due to surface hydrologic processes that are not included in ECHAM5-wiso. Many of the enriched $\delta^{18}O$ values from the Laramide foreland basins and northeastern Nevada and central Utah derive from lacustrine carbonates and limestones. The hydrological balance of inland lakes is a function of riverine, groundwater, and precipitation inputs, and evaporative losses. Unless precipitation dominates the system, lake

water $\delta^{18}O$ may not reflect $\delta^{18}O_p$. In fact, Horton et al. (2004), Bowen et al., (2008) and Davis et al. (2009) conclude that Elko Basin, Flagstaff Basin and other Laramide foreland basins have all been affected by significant evaporation.

Notable mismatches also occur at four high-elevation sites, including two in the core of the NHL (Figure 7b) and two on the eastern flank of the SHL (Figure 7d). The mineral samples from the NHL have $\delta^{18}O_p$ of −13.8 and −15.8‰, values that correspond to simulated $\delta^{18}O_p$ at elevations of ~2000 m (Figure 8a). The mineral $\delta^{18}O_p$ at these locations are converted from the δD of mylonitic quartzite in equilibrium with the meteoric water at the Columbia River detachment bounding Kettle (northeast Washington) and Shuswap metamorphic core complex (southeast British Columbia). The reconstructed $\delta^{18}O_p$ of these locations is likely more enriched than the actual meteoric water due to water-rock interaction (Mulch et al., 2007). However, the isotopic enrichment could also indicate that the highland elevations are overestimated, or that these proxies record elevation of the detachment, which may be lower than the mean elevation. Mineral $\delta^{18}O_p$ on top of the eastern flank of the SHL (the Claron Basin and the Flagstaff Basin) is lower by 2 – 3‰ than the simulated $\delta^{18}O_p$.

2.4.4 Analysis of isotopic fractionation due to lifting

Paleoaltimetry studies have traditionally assumed that the isotopic composition of an ascending air mass fractionates through rainout as a result of adiabatic cooling and condensation (for example, Blisniuk and Stern, 2005). This assumption is the premise for both the application of empirical $\delta^{18}O_p$-lapse rates and RDMs to paleoaltimetry. To evaluate this assumption, we compare GCM and RDM simulations of $\delta^{18}O_p$ across the highlands (Figure 8a-f). RDM predictions are based upon GCM-initial $\delta^{18}O_v$, and with moisture sources located both west and east of the flanks of individual highland (see Section 2.3.2 for details). Justification for an eastern moisture source is shown in Figure 5n-p, which illustrates that summer flow onto the eastern flanks of the highlands is predominantly easterly across the continental interior. Our one-dimensional RDM simulations of $\delta^{18}O_p$ vary solely as a function of altitude; the horizontal trajectory of the parcel is not considered. To more straightforwardly compare the GCM and RDM, we remove $\delta^{18}O_p$ spatial variability in our GCM simulations by averaging annual $\delta^{18}O_p$ over a range of latitudes centered on the NHL, CHL and SHL.

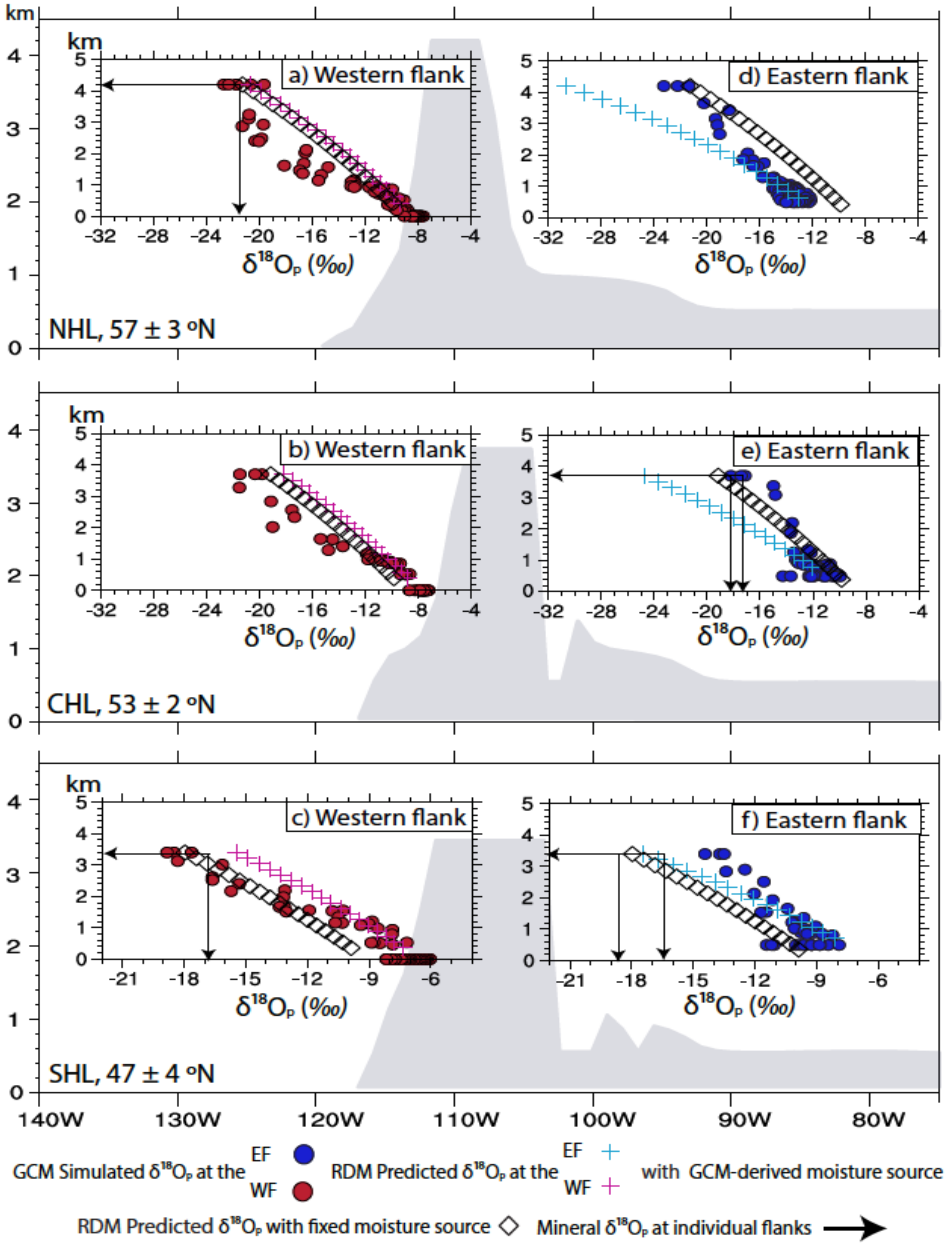

Figure 8 Comparison of GCM and RDM $\delta^{18}O_p$ along the western and eastern flanks of the northern (NHL, (a) and (d)), central (CHL, (b) and (e)), and southern (SHL, (c) and (f)) highlands.

ECHAM5-wiso $\delta^{18}O_p$ is shown as filled circles; $\delta^{18}O_p$ simulated by the RDM with fixed initial $\delta^{18}O_v$ and moisture from the west as open diamonds (values at the eastern flank mirrors those at the western flank since they share the same moisture sources); and $\delta^{18}O_p$ simulated by the RDM with GCM-derived initial $\delta^{18}O_v$ and moisture from both western and eastern flank as crosses. Symbols are shaded red and blue to indicate their location on either western (WF) or eastern flanks (EF). The extent of western and eastern slopes is shown in Figure 4a-c. Arrows point to mineral $\delta^{18}O_p$ values at 4200 m of NHL, 3700 m of CHL and 3400 m of SHL. Notice that the elevations of the mineral-derived $\delta^{18}O_p$ are uncertain. The best estimate of the elevation is where the mineral-derived $\delta^{18}O_p$ values correspond to simulated $\delta^{18}O_p$.

The relationship of mean-annual $\delta^{18}O_p$ with altitude differs substantially between the GCM and RDM with *GCM-moisture source* (dots and crosses in Figure 8a-f). GCM-simulated $\delta^{18}O_p$ decreases nonlinearly with elevation on both flanks. The isotopic lapse rate is greatest at elevations lower than ~2000 m, particularly on western slopes, and decreases to nearly 0 at higher elevations in the NHL and CHL cases (filled circles in Figure 8a, b). In comparison, RDM-simulated $\delta^{18}O_p$ decreases almost linearly with elevation with the highest lapse rate on the eastern flanks (crosses in Figure 8d-f). At peak elevations on the western flank, RDM and GCM $\delta^{18}O_p$ are relatively similar in NHL and CHL, differing by about +1‰ (NHL) and −1‰ (CHL) (compare crosses and filled circles in Figure 8a, b). RDM and GCM $\delta^{18}O_p$ differences are much larger, about −3‰, in SHL (compare crosses and filled circles in Figure 8c). However, due to differences in isotopic lapse rates, the $\delta^{18}O_p$ difference is much larger (by as much as 5‰) at intermediate elevations between ~1000 and 3000 m (Figure 8a, b). $\delta^{18}O_p$ differences are more pronounced on the eastern slopes, where the RDM isotopic lapse rates are very high, leading to very low $\delta^{18}O_p$ (compare light grey markers in Figure 8a-c). At peak elevations (4000 m) on the eastern flank, the RDM and GCM $\delta^{18}O_p$ differ by approximately 9 (NHL), 6 (CHL) and 4‰ (SHL).

The influence of assuming a constant moisture source is demonstrated by the difference between experiments with *fixed*- and *GCM*-moisture sources (Figure 8a-c). Along the western flanks, $\delta^{18}O_p$ is offset by the difference in the composition of the initial condensate, which is minimal for NHL and CHL but approximately −3‰ for SHL. Along the eastern flank, $\delta^{18}O_p$ differences are greater, up to 6 – 8‰ at high elevations of the NHL and CHL, and result from differences in temperature and humidity of the moisture source and the $\delta^{18}O_p$ of initial condensate. Adiabatic cooling and rainout are more dramatic for cooler and drier moisture sources at the eastern flank, which leads to larger adiabatic lapse rate of the $\delta^{18}O_p$.

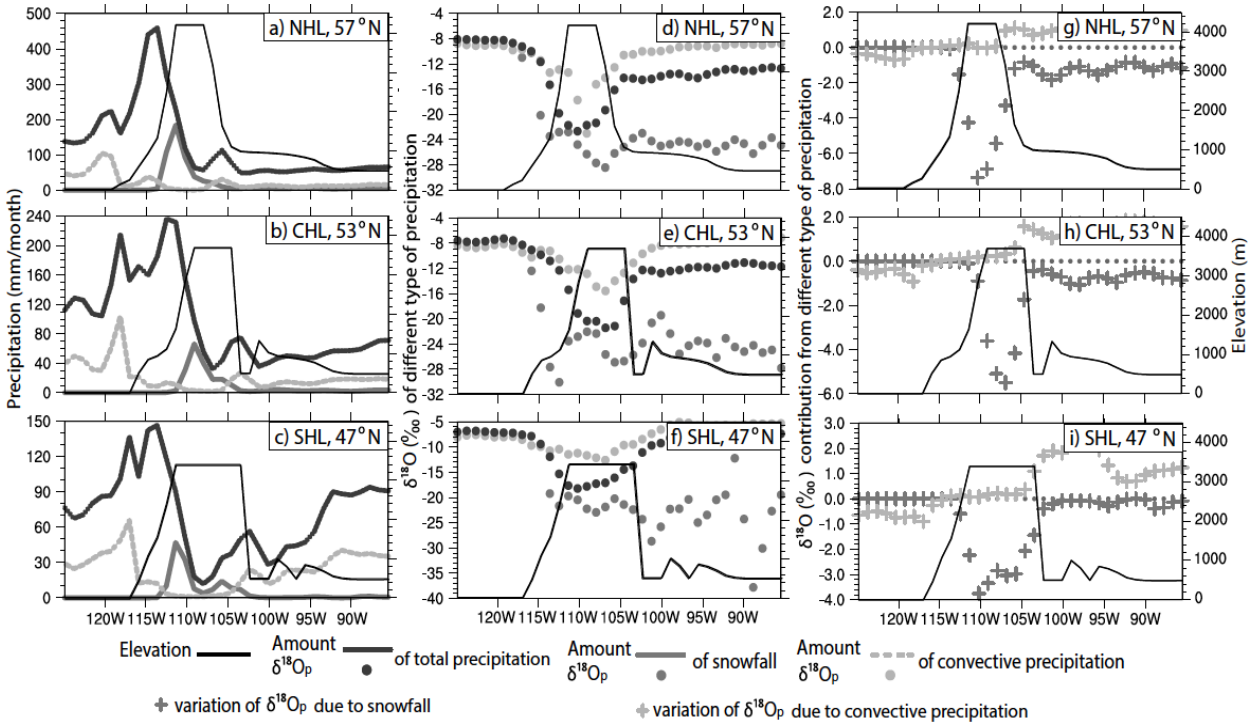

Figure 9 Simulated west-east distribution of the amount (a-c, left column) and $\delta^{18}O$ (d-f, middle column) of total precipitation (dark gray), snowfall (medium gray) and convective precipitation (light gray).
The $\delta^{18}O_p$ variations (g-i, right column) due to inclusion of snowfall (medium gray) and convective precipitation (light gray) at 57 locations on either western (WF) or eastern flanks (EF). The extent of western and eastern slope-scale (a-i, black). The snowfall is from both large-scale and convective precipitation, but it is clearly from large-scale at the western flank and likely from both at the eastern flank.

Our comparison of $\delta^{18}O_p$ estimated by ECHAM5-wiso and an RDM emphasizes the importance of the interaction of different airflow regimes and precipitation physics other than rainout on the isotopic fractionation of vapor and precipitation in the GCM. In the following sections, we investigate these processes.

2.4.4.1 Influence of precipitation type on $\delta^{18}O_p$

ECHAM5-wiso simulates multiple precipitation phases (snow and rain) and types (convective, large-scale). At low elevations (≤ 1500m) on the western flanks of the NHL, CHL, and SHL, the bulk of the precipitation is in the form of large-scale rainfall. In this region, GCM-simulated $\delta^{18}O_p$ is similar to the RDM prediction. The difference between GCM- and RDM-simulated $\delta^{18}O_p$ increases as contributions from snowfall and convective precipitation increase at higher elevations of the western and eastern flank. Snow and convective precipitation contribute differently to the $\delta^{18}O_p$ of total precipitation (Figure 9d-f). Snow is more depleted in ^{18}O than

other precipitation types, because ice crystal condensation is subject to kinetic fractionation due to the lower diffusivity of the heavy isotope in air (Jouzel and Merlivat, 1984); and, isotopic exchange between snowfall and the environment through evaporation, mixing, and re-condensation below the cloud base is greatly reduced (Jouzel and Merlivat, 1984; Gat, 2010). Convective precipitation is enriched in ^{18}O relative to the total precipitation across the highlands, but is more depleted at the coast (Figure 9d-f). Leeside convective precipitation is enriched in ^{18}O likely due to intense evaporation of rain droplets and/or mixing with isotopically enriched moisture, a mechanism proposed to explain the enrichment of modern leeside precipitation (Gat and Rietti-Shati, 1999). This process is the counterpart to the "amount effect" in tropic regions where limited sub-cloud evaporation and the input of ^{18}O depleted moisture occurs, causing isotopic compositions to be relatively low (Risi and Vimeux, 2008).

Snowfall occurs on the western flanks at elevations higher than 1000 m and is the main form of precipitation on the western highlands (Figure 9a-c, medium grey lines). Convective precipitation is common over lowlands and on the flanks but is absent at the highland top. On average, it makes up one-third to one-half of total annual precipitation on the eastern flanks (Figure 9a-c, light grey lines), and increases to one-half to three-fourth of total precipitation during summer (not shown). Moist convection is almost absent in winter, indicating a strong seasonality of the ^{18}O enrichment effect due to moist convection. The relative contribution of snow and convective precipitation to $\delta^{18}O_p$ is estimated as the difference of $\delta^{18}O_p$ in the absence of snow or convective precipitation:

$$\Delta\left[\delta^{18}O_p\right]_i \approx r_i \times \left(\left[\delta^{18}O_p\right]_i - \left[\delta^{18}O_p\right]_o\right)$$

where $[\delta^{18}O_p]_i$ is the $\delta^{18}O_p$ value of snow or convective precipitation; $[\delta^{18}O_p]_o$ is the $\delta^{18}O_p$ of the remaining precipitation; and r_i is the ratio of snow or convective precipitation to total precipitation.

High-elevation snowfall reduces the total $\delta^{18}O_p$ across the highlands and by up to 4–8‰ at the peaks (Figure 9g-i). Convective precipitation increases $\delta^{18}O_p$ on the leeside of the highlands by up to ~2‰ (Figure 9g-i, light grey cross). Snowfall and convective precipitation influence $\delta^{18}O_p$ in opposing ways on the eastern slopes. The relative amounts of convective precipitation and snowfall and their contribution to total precipitation $\delta^{18}O_p$ are not necessarily independent; snow can form from condensation related to large-scale and/or convective

processes. Condensation of convective snow enriches the remaining vapor from which subsequent convective precipitation might condense. This possibility is supported by the anti-correlation between snow and convective precipitation $\delta^{18}O_p$ on the eastern lowlands of the NHL and CHL cases (Figure 9g-h).

Independent geological lines of evidence support the simulation of both snowfall on the highlands and seasonally arid conditions at the leeside of the highlands. Eocene lacustrine bivalves collected from the Green River Basin (Norris et al., 1996) and Power River Basin (Dettman and Lohmann, 2000; although disputed by Morrill and Koch, 2002) and fossil tooth enamel (Fricke, 2003; Fricke and Wing, 2004) and paleosol carbonates collected from the Big Horn Basin (Koch et al., 1995) record seasonal low $\delta^{18}O$ that are purported to represent seasonal snow melt and drainage from adjacent highlands. Pedogenic features (Bown and Kraus, 1981), evaporite deposits (Smoot, 1983), and dry-tolerant paleoflora (Wolfe, 1994; Wing and Greenwood, 1993; Wilf et al., 1998) have all been interpreted to indicate seasonal drought or evaporative conditions on the leeside of the highlands. In addition, paleoprecipitation reconstructions from paleoflora within three foreland basins around Green River, Kisingers Lakes and Wind River support high precipitation seasonality with one-half of the precipitation falling in three growing months and ≤ 10% in three dry months (Wing and Greenwood, 1993), and lend support to our simulations of intense summer precipitation and winter dryness (Figure 5m-o).

2.4.4.2 Influence of vapor mixing on $\delta^{18}O_p$

Isotopic effect of advective vapor mixing is most pronounced on the western slopes of the highlands. In this region, upslope flow contributes substantially to vapor ^{18}O enrichment. In the middle troposphere (500–600 hPa), $\delta^{18}O_c$ advection is alternately positive, negative and positive at the western flank, highland top and eastern flank of NHL and CHL. This pattern reflects vertical advection associated with a standing gravity wave (Figure 10a and 10b, vectors and gray contour) that develops as the Westerlies encounter high topography. This standing gravity wave is not as well pronounced in SHL; as a result, the $\delta^{18}O_c$ advection across the SHL is determined by both the vertical and horizontal advection of the air mass. Positive $\delta^{18}O_c$ advection is brought by ascending air masses from lower altitudes at the western flanks and by southeasterly flow from lower latitudes at the eastern flank (Figure 5p), which lead to locally high $\delta^{18}O_v$ regions.

^{18}O-enrichment due to mixing can explain the flattening of the GCM-simulated $\delta^{18}O_p$-elevation relationship of NHL (Figure 8a) and CHL (Figure 8b) at elevations >2000 m. The influence of mixing on the western slope of the SHL is less apparent (Figure 8c); precipitation likely forms over a range of altitudes that are both isotopically depleted and enriched through mixing (Figure 10c). The $\delta^{18}O_c$ variations due to mixing at the eastern flank are generally small with magnitudes of ≤2‰ and vary in sign from the surface to the middle troposphere.

2.4.4.3 Influence of moisture recycling through surface exchange on $\delta^{18}O_p$

In arid, continental regions, observed $\delta^{18}O_p$ lapse rates are often smaller than expected based on open system Rayleigh distillation models (for example, Rowley and Garzione, 2007; Blisniuk and Stern, 2005; Lechler and Niemi, 2011). This phenomenon, referred to as a "pseudo-altitude effect", is thought to result from an increase in evaporative enrichment of a rain droplet as the falling distance increases from the top to the bottom of the mountain (Moser and Stichler, 1971). Another potentially important factor is the ^{18}O-enrichment of vapor through recycling at the land surface. During the recycling process, surface evaporation enriches and returns much of the precipitation to the boundary layer. In our simulations, vapor recycling is vigorous on the leeside eastern flanks, where evaporation rates are typically 70 to 76% of precipitation rates. Moisture recycling is less important at the western flank, given that the air masses are more humid and the amount of evaporation is less than 30% of precipitation.

We have modified the RDM to account for vapor recycling using the recycling potential (see *Rayleigh Distillation Model of Adiabatic Condensation (RDM)* above) and estimated using GCM-simulated rates. Recycling potentials for the NHL, CHL and SHL experiments are 0.68, 0.73, and 0.76. Accounting for vapor recycling in the RDM increases $\delta^{18}O_p$ on the eastern slopes by ~3 to 5‰, reducing the isotopic lapse rate and the discrepancy between GCM and RDM $\delta^{18}O_p$ in this region (Table 2, Figure 11a-c).

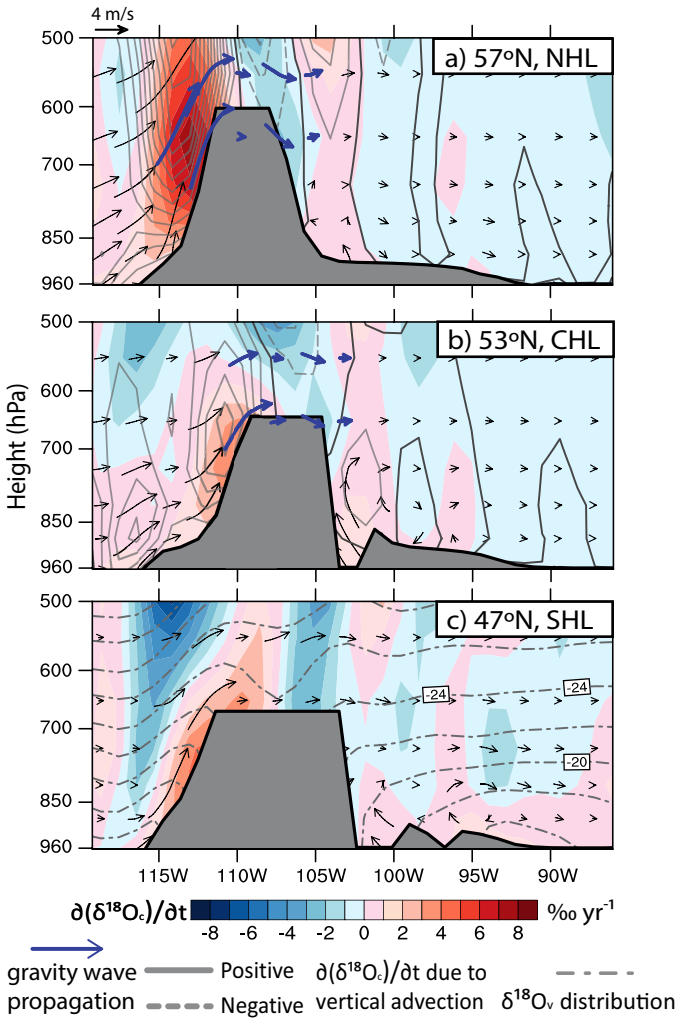

Figure 10. Zonal distribution of variations of $\delta^{18}O$ of condensate ($\frac{\partial \delta^{18}O_c}{\partial t}$) due to the total (shaded) advection of moisture estimated at (a) 57°N of NHL case, (b) 53°N of CHL case and (c) 47°N of SHL case.

Solid and dashed grey contours in (a) and (b) show positive and negative $\frac{\partial \delta^{18}O_c}{\partial t}$ at interval of 0.5‰ yr^{-1} due to vertical advection of moisture. Dotted grey contours in (c) shows the zonal distribution of $\delta^{18}O_v$. The zonal circulations and mountain gravity wave trajectories are shown in black and thick blue arrows.

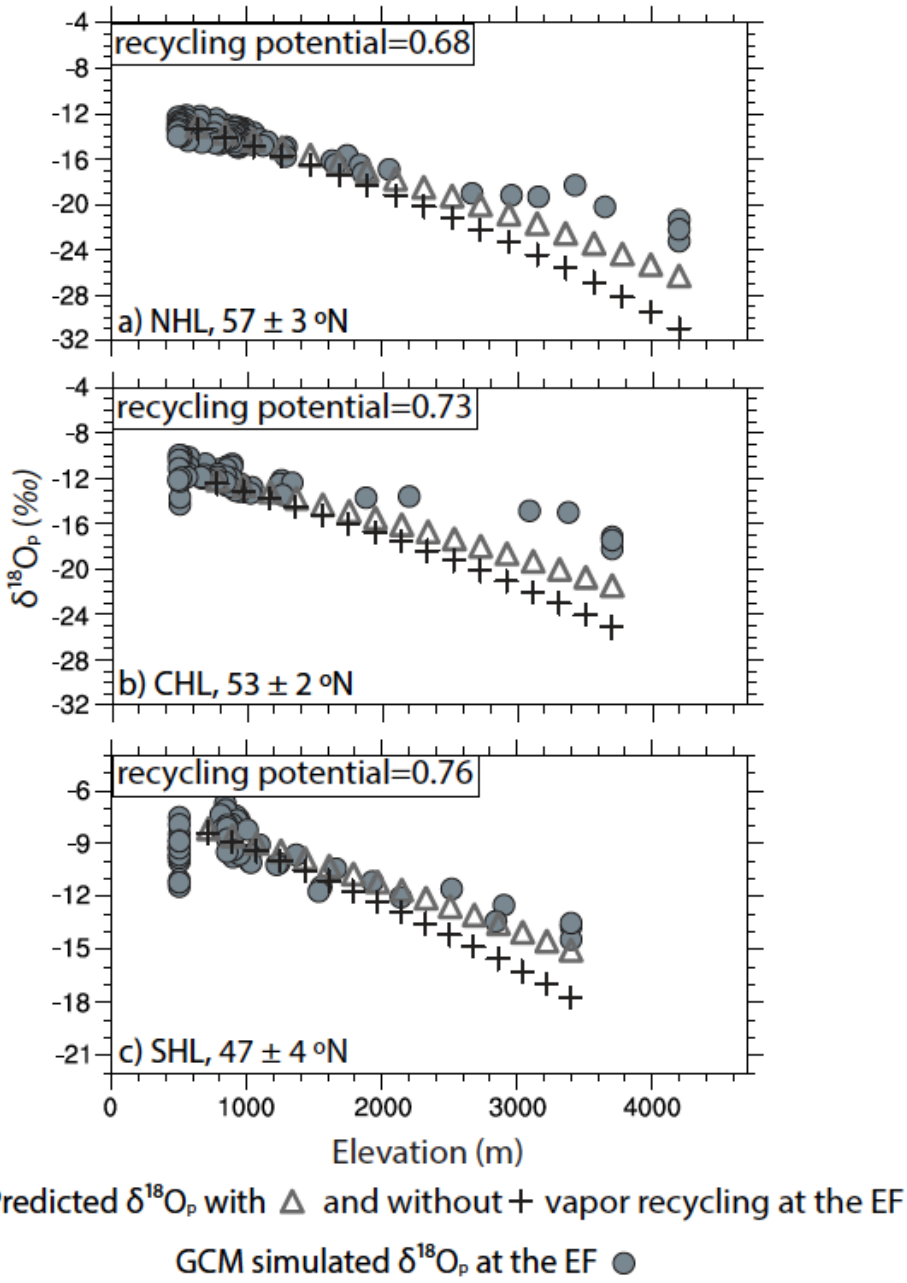

Figure 11 Comparison of $\delta^{18}O_p$ simulated by GCM, RDM and RDM with vapor recycling on the eastern flanks (EF) of (a) northern (NHL), central (CHL), and southern (SHL) highlands.
In a-c, ECHAM5-wiso $\delta^{18}O_p$ is shown as filled circles; RDM $\delta^{18}O_p$ with moisture recycling as open triangles; RDM $\delta^{18}O_p$ without moisture recycling as crosses. The incorporation of moisture recycling on the lee of the highlands increases RDM $\delta^{18}O_p$ by several per mil, bringing it in closer agreement with GCM $\delta^{18}O_p$.

Table 2 Contribution of physical processes to $\delta^{18}O_p$ in orographic regions.
Values represent the approximate isotopic contribution (‰) of each process to the local $\delta^{18}O_p$ simulated by ECHAM5-wiso and are shown for the three topographic scenarios.

		Precipitation type[1]	Total mixing[2]	Varying moisture sources[3]	Vapor recycling[4]
NHL	Western flank	−4 to −8	+5 to +8	NA	NA
	Eastern flank	+2	NA	−8 to −10	+5
CHL	Western flank	−3.5 to −6	+4	NA	NA
	Eastern flank	+2	NA	−6	+3
SHL	Western flank	−2 to −3	NA	+3	NA
	Eastern flank	+2	NA	NA	+3

Note: [1]Calculated as the amount weighted difference of $\delta^{18}O_p$ of snowfall (western flank) or convective precipitation (eastern flank) minus the $\delta^{18}O_p$ in the absence of snowfall or convective precipitation at high elevations. [2]Estimated as the advection potential of condensates along the flank. [3]Measured as the difference of simulated $\delta^{18}O_p$ by Rayleigh distillation model between using *GCM* and *fixed moisture source* at high elevations. [4]Estimated as the RDM simulation with the vapor recycling ratio minus without the vapor recycling ratio. NA: Not appreciable; the contribution is small.

2.4.4.4 Influence of moisture sources on $\delta^{18}O_p$

Moisture sources are expected to change as circulation patterns evolve in response to surface uplift (Figure 5i-p). Back trajectory analyses of air parcels originating on the mountain flanks are performed to identify moisture sources in each topographic scenario (Figure 12 and 13). In the CNTL case, low-level airflow over western North America is predominantly westerly and originates from the northern side of the Pacific subtropical high (Figure 12a-c, colored thin lines). Over the continent, flow splits into northern and southern branches at ~50° N (hereafter referred to as "split flow"; gray lines with black arrows in Figure 12a-c) in response to the development of high-pressure ridges over the western side of the topography.

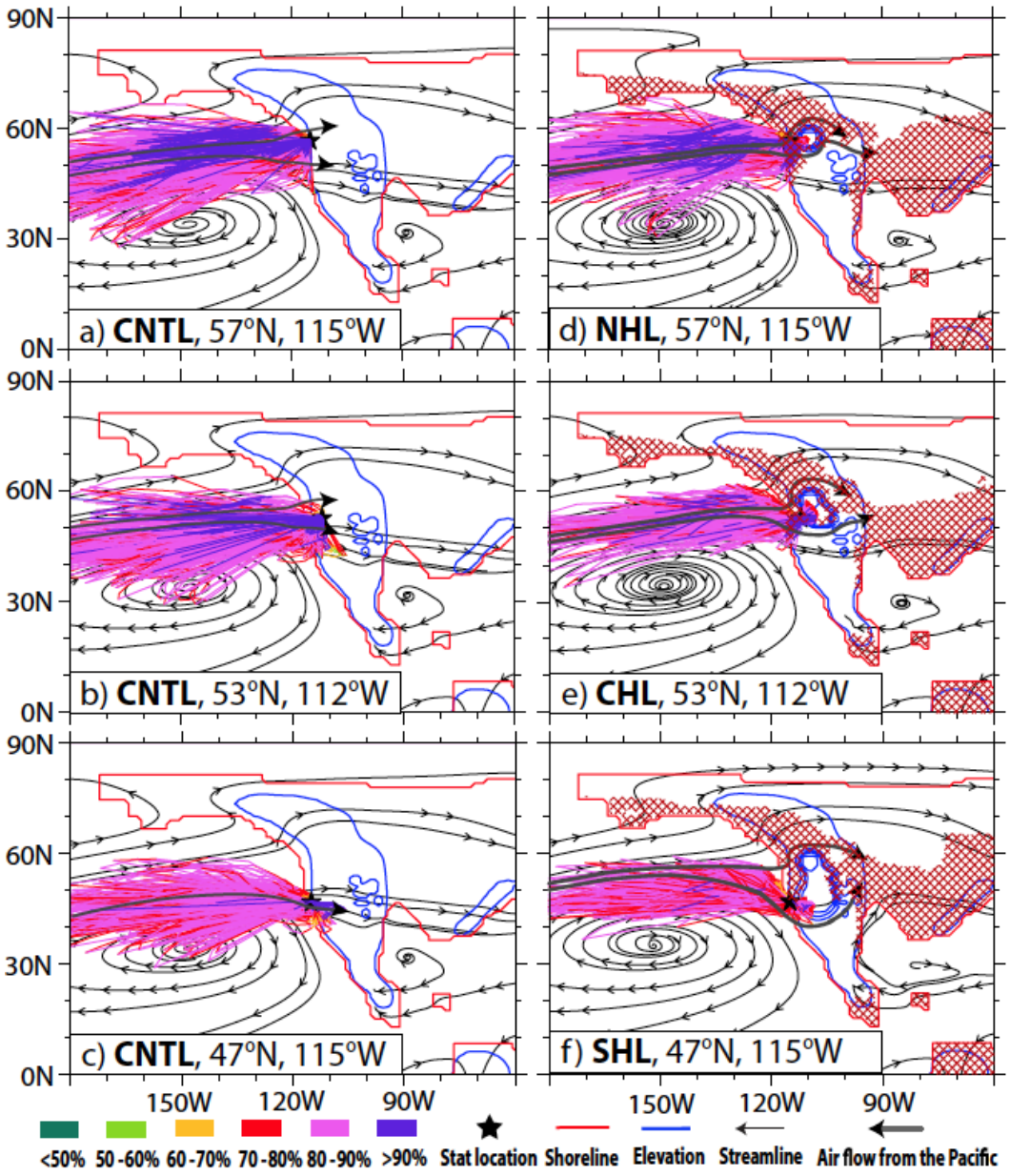

Figure 12. Back trajectory analysis of highland air parcels from the western flank of highlands. The 7-day back trajectory location and relative humidity of air parcels are shown (as colored thin lines) for CNTL (a-c) and NHL (d), CHL (e), and SHL (f). Each line segment is colored with the average relative humidity of a single trajectory within one time interval. Also shown in each figure are the low-level circulation (streamlines, averaged from 850 to 1000 hPa); the start location of back trajectory (black star); topography (blue line); airflow path (grey line with black arrowhead); and the continental shoreline (red line). Areas with evaporation greater than 40 cm/month are indicated by red stipple. Notice that 1) topography enhances separation of the northern and southern airflow paths (compare NHL, CHL, and SHL scenarios with the CNTL case); and 2) air parcels on the SHL tend to originate from more southerly sources in comparison to those on NHL and CHL.

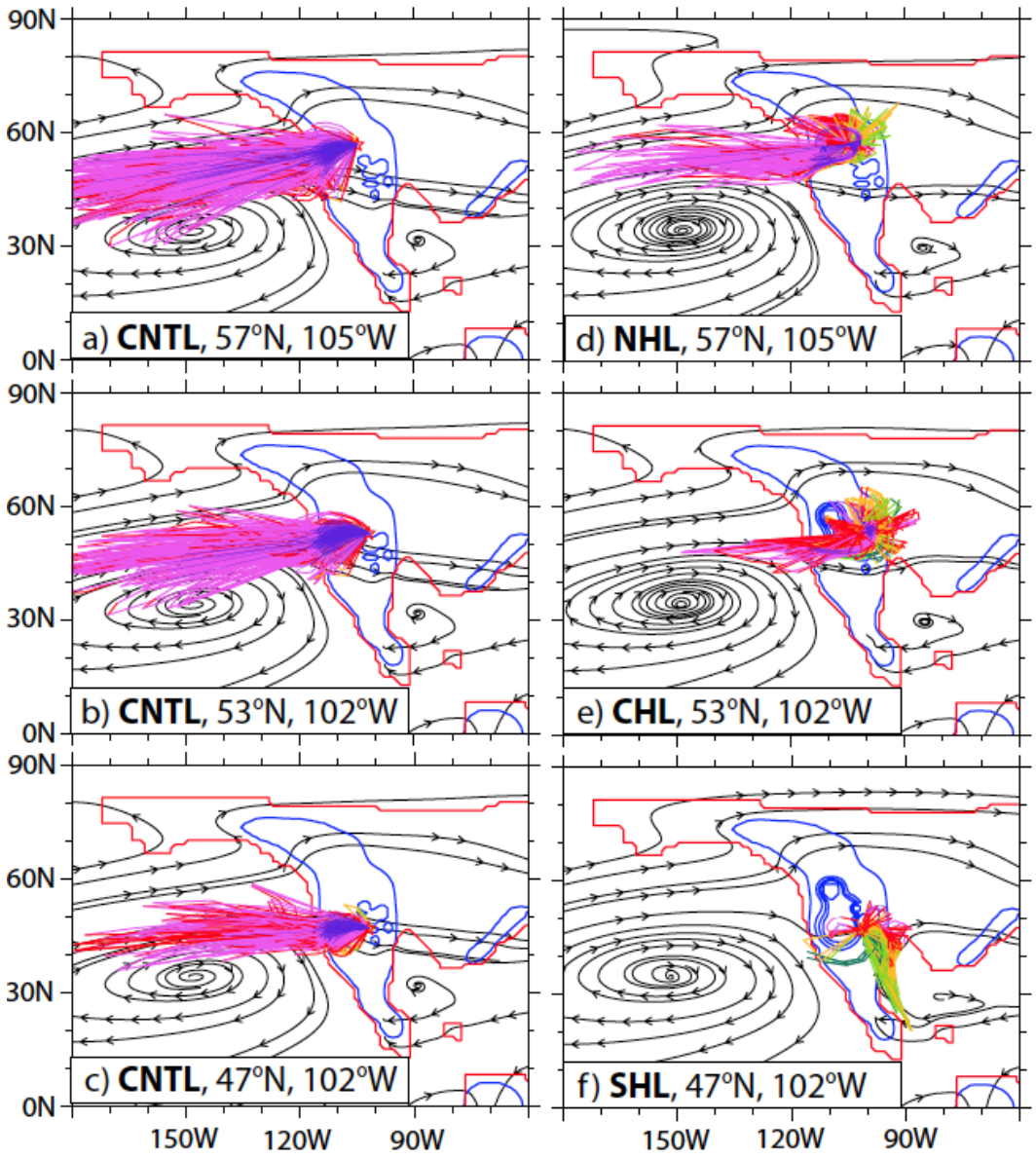

Figure 13. Same as in Figure 12, but for air parcels on the eastern flank of CNTL, NHL, CHL and SHL.
Note that CNTL (pre-uplift) moisture sources (colored thin lines) originate mainly (not entirely) from the Pacific Ocean. In the NHL, CHL, and the SHL (post-uplift) scenarios, a greater portion of moisture sources to the leeside of the highlands originates from the continental interior and the paleo-Gulf of Mexico.

Topographic uplift and southward propagation enhances the separation of northern and southern branches by strengthening the high-pressure ridge to the west and partially blocking the airflow. The split flow affects the moisture path, which then influences the isotopic composition of vapor. At the western flank, all three highlands (NHL, CHL and SHL) receive air parcels that

originate over the northeast Pacific. Air parcels are transported by westerly flow to the NHL and CHL (Figure 12d-e). Air parcels at SHL, however, are transported across warmer low-latitude seawater by northwesterly winds following the southern branch of the split flow along the coast (Figure 12f). As a result, the moisture source of SHL is more humid and more enriched in ^{18}O than the moisture source of the NHL and CHL (Figure 4a-c). Galewsky (2009) reports based on a series of simulations with idealized topography that blocking and lateral deflection by high topography reduces orographic precipitation and increases $\delta^{18}O_p$. In our simulations, blocking is not complete; flow ascends the western flanks, promoting orographic precipitation (Figure 5e-l, Figure 10).

Surface uplift changes moisture transport to the lee of the mountains as well. In the absence of high topography, air parcels are transported to the east flank by a mixture of both northern and southern branches of the split flow (colored thin lines in Figure 13a-c). With uplift, leeward moisture in NHL and CHL mostly derives from the southern branch of the split flow (Figure 13d-e). In the SHL scenario, the paleo-Gulf of Mexico is the dominant source of leeside moisture (Figure 13f). Surface uplift also introduces strong precipitation and circulation seasonality on the leeside of the mountains (Figure 5i-p).

Eastern flank $\delta^{18}O_p$ is strongly influenced by the source of moisture. Moisture from the Pacific Ocean and land evaporation has relatively low $\delta^{18}O_v$ due to greater rainout over long travel distances and evaporation input from isotopically depleted inland sources. In contrast, moisture from local lakes distributed within the Laramide basins and the paleo-Gulf of Mexico is enriched in ^{18}O. As a result of these differences, eastern flank $\delta^{18}O_p$ of NHL and CHL, most of which is derived from a mixture of ^{18}O-depleted land evaporation and east Pacific vapor with limited contribution from lakes (Figure 12d-e, stippled pattern shows evaporation) and the paleo-Gulf of Mexico (Figure 13d-e), is relatively low (Figure 4a-c). On the eastern flank of SHL, the contribution from lake evaporation (Figure 12f, stippled pattern) and Gulf of Mexico moisture is greater (Figure 13f) and so is the $\delta^{18}O_p$.

2.5 Discussion

2.5.1 Rayleigh Distillation as a model for isotopic fractionation of condensation

The challenge of stable isotope paleoaltimetry is to accurately translate mineral proxy $\delta^{18}O_p$ to surface elevation. Modern empirical $\delta^{18}O_p$-elevation relationships are useful for calibration in the modern climate under the existing topographic regime. However, regional

climate change related to both uplift (Poulsen et al., 2010) and global climate (Poulsen and Jeffery, 2011) alter these relationships, rendering the use of modern isotopic lapse rates for stable paleoaltimetry questionable at best. Incidentally, paleoaltimetry estimates using terrestrial paleotemperature proxies (for example, clumped isotopes) and modern temperature lapse rates are prone to many of the same uncertainties that plague isotope lapse rates. In our experiments, $\delta^{18}O_p$ lapse rates vary across the western North American Cordillera and are different from modern empirical lapse rates. $\delta^{18}O_p$ lapse rates on the western flanks of the NHL, CHL and SHL are not linear and differ substantially at low and high elevations. Although $\delta^{18}O_p$ varies with elevations in a more linear manner at the eastern flanks of the Cordillera, the $\delta^{18}O_p$ lapse rates vary with latitude and are influenced by regional climates that are different from modern. As such, applying a $\delta^{18}O_p$ lapse rate-elevation relationship to infer paleoaltimetry in the North American Cordillera is unjustified.

RDMs offer some advantages for paleoaltimetry over modern empirical $\delta^{18}O_p$-elevation relationships. Chief among these is that RDM estimates are not based on modern temperature and humidity conditions, and can account for isotopic fractionation during adiabatic lifting and vapor condensation under different climate conditions. However, as this study demonstrates, in some regions, RDMs provide poor or incomplete representations of $\delta^{18}O_p$ because they neglect many aspects of precipitation physics that can influence $\delta^{18}O_p$. GCMs have the benefit of including these processes. The isotopic variations due to the formation of different precipitation types, vapor mixing and recycling, varying moisture sources and their relative importance at the eastern and western flanks of the highlands are summarized in table 2.

On the western flank of the NHL and CHL, both snow and vapor mixing have a substantial influence on $\delta^{18}O_p$ (table 2). On the SHL, snowfall and moisture source are most important (table 2). These results highlight the fact that physical processes change with environment and with evolution of the mountain range. In the SHL experiment, for example, the presence of an extensive north-south plateau deflects westerly flow, altering circulation patterns and moisture sources. Coincidentally, in all three scenarios, the influence of physical processes on $\delta^{18}O_p$ are opposite in sign and compensate over the highlands (table 2). As a result, GCM and RDM $\delta^{18}O_p$ are similar within ~3‰ at maximum elevations on the western flank (Figure 8a-c) and agree within ~2‰ with mineral proxy $\delta^{18}O_p$ (Figure 8, c, indicated by intersection of vertical and horizontal arrows) with one exception (Figure 8c, note relatively high $\delta^{18}O_p$ indicated by

cross marks). It is important to note, however, that (i) this compensation may not occur in other regions and under different global climate conditions and (ii) that the RDM and GCM $\delta^{18}O_p$ have very different implications for interpreting paleoaltimetry. The RDM simulates very low $\delta^{18}O_p$ matching the proxy data (with values of −21.5 ‰) only at high elevations ≥4000 m of NHL (Figure 8a, unfilled diamonds and cross mark). In contrast, the GCM simulates these low values over a range of elevations at NHL and also CHL, starting as low as 2000 m and extending to >4000 m (Figure 8a-b, filled circles). The GCM results imply that elevations of the NHL and CHL inferred from the proxy $\delta^{18}O_p$ could have been lower than suggested by the *SWEEP* model. Additional GCM experiments are needed to explore this possibility.

On the eastern flank of the highlands, formation of convective precipitation, vapor recycling, and variability of moisture source substantially influence $\delta^{18}O_p$ (Table 2). RDM models are known to severely underestimate (simulate values that are too negative) $\delta^{18}O_p$ on the leeside of mountain ranges. In agreement, our RDM with a GCM-moisture sources simulates $\delta^{18}O_p$ that is very low and substantially lower than that from the GCM (Figure 8d-f, cross marks), a difference which we attribute to neglect of convective processes and vapor recycling, both of which enrich vapor and precipitation in ^{18}O. In contrast, our RDM with a fixed moisture source simulates $\delta^{18}O_p$ that is higher and in good agreement with that from the GCM (Figure 8d-e). This result is entirely due to the prescription in the RDM of a relatively enriched vapor source and high humidity and should not inspire much confidence in the RDM.

ECHAM5-wiso simulates $\delta^{18}O_p$ that is in good agreement with mineral $\delta^{18}O_p$ on the eastern slopes of CHL (Figure 8e) but is too high on the eastern slopes of SHL by ~2 − 3‰ (Figure 8f). This mismatch may derive from several causes presumably, as indicated by good agreement between RDM and mineral $\delta^{18}O_p$ (Figure 8e), not related to the vapor source. Counter to intuition, it may indicate that SHL elevations are too high, blocking flow over the highland and limiting vapor mixing between the eastern and the western air masses (Figure 5p). In support of this interpretation, we note that minimum $\delta^{18}O_p$ on the western flank of SHL is lower (−18‰, Figure 8e) by approximately 4‰ than that on the eastern flank. Alternatively, the mismatch may indicate too vigorous vapor recycling and/or monsoonal circulation on the eastern slopes. If this is the case, good agreement between GCM and proxy $\delta^{18}O_p$ over the CHL eastern slopes suggest that the bias is not systematic.

2.5.2 Caveats

The GCM simulations presented here are sensitivity experiments that were conducted to explore the effect of surface topographic evolution on $\delta^{18}O_p$ and regional circulation and precipitation processes. They do not capture other important environmental changes that are known to have occurred in the early Cenozoic including Eocene to Oligocene global cooling and the initiation of Antarctic glaciation associated with carbon dioxide drawdown (for example, Barker et al., 2007); and, regional and global changes in paleogeography, including the retreat of the Mississippian embayment (for example, Galloway et al., 2011), and filling of Laramide foreland basins (Dickinson et al., 1988). Paleoclimate modeling studies have shown that changes in atmospheric CO_2 and paleogeography can substantially influence climate and precipitation $\delta^{18}O$ over the South American Andes, while the influence of Antarctic glaciation is relatively minor (Jeffery et al., 2011; Poulsen and Jeffery, 2011).

In light of these studies, we suggest that CO_2 drawdown and infilling of the Mississippian Embayment and Laramide foreland basins probably had the most significant influences on $\delta^{18}O_p$ of the North American Cordillera. These events accelerated in the Late Eocene and early Oligocene and, as a consequence, would have mainly influenced $\delta^{18}O_p$ and paleoelevation interpretations associated with the SHL in the following ways: 1. The decrease of CO_2 from 1120 to 560 ppm would lead to a decrease of $\delta^{18}O_p$ due to downward mixing of more ^{18}O-depleted moisture as a response to tropospheric cooling (Poulsen and Jeffery, 2011). 2. Global cooling may have favored snowfall at high elevations, contributing to lower $\delta^{18}O$ at the western flank. 3. Retreat of the Mississippian embayment potentially reduced transport of ^{18}O-enriched moisture to the eastern flank of the highlands. 4. The infilling of the Laramide Basins and more frequent incursion of dry air masses from the Arctic due to an increased equator-to-pole temperature gradient may have increased aridity at the Laramide Foreland, as documented by paleofloras (Wing and Greenwood, 1993; Wolfe, 1994), and intensified a rain shadow along the eastern flank of the highlands. Taken together, climate change and regional geographic adjustments would have led to a decrease in $\delta^{18}O_p$, which have not been considered in either our GCM simulations or in paleoaltimetry reconstructions. Nonetheless, these influences et al. discussed in Chamberlain et al. (2012) would have been secondary to the large $\delta^{18}O_p$ depletion due to southward highland propagation.

2.5.3 Implications for the SWEEP model and paleo-North American Monsoon

Our simulations show a north to south decrease in $\delta^{18}O_p$ in response to surface uplift that is consistent with the proxy $\delta^{18}O_p$ used to infer the *SWEEP* model (Mix et al., 2011; Chamberlain et al., 2012). Data model mismatches at several locations (Figure 6b and 6d) indicate the likelihood for requiring modest adjustments to the *SWEEP* topography, including lowering the interior of the northern Cordillera and the eastern flank of the southern Cordillera. While our simulations are consistent with (and in this way support) the *SWEEP* hypothesis, we cannot discount the feasibility of other tectonic models without additional simulations.

Both proxy data and climate models suggest the existence of a paleo-North American monsoon in the Cretaceous and Paleocene (for example, Poulsen et al., 1999; Sewall and Sloan, 2006; Fricke et al., 2010; Chamberlain et al., 2012). Paleoclimate models indicate that the Western Interior Seaway and, later, the Mississippian embayment may have been crucial to the land-ocean thermal contrast that drove the monsoon, and that as these water bodies retreated, both the strength and extent of the summer monsoon waned. In the Cretaceous, monsoonal circulation may have extended into Alberta (Poulsen et al., 1999; Fricke et al. 2010), but was mainly constrained to the eastern flank of the Rocky Mountain front in the early Paleogene (Sewall and Sloan, 2006). Topography has also been cited as an important inhibitor of the Eocene monsoon. In particular, Chamberlain et al. (2012) speculate that the southward propagation of high topography in the Eocene blocked monsoonal transport of moisture into the northern and central Basin and Range.

Our simulations confirm the absence of monsoonal penetration into the Basin and Range (Figure 5m), but indicate that topographic growth is not the primary reason. In the absence of an extensive embayment, strong westerly flow prevails over this region regardless of topographic scenario (Figure 5m-o). Rather, our results suggest that the paleo-North American monsoon may have been somewhat rejuvenated by topographic migration. In response to uplift of the SHL, summer flow transports moisture from the Gulf of Mexico and intensifies summer precipitation along the eastern slopes of the Cordillera (Figure 5o and 5p).

2.6 Conclusions

Our analysis using an isotope-enabled GCM supports stable isotopic evidence for Cenozoic southward propagation of high topography in the North American Cordillera and highlights the need to use caution in applying traditional $\delta^{18}O_p$ lapse rate-elevation relationships and open-system Rayleigh distillation models (RDM) to infer paleoelevations. Our analysis

demonstrates significant contributions to $\delta^{18}O_p$ due to changes in precipitation phase and type, vapor mixing and recycling, and moisture sources at the windward and leeward side of the Cordillera in response to the growth and propagation of high topography. These processes lead to $\delta^{18}O_p$ variations that are different and sometimes opposite of those estimated using Rayleigh distillation models of moist adiabatic condensation.

Changes in $\delta^{18}O_p$ with uplift and propagation of topography are regionally variable and linked to process. On the windward western slopes of highlands, snow condensation and vapor mixing contribute substantially to precipitation $\delta^{18}O_p$ at high elevations of the northern and central cordillera. Snow condensation and contributions from a more subtropical moisture source dominate changes in precipitation $\delta^{18}O_p$ at the southern cordillera. The isotopic compensation of these processes disguises the isotopic signature of individual processes, causing GCM-simulated $\delta^{18}O_p$ to be similar to RDM $\delta^{18}O_p$ at the top of the highlands. On the eastern slopes, the moisture sources are different from and more ^{18}O-depleted relative to the western slopes by −2 to −4‰ in the northern and central cordillera. These isotopic effects are muted by ^{18}O-enrichment from both evaporative recycling and convective precipitation. At the southern cordillera, however, the moisture source is isotopically similar to the western flank due to moisture contributions from the paleo-Gulf of Mexico. As a result, GCM-simulated $\delta^{18}O_p$ is higher (less negative) than proxy $\delta^{18}O_p$. We suggest that due to partially blocking westward flow and limited zonal mixing, counter to intuition this mismatch may indicate that the *SWEEP* topography is too high.

Our examination of the isotopic signatures of precipitation processes indicates that these processes cannot be ignored in paleoaltimetry studies of the North American Cordillera. Similar processes are very likely to be important in other mountain belts as well and have evolved with surface uplift and regional climate change, altering local $\delta^{18}O_p$ patterns and lapse rates.

2.7 Acknowledgements

This research was supported by NSF grant EAR-1019420. We appreciate the thoughtful and constructive reviews of G. Bowen and J. Galewsky.

Appendix A

Appendix A1

1-D Rayleigh distillation model of adiabatic condensation (RDM)

The RDM model is similar in concept to the model outlined in Rowley and Garzione (2007) for tracking a single near-surface air parcel along ascending, precipitating trajectories. The model is based on the conservation of moist static energy and tracks an unsaturated, ascending air parcel. The air parcel cools at the dry adiabatic lapse rate (K km^{-1}),

$$\Gamma_d = \frac{g}{c_p} \qquad (1)$$

where g is the gravitational acceleration (ms^{-2}) and c_p is the specific heat of dry air (J $kg^{-1}K^{-1}$), until it reaches the lifting condensation level (LCL). The LCL is defined as the first level where the air parcel temperature is less than the dew point temperature. Above this level, the air parcel cools at the moist adiabatic lapse rate,

$$\Gamma_s = -\frac{dT}{dz} = \Gamma_d \frac{\left[1 + L_c q_s / RT\right]}{\left[1 + \varepsilon L_c^2 q_s / \left(c_p R T^2\right)\right]} \qquad (2)$$

where L_c is the latent heat of condensation (J kg^{-1}); q_s is the saturation mixing ratio (kg/kg); R is the gas constant (J $K^{-1}kg^{-1}$); T is the air parcel temperature (K), e is the ratio of the molecular weight of water to that of dry air (0.622); and z (m) is the air-parcel height (Horton, 2004). The $T - z$ curve is modeled with a 210 m interval. The saturated-mixing ratio q_s at each level is calculated from the saturation vapor pressure (Bolton, 1980):

$$e_s = 6.112 \exp\left(\frac{17.67 T_c}{T_c + 243.5}\right) \qquad (3)$$

T_c is the temperature in degree Celsius (other temperatures are in Kelvin) at the j^{th} level. The saturation mixing ratio is calculated:

$$q_s = \frac{\varepsilon e_s}{p - e_s} \qquad (4)$$

with p, the pressure at the j^{th} level, calculated:

$$p = p_{j-1}\left(\frac{T}{T_{j-1}}\right)^{\frac{g}{\Gamma_s R}} \qquad (5)$$

$p_{j-1}$and T_{j-1} is the pressure and temperature at the (j-1)th level. For the jth level, the fractionation factor is calculated using Majoube (1971) for liquid-vapor equilibrium: $1000\ln\alpha = -7.685 + \frac{6.7123\times10^3}{T} - \frac{1.6664\times10^3}{T^2} + \frac{0.35041\times10^9}{T^3}$ (6).

The remaining vapor fraction $f = \frac{(e_s)_j}{(e_s)_{j-1}}$is used to calculate the delta value of remaining vapor and condensation, using:

$$\begin{aligned}(\delta^{18}O_v)_j &= ((\delta^{18}O_v)_{j-1}+1000)f^{(\alpha-1)} - 1000\\ (\delta^{18}O_l)_j &= \alpha((\delta^{18}O_v)_j+1000) - 1000\end{aligned} \quad (7)$$

where $\delta^{18}O_v$ and $\delta^{18}O_l$ are the isotopic composition of the remaining vapor and condensation.

The RDM calculates the $\delta^{18}O_p$-elevation relationship with given surface air temperature (T_s), 1000hPa specific humidity (q_s) and $\delta^{18}O_v$ at the first step. These three values determine the moisture source of the ascending air parcel. In this study, the moisture sources are prescribed as either *fixed* or from *GCM*. The *fixed*-moisture source has $\delta^{18}O_v$ inferred from mineral $\delta^{18}O_p$ (-9.9 ‰, based on the isotopic composition of kaolinitized Eocene river gravel deposited in the ancestral Yuba River near the ancient Pacific shoreline (Mulch et al., 2006)) and T_s, and q_s taken from the western side of the highlands of a GCM simulation. The *GCM-moisture source* is initiated with $\delta^{18}O_v$, T_s, and q_s from a GCM simulation. GCM variables are prescribed on either the western or eastern sides of the highlands.

For both *fixed- and GCM-moisture source*s, the initial values of $\delta^{18}O_v$ is derived from $\delta^{18}O_p$ of initial condensations either from fixed $\delta^{18}O_p$ of -9.9 ‰ or $\delta^{18}O_p$ of GCM condensates, because $\delta^{18}O_v$ varies substantially at low levels (for example, from −16.2 ‰ to −21.4 ‰ between 1000 and 850 hPa over a domain of 53 °±2 °N, 125 °W). We select an appropriate $\delta^{18}O_v$ by first running the RDM with the full range of low-level $\delta^{18}O$ values with given T_s and q_s. We then choose the initial $\delta^{18}O_v$ that best matches the fixed or GCM (≤1200m) $\delta^{18}O_p$ of initial condensations along the mountain slopes of NHL, CHL, and SHL.

T_s, q_s, and $\delta^{18}O_v$ are taken at 125 °W for a western moisture source for NHL, CHL and SHL scenarios, at 90°W for an eastern moisture source in NHL and CHL scenarios and at 95 °W in the SHL scenario. Both T_s and q_s are averaged across a small range of latitudes encompassing the highlands (which are NHL, 57 °±3 °N; CHL, 53 °±2 °N; SHL, 47 °±4 °N).

Appendix A2

RDM with vapor recycling

The RDM is modified to consider vapor input due to expansion of the air parcel in response to both adiabatic and non-adiabatic heating of the environmental atmosphere along the eastern flanks of the mountains. On the leeside of the North American Cordillera, the (environmental) atmosphere is warmer than its surroundings at the same elevations due to non-adiabatic heating through large-scale subsidence and the release of latent heat from convective condensates. The ascending air parcels at the leeside of the mountains are adiabatically warmed by the warmer environmental atmosphere, which leads to additional expansion and enhanced water-holding capacity of ascending air parcels. This effect is approximated by increasing the mixing ratio at each level of calculation assuming isothermal expansion of the air mass and that the added vapor has the same isotopic composition as the existing vapor. At each step above the LCL, q_s, $\delta^{18}O_v$, $\delta^{18}O_p$, T are first calculated from equations (1) through (7), and then q_s is adjusted to include the vapor recycling potential r (the ratio of evaporation to precipitation): $q_s=q_s\times(1+r)$. This modification is included to approximate the re-evaporation process.

Appendix A3

Back trajectories with GCM-moisture source

Back trajectory analysis of air parcels is commonly performed along isentropic (that is uniform potential temperature) surfaces to analyze the origin and path of precipitation (for example, Dirmeyer and Brubaker, 1999). However, in regions of active thermal convection and strong diabatic heating, conditions that were prevalent on the eastern side of the Eocene North American Cordillera, potential temperature is not conserved and flow. Non-isentropic transport of moisture could also be inferred at the western flank as extensive moisture mixing across different altitude is generated by mountain waves.

With these considerations, instead of using strict isentropic tracking, we track bulk moisture in the boundary layer (1000 to 850 hPa) where moisture is concentrated. The horizontal location of a parcel (x, y) is given in explicit form by (Kurita et al., 2004):

$$x^{n+1} = x^n + \int_t^{t+\Delta t} u^*(x,y,t)dt$$

$$y^{n+1} = y^n + \int_t^{t+\Delta t} v^*(x,y,t)dt$$

where u* and v* are zonal and meridional winds weighted by the boundary layer profile of relative humidity. The vertical average (850 – 1000 hPa) of relative humidity is also recorded at (x, y). We report the back trajectories for parcels that arrived at the target location with high relative humidity (≥ 60%) to filter dry parcels that have little potential for precipitation.

Appendix A4

Supplementary data

$\delta^{18}O_p$ values summarized from other studies and calculated from reported mineral $\delta^{18}O$ using inferred paleoflora proxy temperature (Mix et al., 2011; Chamberlain et al., 2012) and recalculated $\delta^{18}O_p$ value using model temperature by this study.

Region	Lat (°N)	Lon (°W)	Age	Temperature (°C)	$\delta^{18}O_p$	Model Surface Temperature (T_s, °C)	$\delta^{18}O_p$ using Model T_s
pre-49Ma							
Axehandle_Basin_(UT)	39.41	111.7	55	22 (1)	-6.7	20.4	-7.1
Axehandle_Basin_(UT)	39.4	111.68	71.3–50	16.9 (1)	-8.3	20.4	-8.1
Bannock_Basin_(ID)	42.09	112.18	50–49	12.5 (2)	-14.3	18.3	-13.0
Bighorn_Basin_(WY)	45	109	57.7–53.2	16 (2)	-7.8	18.0	-7.5
Bighorn_Basin_(WY)	44	108.8	58.8–53.6		-10.3	*	
Bighorn_Basin_(WY)	44.84	108.84	55.8	16.5 (2)	-7.9	18.0	-8.0
Bighorn_Basin_(WY)	42.22	108.53	50.8–51.9	17.5 (2)	-7.1	21.1	-7.4
Crazy_Mtn_Basin_(MT)	46.4	110.2	64.4–59.4		-13.8	*	
Elko_Basin_(NV)	40.56	116.01	54.5–49.0	21.5 (2)	-4	18.6	-4.6
Flagtaff_Basin_(UT)	39	110.5	55	22 (1)	-7	21.1	-7.3
Great_Plains/Rocky_Mts	43.83	108.55	50	10.9 (2)	-11.8	19.8	-9.9
Greater_Green_River_Basin_(WY)	40.76	108.89	51.8–52.0		-7.4	*	
Greater_Green_River_Basin_(WY)	41.5	109	53		-8	*	
Greater_Green_River_Basin_(WY)	41.5	109	54		-10.6	*	
Greater_Green_River_Basin_(WY)	41.5	109	51		-9.4	*	
Greater_Green_River_Basin_(WY)	41.75	108.8	49	17.2 (1)	-2.7	21.3	-2.1
Greater_Green_River_Basin_(WY)	41.5	109.5	52	17.2 (1)	-1.4	20.8	-0.9

Okanagan_Kettle_MCC_(WA)	48.5	118.25	49.1		-13.3	*	-13.3
Piceance_Creek_Basin_(CO)	39.41	108.18	52	22 (1)	-8.4	20.9	-8.7
Powder_River_Basin_(WY)	45.5	106	53.7–57.3		-13.7	*	
Princeton_Basin_(BC)	49.44	120.5	49	8.3 (1)	-19.7	3.7	-21.5
Sage_Creek_Basin_(MT/ID)	44.74	112.61	65–49	11-16 (2)	-8.4	17.7	-7.5
Shuswap_MCC_(BC)	51	118.25	49.0–47.9		-15.8	*	
Uinta_Basin_(UT)	39.81	110.94	55	22 (1)	-9.8	20.3	-10.2
Wind_River_Range_(WY)	43.24	107.5	52.8–52.0	16.5 (2)	-13.6	20.0	-12.8
Wind_River_Range_(WY)	43.33	107.63	53.2–52.7	17.5 (2)	-12.6	20.0	-11.9
Wind_River_Range_(WY)	43.49	109.45	55.5–53.2	19.8 (2)	-8.5	19.2	-8.8
Wind_River_Range_(WY)	43.02	107.08	60–55	21.5 (2)	-9.3	20.0	-9.7
Wind_River_Range_(WY)	43.22	107.3	52–50.9	16.5 (2)	-13.9	20.0	-13.1
49–39Ma							
Bannock_Basin_(ID)	42.09	112.18	48–41	12.3 (2)	-12.3	16.3	-11.4
Elko_Basin_(NV)	40.56	116.02	47.5–39.4	15.8 (2)	-6.7	19.0	-7.1
Elko_Basin_(NV)	40.58	115.99	42.6–40.6	12.4 (2)	-4.1	19.0	-3.0
Flagstaff_Basin_(UT)	38.92	111.81	49–39	13.2 (2)	-8.7	20.6	-7.3
Galisteo_Basin_(NM)	35.5	106	49–39	7.5 (2)	-10	24.5	-6.4
Great_Plains/Rocky_Mts	43.5	108.58	47.9	10 (2)	-12.9	18.5	-11.1
Great_Plains/Rocky_Mts	42.76	107.59	49	10.9 (2)	-13.4	20.8	-11.3
Great_Plains/Rocky_Mts	42.71	108.18	49	10.9 (2)	-13.2	20.8	-11.1
Great_Plains/Rocky_Mts	42.6	108.29	49	10.9 (2)	-11.9	20.6	-9.9
Great_Plains/Rocky_Mts	44.85	110.16	49	10.9 (2)	-18.5	15.7	-17.3
Great_Plains/Rocky_Mts	44.87	111.05	49	10.9 (2)	-17.4	12.5	-16.9
Great_Plains/Rocky_Mts	44.89	111.33	49	10.9 (2)	-18.1	12.5	-17.6
Greater_Green_River_Basin_(WY)	41.75	108.8	48	17.2 (1)	-7.2	21.7	-6.4
Ibapah_Basin_(UT)	40.12	114.12	46–39	13.2 (2)	-10.8	19.4	-9.5
Sage_Creek_Basin_(MT/ID)	44.66	112.58	48.0–39.1	13.4 (2)	-17.1	7.3	-18.2
Sierra_Nevada_(CA)	39.35	120.98	44.9		-9.3	*	
Sierra_Nevada_(CA)	39.18	120.85	44.9		-10.1	*	
Sierra_Nevada_(CA)	39.69	120.93	44.9		-10	*	
Sierra_Nevada_(CA)	39.69	120.98	44.9		-9.8	*	
Uinta_Basin_(UT)	40.05	110.53	49–39	13.2 (2)	-3.6	20.5	-2.3
39–28Ma							
Claron_Basin_(UT)	37.68	112.83	39–28	11 (2)	-16.3	8.0	-16.8
Copper_Basin_(NV)	41.76	115.47	38.7	10.5 (1)	-18.2	7.0	-18.7
Elko_Basin_(NV)	40.55	115.96	36.0–28.0	13 (2)	-16.1	8.5	-17.0
Flastaff_Basin_(UT)	38.93	111.95	39–28	11 (2)	-15.7	6.9	-16.5
Galisteo_Basin_(NM)	35.5	-106	39–28	0 (2)	-11.8	24.1	-6.6

Great_Plains/Rocky_Mts	42.83	-101.7	35	11.5 (2)	-9.8	17.3	-8.6
Great_Plains/Rocky_Mts	43.66	102.66	35.8	11.5 (2)	-8.1	17.0	-7.0
Great_Plains/Rocky_Mts	41.6	103.11	31.25	11.5 (2)	-9.2	18.2	-7.9
Great_Plains/Rocky_Mts	41.7	103.34	31.25	11.5 (2)	-8.6	18.2	-7.2
Great_Plains/Rocky_Mts	42.92	103.49	34.5	11.5 (2)	-10.6	17.5	-9.3
Great_Plains/Rocky_Mts	42.77	103.56	30.3	11.5 (2)	-10.5	17.5	-9.2
Great_Plains/Rocky_Mts	42.76	105.01	35.5	11.5 (2)	-10.9	17.8	-9.6
Great_Plains/Rocky_Mts	42.71	105.37	31.25	11.5 (2)	-12.8	17.8	-11.4
Great_Plains/Rocky_Mts	42.64	106.76	35.65	11.5 (2)	-13.3	19.2	-11.7
Great_Plains/Rocky_Mts	42.76	107.56	32	11.5 (2)	-16.6	20.3	-14.6
Great_Plains/Rocky_Mts	42.58	108.29	32	11.5 (2)	-16.9	19.1	-15.2
Sage_Creek_Basin_(MT/ID)	44.76	112.55	38.8–32.0	10.8 (2)	-17	2.8	-18.7
Sierra_Nevada_(CA)	39.7	120.99	28.5		-14.3	*	
Sierra_Nevada_(CA)	39.85	120.35	28.5		-16.8	*	
Sierra_Nevada_(CA)	39.25	120.93	28.5		-13.2	*	
Sierra_Nevada_(CA)	39.46	120.49	28.5		-15.3	*	
Sierra_Nevada_(CA)	39.56	-120.5	28.5		-16.2	*	
Sierra_Nevada_(CA)	38.19	120.85	28.5		-10.6	*	
Uinta_Basin_(UT)	40.33	109.53	39–28	11 (2)	-13.4	13.9	-12.7
Wind_River_Range_(WY)	42.7	108.19	36.8–28.3	11.3 (2)	-14.1	17.1	-12.9
Wind_River_Range_(WY)	43.34	107.48	37.0–34.0	11.5 (2)	-11.1	15.8	-10.2

(1) Wolfe et al., 1997

(2) Chase et al., 1998

* Used reported $\delta^{18}O$ as $\delta^{18}O_p$

Bibliography

Andreasson, F. P., and B. Schmitz, 1998, Tropical Atlantic seasonal dynamics in the early middle Eocene from stable oxygen and carbon isotope profiles of mollusk shells: Paleoceanography, v. 13, p. 183–192.

Andreasson, F. P., and B. Schmitz, 2000, Temperature seasonality in the early middle Eocene North Atlantic region: Evidence from stable isotope profiles of marine gastropod shells: Geological Society of America Bulletin, v. 112, p. 628–640.

Barker, P. F., B. Diekmann, C. Escutia, 2007, Onset of Cenozoic Antarctic glaciation: Deep-Sea Research II, v. 54, p. 2293–2307.

Beerling, D. J. and D. L., Royer, 2011, Convergent Cenozoic CO_2 history: Nature Geoscience, v. 4, p. 418-420.

Bice, K. L., C. R. Scotese, D. Seidov, and E. J. Barron, 2000, Quantifying the role of geographic change in Cenozoic ocean heat transport using uncoupled atmosphere and ocean models: Palaeogeography, Palaeoclimatology, Palaeoecology, v. 161, p. 295-310.

Bolton, D., 1980, The computation of equivalent potential temperature: Monthly Weather Review, v. 108, p. 1046-1053.

Blisniuk, P. M., and L. A., Stern, 2005, Stable isotope paleoaltimetry: A critical review: American Journal of Science, v. 305, p. 1033–1074, doi:10.2475/ajs.305.10.1033.

Bown, T. M., and M. J., Kraus, 1981, Lower Eocene alluvial paleosols (Willwood Formation, Northwest Wyoming, U.S.A.) and their significance for paleoecology, palcoclimatology and basin analysis: Palaeogeography, Palaeoclimatology, Palaeoecology, v. 34, p. 1-30.

Bowen G. J., R. L. Daniels, and B. B. Bowen, 2008, Paleoenvironmental isotope geochemistry and paragenesis of lacustrine and palustrine carbonates, Flagstaff Formation, Central Utah, U.S.A.: Journal of Sedimentary Research, v. 78, p. 162–174.

Brinkhuis H., S., Schouten, M. E., Collinson, A., Sluijs, J. S., Sinninghe-Damsté, G. R., Dickens, M., Huber, T. M., Cronin, J., Onodera, K., Takahashi, J. P., Bujak, R., Stein, J., van der Burgh, J. S., Eldrett, I. C., Harding, A. F., Lotter, F. Sangiorgi, H., van Konijnenburg-van Cittert, J. W., de Leeuw, J., Matthiessen, J., Backman, K., Moran and the Expedition Scientists, 2006, Episodic fresh surface waters in the Eocene Arctic Ocean: Nature, v. 441, p. 606-609.

Chamberlain, C. P., H. T., Mix, A., Mulch, H. T., Hren, M. L., Kent-Corson, S. J., Davis, T. W.,

Horton, and S. A., Graham, 2012, Cenozoic climatic and topographic evolution of the Western North America Cordillera: American Journal of Science, v. 312, p. 213-262.

Chase, C. G., K. M., Gregory-Wodzicki, J. T., Parrish-Jones, and P. G., DeCelles, 1998, Topographic history of the western Cordillera of North America and controls on climate, in: Crowley, T. J., and Burke, K., (Eds.), Tectonic boundary conditions for climate model simulations: New York, Oxford University Press, p. 73-99.

Clark, M. K., 2007, The significance of paleotopography: Reviews in Mineralogy and Geochemistry, v. 66, p. 1–21.

Clementz, M. T., and J. O., Sewall, 2011, Latitudinal gradients in greenhouse seawater $\delta^{18}O$: Evidence from Eocene Sirenian tooth enamel: Science, v. 332, p. 455 – 458.

Cook, K. H., K. V., Edward, Z. S., Launer, C. M., Patricola, 2008, Springtime Intensification of the Great Plains Low-Level Jet and Midwest Precipitation in GCM Simulations of the Twenty-First Century: Journal of Climate, v. 21, p. 6321–6340.

Davis, S. J., H. T., Mix, B. A., Wiegand, A. R., Carroll, and C.P., Chamberlain, 2009, Synorogenic evolution of large-scale drainage patterns: Isotope paleohydrology of sequential Laramide basins: American Journal of Science, v. 309, p. 549-602.

DeCelles, P. G., 2004, Late Jurassic to Eocene evolution of the Cordilleran thrust belt and foreland basin systems, western USA: American Journal of Science, v. 304, p. 105-168.

Dettman D. L., and K. C., Lohmann, 2000, Oxygen isotope evidence for high-altitude snow in the Laramide Rocky Mountains of North America during the Late Cretaceous and Paleogene: Geology, v. 28, p. 243-246.

Dickinson, W. R., M. A., Klute, M. J., Hayes, S. U., Janecke, E. R., Lundin, M. A., McKittrick, and M. D., Olivares, 1988, Paleogeographic and paleotectonic setting of Laramide sedimentary basins in the central Rocky Mountain region: Geological Society of America Bulletin, v. 100, p. 1023–1039.

Dickinson, W. R., 2004, Evolution of the North American cordillera: Annual Review of Earth and Planetary Science, v. 32, p. 13-45.

Dirmeyer, P. A., Brubaker, K. L., 1999, Contrasting evaporative moisture sources during the drought of 1988 and the flood of 1993: Journal of Geophysical Research, v. 104, p. 19383.

Ehlers, T. A. and C. J., Poulsen, 2009, Large paleoclimate influence the interpretation of Andean Plateau paleoaltimetry: Earth and Planetary Science Letters, v. 281, p. 238-248.

Frankenberg, C., K. Yoshimura, T. Warneke, , I. Aben, A. Butz, N. Deutscher, D. Grith, F. Hase, J. Notholt, M. Schneider, H. Schrijver, and T. Roeckmann, 2009, Dynamic Processes Governing Lower-Tropospheric HDO/H2O ratios as observed from space and ground. Science, v. 325, p. 1374.

Fricke, H. C., 2003, Investigation of early Eocene water-vapor transport and paleoelevation using oxygen isotope data from geographically widespread mammal remains: Geological Society of America Bulletin, v. 115, 1088-1096.

Fricke, H. C., and S. L., Wing, 2004, Oxygen isotope and paleobotanical estimates of temperature and δ18O-latitude gradients over North America during the early Eocene: American Journal of Science, v. 304, p. 612-635.

Fricke, H. C., B. Z., Foreman, and J., Sewall, 2010, Integrated climate model-oxygen isotope evidence for a North American monsoon during the Late Cretaceous: Earth and Planetary Science Letters, v. 289, p. 11-21.

Forte, A. M., R., Moucha, N. A., Simmons, S. P., Grand, and J. X., Mitrovica, 2010, Deep-mantle contributions to the surface dynamics of the North American continent: Tectonophysics, v. 481, p. 3-15.

Galewsky, J., 2009, Orographic precipitation isotopic ratios in stratified atmospheric flows: Implications for paleoelevation studies: Geology, v. 37, p. 791–794.

Galloway, W. E., T. L., Whiteaker and P., Ganey-Curry, 2011, History of Cenozoic North American drainage basin evolution, sediment yield, and accumulation in the Gulf of Mexico basin: Geosphere, v. 7, p. 938-973.

Gat, J. R., and M., Rietti-Shati, 1999, The meteorological vs. the hydrological altitude effect on the isotopic composition of meteoric waters, in: IAEA-CSP2/C (Eds.), Isotope techniques in water resources development and management, p. 5.

Gat, J. R., 2010, Snow and snowmelt processes, in Gat, J. R., Isotope Hydrology: a study of the water cycle: World Scientific, p. 67-69.

Gedzelman, S. D., 1988, Deuterium in water vapor above the atmospheric boundary layer. Tellus B, v. 40, p. 134-147.

Greenwood, D. R., and S. L., Wing, 1995, Eocene continental climates and latitudinal temperature-gradients: Geology, v. 23, p. 1044-1048.

Hagemann, S., 2002, An improved land surface parameter dataset for global and regional climate

models: Rep. 336, Max Planck Institute for Meteorology, v. 53, p. 21.

Heinemann, M., J. H., Jungclaus, and J., Marotzke, 2009, Warm Paleocene/Eocene climate as simulated in ECHAM5/MPI-OM: Climate of the Past, v. 5, p. 785-802.

Hoffmann G., M. Werner, and M. Heimann, 1998, The Water Isotope Module of the ECHAM Atmospheric General Circulation Model -A Study on Time Scales from Days to Several Years: Journal of Geophysical Research, v. 103, p. 871-896.

Hoffmann, G., J. Jouzel, and V., Masson, 2000, Stable water isotopes in atmospheric general circulation models: Hydrological Processes, v. 14, p. 1385–1406.

Horton, T. W., D. J., Sjostrom, M. J., Abruzzese, M. A., Poage, J. R., Waldbauer, M., Hren, J., Wooden, and C. P., Chamberlain, 2004, Eocene uplift and Miocene subsidence of the great Basin and southern Sierra Nevada: American Journal of Science, v. 304, p. 862-888.

Holton, J. R., 2004, Moisture variables, in An introduction to dynamic meteorology: Academic press, p. 503.

Humphreys, E. D., 1995, Post-Laramide removal of the Farallon slab, western United States: Geology, v. 23, p. 987-990.

Insel, N., C. J., Poulsen, and T. A., Ehlers, 2009, Influence of the Andes Mountains on South American moisture transport, convection, and precipitation: Climate Dynamics, v. 35, p. 1477-1492, doi:10.1007/s00382-009-0637-1.

Insel, N., C. J., Poulsen, T. A., Ehlers, and C., Sturm, 2012, Response of meteoric d18O to surface uplift - Implications for Cenozoic Andean Plateau growth: Earth and Planetary Science Letters, v. 317-318, p. 262-272.

Ivany, L. C., K. C., Lohmann, F., Hasiuk, D. B., Blake, A., Glass, R. B., Aronson, and R. M., Moody, 2008, Eocene climate record of a high southern latitude continental shelf: Seymour Island, Antarctica: Geological Society of America Bulletin, v. 120, p. 659-678.

Jeffery, M. L., C. J., Poulsen, and T. A., Ehlers, 2012, Impacts of global cooling, surface uplift and an inland seaway on South American paleoclimate and precipitation δ18O: Geological Society of America Bulletin, v. 124, p. 335-351.

Jouzel, J., and L., Merlivat, 1984, Deuterium and oxygen-18 in precipitation: Modeling of the isotopic effects during snow formation: Journal of Geophysical Research, v. 89, doi: 10.1029/0JGREA0000890000D7011749000001. issn: 0148-0227.

Kharin, V., V. F., Zwiers, X., Zhang, and G. C., Hegerl, 2007, Changes in Temperature and

Precipitation Extremes in the IPCC Ensemble of Global Coupled Model Simulations: Journal of Climate, v. 20, p. 1419–1444.

Koch, P. L., J. C., Zachos, D. L., Dettman, 1995, Stable isotope stratigraphy and paleoclimatology of the Paleogene Bighorn Basin, (Wyoming, U.S.A.): Palaeogeography, Palaeoclimatology, Palaeoecology, v. 115, p. 61-89.

Kurita, N., N. Yoshida, G. Inoue, E. A. Chayanova, 2004, Modern isotope climatology of Russia: A first assessment: Journal of Geophysical Research, v. 109, D03102, doi:10.1029/2003JD003404

Lechler, A. R. and N. A., Niemi, 2011, Controls on the spatial variability of modern meteoric $\delta^{18}O$: empirical constraints from the western US and east Asia and implications for stable isotope studies: American Journal of Science, v. 311, p. 664–700.

Lechler, A. R. and Galewsky, J., 2013, Refining paleoaltimetry reconstructions of the Sierra Nevada, California, using air parcel trajectories: Geology, v. 41, p. 259–262.

Liu, Z., M., Pagani, D., Zinniker, R., DeConto, M., Huber, H., Brinkhuis, S. R., Shah, R. M.,Leckie, and P. N., Pearson, 2009, Global cooling during the Eocene-Oligocene climate transition: Science, v. 323, p. 1187-1190.

Majoube, M., 1971, Fractionnement en oxygen et en deuterium entre l'eau et sa vapeur: Journal de Chimie et de Physique, v. 68, p. 1423-1436.

Mix, H. T., A., Mulch, M. L., Kent-Corson, and C. P., Chamberlain, 2011, Cenozoic migration of topography in the North American Cordillera: Geology, v. 39, p. 87-90.

Moser, H., and Stichler, W., 1971, Die Verwendung des Deuterium- und Sauerstoff-18-Gehalts bei hydrologischen Untersuchungen: Geologica Bavaria, v. 64, p. 7–35.

Morrill, C., and P. L., Koch, 2002, Elevation or alteration? Evaluation of isotopic constraints on paleoaltitudes surrounding the Eocene Green River Basin: Geology, v. 30, p. 151-154, 2002.

Mulch, A., S. A., Graham, and C. P., Chamberlain, 2006, Hydrogen isotopes in Eocene river gravels and paleoelevation of the Sierra Nevada: Science, v. 313, p. 87–89.

Mulch, A., C., Teyssier, M. A., Cosca, and C. P., Chamberlain, 2007, Stable isotope paleoaltimetry of Eocene Core Complexes in the North American Cordillera: Tectonics, v. 26, TC4001, doi:10.1029/2006TC001995.

Norris, R. D., L. S., Jones, R. M., Corfield, and J. E., Cartlidge, 1996, Skiing in the Eocene Uinta Mountains? Isotopic evidence in the Green River Formation for snow melt and large

mountains: Geology, v. 24, p. 403-403.

Pearson, P. N., B. E., van Dongen, C. J., Nicholas, R. D., Pancost, S., Schouten, J. M., Singano, and B. S., Wade, 2007, Stable warm tropical climate through the Eocene Epoch: Geology, v. 35, p. 211– 214.

Peppe, D. J., D. L., Royer, P., Wilf, and E. A., Kowalski, 2010, Quantification of large uncertainties in fossil leaf paleoaltimetry: Tectonics, v. 29, TC3015,doi:10.1029/2009TC002549.

Pierrehumbert, R. T. and H., Yang, 1993, Global Chaotic Mixing on Isentropic Surfaces: Journal of Atmospheric Science, v. 50, p. 2462–2480.

Pierrehumbert, R. T., 1998, Lateral mixing as a source of subtropical water vapor:

Geophysical Research Letters, v. 25, p. 151–154.

Poage, M. A., and C. P., Chamberlain, 2001, Empirical relationships between elevation and the stable isotope composition of precipitation and surface waters: considerations for studies of paleoelevation change: American Journal of Science, v. 301, p. 1-15.

Poulsen, C. J., E. J., Barron, C. C., Johnson, and P., Fawcett, 1999, Links between climatic factors and regional oceanic circulation in the mid-Cretaceous, in Barrera, E., and Johnson, C.C., eds., Evolution of the Cretaceous Ocean-Climate System: Geological Society of America Special Paper, v. 332, p. 73-89.

Poulsen, C. J., and M. L., Jeffery, 2011, Climate change imprinting on stable isotopic compositions of high-elevation meteoric water cloaks past surface elevations of major orogens: Geology, 39, 595-598.

Poulsen, C. J., T. A., Ehlers, and N., Insel, 2010, Onset of convective rainfall during gradual Late Miocene rise of the Central Andes: Science, v. 328, p. 490-493.

Risi, C., S. Bony, and F. Vimeux, 2008, Influence of convective processes on the isotopic composition ($\delta^{18}O$ and δD of precipitation and atmospheric water in the tropics: 2. Physical interpretation of the amount effect: Journal of Geophysical Research, v. 113, D19306, doi:10.1029/2008JD009943.

Roeckner, E. G., Bäuml, L., Bonaventura, R., Brokopf, M., Esch, M., Giorgetta, S., Hagemann, I., Kirchner, L., Kornblueh, E., Manzini, A., Rhodin, U., Schlese, U., Schulzweida, A., Tompkins, 2003, The general circulation model ECHAM5. Part I: Model description: MPI-Rep. v. 349, Max Planck Inst. for Meteorol., Hamburg, Germany.

Rowley, D. B., 2007, Stable Isotope-Based Paleoaltimetry: Theory and Validation: Reviews in Mineralogy and Geochemistry, v. 66, p. 23-52.

Rowley, D. B., and C. N., Garzione, 2007, Stable Isotope-based paleoaltimetry: Annual Review of Earth and Planetary Sciences, v. 35, p. 463-508.

Salati, E., A. Dall'Olio, E. Matsui, and J. R. Gat (1979), Recycling of water in the Amazon Basin: An isotopic study, Water Resource Research, v. 15, p. 1250–1258, doi:10.1029/WR015i005p01250.

Salathé Jr., E. P., 2006, Influences of a shift in North Pacific storm tracks on western North American precipitation under global warming: Geophysical Research Letters, v. 33, L19820, doi:10.1029/2006GL026882.

Schmandt, B., and E. D., Humphreys, 2011, Seismically imaged relict slab from the 55 Ma Siletzia accretion to the northwest United States: Geology, v. 39, p. 175-178.

Schmidt, G. A., G. R. Bigg, and E. J. Rohling, 1999, Global Seawater Oxygen-18 Database - v1.21, http://data.giss.nasa.gov/o18data/.

Sewall, J.O., and L. C., Sloan, 2006, Come a little bit closer: A high-resolution climate study of the early Paleogene Laramide foreland: Geology, v. 34, p. 81-84.

Sewall, J.O., L. C., Sloan, M., Huber, and S. L., Wing, 2000, Climate sensitivity to changes in land surface characteristics: Global and Planetary Change, v. 26, p. 445-465.

Sherwood, S. C., and A. E. Dessler, 2001, A model for transport across the tropical tropopause: Journal of the Atmospheric Sciences, v. 58, p. 765-779.

Sjostrom, D., J., M. T., Hren, T. W., Horton, J. R., Waldbauer, C. P., Chamberlain, 2006, Stable isotopic evidence for an Early Tertiary elevation gradient in the Great Plains - Rocky Mountain region, in: Willett, S., Hovius, N., Fisher, D., and Brandon, M., (Eds.), Tectonics, Climate, and Landscape Evolution: Geological Society of America Special Paper, v. 398, p. 309-319.

Smoot, J. P., 1983, Depositional sub-environments in an arid closed basin, the Wilkins Peak Member of the Green River Formation (Eocene), Wyoming, U.S.A: Sedimentology, v. 30, p. 801-827.

Werner, M., P. M. Langebroek, T. Carlsen, M. Herold, and G. Lohmann, 2011, Stable water isotopes in the ECHAM5 general circulation model: Towards high-resolution isotope modeling on a global scale: Journal of Geophysical Research, v. 116, D15109,

doi:10.1029/2011JD015681.

Wilf, P., S. L., Wing, D. R., Greenwood, and C. L., Greenwood, 1998, Using fossil leaves as paleoprecipitation indicators: An Eocene example: Geology, v. 26, p. 203-206.

Wing, S. L., and D. R., Greenwood, 1993, Fossils and fossil climate - the case for Equable continental interiors in the Eocene: Philosophical Transactions of the Royal Society. B, v. 341, p. 243-252.

Wolfe, J. A., 1994, Tertiary climatic changes at middle latitudes of western North America: Palaeogeography, Palaeoclimatology, Palaeoecology, v. 108, p. 1-2.

Wolfe, J. A., H. E., Schorn, C. E., Forest, and P., Molnar, 1997, Paleobotanical evidence for high altitudes in Nevada during the Miocene: Science, v. 276, p. 1672–1675, doi: 10.1126/science.276.5319.1672.

Worden, J., D. Noone, K. Bowman, et al., 2007, Importance of rain evaporation and continental convection in the tropical water cycle: Nature, v. 445, p. 528-532.

Zachos, J. C., L. D., Stott, and K. C., Lohmann, 1994, Evolution of Early Cenozoic marine temperatures: Paleoceanography, v. 9, p. 353–387, doi:10.1029/93PA03266.

Zimmermann, U., D. Ehhalt, and K. O. Mfinnich, 1967, Soil water movement and evapotranspiration change in the isotopic composition of the water: in IAEA (eds), Isotopes in Hydrology, p. 567-585.

Zhou, J., C. J., Poulsen, D., Pollard, and T. S., White, 2008, Simulation of modern and middle Cretaceous marine $\delta^{18}O$ with an ocean-atmosphere GCM: Paleoceanography, doi:10.1029/2008PA001596.

Chapter 3

Refinement of Eocene lapse rates, fossil-leaf altimetry, and North American Cordilleran surface elevation estimates

3.1 Abstract

Estimates of continental paleoelevation using proxy methods are essential for understanding the geodynamic, climatic, and geomorphoric evolution of ancient orogens. Fossil-leaf paleoaltimetry, one proxy approach, uses fossil-leaf traits to quantify differences in temperature or moist enthalpy between coeval coastal and inland sites along latitudes. These environmental differences are converted to elevation differences using their rates of change with elevation (lapse rate). Here, we evaluate the uncertainty associated with this method using the Eocene North American Cordillera as a case study. To do so, we develop a series of paleoclimate simulations for the Early (~55 – 49 Ma) and Middle Eocene (49 – 40 Ma) period using a range of elevation scenarios for the western North American Cordillera.

Simulated Eocene lapse rates over western North America are ~5 °C km^{-1} and 9.8 kJ km^{-1}, close to moist adiabatic rates but significantly different from modern rates of temperature in the southwestern U.S. and rates of moist enthalpy across the entire western U.S. Further, using linear lapse rates underestimates high-altitude (> 3 km) temperature variability and loss of moist enthalpy induced by non-linear circulation changes in response to increasing surface elevation. Ignoring these changes leads to kilometer-scale biases in elevation estimates. In addition to these biases, we demonstrate that previous elevation estimates of the western Cordillera are affected by local climate variability at coastal fossil-leaf sites of up to ~8 °C in temperature and ~20 kJ in moist enthalpy, a factor which further contributes to elevation overestimates of ~1 km for Early Eocene floras located at the Laramide foreland basins and underestimates of ~1 km for late Middle Eocene floras at the southern Cordillera.

We suggest a new approach for estimating past elevations by comparing proxy reconstructions directly with simulated distributions of temperature and moist enthalpy under a range of elevation scenarios. Using this method, we estimate mean elevations for the North

American Cordillera of ~2 km using proxy temperatures and ~3 km using proxy moist enthalpy. This discrepancy is likely related to an inconsistency between the proxy data for temperature and moist enthalpy. The combination of temperature and moist enthalpy estimates implies a warm and dry environment, which is inconsistent with geological evidence for humid conditions. Our study emphasizes that lapse rates in warm climate were likely much different than today's, and highlights the advantages of using climate models to understand past climate states and regional circulation patterns to derive more accurate paleoelevation estimates using proxy temperature and moist enthalpy.

3.2 Introduction

The development of surface elevation informs our understanding of past geodynamic processes, regional climate patterns, and the distribution and evolution through allopatric speciation of ancient flora and fauna. Paleoaltimetry techniques have been widely used to constrain the surface uplift history of the North American Cordillera (e.g., Chase et al., 1998; Wolfe, 1998). Geological evidence suggests that this region was higher in the past, but how high and when the peak elevations were reached remains controversial (e.g., Sonder and Jones, 1999). Erosional dissection across the Rockies has long been viewed as evidence that Cordilleran uplift occurred during the Late Cenozoic (~10 Ma) (Graf, 1987). However, geophysical, tectonic, structural, and sedimentological evidence indicate that the crustal conditions necessary to support a high plateau existed across western North America during the late Cretaceous (~71 – 55 Ma) (DeCelles, 2004) and early Cenozoic (55 Ma to 28 Ma) (Chamberlain et al., 2012). Paleoaltimetry estimates based on stable isotopic compositions of soil and lacustrine carbonates, volcanic deposits, and organic materials support the presence of an early, high plateau and indicate that western North American Cordilleran may have been as high as 3 - 4 km during the Eocene (Mix et al., 2011; Chamberlain et al., 2012; Feng et al., 2013).

Studies using fossil-leaf paleoaltimetry indicate somewhat different elevations depending on whether temperature or moist enthalpy was used as an altimeter. Estimates using temperature suggest a high plateau with peak elevations ≥ 3 km across the Laramide foreland province but relatively low elevations in the hinterland region during the Early to Middle Eocene (~55 to ~40 Ma) (Chase et al., 1998). Estimates using moist enthalpy, in contrast, yield elevations of ~3 km in the northern reaches of the Cordillera, but relatively low elevations (2 km) to the south (Wolfe, 1998). The discrepancies in the paleoelevation and topographic gradient of the

Cordillera estimated by fossil leaf altimetry confound our understanding of the tectonic history of the region. For example, peak elevations in the hinterland and a significant north-south topographic gradient, inferred from moist enthalpy, are consistent with the idea that high topography propagated from north to south with piecemeal removal of mantle lithosphere (Chamberlain et al., 2012). Alternatively, the occurrence of peak elevations in the Laramide foreland province, as indicated by temperature estimates, provides support for the idea that underthrusting of the oceanic plate beneath North American continental lithosphere and eastward propagation of basal décollement might have driven the uplift (Decelles, 2004).

Methods for reconstructing past surface elevations rely on proxies of environmental properties, such as fossil leaves, that can be related to surface elevation. Characteristics of fossil leaves including leaf size and margin, have been related to near-surface temperature and moist enthalpy, both of which vary as a function of surface elevation. Fossil-leaf altimetry uses the inferred temperature (e.g. Meyer, 2007) or moist enthalpy (e.g. Forest et al., 1999; Forest et al., 2007) difference between two different fossil locations, in combination with modern or theoretical lapse rates, to calculate surface relief between the sites.

In previous studies that apply fossil-leaf altimetry, temperature lapse rates have typically been estimated by dividing surface temperature differences between two coeval sites at similar latitudes by their elevation offset, resulting in values of ~2 – 5 °C km^{-1} across the western U.S. (Wolfe et al., 1992). The moist enthalpy lapse rate has been taken to be 9.8 kJ km^{-1} based on the theoretical considerations of the conservation of energy within an air parcel (see Section 3.3.1, Forest et al., 1999). To estimate absolute surface elevations, coastal fossil sites have often been used to provide a sea-level reference (see review by Meyer et al., 2007).

Uncertainties in fossil-leaf altimetry have been attributed to the interpretation and scoring of leaf characteristics. Leaf-climate relationships are calibrated from modern studies, and have uncertainties of ~2 – 5 °C (Forest, 2007; Miller et al., 2006; Peppe et al., 2011; Spicer et al., 2005; Teodoridis et al., 2010; Wilf et al., 1997), and ~5.5 kJ from analytical uncertainty (Forest et al., 1999) and 13.4 kJ from combined analytical and leaf area bias uncertainty (Peppe et al., 2010), equivalent to surface elevation uncertainties of ~0.5 – 1.4 km assuming modern global (5 °C km^{-1}) or theoretical (9.8 kJ km^{-1}) lapse rates. Leaf-climate relationships, however, are weakened by the complicated responses of leaf physiognomy to the growing environment. For example, toothed margins of fossil leaves are usually related to temperature, but other factors

such as local water, plant type (deciduous vs evergreen and woody vs non-woody), leaf thickness, and wood type (ring-porous vs diffuse-porous) (Peppe et al., 2011; Royer et al., 2012) are also closely linked to this trait. To further complicate matters, leaf shape, size, and margin are shown to be controlled by phylogeny and may not maintain the same climate-leaf characteristics relationship in the past as present (Little et al., 2010). This complication could be alleviated through careful calibration of these relationships by incorporating phylogeny into the calculations (Peppe et al., 2011), a practice that has not been widely adopted. The scoring of leaf traits is another source of uncertainty. Estimates of leaf size, from which humidity and moist enthalpy are derived, can vary depending on the method of measurement (Peppe et al., 2010) and the classification system used (Wilf, 1998). Uncertainties in measured leaf size can lead to biases in the estimate of present-day North American elevations of up to 2 kms (Peppe et al., 2010).

The temperature and moist enthalpy lapse rates used to translate proxy differences between sites to elevation estimates are another potential source of bias that have not been investigated. In the absence of a good alternative, most previous studies have used modern lapse rates (e.g. Chase et al., 1998; Ghosh et al., 2006; Wolfe et al., 1998). However, there is no reason to think that lapse rates have remained constant through time especially on regional scales. Different climate and topographic conditions can profoundly influence both temperature and moist enthalpy lapse rates. For example, in climate simulations with elevated CO_2, the middle troposphere undergoes preferential moistening and warming, which weakens vertical stratification and giving rise to shallower lapse rates (Poulsen and Jeffery, 2011; Soden, 2005). Conversely, cold climates likely exhibit stronger tropospheric stratification and greater lapse rates. In addition, climate models simulate substantial changes in temperature and humidity due to Andean and Tibetan Plateau surface uplift. The uplift of southern Tibet leads to a regional increase of ~5 – 10 kJ in moist enthalpy (Boos and Kuang, 2010). Similarly, diabatic heating in response to Andean uplift enhances moisture convergence over the range (e.g., Feng et al., 2014; Insel, et al., 2009; Poulsen et al., 2010) and doubles the moisture content of local air masses (Insel et al., 2009) at high altitudes, leading to a potential reduction in temperature and moist enthalpy lapse rates.

Similar complexities likely contribute to discrepancies in elevation estimates of the Eocene North American Cordillera between using fossil leaf temperature and moist enthalpy altimetry. In order to resolve these discrepancies, we re-evaluate and refine hypsometric

estimates using a global climate model. First, we explore differences between Eocene and modern lapse rates across the western U.S. using estimates from high-resolution modern observations and Eocene climate simulations. Then, we discuss possible biases in elevation estimates introduced by changes in local atmospheric circulation due to the uplift. Finally, we utilize our Eocene climate simulations to estimate elevations of the western North American Cordillera through a comparison of model simulations and proxy data. Differences in our estimates from published results are subsequently analyzed and discussed.

3.3 Methods and data

3.3.1 Calculation of moist static energy and moist enthalpy

The use of moist enthalpy to deduce past surface elevations was pioneered by Forest et al. (1995) with the assumption that under adiabatic conditions, and ignoring small changes in kinetic energy ($\ll$ 1 %), the moist static energy of an air parcel is conserved. Moist static energy is defined as:

$$MSE = C_p'T + L_v q + gH \qquad (1)$$

where C_p' is the specific heat capacity at constant pressure of moist air; T (K) is the surface temperature (K); L_v (J kg^{-1}) is the latent heat of evaporation for temperatures between 238 and 308 K (List, 1984); q is the specific humidity (kg/kg); g (9.8 kg m s^{-2}) is the gravitational acceleration and H (m) is altitude. In (1), the specific heat capacity for moist air is calculated as:

$$C_p' = C_p(1-q) + C_w q \qquad (2)$$

where C_w and C_p are the specific heat of liquid water (4190 J kg^{-1} K^{-1}) and dry air (1004 J kg^{-1} K^{-1}).

The moist static energy of an air parcel is equal to the sum of its moist enthalpy (ME) and and gravitational potential (gH). The ME is defined as:

$$ME = C_p'T + L_v q \qquad (3)$$

If MSE is conserved, the change in ME (ΔME) is equal to the change in gH (ΔgH, $\Delta MSE = \Delta(ME + gH) = 0$). This relationship can be rewritten as the lapse rate of moist enthalpy ($-\Delta ME/\Delta H$):

$$-\Delta ME/\Delta H = g \qquad (4)$$

which is equivalent to 9.8 °C km^{-1}.

The conservation of moist static energy implies that thermo-dynamic changes to an air parcel during lifting are purely adiabatic, an assumption that is not met under many circumstances. At any given location, the moist static energy is determined by the net energy transport and radiation flux. These fluxes sum to zero if averaged over a sufficiently large region and through the atmospheric column. However, the conservation is not always met locally within the lower troposphere where the paleoelevation is of research interest.

3.3.2 Moist adiabatic lapse rate

The moist adiabatic lapse rate is another atmospheric characteristic that can be potentially exploited by fossil-leaf paleoaltimetry. Present-day zonal mean tropospheric temperature lapse rates are nearly moist adiabatic within tropical (Xu and Emanuel, 1989) and extratropical regions during wet seasons (Schneider and O'Gorman, 2008). We compare simulated Eocene temperature-elevation distributions with those predicted by moist adiabatic lapse rates in order to understand whether these theoretic lapse rates are applicable to paleoaltimetry of the Eocene North American Cordillera. The derivation of moist adiabatic temperature lapse rates requires stricter assumptions than derivation of moist enthalpy lapse rates, including that cooling and condensation is both adiabatic and unidirectional and that all condensation is immediately removed from the parcel. The moist adiabatic lapse rate (Γ_s) can be calculated using the equation (Holton, 2004):

$$\Gamma_s = \frac{g}{C_p} \frac{[1+L_v q_s/RT]}{[1+\varepsilon L_v^2 q_s/(C_p R T^2)]} \qquad 5)$$

where ε here is the ratio of molecular weight of water to that of dry air and q_s is the saturation specific humidity; R=287 J kg^{-1} K^{-1} is the gas constant. Typical values of Γ_s are between 4 and 5 °C km^{-1} in warm and humid environments. Calculation of Γ_s requires knowledge of T and q_s at the condensation level. These values are prescribed as averages at an elevation of 1 km above the sea-level using ensemble Eocene simulations. At this elevation, all cases display relative humidity > 90 % across the Cordilleran region.

3.3.3 GCM experimental design

We developed a series of Eocene simulations, using ECHAM5, for two purposes: (i) to evaluate lapse rates under past climate conditions, and (ii) to compare simulated temperature and moist enthalpy with fossil leaf estimates as a means to identify likely elevation conditions for the Eocene fossil-leaf reconstructions. ECHAM5 is a global three-dimensional atmospheric general circulation model (Roeckner et al, 2003). The atmospheric model is configured with 19 vertical

levels and a spectral triangular truncation of 106 horizontal waves (~1° horizontal grid spacing). All simulations include early Eocene boundary conditions and fixed sea-surface temperatures (SSTs). Eocene paleogeography and topography are based on reconstructions from Scotese et al (1998) and Bice et al. (2000), and the vegetation distribution is from Sewall et al. (2000). Sedimentary and stratigraphic evidence suggests that the foreland region of the Cordillera was occupied by numerous closed basins that at times contained large lakes (Dickinson et al., 1988). These basins are represented in our simulations with low elevations of 0.5 km and a lake fraction of 50% (Figure 14). Atmospheric CO_2 is specified as 1120 ppm, consistent with proxy reconstructions (Beerling and Royer, 2011). Atmospheric N_2O and CH_4 are set to present-day values of 306 ppb and 1.65 ppm. Monthly SSTs were calculated using the procedure described in Feng et al. (2013), which consists of 1) using ECHAM5 with a slab ocean model and present-day observational ocean heat flux to estimate the zonal distribution of SST, and 2) then adjusting the resulted meridional SST distribution to replicate the reconstructed meridional gradient of Eocene SSTs (See Figure 1. in Feng et al., 2013).

Our simulations differ only by the prescribed heights of the North American Cordillera. The Cordilleran hinterland is represented as an ellipsoidal plateau with the peak elevation raised incrementally from 1 to 4 km at 0.5 km intervals (Figure 14). The spatial extent of the hinterland is prescribed based on the distribution of stable isotopic compositions of oxygen ($\delta^{18}O$) and hydrogen (δD) in authigenic minerals and organic materials (Chamberlain et al., 2012; Mix et al., 2011). Sharp spatial gradients in $\delta^{18}O$ and δD are typically interpreted to result from isotopic rainout during orographic precipitation, and as a result signify topographic gradients. Strong Eocene isotopic gradients are found along slopes of the northern Sierra Nevada (~25 ‰ in δD) (Mulch et al., 2006) and between the Yellowstone region and central Wyoming (~8 ‰ in $\delta^{18}O$) (Sjostrom et al., 2006). Based on these gradients, the western boundary of the Eocene Cordilleran hinterland in the model is placed along the Sierra Nevada Mountains and eastern boundary along the central Rockies and roughly follows the Cordilleran thrust belt to the south. All experiments were run for 20 model years and reach equilibrium within the first 5 years. Model results are reported as averages of the last 15 years. No apparent trends (<0.03 °C/decade) in global mean land surface temperature are detected over this period. An additional simulation with present-day boundary conditions was also conducted in order to evaluate model skill in simulating temperature and moist enthalpy across the modern western U.S.

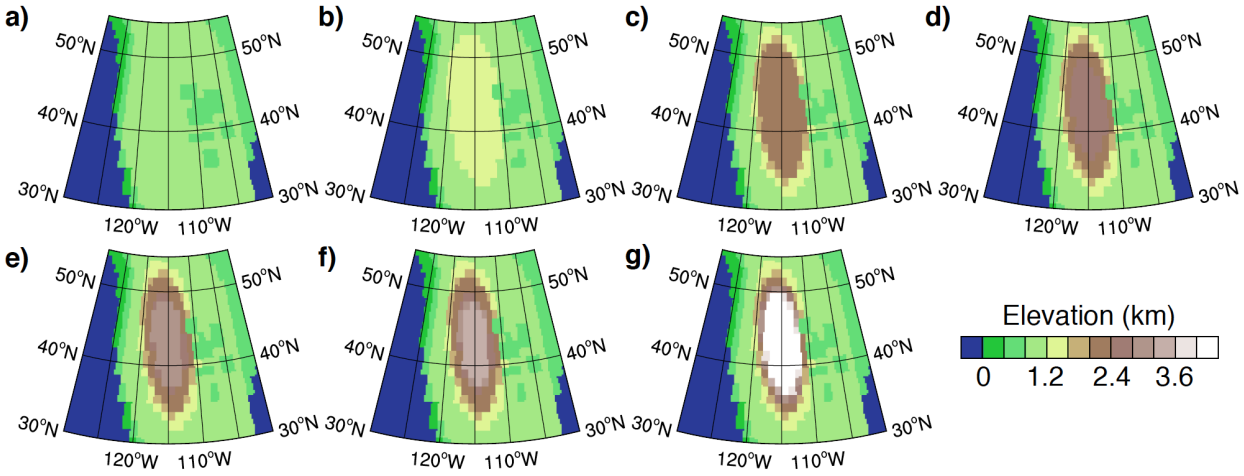

Figure 14 Prescribed western North American elevations (km).
The North American Cordillera is systematically raised from a maximum elevation of 1 to 4 km in 0.5 km intervals (a-g). Foreland basins east of the Cordilleran hinterland are 0.5 km high and have a 50% lake fraction.

ECHAM5 was chosen for this study because it exhibits reasonable skill in simulating many aspects of modern and Eocene North American climate including the distribution of modern precipitation over western North America (Cook et al., 2008; Salathé, 2006) and the strength and location of the Aleutian low and the storm track over the Pacific Northwest (Salathé, 2006). In addition, ECHAM5 simulates Eocene temperature and precipitation patterns in agreement with the majority of flora-based mean annual temperature and precipitation reconstructions across lowland western North America (Appendix B1, and Feng et al., 2013) and with previous modeling results using a high-resolution (50 km) regional climate model (Sewall and Sloan, 2006). The model underestimates precipitation amounts derived from early Eocene paleofloras across low elevation regions (Wilf et al., 1998), a bias also noted in other modeling studies (Sewall and Sloan, 2006).

3.3.4 Calculations of modern and Eocene lapse rates

We calculate and compare lapse rates of surface temperature and moist enthalpy from Eocene simulations and modern observations. Lapse rates are determined as the slopes of the least square regression between either surface temperature or moist enthalpy and elevation at locations of observations and simulations. The uncertainty is reported as the 95% confidence interval of the slope. All results are calculated using mean annual climatologies.

Simulated lapse rates are derived from mean-annual 2-m temperature and moist enthalpy at each model grid point. Modern lapse rates of temperature are calculated from station observations of at least two years in duration, of which there are a total of 2002 across the western continental U.S. (34 °N to 49 °N, west of 104 °W) (http://www.ncdc.noaa.gov/cdo-web/). Previous estimates of temperature lapse rates were calculated by dividing differences between individual inland and coastal stations along latitudes by their elevation differences (Wolfe, 1992). The application of high-resolution observational data allows refinement of these lapse rates over a continuous space. Due to the small number of stations (38) with complete observational records of all the parameters (surface temperature, dew point and pressure) required to calculate moist enthalpy, moist enthalpy lapse rates are calculated using the Modern Era Retrospective-analysis for Research and Applications (MERRA) data (Rienecker et al., 2011). Co-located surface elevation values are estimated by bin-averaging 10' USGS elevation data (derived from the 30" GTOPO30 dataset, US Geological Survey) into the MERRA grid (0.5° grid spacing). We calculate moist enthalpy using 33-yr mean annual climatological averages (1979-2011). We have also estimated lapse rates using the North American Regional Reanalysis data (Mesinger et al., 2006). The results are similar for both reanalysis data. For simplicity, only the MERRA results are reported here.

Lapse rates of temperature and moist enthalpy are reported for three regions including: the western coastal region (Figure 15, red filled circles), the central Basin and Range and Columbia Basin region (Figure 15, cyan filled circles), and the eastern Rocky Mountain and Colorado Plateau area (Figure 15, green filled circles).

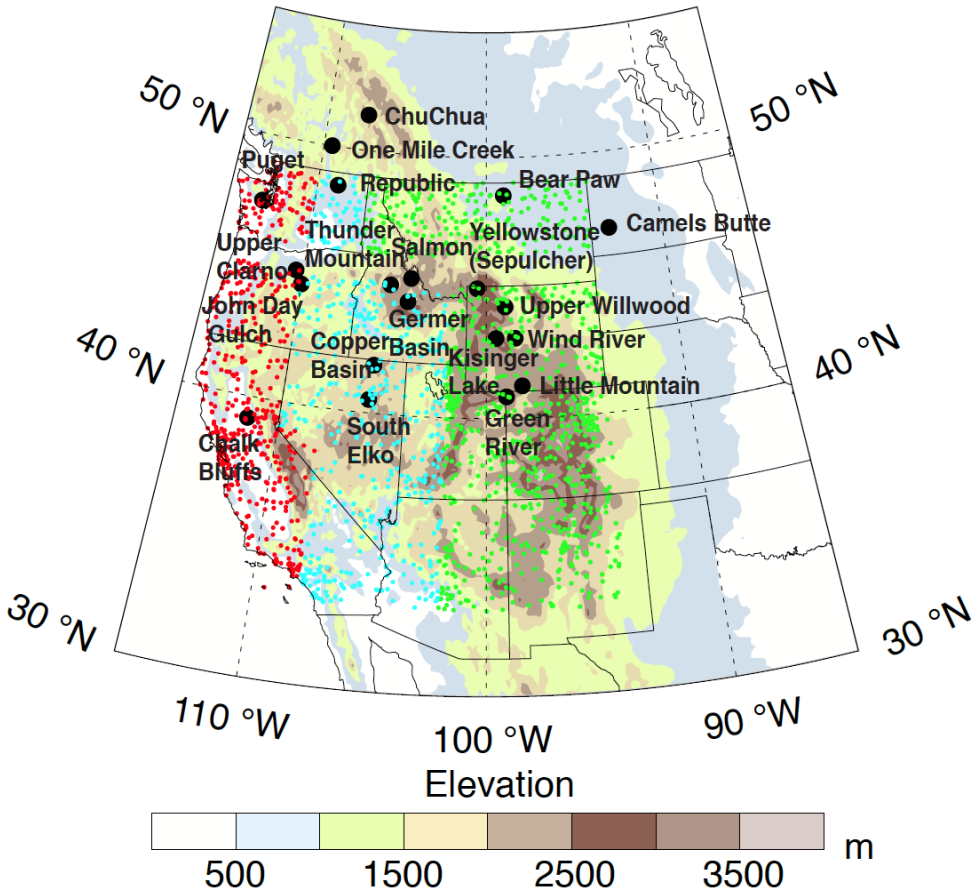

Figure 15 Locations of climate stations in the NCDC database (small filled circles) and Eocene fossil sites (large filled circles).
Modern observations are grouped into three sets according to different topographic conditions (red filled circles: coastal; cyan filled circles: Columbia Basin and Basin and Range; green filled circles: Rocky Mountains and Colorado Plateau). Gridded MERRA data are grouped into the same groups using the same latitude and longitude boundaries. Eocene sites (black filled circles) are complied from Chase et al. (1998) and Wolfe et al. (1998).

3.3.5 Lapse rate-independent paleoaltimetry

We estimate Eocene North American Cordilleran elevations by directly comparing proxy reconstructions of mean-annual temperature and moist enthalpy with values from each of our Eocene simulations. Our hypsometric estimates are the heights in the model at which simulated mean-annual temperature and moist enthalpy match those derived from fossil leaves. This approach has the distinct advantage of taking into account non-linear variations in temperature and moist enthalpy associated with uplift-induced circulation changes, which is overlooked when adopting the traditional fossil-leaf altimetry method based on using linear lapse rates. Hypsometric estimates are derived for three zonal transects centered at 42, 44, and 47 °N.

Simulated temperature and moist enthalpy are averaged over 5° latitudinal swaths for each transect. Proxy temperature and moist enthalpy are binned into these transects by proximity.

3.4 Results

3.4.1 Modern and Eocene lapse rates of temperature and moist enthalpy

Modern lapse rates of temperature and moist enthalpy display distinct spatial variability across the western continental U.S. (Figure 16 and Table 3). Temperature lapse rates are close to moist adiabatic rates (~4 - 5 °C km^{-1}) in the humid northern and central regions but approach the dry adiabatic rate (9.8 °C km^{-1}) in the semi-arid southwestern U.S. Lapse rates in this region are much higher than the ~3 °C km^{-1} lapse rate reported by Wolfe (1992). This difference arises from the fact that lapse rates in Wolfe (1992) were estimated using California coastal temperatures (~13 - 16 °C from 33 to 38 °N), which are ~10 °C colder than low elevation continental interior temperatures (Figure 16b and c).

Moist enthalpy lapse rates (Figure 16 and Table 3) over the western U.S. are lower than the theoretical lapse rate (9.8 kJ km^{-1}, Section 3.3.1), indicating that moist static energy is not strictly conserved and increases at high altitudes. The budget of moist static energy is determined by the net radiative flux and transport of moist static energy. Spatial variations in net surface radiative flux across the western U.S. are quite small (< 5 W/m^2, based on MERRA data). Consequently, the additional moist static energy comes from energy transport. The climatologic mean meridional circulation shows net northward transport of tropical air masses with high moist static energy towards high altitudes of the Cordillera (Figure 17a). This additional input of moist static energy increases the high-altitude moist enthalpy and lowers the moist enthalpy lapse rate.

ECHAM5 simulates reasonable elevation distributions of present-day temperature (Appendix B2A-C) and moist enthalpy (Appendix B2D-F) across the western U.S. (compare Appendix B2 to Figure 16). Simulated present-day lapse rates are close to observed rates (Table 3). The model underestimates temperature lapse rates across the Coastal Range and Sierra Nevada Mountains most likely because it does not adequately resolve the sharp topographic gradients across these ranges. This bias may be smaller in our Eocene simulations, since the Western Cordillera is thought to have been broader during the Eocene (DeCelles, 2004), and therefore, is better resolved in the model.

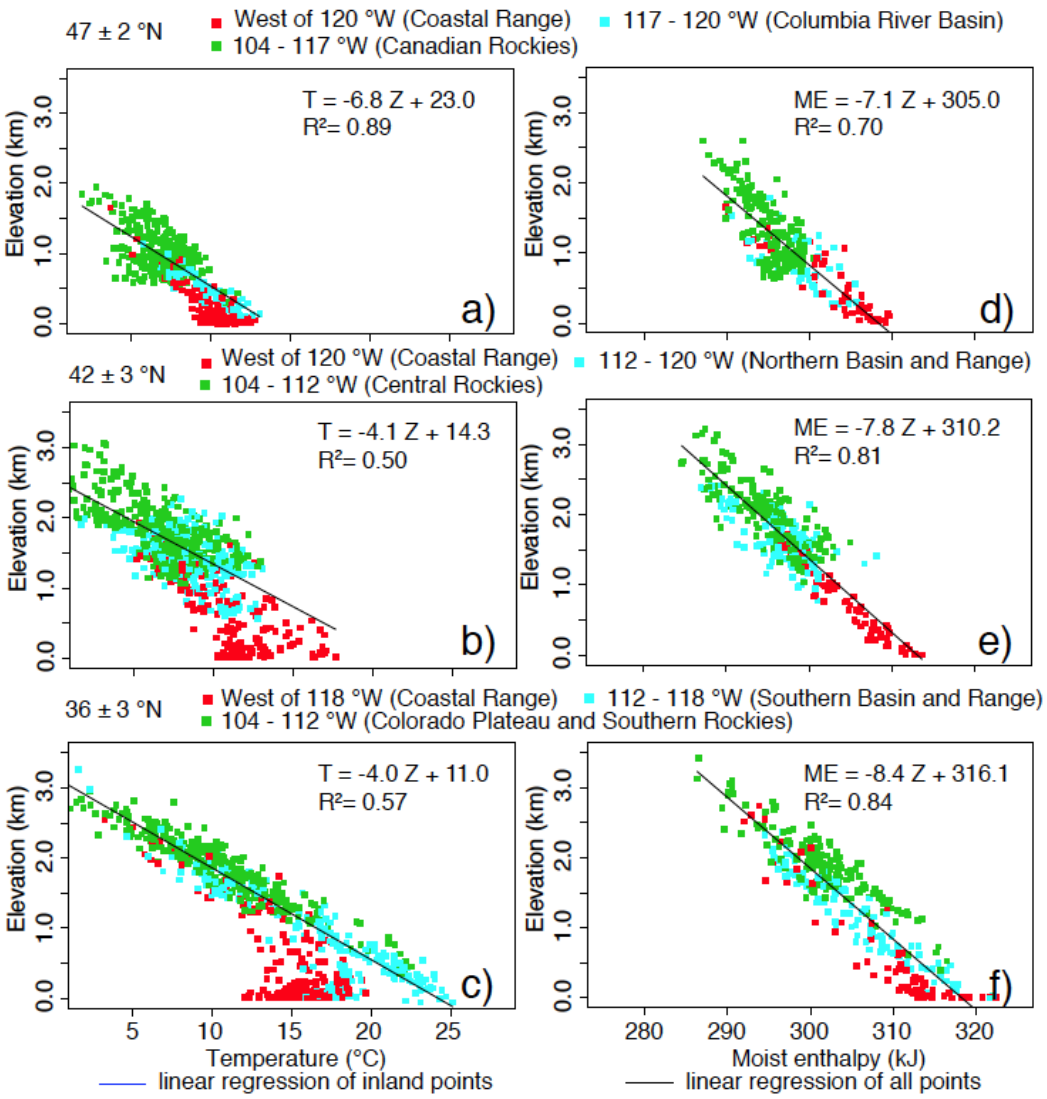

Figure 16 Observed modern temperature (T, left) and moist enthalpy (ME, right) versus elevation (Z).
a-c) Mean-annual 2-m air temperature and elevation across zonal swaths at a) 47 ± 2 °N, b) 42 ± 3 °N, and c) 36 ± 3 °N. d-f) Mean-annual moist enthalpy and elevation across the same zonal swaths. Locations are indicated by color-coding and correspond to the regions indicated in Figure 15 for both temperature and moist enthalpy.

Table 3 Modern and Eocene lapse rates of terrestrial temperature and moist enthalpy calculated from observations and simulations across each transect of the North American Cordillera.

	Modern		
	Observed lapse rates		
	Northern Cordillera	Central Cordillera	Southern Cordillera
Temperature (°C km^{-1})	4.0 ± 0.4	4.1 ± 0.3	6.8 ± 0.2
Moist enthalpy (kJ km^{-1})	7.1 ± 0.5	7.8 ± 0.3	8.4 ± 0.3
	Simulated lapse rates		
Temperature (°C km^{-1})	3.9 ± 1.2	3.7 ± 1.5	7.2 ± 1.6
Moist enthalpy (kJ km^{-1})	7.3 ± 1.1	8.1 ± 0.8	8.4 ± 0.8
	Eocene		
	Simulated lapse rates		
	Northern Cordillera (47 ± 2 °N)	Central Cordillera (42 ± 2 °N)	Southern Cordillera (36 ± 3 °N)
Temperature (°C km^{-1})	4.8 ± 0.2	4.9 ± 0.2	5.1 ± 0.3
Moist enthalpy (kJ km^{-1})	10 ± 0.3	10.7 ± 0.3	11.6 ± 0.3

Simulated Eocene lapse rates differ significantly from modern rates (Table 3). Eocene ensemble lapse rates of temperature and moist enthalpy are nearly invariant for the northern, central, and southern transects of the Cordillera and are close to the adiabatic lapse rates (Figure 18a-b, red lines for temperature (section 3.3.2) and 9.8 kJ km^{-1} for moist enthalpy (section 3.3.1)). The differences between modern and Eocene lapse rates reflect changes in the mean climate and topography. Under warm Eocene conditions, the southern transect has greater low-level humidity, a source of latent heat, leading to lower temperature lapse rates than under the modern semi-arid conditions in the same region. In contrast, enhanced Eocene moist enthalpy

lapse rates are associated with a reduction in the influence of meridional energy transport due to 1) a shallowing of the meridional gradient of moist static energy in the Eocene resulting from a shallower meridional SST gradient, which reduces the effect of energy transport; and 2) blocking of meridional airflow due to the higher elevations of the Cordillera, which reduces the transport by airflow (Figure 17b).

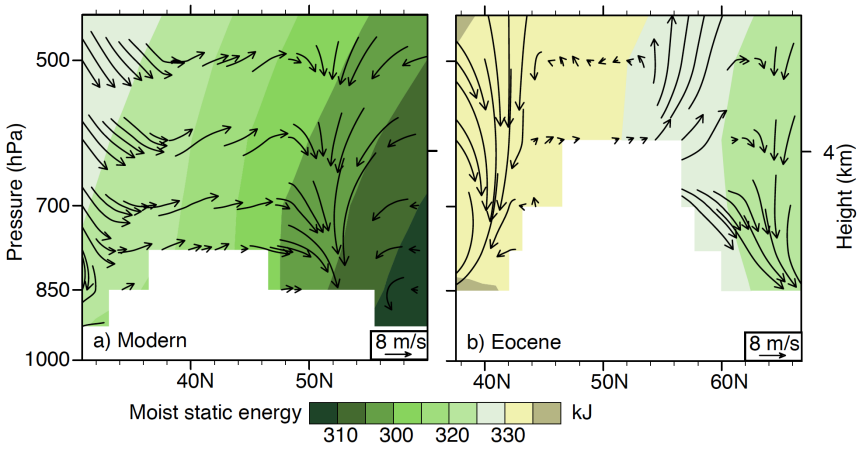

Figure 17 Simulated mean annual moist static energy (shaded) and circulation (vectors) averaged between 110 and 120 °W.
(a) modern and (b) Eocene North American Cordillera. White regions represent topography.

3.4.2 Uplift-induced circulation change at high latitude

Simulated Eocene temperature and moist enthalpy vary considerable from the means for specific elevations, as indicated by the width of the boxplots (Figure 18).The ranges of simulated temperature and moist enthalpy tend to be high but invariant across low-elevation region (≤ 2 km), which primarily reflects the strong coastal variability of temperature and moist enthalpy, resulting from active convective mixing associated with strong orographic precipitation . Substantial data spread also occurs at high altitudes (≥ 3 km) in our Eocene high-elevation cases. Above 2.5 km, spreading of temperature and moist enthalpy from their elevation means increases with height and reach ~8 °C and 8 kJ in the 4-km case (Figure 18, note the increase in width of box plots with elevation). These deviations highlight the non-linear responses of temperature and moist enthalpy to increasing Cordilleran elevations, and the uncertainty inherent in assuming a constant lapse rate. These high altitude deviations can be linked to two distinctive aspects of uplift induced circulation changes: 1) the warming and influx of moist static energy due to development of the paleo-North American Monsoon at the leeward side of the Cordillera;

and 2) the cooling and loss of moist static energy due to intensification of mountain gravity waves.

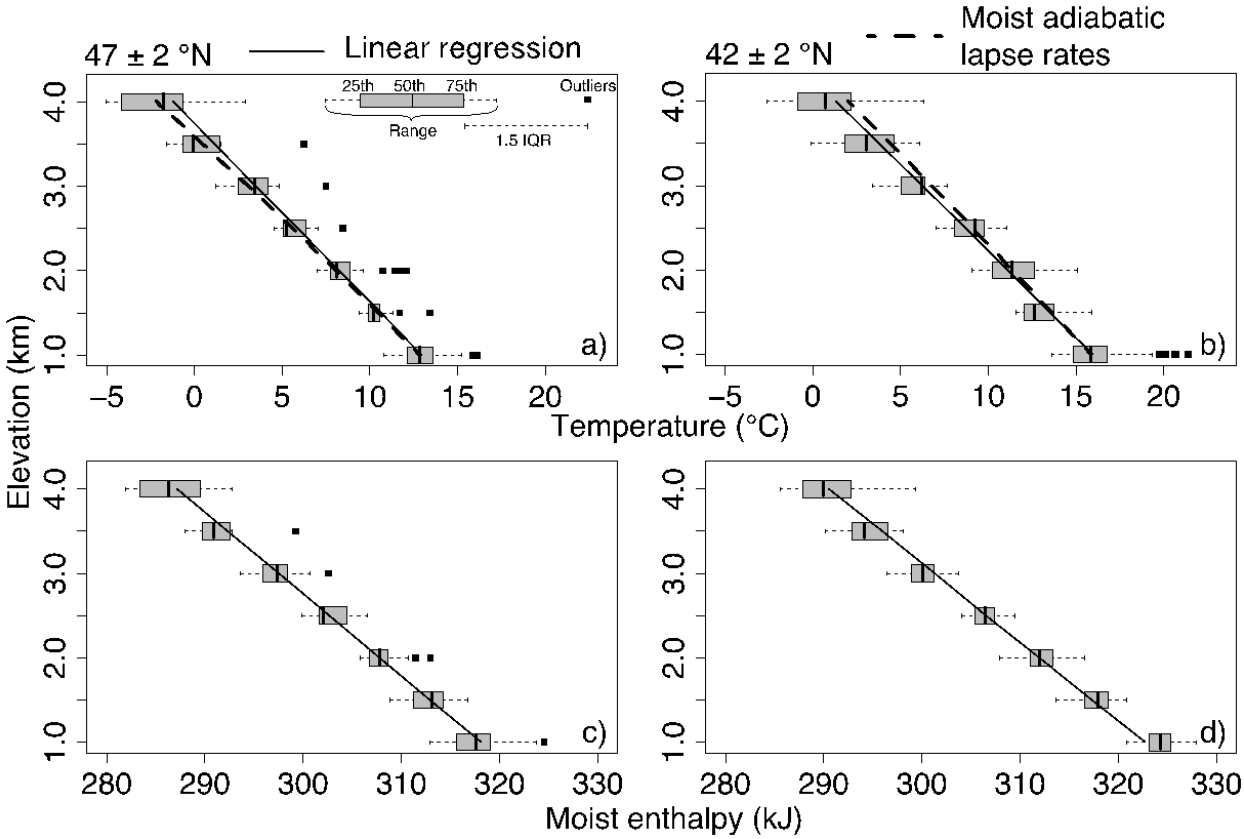

Figure 18 Simulated mean-annual Eocene temperature (top) and moist enthalpy (bottom) versus elevation for all prescribed-topography experiment.
Black lines are least-square regressions. Thick dashed lines in (a-b) depict temperature changes following the moist adiabatic lapse rates calculated according to section 3.3.2. To identify spatial variability of lapse rates, the North American Cordillera region is separated into northern (47 ± 2 °N, top) and southern (42 ± 2 °N, bottom) regions. Boxplots are overlaid to display the spread of data at each elevation (25th, 50th, 75th: data ranks; IQR: interquantile range). Both alpine temperature and moist enthalpy increasingly spread away from linear regressions with elevations ≥ 3 km.

Monsoonal circulation is largely absent in the low-elevation cases (< 3 km), but becomes prominent on the leeside of the Cordillera in the high-elevation cases. The development of leeside monsoonal circulation in response to the uplift has been observed by previous studies (Sewall and Sloan, 2006; Feng et al., 2013). This monsoonal circulation brings warm tropical air from the Gulf of Mexico to the high altitudes of the eastern Cordillera, leading to significant warming at alpine sites. Without *a priori* knowledge of this warming effect, proxies that capture

this warming are likely to be interpreted as having existed at lower elevations than they actually were. In fact, using a simulated mean Eocene lapse rate of 5 °C km^{-1} results in elevation underestimates by ~1 km at the eastern flank of the Cordillera in high elevation (≥ 3 km) cases (Figure 19a-c).

Similar to the monsoonal circulation, mountain gravity waves intensify in high-elevation (> 3 km) cases as signified by 500-hPa vertical velocities, which are similar and weak in low elevation cases, but become strong in high elevation cases. The vertical velocities indicate strong subsidence above the plateau, and oscillate between positive and negative values in the downwind direction (Figure 19g-i), characteristics of the wave trajectory. Mountain gravity waves are known to affect vapor $\delta^{18}O$ lapse rate by downward mixing of air parcels above high topography (Galewsky, 2009; Poulsen and Jeffery, 2011; Feng et al., 2013). Likewise, enhanced subsidence above the plateau (Figure 19g-i) promotes downward mixing of upper-level air parcels low in moist enthalpy, causing high altitude depletion of moist enthalpy in our experiments and a depression of the moist enthalpy. The use of the theoretical lapse rate (9.8 kJ km^{-1}), without considering this circulation change, leads to overestimate of paleoelevations by up to ~1 km (Figure 19d-f). This result suggests stronger elevation biases using moist enthalpy altimetry at high elevations (> 3 km) than using temperature altimetry in the western and central regions of the Cordilleran plateau . In the process of air mass mixing, moist enthalpy is more sensitive to changes in humidity, while humidity changes only affect temperature through condensation, typically small amount in the alpine regions. As a result, drying resulted from downward mixing of air masses degrades the accuracy of moist enthalpy altimetry more than temperature altimetry.

Uplift-induced circulation changes, including mountain gravity waves and leeward side monsoonal circulation, are overlooked in previous studies of fossil-leaf paleoaltimetry (and other types of paleoaltimetry). Although these changes mainly occur when the plateau rises above a critical elevation (~3 km in our case), without prior knowledge of the height of the Cordillera, it is precarious to rule out this possibility and adopting any linear lapse rates.

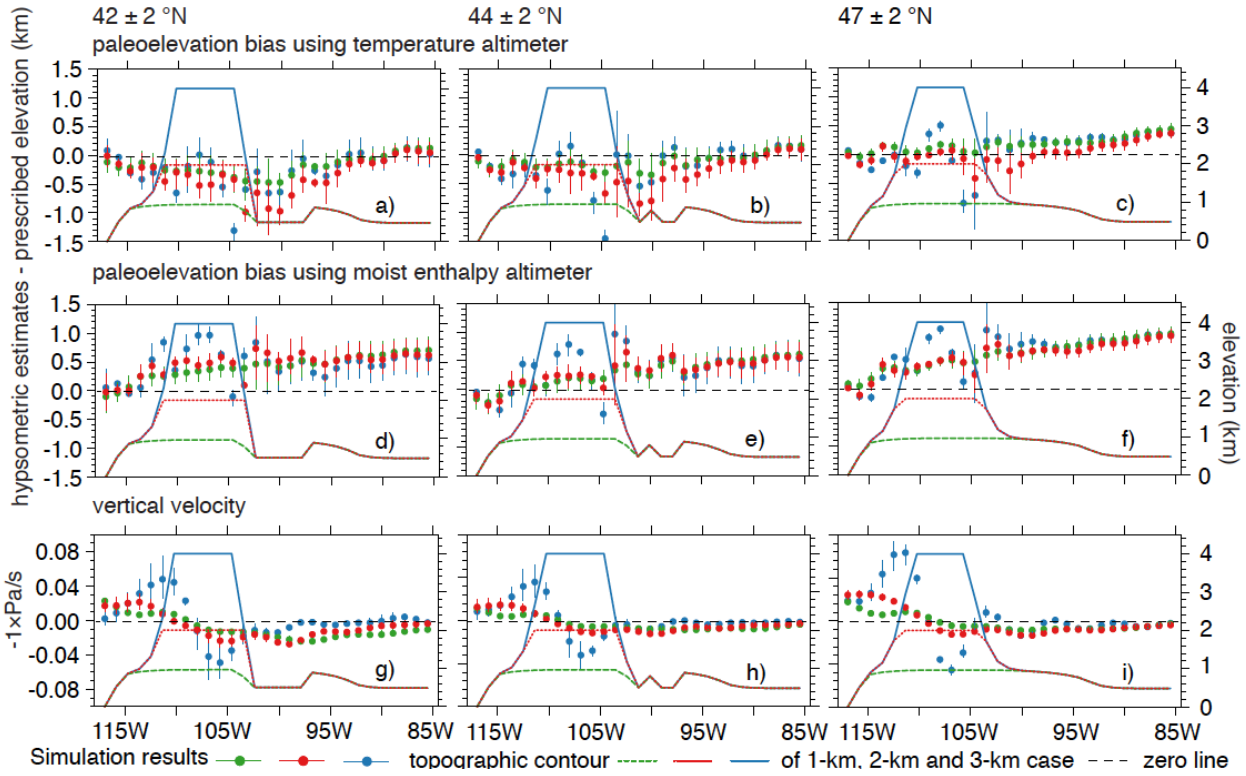

Figure 19 (a-f) Elevation biases resulting from assuming a linear lapse rate of 9.8 kJ km^{-1} for moist enthalpy and 5 °C km^{-1} for temperature.
The bias is measured as the departure from the prescribed elevations, i.e., negative values indicate underestimates and positive overestimates. (g-i) Zonal distribution of the vertical motion at 500 hPa. The pressure velocity is multiplied by -1 to have negative values indicate subsidence and positive values indicate upward motion. Error bars on each point represent the full range of values across the meridional extent of 5° latitude of each transect centered at 42 °N, 44 °N and 47 °N.

3.4.3 Lapse rate-independent elevation estimates using Eocene climate simulations

To avoid biases in paleoelevation estimates due to changing climate states and uplift-induced circulation changes, we derive elevation estimates based on the direct comparison between our paleoclimate simulations and proxy reconstructions of temperature and moist enthalpy (Section 3.3.4). Using this method, simulated temperatures match proxy values when prescribed maximum elevations are between 1.5 to 2 km for the northern Cordilleran hinterland and between 2 to 2.5 km for the central and southern Cordilleran hinterland (Figure 20a - c). In contrast, the match between simulated and proxy moist enthalpy occurs for a Cordillera with maximum elevations of 3 to 3.5 km across Cordilleran hinterland of all transects (Figure 20d - f).

The estimates of maximum elevation derived from temperature and moist enthalpy comparisons differ by ~1 km. Even for lowland sites, elevation estimates from proxy moist enthalpy are generally higher than those based on temperature.

3.5 Discussion

3.5.1 Paleoelevation biases across the Eocene Cordillera from proxy reconstructions of temperature and moist enthalpy and model biases

3.5.1.1 Inconsistent paleoelevation estimates from temperature and moist enthalpy altimetry

The lower elevation (~1 km) from temperature altimetry relative to moist enthalpy altimetry as shown in Figure 20 could be related to either model or proxy biases. Simulated temperatures match the low-elevation proxy temperatures reasonably well (Appendix B1). Yet, the model may overestimate alpine cooling rate indicated by fossil leaves. This overestimate could be associated with underestimates of precipitation (Appendix B1) due to the neglect of climate forcing factors (for example, Poulsen et al. (2015) has recently reported that variations in atmospheric oxygen concentrations may influence precipitation rates). This underestimates indicate overall sluggish hydrological regional hydrological cycle in our simulations. A more active hydrological cycle would lead to warmer alpine temperatures due to latent heating from condensation. However, stronger hydrological cycle also increases alpine humidity, and the associated moist enthalpy. Consequently, underestimates of strength of hydrological cycle only have limited effect on reconciling current elevation discrepancy between temperature and moist enthalpy altimetry estimates.

Alternatively, the proxies themselves could be inconsistent. This is shown by estimating surface humidity (q) from proxy temperature (T) and moist enthalpy (ME) using equation (3) ($ME = Lq + C_pT$). At fossil sites on the Cordilleran plateau, proxy moist enthalpy estimates are between 295 to 300 kJ and temperatures between 10 to 12 °C (Figure 20). From equation 1, we estimate alpine specific humidity to be between 4.3 and 5.5 g/kg. These estimates are comparable to MERRA observations for the present-day western U.S. (3.7 – 5.3 g/kg, 33 - 49 °N, 112 – 103 °W) and are systematically lower than simulated specific humidity values on the Eocene Cordillera at elevations of 1 to 3.5 kms. Notably, these estimates are inconsistent with annual rainfall abundances reconstructed based on multi-regression analysis of data using the climate leaf analysis multivariate program (CLAMP) (Wing and Greenwood, 1993; Gregory and Chase, 1992) and leaf area analysis (Wilf et al., 1998), and with the presence of conifer forests in

central Idaho (Erwin and Schorn, 2005), northeastern Nevada (Axelrod and Bailey, 1969), southern British Columbia, and northeastern Washington (Greenwood et al., 2005), all of which indicate a humid alpine environment in the early Eocene.

A more humid alpine environment requires a higher moist enthalpy than indicated by proxy estimates given current proxy temperature. Proxy estimates may in fact underestimate these quantities; Peppe et al. (2010) show that traditional categorical measurement methods underestimate leaf areas, which are used to infer temperature and moist enthalpy. This bias results in greater underestimates of moist enthalpy than temperature based on present-day CLAMP climate-leaf traits dataset (13 kJ versus 3 °C in Figure 3 of Peppe et al., 2010). Similar biases may also be applicable to Eocene fossil leaves, resulting in greater underestimates of Eocene moist enthalpy across the western North America than temperature, and apparent dry environment indicated by these proxy estimates.

3.5.1.2 Elevation underestimates due to limited model resolution

Another source of bias in elevation estimates of Eocene North American Cordillera arises from the comparison of relatively coarse resolution climate model results with sparse fossil floras. This bias may lead to overall elevation underestimates by both temperature and moist enthalpy altimetry using our climate simulations. Fossil floras are mostly found within basins that tend to be lower, warmer and moister than their alpine surroundings. Our simulations do not capture these fine-scale topographic conditions. Therefore, the assumption (by us and previous workers) that fossil floras record mean alpine environments may lead to an underestimate of the broad-scale elevation. Future high-resolution reconstructions and the development of additional fossil floral sites will refine these elevation reconstructions.

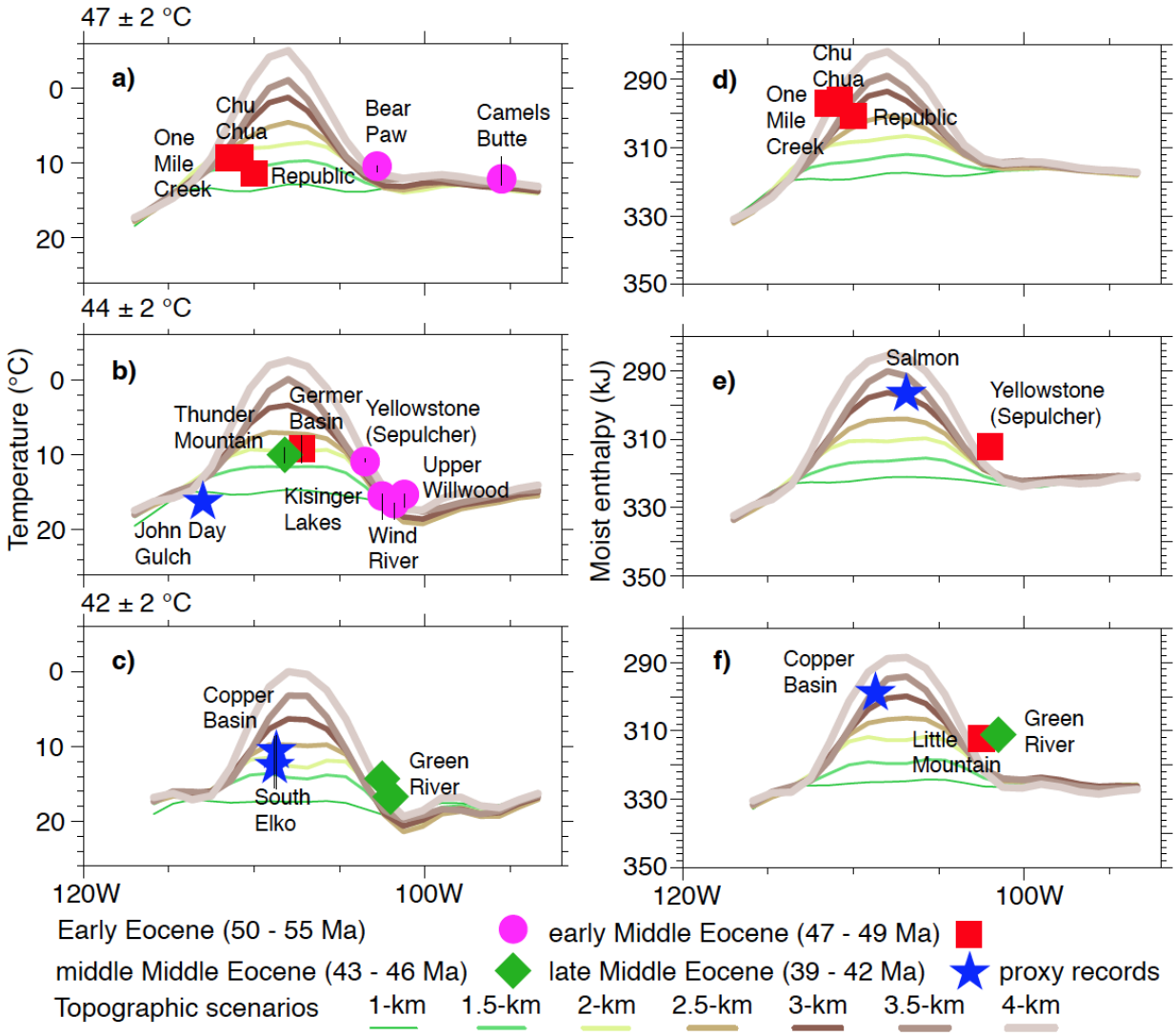

Figure 20 Zonal distribution of proxy and simulated Eocene temperature (left, a-c) and moist enthalpy (right, d-f) at inland sites.
Simulated-values represent 5° zonal averages across the Cordillera for each elevation scenarios centered at 47 °N (top), 44 °N (middle) and 42 °N (bottom). Proxy records are mapped to each transect based on proximity and are colored and shaped by age. The error bars on the proxy temperature records depicts the ranges of estimates compiled from Gregory and Chase, (1994), Povey et al., (1994), Wing and Greenwood, (1993), Greenwood and Wing, (1995), and Chase et al., (1998).

3.5.2 Comparison of paleoelevation estimates for the North American Cordillera

Our elevation estimates based on our Eocene simulations differ from previous reconstructions using lapse rates of temperature and moist enthalpy in two ways. First, our estimates using proxy temperatures are systematically lower than previous estimates by up to 2 km at Cordilleran foreland sites (Figure 21). Second, we find high elevations of 2-3 km along

the Western Cordillera and lower elevations of 1-2 km in the foreland basins to the east across eastern Montana and Wyoming (Figure 21). This topographic gradient is absent in previous studies.

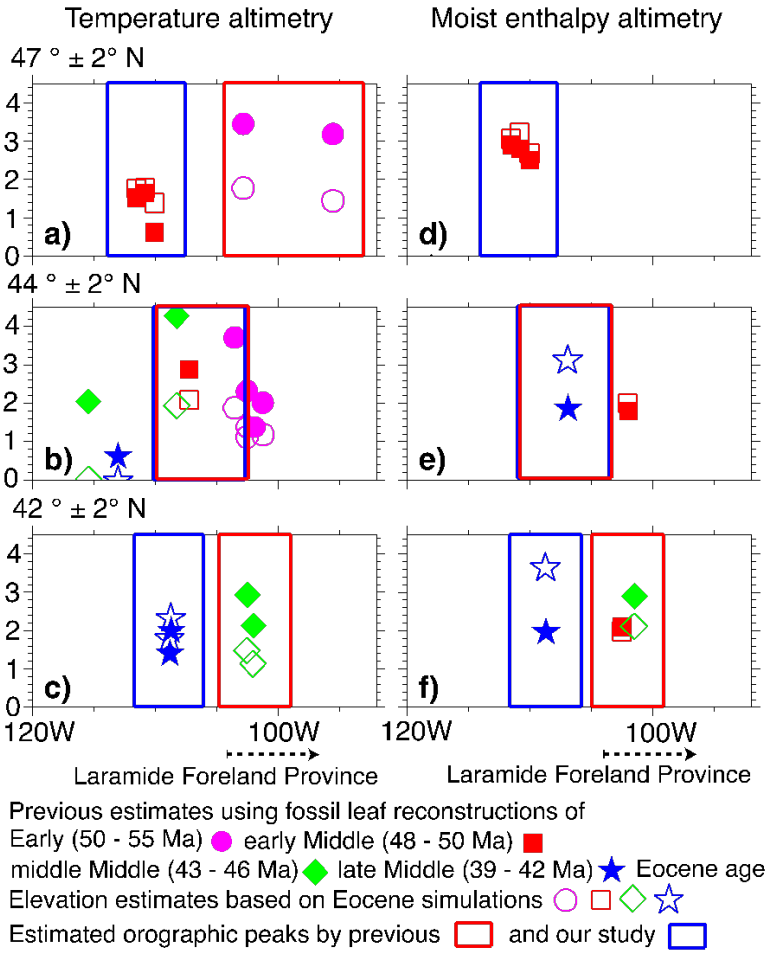

Figure 21 Comparison between published paleoelevation estimates (filled markers) and our estimates based on Eocene climate simulations (hollow markers) using temperature (left column, a - c) and moist enthalpy (right column, d - f) altimetry.
Proxy estimates of temperature and moist enthalpy are colored and shaped by age. The locations of maximum topography are indicated by the rectangular boxes, corresponding to estimates from previous studies (red) and in this study (blue). Thick dash lines indicate the longitudinal range of the Laramide foreland province.

There are several reasons for these differences. First, previous hypsometric estimates assumed a temperature lapse rate of 3 °C km^{-1} (Wolfe, 1998) that is lower than that the lapse rates (~5 °C km^{-1}, Table 3) simulated in our runs. The higher lapse rates in our simulation lower hypsometric estimates by up to ~1.3 km. Second, our estimates are derived from direct comparisons between simulations and proxy values at inland sites, while previous estimates were

based on temperature and moist enthalpy differences between coastal and inland sites. This latter approach assumes that temporal climate variability along the coast is representative of inland sea-level conditions at equivalent latitudes. However, modern observations (Figure 16) and Eocene reconstructions do not support this assumption. Proxy mean values of coastal temperature and moist enthalpy are 18.8 °C and 325.4 kJ from Early to late Middle Eocene (~15 Million years), approximately 5 °C and 13 kJ lower than Early and middle Middle Eocene values and higher by 3 - 4 °C and ~12 kJ than late Middle Eocene values (Figure 22). Among inland sites of similar latitudes, proxy temperature and moist enthalpy are similar during the Early to Middle Eocene and do not exhibit large temporal variability. This strong climate contrast suggests a discontinuity between the Pacific coast and continental interior, which may result from the insulation of climate influences from the Pacific by the North American Cordillera barrier. Alternatively, the lack of inland climate variability may be explained by compensating elevation changes. For this explanation to hold, the inland sites must have all experienced the same elevation adjustments, i.e., uplift from the early to early middle Eocene, subsidence from the early to middle Middle Eocene, and uplift again in the late Middle Eocene, in order to counteract the coastal cooling, warming (increasing moist enthalpy), and cooling (lowering of moist enthalpy) during the Early to late Middle Eocene. This multiphase elevation adjustment of the Eocene Cordillera is unsupported by geological evidence.

The use of Eocene coastal temperature and moist enthalpy records, with large variability that is not representative of continental interior conditions, significantly biases the North American paleoelevation estimates. We estimate these elevation biases using mean coastal temperature and moist enthalpy values recorded by Early to Middle Eocene fossil leaves and simulated Eocene temperature and moist enthalpy lapse rates (5 °C km^{-1} and 10 kJ km^{-1}) across the western North America. These lapse rates are applicable for low- and moderate-elevation scenarios for the Eocene North American Cordillera (≤ 3 km) (Figure 18), including most of our elevation estimates of the Cordillera (Figure 21).

The coastal warming (~5 °C) and high moist enthalpy (~13 kJ) lead to ~1 - 1.3 km elevation overestimates for the early Eocene and middle Middle Eocene proxies. The cooling (3 - 4 °C) and low moist enthalpy leads (~12 kJ) to ~0.6 - 1.2 km underestimates for the late Eocene proxies. Removing these biases would decrease elevation estimates in the foreland basins where Early to early Middle Eocene reconstructions reside (Figure 21a-c, f) and increase estimates in

the central and southern Cordillera for the late Middle Eocene (Figure 21c, e-f), revealing a topographic gradient of ~1 – 1.5 km between the Cordillera and the Laramide foreland basins. This topographic gradient is consistent with authigenic mineral $\delta^{18}O$ reconstructions with strong depletion across the central Rockies (Sjostrom et al., 2006; Fan et al., 2014) and relatively enriched values from the foreland basins (Fan and Dettman, 2009).

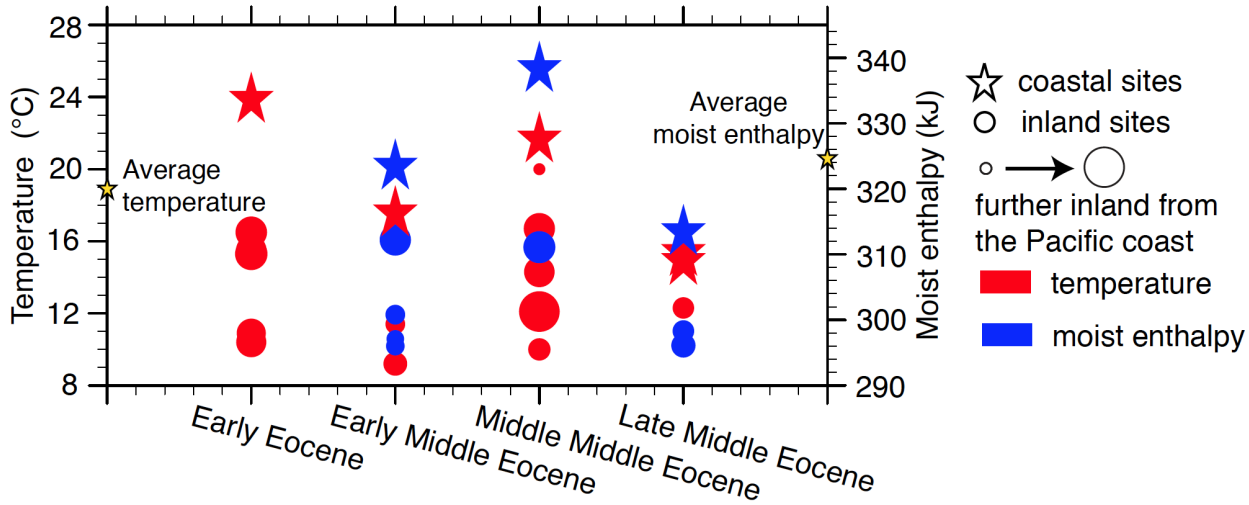

Figure 22 Temporal evolution of fossil leaf temperature (red) and moist enthalpy (blue) at coastal (stars) and inland sites (filled circles).
The sizes of the filled circles indicate the longitudes of the sites and increase eastward from the Pacific coast. The inland sites with the same marker size are from the same longitude, and have similar continentality (similar distance from the coast). It can be seen that inland sites of similar longitudes have roughly invariable temperature and moist enthalpy during the Early to Middle Eocene.

3.5.3 Implications for paleoaltimetry using fossil leaf characteristics

A common practice in fossil-leaf paleoaltimetry is to use modern lapse rates as approximations for paleo-lapse rates. Our experiments do not support this practice. Similar to our Eocene case, in the past greenhouse climates, enhanced saturation state of the lower troposphere and reduced meridional heat transport by shallow tropospheric thermo-gradient likely vary the lapse rates away from modern but approaching the adiabatic lapse rates. In contrast, in colder and drier, more modern-like climates, temperature lapse rates are likely higher due to steeper cooling rate of dry air, and moist enthalpy lapse rates shallower, due to meridional heat transport to higher latitudes. Likewise, tropospheric lapse rates of stable oxygen and hydrogen isotope compositions of meteoric water are shown to be higher in greenhouse climates than icehouse

(e.g. Poulsen and Jeffrey, 2011). As a result, changes in these lapse rates between climate states must be considered when applying lapse rates to proxies including fossil leaves, clumped isotope ratios, or stable oxygen and hydrogen isotope compositions.

Apart from climate states, temperature and moist enthalpy distributions are strongly influenced by non-linear regional circulation responses to the uplift. These circulation responses, including the mountain gravity waves and monsoonal circulation shown in our study, likely also occur during the uplift of other orogenic regions, such as the Tibet (Boos and Kang, 2010) and Sierra Nevada (e.g. Galewsky, 2009). Previous paleoaltimetry studies assuming modern (e.g. Ghosh et al., 2006) or simplified theoretical lapse rates (Wolfe et al., 1997; Spicer et al., 2003) may need to be re-visited by taking into account lapse rates and circulation responses to changing climate, and elevation conditions.

In addition, the temporal climate variability between the coastal and inland sites is likely different across regions with significant topographic barrier, such as Eocene western North America, and present-day Tibet-India subcontinent. As a result, coastal climate variability should not be included in paleoaltimetry estimate unless strong correlations in proxy inland and coastal reconstructions are identified.

In sum, as we have shown in this study, large methodological uncertainties in paleoelevation estimates are expected from using simplified relationships between climate variables (temperature and moist enthalpy) and elevation across climatic and topographic complex regions such as the Eocene North American Cordillera. Climate models are key to constrain these uncertainties, and should be adopted by future paleoaltimetry studies.

3.6 Conclusions

Temperature and moist enthalpy are thermodynamical attributes commonly used to infer past elevations from proxy archives. The lapse rates of these attributes are dependent on the background state of the climate. Under the warm and moist conditions of the early Cenozoic, the mid-latitude lapse rates were similar to present-day tropical lapse rates (Xu and Emanuel, 1989) due to reduced lower-tropospheric drying and large-scale meridional mixing. Both processes are more pronounced in present-day relatively dry climate with stronger meridional gradients of temperature and moisture.

On the basis of a comparison of fossil leaf and simulated early Eocene temperature and moist enthalpy, we estimate paleoelevations for the Eocene western North American Cordillera

and the adjacent Laramide foreland basins of ~2-3 km and ~1-2 km, respectively. The topographic gradient between the Cordillera and Laramide foreland basins is absent in previous fossil-leaf altimetry estimates, but occurs in our estimates and independent estimates using stable isotope paleoaltimetry (Mix et al., 2011; Feng et al., 2013). These differences are likely due to two factors: First, simulated Eocene temperature lapse rates (~ 5 °C km^{-1}) are significantly higher than previously assumed, accounting for elevation differences of ~1 km. Second, large temporal variations in coastal proxy temperature and moist enthalpy during the Early to Middle Eocene, which are absent at inland sites, were included in previous elevation reconstructions, accounting for a further ~1 km elevation bias.

Our elevation estimates, using temperature and moist enthalpy, disagree by ~1 km. The higher range of estimates, using moist enthalpy, are close to stable isotope based estimates (Mix et al., 2011; Feng et al., 2013), but the lower range, using temperature, is systematically lower by 1 - 2 km. This disagreement likely arises from the proxy reconstructions of temperature and moist enthalpy, which seem to be incompatible. Specific humidity derived from these reconstructions imply surprisingly semi-arid conditions, similar to modern, across the Cordillera during the Early to Middle Eocene, which are inconsistent with humid conditions indicated by fossil evidence of abundant alpine forests and proxy estimates of high precipitation rates.

Our results illustrate the danger of estimating paleoelevation using modern lapse rates. We find that lapse rates vary significantly between climate states. And distributions of paleo-altimeters, including both temperature and moist enthalpy, do not always follow linear lapse rates but are sensitive to moisture, circulation and topographic conditions. Ignoring changes of these conditions result in kilometer-scale elevation bias over the Eocene North American Cordillera and may lead to even larger biases over orogenic regions (such as Tibet) that are thought to have more substantial changes in elevation and climate in the past.

Appendix B

Appendix B1

Comparison between simulated (bold font) and proxy (regular font) surface temperature and precipitation (in italics) reconstructed from paleoflora of western North America (black dots).

WG: Wing and Greenwood, (1993); W1: Wolfe, 1994. W2: Wilf et al. (1998); K: Koch et al. (1995); FW: Fricke and Wing (2004). The ranges of proxy temperatures are reported from the individual studies. The ranges of proxy precipitation are reported as the averages added with the uncertainties of estimations of precipitation. Figure is adapted from Feng et al., (2013).

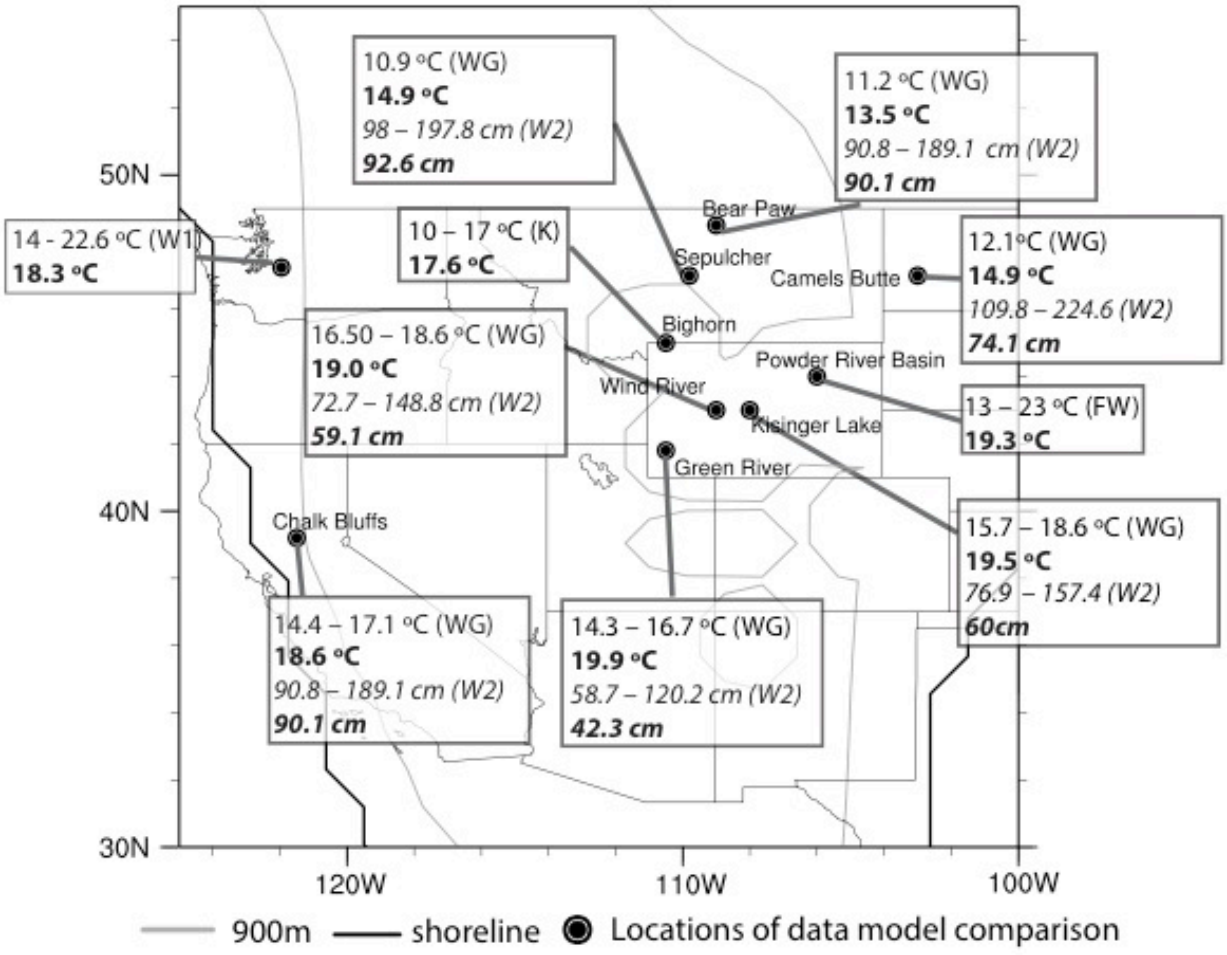

Appendix B2

Simulated modern mean-annual 2-m temperature (left) and moist enthalpy (right) versus elevation.

a-c) 2-m air temperature and elevation across zonal swaths at a) 47 ± 2 °N, b) 42 ± 3 °N, and c) 36 ± 3°N. d-f) moist enthalpy and elevation across the same zonal swaths. To avoid the coastal influences on calculating temperature lapse rates, slopes in a) - c) are calculated for locations above 1.5 km.

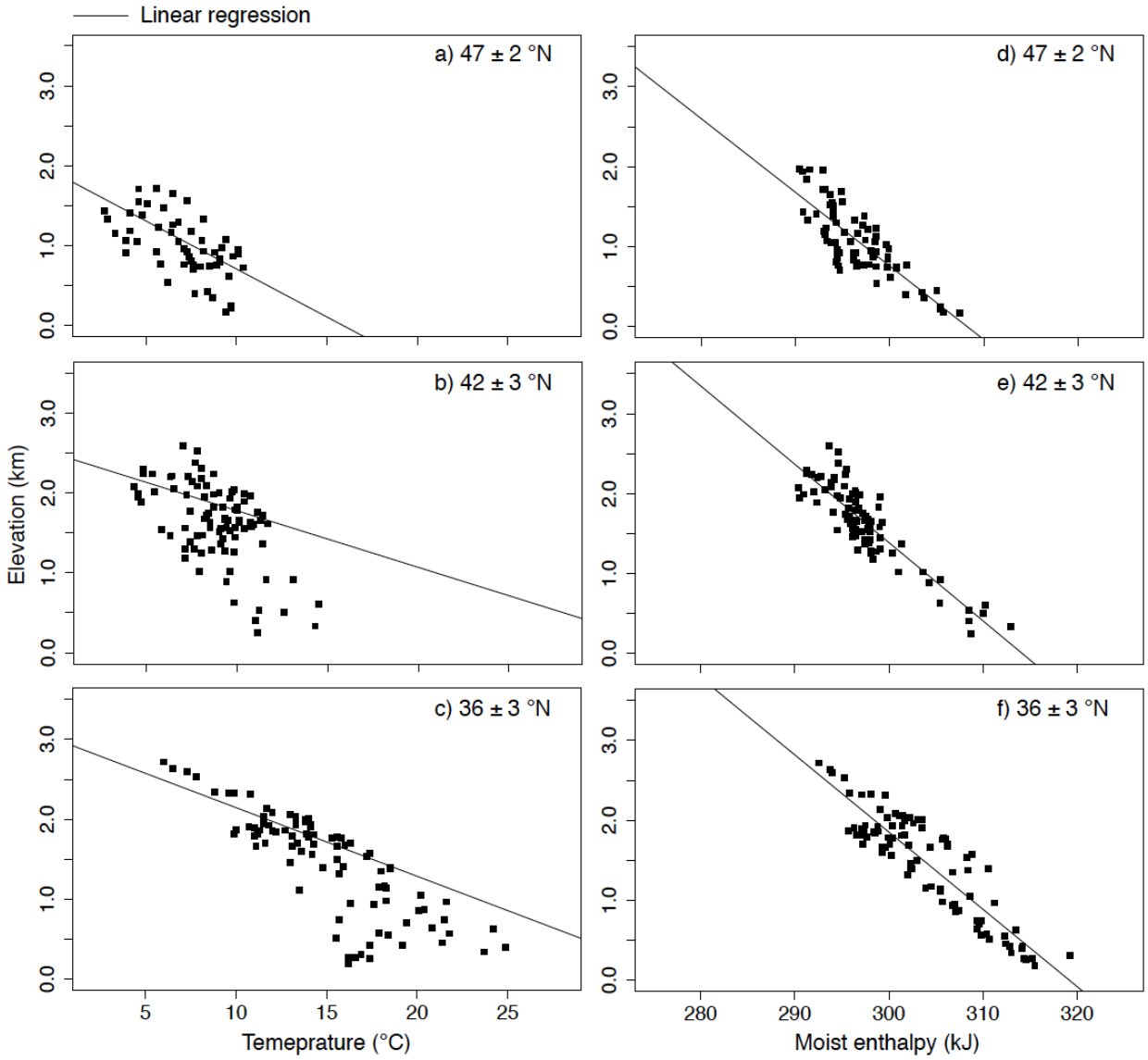

Bibliography

Axelrod, D.I., Bailey, H.P., 1969. Paleotemperature analysis of tertiary floras. Palaeogeography, Palaeoclimatology, Palaeoecology 6, 163–195. doi:10.1016/0031-0182(69)90013-3

Beerling, D.J., Royer, D.L., 2011. Convergent Cenozoic CO_2 history. Nature Geosci 4, 418–420. doi:10.1038/ngeo1186

Boos, W.R., Kuang, Z., 2010. Dominant control of the South Asian monsoon by orographic insulation versus plateau heating. Nature 463, 218–222. doi:10.1038/nature08707

Chamberlain, C.P., Mix, H.T., Mulch, A., Hren, M.T., Kent-Corson, M.L., Davis, S.J., Horton, T.W., Graham, S.A., 2012. The Cenozoic climatic and topographic evolution of the western North American Cordillera. American Journal of Science 312, 213–262. doi:10.2475/02.2012.05

Chase, C. G., Gregory-Wodzicki, K. M., Parrish-Jones, J. T., and DeCelles, P. G., 1998. Topographic history of the western Cordillera of North America and controls on climate, in: Crowley, T.J., and Burke, K., eds., Tectonic boundary conditions for climate model simulations, New York, Oxford University Press, 73-99.

Cook, K.H., Vizy, E.K., Launer, Z.S., Patricola, C.M., 2008. Springtime intensification of the Great Plains low-level jet and Midwest precipitation in GCM simulations of the twenty-first century. J. Climate 21, 6321–6340.

DeCelles, P.G., 2004. Late Jurassic to Eocene evolution of the Cordilleran thrust belt and foreland basin system, western USA. American Journal of Science 304, 105–168.

Dickinson, W.R., Klute, M. A., Hayes, M. J., Janecke, S. U., Lundin, E.R., McKittrick, M.A., Olivares, M.D., 1988. Paleogeographic and paleotectonic setting of Laramide sedimentary basins in the central Rocky Mountain region. Geol Soc America Bull 100, 1023–1039.

Erwin, D. M., and Schorn, H. E. (2005). Revision of the conifers from the Eocene Thunder Mountain flora, Idaho, USA. Review of Palaeobotany and Palynology, 137(3), 125-145.

Fan, M., Dettman, D.L., 2009. Late Paleocene high Laramide ranges in northeast Wyoming: Oxygen isotope study of ancient river water. Earth and Planetary Science Letters 286, 110–121. doi:10.1016/j.epsl.2009.06.024

Fan, M., Hough, B.G., Passey, B.H., 2014. Middle to late Cenozoic cooling and high topography in the central Rocky Mountains: Constraints from clumped isotope geochemistry. Earth and Planetary Science Letters 408, 35–47. doi:10.1016/j.epsl.2014.09.050

Feng, R., Poulsen, C.J., Werner, M., Chamberlain, C.P., Mix, H.T., Mulch, A., 2013. Early Cenozoic evolution of topography, climate, and stable isotopes in precipitation in the North American Cordillera. American Journal of Science 313, 613–648. doi:10.2475/07.2013.01

Feng, R., Poulsen, C.J., 2014. Andean elevation control on tropical Pacific climate and ENSO. Paleoceanography 29, 795–809. doi:10.1002/2014PA002640

Forest, Chris E., Peter Molnar, and Kerry A. Emanuel, 1995. Palaeoaltimetry from energy conservation principles, Nature, 374, 347 – 350, doi:10.1038/374347a0.

Forest, C.E., Wolfe, J.A., Molnar, P., Emanuel, K.A., 1999. Paleoaltimetry incorporating atmospheric physics and botanical estimates of paleoclimate. Geol Soc America Bull 111, 497–511.

Forest, C.E., 2007. Paleoaltimetry: A Review of Thermodynamic Methods. Reviews in Mineralogy and Geochemistry 66, 173–193. doi:10.2138/rmg.2007.66.7

Galewsky, J., 2009. Orographic precipitation isotopic ratios in stratified atmospheric flows: Implications for paleoelevation studies. Geol 37, 791–794.

Ghosh, P., 2006. Rapid Uplift of the Altiplano Revealed Through 13C-18O Bonds in Paleosol Carbonates. Science 311, 511–515. doi:10.1126/science.1119365

Graf, W. L. (eds.), 1987. Geomorphic Systems of North America. Boulder, Colorado, Boulder, Geological Society of America, 1-643.

Greenwood, D.R., Archibald, S.B., Mathewes, R.W., Moss, P.T., 2005. Fossil biotas from the Okanagan Highlands, southern British Columbia and northeastern Washington State: climates and ecosystems across an Eocene landscape. Canadian Journal of Earth Sciences 42, 167–185.

Greenwood, D. R., Wing, S. L., 1995. Eocene continental climates and latitudinal temperature gradients. Geol 23, 1044–1048. doi: 10.1130/0091-7613(1995) 023<1044:ECCALT> 2.3.CO;2

Gregory, K. M., and Chase, C. G. (1992). Tectonic significance of paleobotanically estimated climate and altitude of the late Eocene erosion surface, Colorado. Geology, 20(7), 581-585. doi: 10.1130/0091-7613(1992) 020<0581:TSOPEC> 2.3.CO;2

Gregory, K.M., Chase, C.G., 1994. Stable isotope study of fluid inclusions in fluorite from Idaho: Implications for continental climates during the Eocene: Comment. Geology 22, 275. doi:10.1130/0091-7613(1994)022<0275:SISOFI>2.3.CO;2

Holton, J.R., 2004, An introduction to dynamic meteorology (fourth Edition), Academic press, 503.

Insel, N., Poulsen, C.J., Ehlers, T.A., 2009. Influence of the Andes Mountains on South American moisture transport, convection, and precipitation. Clim Dyn 35, 1477–1492. doi:10.1007/s00382-009-0637-1

List, R. J. 1984. Smithsonian meteorological tables. Smithsonian Institution Press.

Little, S.A., Kembel, S.W., Wilf, P., 2010. Paleotemperature proxies from leaf fossils reinterpreted in light of evolutionary history. PLoS One 5, e15161.

Mesinger, F., DiMego, G., Kalnay, E., Mitchell, K., Shafran, P.C., Ebisuzaki, W., Jović, D., Woollen, J., Rogers, E., Berbery, E.H., Ek, M.B., Fan, Y., Grumbine, R., Higgins, W., Li, H., Lin, Y., Manikin, G., Parrish, D., Shi, W., 2006. North American Regional Reanalysis. Bulletin of the American Meteorological Society 87, 343–360.

Meyer, H.W., 2007. A Review of Paleotemperature Lapse Rate Methods for Estimating Paleoelevation from Fossil Floras. Reviews in Mineralogy and Geochemistry 66, 155–171. doi:10.2138/rmg.2007.66.6.

Miller, I. M., Brandon, M. T., and Hickey, L. J. (2006). Using leaf margin analysis to estimate the mid-Cretaceous (Albian) paleolatitude of the Baja BC block. Earth and Planetary Science Letters, 245(1), 95-114. doi:10.1016/j.epsl.2006.02.022

Mix, H.T., Mulch, A., Kent-Corson, M.L., Chamberlain, C.P., 2011. Cenozoic migration of topography in the North American Cordillera. Geology 39, 87–90.

Mulch, A., 2006. Hydrogen Isotopes in Eocene River Gravels and Paleoelevation of the Sierra Nevada. Science 313, 87–89. doi:10.1126/science.1125986

Peppe, D.J., Royer, D.L., Wilf, P., Kowalski, E.A., 2010. Quantification of large uncertainties in fossil leaf paleoaltimetry. Tectonics 29, n/a–n/a. doi:10.1029/2009TC002549

Peppe, D. J., Royer, D. L., Cariglino, B., et al. (2011). Sensitivity of leaf size and shape to climate: global patterns and paleoclimatic applications. New Phytologist, 190(3), 724-739. DOI: 10.1111/j.1469-8137.2010.03615.x

Poulsen, C.J., Ehlers, T.A., Insel, N., 2010. Onset of convective rainfall during gradual late Miocene rise of the central Andes. Science 328, 490–493.

Poulsen, C.J., Jeffery, M.L., 2011. Climate change imprinting on stable isotopic compositions of high-elevation meteoric water cloaks past surface elevations of major orogens. Geology 39, 595–598.

Poulsen, C.J., Tabor, C.R., and White, J.D. (2015) Long-term climate forcing by atmospheric oxygen concentrations, Science, 348, 1238-1241.

Povey, D.A.R., Spicer, R.A., England, P.C., 1994. Palaeobotanical investigation of early tertiary palaeoelevations in northeastern Nevada: initial results. Review of Palaeobotany and Palynology 81, 1–10. doi:10.1016/0034-6667(94)90122-8

Rienecker, M.M., Suarez, M.J., Gelaro, R., Todling, R., Bacmeister, J., Liu, E., Bosilovich, M.G., Schubert, S.D., Takacs, L., Kim, G.-K., Bloom, S., Chen, J., Collins, D., Conaty, A., da Silva, A., Gu, W., Joiner, J., Koster, R.D., Lucchesi, R., Molod, A., Owens, T., Pawson, S., Pegion, P., Redder, C.R., Reichle, R., Robertson, F.R., Ruddick, A.G., Sienkiewicz, M., Woollen, J., 2011. MERRA: NASA's modern-era retrospective analysis for research and applications. J. Climate 24, 3624–3648.

Roeckner, Erich, G. Bäuml, L. Bonaventura, Renate Brokopf, Monika Esch, Marco Giorgetta, Stefan Hagemann et al, 2003, The atmospheric general circulation model ECHAM5: Part 1: Model description. Max-Planck-Institut für Meteorologie, Report No. 349.

Royer, D. 2012. Climate reconstruction from leaf size and shape: New developments and challenges. In L. C. Ivany, and B. T. Huber (eds.), Reconstructing Earth's Deep-Time Climate: The State of the Art in 2012. Paleontological Society Papers, v. 18.

Royer, D.L., Peppe, D.J., Wheeler, E.A., Niinemets, U., 2012. Roles of climate and functional traits in controlling toothed vs. untoothed leaf margins. American Journal of Botany 99, 915–922. doi:10.3732/ajb.1100428

Salathé, E.P., Jr., 2006. Influences of a shift in North Pacific storm tracks on western North American precipitation under global warming. Geophys. Res. Lett. 33, L19820. doi:10.1029/2006GL026882.

Sewall, J.O., Sloan, L.C., 2006. Come a little bit closer: A high-resolution climate study of the early Paleogene Laramide foreland. Geol 34, 81. doi:10.1130/G22177.1

Sewall, J.O., Sloan, L.C., Huber, M., Wing, S., 2000. Climate sensitivity to changes in land surface characteristics. Global and Planetary Change 26, 445–465.

Sjostrom, D.J., Hren, M.T., Horton, T.W., Waldbauer, J.R., Chamberlain, C.P., 2006. Stable isotopic evidence for a pre–late Miocene elevation gradient in the Great Plains–Rocky Mountain region, USA. Geological Society of America Special Papers 398, 309–319.

Schneider, T., & O'Gorman, P. A., 2008. Moist Convection and the Thermal Stratification of the Extratropical Troposphere. Journal of Climate, 65(11), 3571–3583. http://doi.org/10.1175/2008JAS2652.1

Soden, B.J., 2005. The Radiative Signature of Upper Tropospheric Moistening. Science 310, 841–844. doi:10.1126/science.1115602

Spicer, R.A., Harris, N.B.W., Widdowson, M., Herman, A.B., Guo, S., Valdes, P.J., Wolfe, J.A., Kelley, S.P., 2003. Constant elevation of southern Tibet over the past 15 million years. Nature 421, 622–624. doi:10.1038/nature01356

Spicer, R.A., Herman, A.B., and Kennedy, E.M. 2005. The Sensitivity of CLAMP to Taphonomic Loss of Foliar Physiognomic Characters. Palaios, 20(5):429-438. doi: 10.2110/palo.2004.P04-63

Teodoridis, V., Mazouch, P., Spicer, R. A., and Uhl, D. (2011). Refining CLAMP—investigations towards improving the Climate Leaf Analysis Multivariate Program. Palaeogeography, Palaeoclimatology, Palaeoecology, 299(1), 39-48. doi:10.1016/j.palaeo.2010.10.031

Wilf, P. 1997. When are leaves good thermometers? A new case for Leaf Margin Analysis. Paleobiology 23:373-390.

Wilf, P., Wing, S.L., Greenwood, D.R., Greenwood, C.L., 1998. Using fossil leaves as paleoprecipitation indicators: an Eocene example. Geol 26, 203–206.

Wing, S.L., Greenwood, D.R., 1993. Fossils and Fossil Climate: The Case for Equable Continental Interiors in the Eocene. Philosophical Transactions of the Royal Society B: Biological Sciences 341, 243–252. doi:10.1098/rstb.1993.0109.

Wolfe, J. A., 1992. An analysis of present-day terrestrial lapse rates in the western conterminous United States and their significance to paleoaltitudinal estimates. US Geol Surv Bull 1964, 1-35.

Wolfe, J. A., Schorn, H. E., Forest, C. E., and Molnar, P. (1997). Paleobotanical evidence for high altitudes in Nevada during the Miocene. Science, 276(5319), 1672-1675. doi: 10.1126/science.276.5319.1672

Xu, K.-M., & Emanuel, K. A., 1989. Is the Tropical Atmosphere Conditionally Unstable? Monthly Weather Review, 117, 1471. http://doi.org/10.1175/1520-0493(1989)117<1471:ITTACU>2.0.CO;2

Chapter 4

Imprints of Hadley circulation intensification and tectonic extension on Neogene $\delta^{18}O$ records of the western U.S.

4.1 Abstract

Neogene (since ~20 Ma) $\delta^{18}O$ and δD records from the western U.S. display strong enrichment in the vicinity of the Sierra Nevada and eastern Rockies, but weak enrichment or depletion in the northern Great Basin. Neogene increases in $\delta^{18}O$ and δD have been interpreted to reflect surface lowering through tectonic extension of the western U.S. The influences of elevation-independent environmental changes on $\delta^{18}O$ and δD records have been largely neglected. In this study, we use a coupled atmosphere-land model with water-isotopologue tracking capabilities, ECHAM5-JSBACH-wiso, to simulate precipitation and isotopic responses to Neogene changes in geography, equator-to-pole temperature gradient, grassland expanse, and tropical Pacific sea-surface conditions. Both precipitation and soil water $\delta^{18}O$ respond strongly to the Neogene increase of equator-to-pole temperature gradient, but weakly or negligibly to other Neogene changes. A steepened equator-to-pole temperature gradient leads to significant drying and enrichment (3 – 5 ‰) of soil water $\delta^{18}O$ ($\delta^{18}O_{sw}$) over the northern Sierra Nevada and central Rockies as a result of strengthened Hadley circulation and subtropical subsidence. These $\delta^{18}O_{sw}$ responses could explain 50 – 100% of the proxy isotopic enrichment over these two regions, suggesting dominant climate controls on local proxy $\delta^{18}O$ records. To the contrary, $\delta^{18}O$ responses to climate changes are small in the Great Basin, indicating dominant elevation controls on proxy $\delta^{18}O$ variability. The proxy enrichment over this region suggests significant subsidence with elevation lowering up to 1 – 1.5 km. The resulted subsidence pattern, i.e., great elevation lowering within the Great Basin and small elevation adjustments of surrounding mountain ranges of northern Sierra Nevada and central Rockies, is consistent with independent structural and paleoaltimetry reconstructions suggesting the existence of pre-extensional high plateau over the Great Basin and its subsequent Neogene destruction.

4.2 Introduction

Despite the plethora of geophysical, structural, and sedimentological reconstructions, the Cenozoic topographic history of the western U.S. remains uncertain. The majority of paleoaltimetry estimates for this region are derived from stable oxygen and hydrogen compositions ($\delta^{18}O$ and δD) of terrestrial sediments and organic materials, which preserve the isotopic compositions of ancient surface and soil waters. Oxygen and hydrogen isotope compositions of precipitation are shown to display strong negative correlations with elevation across modern Coast Ranges and Sierra Nevada (Blisnuik et al., 2005), and are therefore commonly assumed to scale with past elevation changes. However, the application of stable isotope paleoaltimetry leads to conflicting reconstructions of Cenozoic surface elevations across the Great Basin and its surrounding mountain ranges.

Proxy $\delta^{18}O$ records of Early Cenozoic age (55 – 28 Ma) have been shown to be strongly negative and interpreted to indicate the presence of a high (3 – 4 km) plateau across the Great Basin (Mix et al., 2011; Feng et al., 2013). The lack of $\delta^{18}O$ contrast between the Great Basin, and adjacent northern Sierra Nevada (Mulch et al., 2006; Henry and Faulds, 2010; Cassel et al., 2014) and central Rockies (Sjostrom et al, 2006) suggests little elevation distinctions between these regions. In this scenario, modern Great Basin elevations (~1.5 – 2 km) were subsequently achieved by subsidence through Basin and Range extension during the Neogene. Crustal thinning of the Great Basin is supported by seismic evidence of thin crust underlying the basin surrounded by thick crust beneath both the Sierra Nevada and central Rockies (Chulick and Mooney, 2002) and widespread extensional deformation across the Great Basin (Dickinson, 2006). Neogene isotopic records suggest a somewhat different elevation history. These records exhibit large ^{18}O-enrichment of up to 8‰ across the Sierra Nevada (Horton and Chamberlain, 2006) and central Rockies (e.g., Chamberlain et al., 2012), indicating kilometer-scale elevation loss, whereas smaller ^{18}O-enrichment or even depletion in the northern Great Basin (e.g., Horton et al, 2004), indicating small elevation loss or even uplift. These records are at odds with the early Cenozoic elevation reconstructions and with interpretations of Neogene extension pattern from seismic, structural and sedimentological data.

Here, we investigate whether this inconsistency in subsidence history between stable isotope and other reconstructions may be due to a misinterpretation of the isotopic records from the western U.S. The Neogene was a transitional period in Earth's climate and environment that included a 5 – 8 °C increase of equator-to-pole SST gradient (based on early-to-middle Miocene

reconstructions (Goldner et al., 2014) associated with drawdown of CO_2, high-latitude cooling and glaciation, a 2 – 6 °C enhancement of east-west tropical pacific SSTs gradient (e.g. Zhang et al., 2014), the widespread expansion of grasslands (e.g., Strömberg, 2011), as well as global continental drift and topographic reconfiguration. The influences of environmental factors on Neogene isotopic records from the western U.S. have largely been overlooked and have not been systematically analyzed.

Further, proxy reconstructions from fossil leaves (Pound et al., 2012), soil chemistry (Retallack et al., 2002) and herbivore mammal hypsodonty (Eronen et al., 2012) all suggest significant reduction of Neogene precipitation on an order of 10^2 mm across the western U.S. Precipitation reduction can be linked to ^{18}O-enrichment in soil and meteoric water through altering local hydrological and isotopic balance from moisture surplus, and ^{16}O influx, to moisture deficit and ^{16}O outflux within a region. However, whether such a link existed across the Neogene western U.S., and what the environmental factors are responsible for these changes are unclear.

The ^{18}O-enrichment of surface and soil water in the western U.S. during the Neogene has previously been linked to hydrological responses associated with the replacement of forests with grasslands (Mix et al., 2013; Chamberlain et al., 2014). However, phytolith records indicate that grassland expansion in the western U.S. occurred much earlier, in the late Oligocene-early Miocene (see a review by Strömberg, 2011), and thus do not support this idea. Nonetheless, other environmental factors might have played a role. Studies have shown strong $\delta^{18}O$ variations in proxy records may record atmospheric CO_2 variations (Poulsen and Jeffery, 2011). Besides, $\delta^{18}O$ (Winnick et al., 2012) and precipitation variations (Goldner et al., 2011) may record changing atmospheric circulations forced by El Niño-like SST pattern. However, the amount of $\delta^{18}O$ and precipitation responses across the western U.S. to SST and CO_2 changes during the Neogene climate transition, as well as responses to other Neogene environmental changes are unknown.

In order to quantify and understand responses of precipitation, and $\delta^{18}O$ of soil and meteoric water to Neogene environmental changes, in this study, we conducted a series of experiments using an isotope-tracking coupled atmosphere-land model to constrain and compare precipitation and $\delta^{18}O$ responses to Neogene environmental changes. The implications of our

simulated precipitation and $\delta^{18}O$ responses for Neogene aridification and surface elevation changes in the western U.S are analyzed and discussed.

4.3 Model, data description and experiments

We use the coupled atmosphere-land model, ECHAM5-JSBACH-wiso, to quantify $\delta^{18}O_{sw}$ responses to Neogene environmental changes. ECHAM5-JSBACH is a three-dimensional global climate model equipped with isotope tracking modules that simulate both equilibrium and kinetic fractionation of water isotopologue species H_2O^{18} and HDO during phase transitions in the atmosphere (Werner et al., 2011) and on land (Haese et al., 2013). The atmosphere model, ECHAM5, calculates isotopic fractionation and advection following both grid-scale simulations of condensation and advection, and sub-grid scale parameterization of moist convection and mixing. The land model, JSBACH, simulates column average $\delta^{18}O$ of soil water ($\delta^{18}O_{sw}$) from the surface to the depth of shallow soil water pool (typically $\leq$ ~1 m). Each land grid cell may contain up to four land-cover types, lake, bare ground, vegetated or snow-covered. The fractional coverage of the lake is prescribed. The rest of land cover depends on the simulated climate and vegetation conditions. In JSBACH, soil waters undergo isotopic fractionation only during evapotranspiration. Fractionation of evaporation from bare ground is estimated by the bulk formula of Hoffmann et al. (1998), from lakes is calculated the same as sea surface (Werner et al., 2011). Transpiration is treated as equilibrium fractionation in order to constrain the maximum fractionation between the plant water pool and environmental vapor. Snow sublimation (Friedman, 1991), melting and recharge are treated as non-fractionating processes.

All experiments were run at a spectral T63 resolution (96 × 192 grid cells) with 31 vertical levels. At this resolution, the model simulates reasonable present-day distributions of temperature, precipitation amounts, and precipitation $\delta^{18}O$ ($\delta^{18}O_p$) across the western U.S. (see the Appendix C, Appendix C1A-C and Appendix C2A). Comparison between simulated and observed $\delta^{18}O_{sw}$ from the western U.S. is complicated by the short duration of existing observations. Most observational records of $\delta^{18}O_{sw}$ are only a few months in duration and are therefore not suitable for comparing with simulated climatological $\delta^{18}O_{sw}$. Relatively long-term (~1.5 yr) $\delta^{18}O_{sw}$ records are available at several sites in central New Mexico (Breecker et al., 2009). Simulated $\delta^{18}O_{sw}$ (~2.1 ‰) is close to annual mean $\delta^{18}O_{sw}$ (1.2 – 1.6 ‰) below 50 cm depth at these sites (see a detailed discussion in Appendix C).

We individually evaluate four aspects of Neogene environmental change in our simulations including: 1) increase of the equator-to-pole surface temperature gradient, 2) intensification of the tropical Pacific zonal SST gradient, 3) changes in global geographic and topographic configuration, and 4) expansion of grassland coverage. Each aspect is investigated with a pair of experiments, including a control experiment, featuring modern conditions, and a sensitivity experiment, replacing individual modern conditions, such as SSTs and CO_2, vegetation coverage, or global geographic and topographic configuration (outside the western U.S.), with early Neogene conditions. Boundary conditions for each experiment pair are listed in Table 1. Detailed description and maps of boundary conditions can be found in the Appendix C. Climate and isotopic responses are reported as 15-yr averages of differences between control and sensitivity experiments.

Table 4 Key boundary conditions for testing isotopic responses to four major aspects of Neogene environmental changes.

Environmental changes		**Boundary conditions**
Increasing equator-to-pole temperature gradient	Sensitivity	560 ppm CO_2, Mid-Miocene glacier coverage and SST pattern (Herold et al., 2011), equator-to-pole SST gradient adjusted to mimic proxy values (Golder et al., 2014), modern conditions otherwise
	Control	280 ppm CO_2, modern conditions
Termination of El Niño-like SST state	Sensitivity	280 ppm CO_2, El Niño SST pattern (estimated using SST anomalies of 1997-1998 El Niño event, based on Molnar and Cane, 2007), modern conditions otherwise
	Control	280 ppm CO_2, modern conditions
Grassland expansion	Sensitivity	280 ppm CO_2, forested North America, modern conditions otherwise
	Control	280 ppm CO_2, modern conditions

Geographic changes	Sensitivity	280 ppm CO_2, global average of modern vegetation cover, Mid-Miocene geographic and topographic conditions outside the North America (Herold, et al., 2011), modern conditions otherwise
	Sensitivity	280 ppm CO_2, global average of modern vegetation cover, modern conditions otherwise

We compare simulated $\delta^{18}O$ changes with Neogene records from pedogenic carbonates, volcanic glasses (converted from δD to $\delta^{18}O$ using the slope of the global meteoric water line) and smectite. These minerals are formed in equilibrium with surface or soil water, and therefore, are comparable to simulated $\delta^{18}O_{sw}$ changes. Comparison of simulated $\delta^{18}O$ with lacustrine and fluvial materials such as calcite cement, chert, limestone and organic shells requires detailed model representation of fine-scale local drainage, which is beyond the capabilities of the current model resolution and land-hydrology model scheme. The magnitudes of Neogene isotopic changes are quantified as the coefficients of least square regressions of proxy $\delta^{18}O$ against age (Appendix C3).

Apart from the depositional environment, the seasonality of mineral formation also needs to be considered in order to compare proxy records and simulations. Pedogenic carbonate formation is known to have a seasonal bias (Breecker et al., 2009). Calcite formation activity increases with increasing temperature and Ca^{2+} concentration, and decreasing soil CO_2. These conditions commonly occur during warm and dry seasons (Breecker et al., 2009). In our simulations, soil wetness reaches a minimum during the boreal fall season (September, October and November) while soil temperature remains warm across the western U.S. (Appendix C5). Therefore, we compare proxy carbonate $\delta^{18}O$ ($\delta^{18}O_c$) with simulated fall soil water $\delta^{18}O$. In contrast, the hydration of volcanic glasses and ashes (parent material of smectite) is not known to have a seasonal bias. Accordingly, our comparison is based on mean annual soil water $\delta^{18}O$. Simulated $\delta^{18}O_{sw}$ is converted to mineral $\delta^{18}O$ ($\delta^{18}O_m$) using mean surface and deep soil temperature (averaged below 78 cm) and assuming equilibrium fractionation between the soil water and carbonates, volcanic glasses, and smectite (Appendix C4).

4.4 Climate model results

The hydrological cycle across the western U.S. weakened during the Neogene. Annual precipitation rates, inferred from fossil flora and paleosols, decreased by ~75 – 814 mm/yr since the early-to-middle Miocene (12 – 18 Ma) (Appendix C5). The reduction in precipitation ranged from 750 – 877 mm/yr in the western central Idaho to 124 – 275 mm/yr in northern Texas. Over half of the reduction in precipitation can be explained by the equator-to-pole temperature gradient increase (3 – 497.5 mm/yr reduction at proxy sites) (Figure 23A), while precipitation responses to the other Neogene environment changes are either small or opposite in signs between regions of the western U.S. (Figure 23B – D). The response pattern also matches spatial distribution of precipitation reduction indicated by proxies, showing smaller reduction in the vicinity of Gulf of Mexico and stronger reduction to the west (Figure 23A).

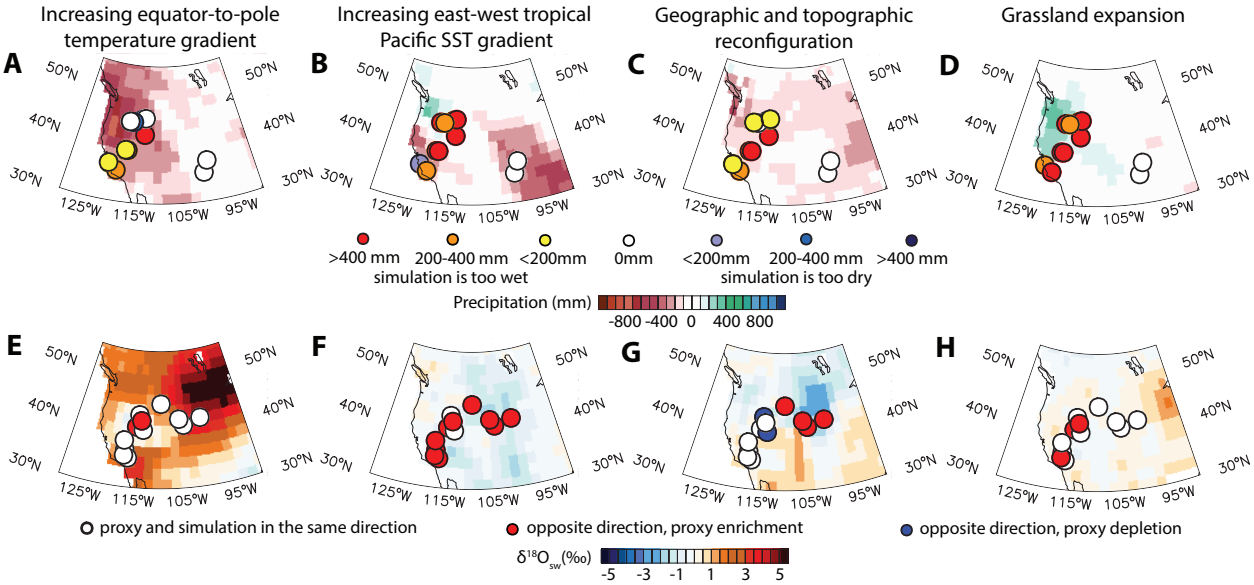

Figure 23 Comparison of proxy records (filled circles) and simulated precipitation and fall-season (September, October and November) $\delta^{18}O_c$ responses to Neogene environmental changes. A-D: precipitation. E-H: fall season $\delta^{18}O_c$ responses.

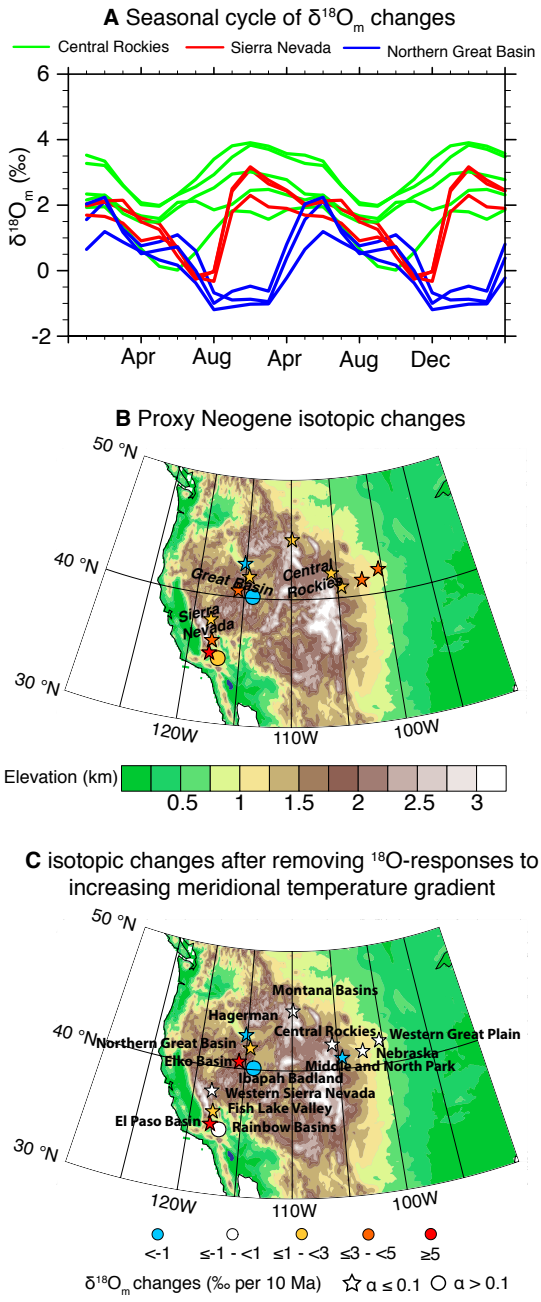

Figure 24 Seasonal cycle of mineral $\delta^{18}O$ ($\delta^{18}O_m$) responses to Neogene strengthening of equator-to-pole temperature gradient and their contributions to proxy $\delta^{18}O_m$ enrichment across the western U.S.

A: Seasonal cycle of $\delta^{18}O_m$ responses at proxy sites with trends of proxy $\delta^{18}O_m$ significant above 90% confidence level. B: the original and C: adjusted amount of Neogene proxy $\delta^{18}O_m$ enrichment (‰/10 Ma) by removing $\delta^{18}O_m$ responses to strengthened equator-to-pole temperature gradient. Color-coding in A reflect geographic locations, i.e., green: eastern Rockies; blue: northern Great Basin; and red: Sierra Nevada. The reconstructed amount is the linear regression coefficients of $\delta^{18}O_m$ against age scaled by 10 million years. Stars and circles: p-value (α) ≤ 0.1 and > 0.1. Color shading: modern elevation.

Similarly, strengthening of the equator-to-pole temperature gradient leads to the largest $\delta^{18}O$ responses (~2 – 5 ‰) (Figure 23E, shown for $\delta^{18}O_c$), which are about twice the magnitude of $\delta^{18}O$ responses to other individual Neogene environmental changes (≤ 2 ‰) (Figure 23F-H). Further, the spatial distribution of $\delta^{18}O$ responses to a larger temperature gradient is similar to the proxy pattern of Neogene $\delta^{18}O_m$ changes, which shows ^{18}O-enrichment in the Sierra Nevada and central Rockies, but muted $\delta^{18}O_m$ changes within the Great Basin (Figure 23E). The concurrence between regional precipitation reduction, and $^{18}O_{sw}$-enrichment across the western U.S. suggest a linkage between these recorded changes through strengthening of equator-to-pole temperature gradient. Given that precipitation and isotopic responses to other changes are small, the following analysis will only focus on responses to strengthening of equator-to-pole temperature gradient.

This simulated pattern of ^{18}O-enrichment is strongest during the fall season but persists throughout the year (Figure 24A, note that $\delta^{18}O$ values at proxy locations of the Sierra Nevada and Central Rockies are systematically higher than the northern Great Basin, and the differences are the greatest during the fall). At Neogene proxy sites, $\delta^{18}O_m$ responses to a larger equator-to-pole temperature gradient are ~4‰ and 3‰ in the eastern Rockies and Sierra Nevada, which could account for 50% to 100% of the isotopic enrichment observed in pedogenic carbonates (Figure 24B). $\delta^{18}O_m$ responses to a larger equator-to-pole temperature gradient are small in the northern Great Basin and. As such, the isotopic responses to the temperature gradient contribute little to the Neogene proxy $\delta^{18}O_m$ changes over this region (Figure 24C).

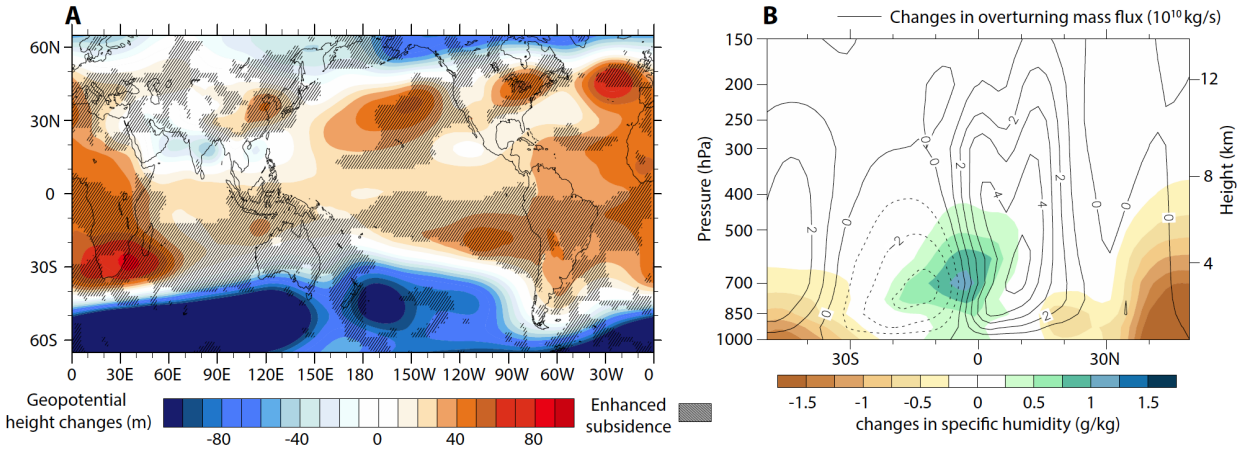

Figure 25 Boreal summer (June, July, August) responses of the Hadley circulation and subtropical subsidence to Neogene increase of equator-to-pole temperature gradient.
A: 600 hPa geopotential height (shaded) and subsidence (hatched). B: zonal-mean overturning mass flux (contour) and specific humidity (shaded).

The simulated fall season $\delta^{18}O_{sw}$ enrichment corresponds to strengthening of tropospheric subsidence and extension of the subtropical high-pressure system over the eastern Pacific and western Atlantic during the summer (Figure 25A). These circulation changes diminish moving inland from the Pacific and Atlantic coast, which could explain the lack of $\delta^{18}O_{sw}$ changes across the continental interior region of the Great Basin in response to the increasing equator-to-pole temperature gradient. Yet, the precipitation remains to be reduced across the Great Basin as a result of colder surface temperature (reducing moist convection), and southward entrainment of high-latitude dry air. Across regions under the influences of Pacific and Atlantic, the enhancement of subtropical high pressure, and subsidence leads to a summer to fall decrease in precipitation, and increases in evapotranspiration, and rainwater evaporation ($\delta^{18}O$ of summer precipitation is ~3 ‰ more enriched), which drive ^{18}O-enrichment of soil water across the Sierra Nevada and central Rockies. On the broader scale, these changes are part of zonally symmetric responses across the subtropical ocean to large-scale strengthening of the Hadley circulation (Figure 25B). The strength of the Hadley circulation, defined by overturning mass flux between 30 °S and 30 °N, increases by ~23% (3.8×10^{11} kg s^{-1} total).

Hadley circulation strengthening is linked to the greater meridional surface temperature gradient through increasing lower tropospheric convergence and upper level condensation heating. The stronger gradient drives stronger surface convergence towards the tropical ocean, which destabilizes the marine boundary layer and enhances tropical moist convection. The

enhanced latent heat release from condensation warms the surrounding air and fuels even stronger updrafts. This process strengthens the upward branch of the Hadley circulation, resulting in stronger compensating subsidence over the subtropics (Figure 25A). The zonal mean circulation is more pronounced over the ocean and land areas with strong marine influences relative to continental regions, which are mostly influenced by continental air masses with distinct thermodynamical properties. This heterogeneous Hadley circulation imprint leads to heterogeneous $\delta^{18}O_{sw}$ responses across the western U.S. with stronger isotopic enrichment over areas proximal to the ocean, including the Sierra Nevada and central Rockies, but muted responses in the continental interior (Great Basin).

4.5 Discussions and implications

4.5.1 Model responses to grassland expansion

The Neogene isotopic enrichment across the western U.S. has previously been attributed to grassland expansion, which increases precipitation $\delta^{18}O$ relative to forests through enhancing water recycling, increasing the proportion of warm season precipitation, and transpiring higher amount of isotopically enriched soil water at shallow depth (Mix et al., 2013). Isotopic responses to grassland expansion are muted in our experiments even during the warm seasons. We suspect that the $\delta^{18}O$ responses in the previous study were exaggerated due to 1) an overestimation of the changes in the grassland evapotranspiration ratio and 2) an underestimation of climate responses. A high ratio of evapotranspiration to precipitation leads to damped ^{18}O rainout rate and high precipitation $\delta^{18}O$, as a result of higher percentage of recycling of ^{18}O-enriched surface and meteoric water back to form precipitation through evapotranspiration. In Mix et al. (2013), changes in this ratio due to grassland expansion were estimated by differencing observed ratios between semi-arid sites in Colorado (CO) and forested, humid sites in North Carolina (NC). The annual amount of transpiration at the forest sites (338.5 mm/yr) (Oishi et al., 2008), however, is even greater than the grassland sites (241.5 mm/yr) (Ferretti et al., 2003). Therefore, the low evapotranspiration ratio of forest sites mainly reflects differences in the amounts of evaporation and precipitation that are more closely related to large-scale climate patterns than to plant physiological differences. Additionally, we simulate strong climate responses to grassland expansion that counteract the potential enrichment effect due to increasing evapotranspiration ratio. Grassland expansion leads to significant cooling (~2 °C) and increase in snowfall (up to 40% increase) in our simulations (Appendix C5), both of which contribute to $\delta^{18}O_{sw}$ depletion.

Additional ^{18}O-enrichment associated with grassland expansion is from the shallow rooting depth of the grasslands, which preferentially extract ^{18}O-enriched upper layer soil water. This effect is not included in the model, but is likely small given its dependence on simulated responses of evapotranspiration to precipitation ratio, which only shows slight increase (~10 %) in the model.

4.5.2 Implications to the Neogene elevation history of the Great Basin

We extract elevation-dependent Neogene proxy $\delta^{18}O_m$ changes by subtracting the $\delta^{18}O_m$ responses to Neogene strengthening of the equator-to-pole temperature gradient from the proxy records ($\Delta\delta^{18}O_m$). Modeled $\delta^{18}O_m$ responses to other Neogene environmental changes (tropical Pacific SSTs, grassland expansion, and geographic and topographic changes) are quite small (-2.7 – 0.5 ‰), and are comparable to inter-sample variability of the proxy $\delta^{18}O_m$, e.g. the $\delta^{18}O_m$ of Elko Basin samples of 15 Ma age range from ~12 ‰ to 15.2 ‰ (Chamberlain et al., 2012). Therefore, we ignore the contributions from these factors in our analysis.

Our $\Delta\delta^{18}O_m$ distribution shows minimal enrichment (< 1 ‰) in the eastern Rockies and in the vicinity of the northern Sierra Nevada, which we argue indicates that these regions experienced only small elevation adjustments (< 1 km) during the Neogene. Our interpretation of the isotopic data is consistent with independent paleoelevation estimates that these regions had attained near-modern elevations in the late Eocene (e.g. Mulch et al., 2006; Cassel et al., 2014; Fan et al., 2014). Conversely, $\Delta\delta^{18}O_m$ in the northern Great Basin remains substantial, featuring ^{18}O-enrichment of 3 – 5‰ and depletion of 3 – 4 ‰ (Figure 24C). Assuming that the enrichment signal mainly reflects regional tectonic extension, applying a pre-extension Eocene lapse rates of ~3 ‰/km (Feng et al., 2013) to the amount of enrichment results in estimates of surface lowering of ~1 – 1.6 km. Adding this elevation loss to present-day elevations (~1.6 – 2 km) would bring pre-extension elevations close to proposed for Eocene elevation of this region (3.4 km, Mix et al., 2011; Feng et al., 2013).

The negative $\Delta\delta^{18}O_m$ in the northern Great Basin (Ibapah badland, Middle and North Park, and Hageman site in Figure 24C) and strong positive $\Delta\delta^{18}O_m$ in the El Paso Basin (11.4 ‰) of southern Sierra Nevada cannot be explained by an enhanced equator-to-pole gradient or tectonic subsidence. The strong proxy enrichment in El Paso Basin likely reflects the Neogene drying out of a hydrologically-closed basin. The Sr/Ca ratio and covariance of $\delta^{13}C$ and $\delta^{18}O$ of carbonates indicate high salinity lake water likely resulted from this process (Horton and

Chamberlain, 2006). The small-scale topography of the El Paso Basin, and associated hydrological changes, however, are not resolved by the current model configuration. The same model limitation in representing subgrid scale topography and associated hydrological features may explain the lack of ^{18}O-depletion of simulated soil water in the northern Great Basin and central Rockies. Simulated snowfall increases at high altitude sites across the Rockies and Northern Great Basin due to Neogene cooling. Abundant snow-water discharge from surrounding reliefs may overwhelm warm season O^{18}-enrichment at proxy sites located within intermountain basins. Alternatively, depletion signals from these sites may record small amounts of local uplift.

Collectively, both early Cenozoic (e.g. Mix et al., 2011; Chamberlain et al., 2012; Feng et al., 2013; Cassel et al., 2014; Fan et al., 2014) and Neogene proxy $\delta^{18}O$ and δD offer strong support for the existence of an early Cenozoic plateau across the Great Basin bounded by northern Sierra Nevada and central Rockies that are similar in elevation to present-day. Apart from paleoelevations, we suggest that these Neogene isotopic records preserve a history of strengthening of Hadley circulation. Further, both Neogene aridification and isotopic enrichment across the western U.S. likely reflect different aspects of regional climate responses to increasing equator-to-pole temperature gradient.

Appendix C

Appendix C1

Comparison between simulated and observed present-day climate and isotopic compositions of precipitation ($\delta^{18}O_p$) and soil water ($\delta^{18}O_{sw}$) across the western North America

Simulation skill of the ECHAM5-JSBACH-wiso is evaluated by comparing simulated present-day temperature and precipitation to observational data of Modern Era Retrospective-analysis for Research and Applications (MERRA) (Rienecker et al., 2011) (Figs. DR1A-C). The simulation reaches equilibrium in the first 5 years and no discernable trend is identified in the following 15 model years. Model results are therefore averaged over this period. MERRA data are annual averages over the period of 1979 to 2011. Simulated spatial distributions, including the meridional gradients and east-west contrast of temperature and precipitation between the western Cordillera and central Great plain are broadly consistent with observations. The model, underestimates topographic gradients of temperature and precipitation across local-scale reliefs of the western Cordillera. This bias is mostly related to the model resolution: the surface elevation is averaged over each of ~200 km^2 grid cell in the model, which does not resolve the topographic gradient and associated climate variability across local reliefs and basins.

Model simulations of broad-scale continental $\delta^{18}O_p$ gradients between the Great Basin and its surrounding mountains match observations (Fig. DR2A). Limited by resolution, local variability of $\delta^{18}O_p$ is underestimated. Simulated present-day $\delta^{18}O$ of soil water ($\delta^{18}O_{sw}$) (2.1 ‰) is close to the derived $\delta^{18}O_{sw}$ below 50cm depth at central New Mexico sites (~34 °N, 106 °W) with shrubland vegetation type (1.2 – 1.6 ‰) (Great Basin Shrubland and Chihuahuan Shrubland). Simulated $\delta^{18}O_{sw}$ is more enriched than the measured $\delta^{18}O_{sw}$ at Pinon-Juniper woodland site (-6.4 ‰) (Breecker et al., 2009). The $\delta^{18}O_{sw}$ mismatch at this site may reflect local interannual climate variability that is not represented in the model. Anomalous amount of winter snowfall occurred in central New Mexico during the measurement time of 2006 - 2007. The soil water pool around Pinon-Juniper site may have stored higher portion of snowmelt water than the other sites, leading to anomalous $\delta^{18}O_{sw}$ depletion signal.

Appendix C2

Climate model boundary conditions

We conducted four sets of experiments to explore climatic and isotopic responses across the western U.S. to four major aspects of Neogene environmental changes, including 1) increasing meridional temperature gradient, and 2) tropical Pacific zonal SST gradient, 3) grassland expansion and 4) geographic and topographic reconfiguration changes. Details of how these boundary conditions are designed are discussed in the following. Corresponding maps of boundary conditions are shown in Appendix C8.

1) Increasing meridional temperature gradient. The shrunken high-latitude glacier, low meridional SST gradient (Appendix C8A and Appendix C8D) and higher CO_2 level all contribute to lowering equator-to-pole temperature gradient during the early-to-middle Miocene (Goldner et al., 2014). The Mid-Miocene SST is modified from results of atmosphere-ocean coupled simulation of Mid-Miocene climate by Herold et al., (2011). This simulation features steep meridional SST gradient with near modern values in the tropics and freezing polar SSTs (-1.8 °C). This SST gradient is adjusted to correctly represent the Mid-Miocene reconstructions. A zonally uniform adjusting factor is added to each latitudes of the SST data: $\Delta SST = \sin\left(\left|\frac{SST_{mean-20}-20}{44}\right| \times \pi\right) \times 7$, $SST_{mean\text{-}20}$ is the zonal SST average (°C) with SSTs warmer than 20 °C set to 20 °C. $\Delta SST=0$ for regions with zonal mean SSTs ≥ 20 °C, $\Delta SST=\sim 7$°C for polar SSTs. The resulted ~5°C SST at the poles is close to the median of the proxy reconstructions (Fig. 1a in Goldner et al., 2014).

2) Increasing tropical Pacific zonal SST gradient. We use SST anomalies of the 1997-1998 El Niño event to construct an El Niño SST pattern, featuring reduced tropical Pacific zonal SST gradient (Appendix C8E). The choice of this El Niño event is based on (Molnar and Cane, 2007), which suggests that terrestrial reconstructions of early Pliocene temperature and precipitation reflect an El Niño pattern most similar to the 1997–1998 event. The SST anomalies are calculated as departures of mean annual SSTs during the event between April 1997 to March 1998 from 30-yr climatology using NOAA ERSST.v3 (Smith and Reynolds, 2004).

3) Grassland expansion. We infer forest biomes at places that are currently covered by grassland using nearest neighborhood extrapolation, i.e. for each cell, if the dominant vegetation cover is grassland, vegetation related variables are replaced with values from the nearest cells with considerable (≥ 40%) forest coverage (Appendix C8C and Appendix C8G).

4) Geographic and topographic changes. The Mid-Miocene reconstructions of coastal line and topographic configurations (Herold et al., 2008) outside the North America are applied

to test climatic and isotopic responses to global-scale geographic and topographic reconfiguration (Appendix C83B and Appendix C8F). In order to minimize the associated changes in vegetation cover associated, uniform global mean present-day vegetation is prescribed for both control and sensitivity experiments.

5) Tectonic extension. The longitudinal width of Great Basin is kept the same for all experiments. The Neogene extension of Great Basin may contribute to its lateral growth of ~235 km (McQuarrie and Wernicke, 2005). The $\delta^{18}O_{sw}$ responses to extension can be estimated with isotopic gradient along the airflow trajectory from the Gulf of Mexico (black line in Appendix C7A). This gradient is ~0.005 ‰ km^{-1} , suggesting ~1.2 ‰ potential enrichment due to extension. This effect is relatively small in comparison to proxy changes and to simulated $\delta^{18}O_{sw}$ responses to increasing equator-to-pole temperature gradient. We consider the contribution of extension to Neogene proxy $\delta^{18}O$ changes is secondary and therefore is not included in the experiments.

Appendix C3

Neogene proxy $\delta^{18}O$ trends across the western U.S.

lat (Modern)	lon (Modern)	minerals	Significance Level	Trend (‰/10Ma)	locations
44.9	-111.9	Pedogenic carbonate	0.0038	1.4	Montana Basins, MO[1]
40.6	-115.7	Pedogenic carbonate	0.0001	4.5	Elko Basin,NV[1]
42.8	-115.2	Pedogenic carbonate	0.0000	-4.0	Hagerman, ID[1]
40.6	-106.4	Pedogenic carbonate	0.0002	1.0	Middle and North Park, CO[2]
40.1	-114.1	Pedogenic carbonate	0.3355	-6.3	Ibapah Badlands, UT[3]
36.4	-117.8	Pedogenic carbonate	0.0217	3.9	Fish Lake Valley, NV[4,5]
42.0	-103.4	glasses	0.0048	3.9	Western Great Plain, NE[6]
42.1	-107.6	glasses	0.0028	2.9	Central Rockies, WY[6]
35.0	-117.0	smectite	0.1854	1.0	Rainbow Basin, CA[7]
35.4	-117.9	smectite	0.0000	11.4	El Paso Basin, CA[7]
38.0	-118.2	smectite	0.0590	1.2	Western Sierra Nevada, NV[8]
41.8	-114.6	smectite	0.0024	2.7	Northern Basin and Range, ID[9]
41.3	-102.3	Pedogenic carbonate	0.0040	3.3	Nebraska Composite section, NE[10]

[1] Chamberlain, C. P., Mix, H. T., Mulch, A., Hren, M. T., Kent-Corson, M. L., Davis, S. J., et al., 2012. The Cenozoic climatic and topographic evolution of the western North American Cordillera. American Journal of Science, 312, 213–262. http://doi.org/10.2475/02.2012.05

[2] Montagne, J.D.L., Barnes, W.C., 1957. Stratigraphy of the North Park Formation, in the North Park area, Colorado. In: Rocky Mountain Association of Geologists Guidebook to the Geology of North and Middle Park Basins, Colorado, p. 55–60.

[3] Perkins, M.E., Brown, F.H., Nash, W.P., McIntosh, W., Williams, S.K., 1998. Sequence, age, and source of silicic fallout tuffs in middle to late Miocene basins of the northern Basin and Range province. GSA Bull. 110, 344–360.

[4] Reheis, M.C., Block, D., 2007. Surficial Geologic Map and Geochronologic Database, Fish Lake Valley, Esmeralda County, Nevada, and Mono County, California. U.S. Geol. Surv. Data Ser., vol. 277.

[5] Reheis, M.C., Sawyer, T.L., 1997. Late Cenozoic history and slip rates of the Fish Lake Valley, Emigrant Peak, and Deep Springs fault zones, Nevada and California. GSA Bull. 109, 280–299.

[6] Fan, M., Heller, P., Allen, S. D., & Hough, B. G., 2014. Middle Cenozoic uplift and concomitant drying in the central Rocky Mountains and adjacent Great Plains. Geology, 42(6), 547–550. http://doi.org/10.1130/G35444.1

[7] Horton, T. W., & Chamberlain, C. P., 2006. Stable isotopic evidence for Neogene surface downdrop in the central Basin and Range Province. Geological Society of America Bulletin, 118(3-4), 475–490. http://doi.org/10.1130/B25808

[8] Poage, M. A., and Chamberlain, C. P., 2001. Stable isotopic evidence for a Pre-Middle Miocene rain shadow in the western Basin and Range: Implications for the paleotopography of the Sierra Nevada. Tectonics, 21(4). http://doi.org/10.1029/2001TC001303

[9] Horton, T. W., Sjostrom, D. J., Abruzzese, M. J., Poage, M. A., Waldbauer, J. R., Hren, M., et al., 2004. Spatial and temporal variation of Cenozoic surface elevation in the Great Basin and Sierra Nevada. American Journal of Science, 304(10), 862–888. http://doi.org/10.2475/ajs.304.10.862

[10] Mix, H. T., Winnick, M. J., Mulch, A., & Page Chamberlain, C., 2013. Grassland expansion as an instrument of hydrologic change in Neogene western North America. Earth and Planetary Science Letters, 377-378, 73–83. http://doi.org/10.1016/j.epsl.2013.07.032

Appendix C4

^{18}O fractionation factors between soil water and different types of minerals used in the study.

Mineral	Fractionation factor (α)	References
Calcite	$1000\ln\alpha_{calcite-water} = 2.78 \times 10^6 \times T^{-2} - 2.89$	Friedman and O'Neil, 1977
Volcanic glasses	$1000\ln\alpha_{glass-water} = 1/1.0343$	Friedman, et al., 1993
Smectite	$1000\ln\alpha_{smectite-water} = 2.55 \times 10^6 \times T^{-2} - 4.05$	Sheppard and Gilg, 1996

Appendix C5

Comparison of present-day observation and early-to-middle Miocene reconstructions of precipitation

lat (Modern)	lon (Modern)	Age (Ma)	Min (mm)	Max (mm)	Location	Modern(MERRA data)	Modern - Proxy (Min)	Modern - Proxy (Max)
36.3	-121.4	17	653	760	Carmel Valley[1]	457.3	-195.7	-302.7
39	-118.2	18.5	760	890	Middlegate Basin[2]	304.8	-455.2	-585.2
39	-117.7	18	890	1000	Buffalo Canyon[3]	304.8	-585.2	-695.2
35.3	-119.7	15	635	635	Tembler California[4]	213.3	-421.7	-421.7
44.8	-114.7	16.0–15.4	700	700	Picture Gorge Subgroup[5]	555.3	-144.7	-144.7
42	-114	9–11.8	1143	1270	Trapper Creek Formation[6]	392.2	-750.8	-877.8
35	-101	10.–12.	475	875	Clarendon, TX[1]	599.9	124.9	-275.1
37	-100	10.–12.	550	950	Beaver, Oklahoma[1]	570.4	20.4	-379.6
44.2	-118	~12	623	879	Ironside, Oregon[7]	319.9	-303.1	-559.1

[1] Axelrod D. I., 1979. Desert vegetation, its age and origin. In: Goodin JR & DK Northington (eds). Arid Land Plant Resources: 1-72. International Center for Arid and Semi-arid Land Studies, Texas Tech University, Lubbock, Texas.

[2] Axelrod D. I., 1985. Miocene floras from the Middlegate basin, west-central Nevada. University of California Publications in Geological Sciences 129.

[3] Axelrod D. I., 1991. The Miocene Buffalo Canyon flora, western Nevada. University of California Publications in Geological Sciences 135.

[4] Axelrod D. I., 1995. The middle Miocene Purple Mountain flora of western Nevada: Univ. of California Publ. Geol. Sci., 139, 62 p.

[5] Sheldon, N. D., 2006. Using paleosols of the Picture Gorge Basalt to reconstruct the middle Miocene climatic optimum. PaleoBios, 26(2), 27-36.

[6] Leopold, E. B., and Denton, M. F., 1987. Comparative age of grassland and steppe east and west of the northern rocky mountain. Annals of the Missouri Botanical Garden, 841-867.

[7] Retallack, G. J., 2004. Late Miocene climate and life on land in Oregon within a context of Neogene global change. Palaeogeography, Palaeoclimatology, Palaeoecology, 214(1), 97-123.

Appendix C6

Comparison of simulated present-day climate with observations.

A: mean annual 2-m temperature. B: mean-annual precipitation. Black contours: present-day elevations using 9-point smoothing on 10" GTOPO30 data (upper row) and prescribed modern topography in the model (lower row). The model reproduces observed broad scale patterns of temperature and precipitation, but lacks sufficient horizontal resolution to simulate local variability associated with small-scale topographic gradients.

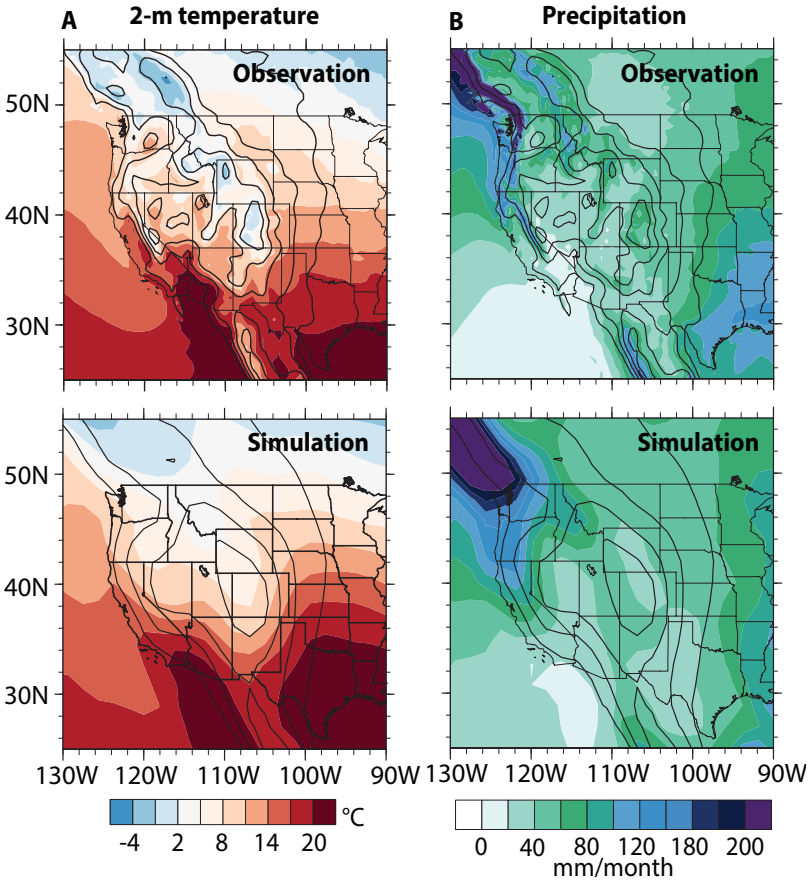

Appendix C7

Comparison of simulated and observed $\delta^{18}O$ in precipitation ($\delta^{18}O_p$).

Color shading and filled circles: observed $\delta^{18}O_p$ from GNIP and USNIP datasets complied by Bowen and Revenaugh, (2003). The thick black line shows the trajectory along which the modern continental $\delta^{18}O_{sw}$ gradient is measured.

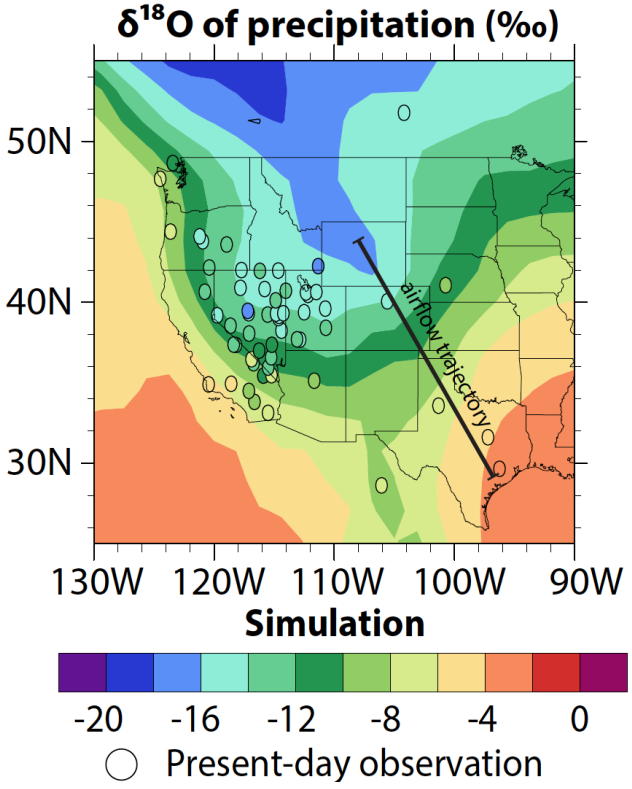

Appendix C8

Prescribed boundary conditions in the model.

A-C: present-day global SSTs, geography and North America vegetation cover. D-G: prescribed early Neogene boundary conditions for individual sensitivity experiments featuring steepened equator-to-pole temperatures gradient (D), and tropical Pacific zonal SST gradient (G), early Neogene geographic and topographic configuration (F), and reforestation of the North America (G), respectively.

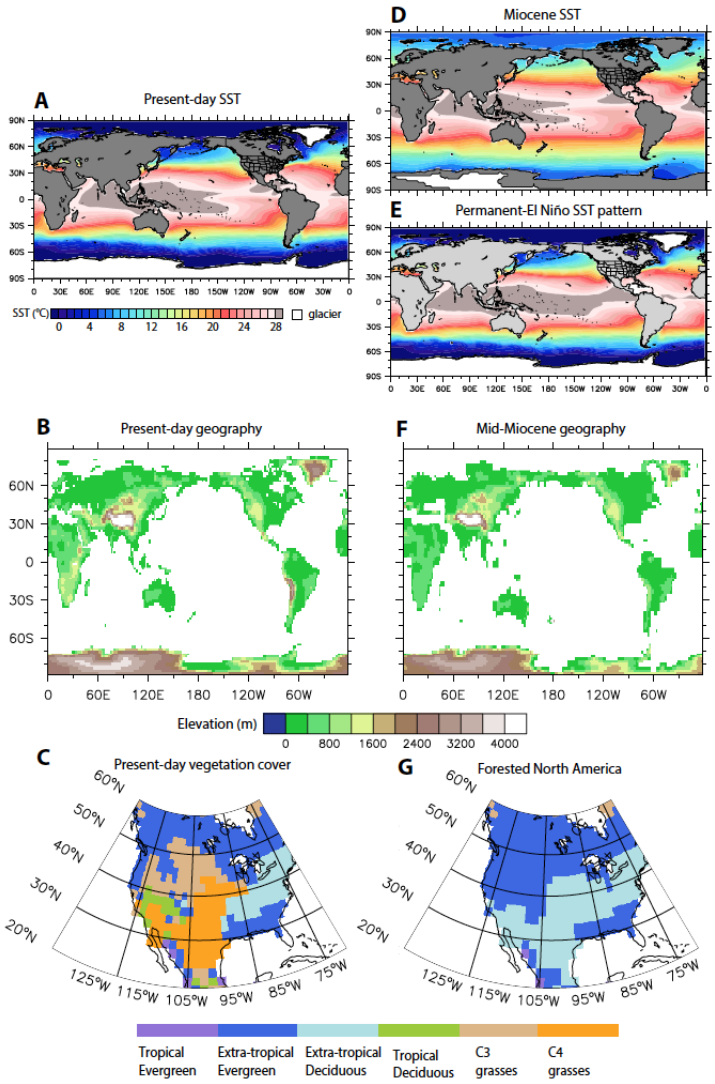

Appendix C9

Simulated climate responses to Neogene grassland expansion.

A: fractionation responses of water recycling ratio, defined as the ratio of evapotranspiration versus precipitation. B: fractional responses of surface albedo relative to the albedo of forested western U.S. C: responses of annual total amount of snowfall. Grassland expansion, although increases water recycling ratio, leads to cooling, increase in surface albedo and high altitude snowfall across the western U.S. Consequently, the $\delta^{18}O_{sw}$ responses show melting season depletion and negligible annual average amount.

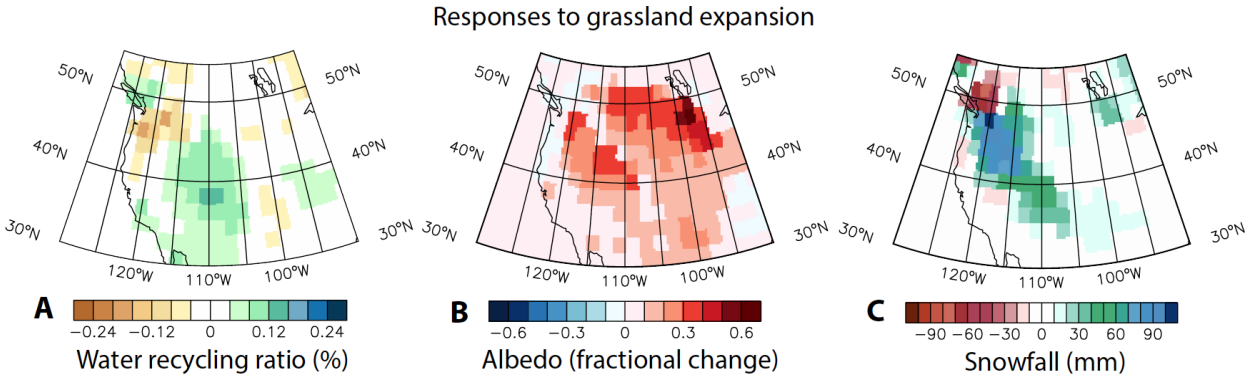

Bibliography

Bowen, G.J., Revenaugh, J., 2003. Interpolating the isotopic composition of modern meteoric precipitation. Water Resources Research 39. doi:10.1029/2003WR002086

Breecker, D.O., Sharp, Z.D., and McFadden, L.D. Seasonal bias in the formation and stable isotopic composition of pedogenic carbonate in modern soils from central New Mexico, USA: Geological Society of America Bulletin, v. 121, p. 630–640, doi: 10.1130/B26413.1.

Cassel, E.J., Breecker, D.O., Henry, C.D., Larson, T.E., and Stockli, D.F., 2014, Profile of a paleo-orogen: High topography across the present-day Basin and Range from 40 to 23 Ma: Geology, v. 42, no. 11, p. 1007–1010, doi: 10.1130/G35924.1.

Chamberlain, C.P., Mix, H.T., Mulch, A., Hren, M.T., Kent-Corson, M.L., Davis, S.J., Horton, T.W., and Graham, S.A., 2012, The Cenozoic climatic and topographic evolution of the western North American Cordillera: American Journal of Science, v. 312, p. 213–262, doi: 10.2475/02.2012.05.

Chulick, G.S., and Mooney, W.D., 2002, Seismic Structure of the Crust and Uppermost Mantle of North America and Adjacent Oceanic Basins: A Synthesis: Bulletin of the Seismological Society of America, v. 92, no. 6, p. 2478–2492, doi: 10.1785/0120010188.

Dickinson, W. R., 2006. Geotectonic evolution of the Great Basin. Geosphere,2(7), 353-368.

Eronen, J. T., Fortelius, M., Micheels, A., Portmann, F. T., Puolamäki, K., & Janis, C. M. (2012). Neogene aridification of the Northern Hemisphere. Geology, 40(9), 823–826. http://doi.org/10.1130/G33147.1

Fan, M., Heller, P., Allen, S.D., and Hough, B.G., 2014, Middle Cenozoic uplift and concomitant drying in the central Rocky Mountains and adjacent Great Plains: Geology, v. 42, no. 6, p. 547–550, doi: 10.1130/G35444.1.

Feng, R., Poulsen, C.J., Werner, M., Chamberlain, C.P., Mix, H.T., and Mulch, A., 2013, Early Cenozoic evolution of topography, climate, and stable isotopes in precipitation in the North American Cordillera: American Journal of Science, v. 313, no. 7, p. 613–648, doi: 10.2475/07.2013.01.

Ferretti, D. F., Pendall, E., Morgan, J. A., Nelson, J. A., LeCain, D., and Mosier, A. R., 2003, Partitioning evapotranspiration fluxes from a Colorado grassland using stable isotopes: Seasonal variations and ecosystem implications of elevated atmospheric CO2. Plant and Soil, 254(2), 291–303. http://doi.org/10.1023/A:1025511618571

Friedman I, O'Neil JR. 1977. Compilation of stable isotope fractionation factors of geochemical interest. In USGS Prof. Pap. 440-KK, Data of Geochemistry, ed. M Fleischer, pp. KK1–12. Reston, VA: U.S. Geol. Surv., 6th ed.

Friedman, I., Gleason, J., and Warden, A., 1993, Ancient climate from deuterium content of water in volcanic glass, in Swart, P.K., et al., eds., Climate change in continental isotopic records: American Geophysical Union Geophysical Monograph 78, p. 309–319.

Galewsky, J., 2009. Orographic precipitation isotopic ratios in stratified atmospheric flows: Implications for paleoelevation studies. Geology, 37(9), 791–794. http://doi.org/10.1130/G30008A.1

Goldner, A., Herold, N., Huber, M., 2014. The challenge of simulating the warmth of the mid-Miocene climatic optimum in CESM1. Clim. Past 10, 523–536. doi:10.5194/cp-10-523-2014

Haese, B., Werner, M., and Lohmann, G., 2013, Stable water isotopes in the coupled atmosphere–land surface model ECHAM5-JSBACH: Geoscientific Model Development, v. 6, no. 5, p. 1463–1480, doi: 10.5194/gmd-6-1463-2013.

Henry, C.D., and Faulds, J.E., 2010, Ash-flow tuffs in the Nine Hill, Nevada, paleovalley and implications for tectonism and volcanism of the western Great Basin, USA: Geosphere, v. 6, no. 4, p. 339–369, doi: 10.1130/GES00548.1.

Herold, N., Huber, M., Muller, R.D., 2011. Modeling the Miocene Climatic Optimum. Part I: Land and Atmosphere*. J. Climate 24, 6353–6372. doi:10.1175/2011JCLI4035.1

Herold, N., Seton, M., Muller, R.D., You, Y., Huber, M., 2008. Middle Miocene tectonic boundary conditions for use in climate models. Geochemistry, Geophysics, Geosystems 9.

Hoffmann, G., Werner, M., and Heimann, M., 1998, Water isotope module of the ECHAM atmospheric general circulation model: A study on timescales from days to several years: Journal of Geophysical Research: Solid Earth, v. 103, no. D14, p. 16871–16896, doi: 10.1029/98JD00423.

Horton, T.W., and Chamberlain, C.P., 2006, Stable isotopic evidence for Neogene surface downdrop in the central Basin and Range Province: Geological Society of America Bulletin, v. 118, no. 3-4, p. 475–490, doi: 10.1130/B25808.

Horton, T.W., Sjostrom, D.J., Abruzzese, M.J., Poage, M.A., Waldbauer, J.R., Hren, M., Wooden, J., and Chamberlain, C.P., 2004, Spatial and temporal variation of Cenozoic surface elevation in the Great Basin and Sierra Nevada: American Journal of Science, v. 304,

no. 10, p. 862–888, doi: 10.2475/ajs.304.10.862.

Lechler, A.R., and Galewsky, J., 2013, Refining paleoaltimetry reconstructions of the Sierra Nevada, California, using air parcel trajectories: Geology, v. 41, no. 2, p. 259–262, doi: 10.1130/G33553.1.

McQuarrie, N., and Wernicke, B.P., 2005, An animated tectonic reconstruction of southwestern North America since 36 Ma: Geosphere, v. 1, no. 3, p. 147–172, doi: 10.1130/GES00016.S1.

Molnar, P., Cane, M.A., 2007. Early pliocene (pre-Ice Age) El Nino-like global climate: Which El Nino? Geosphere 3, 337–365. doi:10.1130/GES00103.1

Mix, H.T., Mulch, A., Kent-Corson, M.L., and Chamberlain, C.P., 2011, Cenozoic migration of topography in the North American Cordillera: Geology, v. 39, no. 1, p. 87–90, doi: 10.1130/G31450.1.

Mix, H.T., Winnick, M.J., Mulch, A., and Page Chamberlain, C., 2013, Grassland expansion as an instrument of hydrologic change in Neogene western North America: Earth and Planetary Science Letters, v. 377-378, p. 73–83, doi: 10.1016/j.epsl.2013.07.032.

Mulch, A., 2006, Hydrogen Isotopes in Eocene River Gravels and Paleoelevation of the Sierra Nevada: Science, v. 313, no. 5783, p. 87–89, doi: 10.1126/science.1125986.

Oishi, A. C., Oren, R., & Stoy, P. C., 2008, Estimating components of forest evapotranspiration: A footprint approach for scaling sap flux measurements. Agricultural and Forest Meteorology, 148(11), 1719–1732. http://doi.org/10.1016/j.agrformet.2008.06.013

Poulsen, C. J., Ehlers, T. A., and Insel, N., 2010, Onset of Convective Rainfall During Gradual Late Miocene Rise of the Central Andes. Science, 328(5977), 490–493. http://doi.org/10.1126/science.1185078

Poulsen, C.J., and Jeffery, M.L., 2011, Climate change imprinting on stable isotopic compositions of high-elevation meteoric water cloaks past surface elevations of major orogens: Geology, v. 39, no. 6, p. 595–598, doi: 10.1130/G32052.1.

Rienecker, M.M., Suarez, M.J., Gelaro, R., Todling, R., Bacmeister, J., Liu, E., Bosilovich, M.G., Schubert, S.D., Takacs, L., Kim, G.-K., Bloom, S., Chen, J., Collins, D., Conaty, A., da Silva, A., Gu, W., Joiner, J., Koster, R.D., Lucchesi, R., Molod, A., Owens, T., Pawson, S., Pegion, P., Redder, C.R., Reichle, R., Robertson, F.R., Ruddick, A.G., Sienkiewicz, M., Woollen, J., 2011. MERRA: NASA's modern-era retrospective analysis for research and applications. J. Climate 24, 3624–3648.

Sheppard S. M. F. and Gilg H. A., 1996. Stable isotope geochemistry of clay minerals. Clay Miner. 31, 1–24.

Smith, T. M., and Reynolds, R. W., 2004. Improved extended reconstruction of SST (1854-1997). Journal of Climate, 17(12), 2466-2477.

Strömberg, C.A.E., 2011, Evolution of Grasses and Grassland Ecosystems: Annual Review of Earth and Planetary Sciences, v. 39, no. 1, p. 517–544, doi: 10.1146/annurev-earth-040809-152402.

Werner, M., Langebroek, P.M., Carlsen, T., Herold, M., and Lohmann, G., 2011, Stable water isotopes in the ECHAM5 general circulation model: Toward high-resolution isotope modeling on a global scale: Journal of geophysical research, v. 116, no. D15, p. D15109, doi: 10.1029/2011JD015681.

Zhang, Y.G., Pagani, M., Liu, Z., Bohaty, S.M., and DeConto, R., 2013, A 40-million-year history of atmospheric CO2: Philosophical Transactions of the Royal Society of London A: Mathematical, Physical and Engineering Sciences, v. 371, no. 2001, p. 20130096, doi: 10.1098/rsta.2013.0096.

Chapter 5

Andean elevation control on tropical Pacific climate and ENSO

5.1 Abstract

Late Cenozoic marine proxy data record a long-term transition in the tropical Pacific from El Niño-like conditions with reduced zonal sea surface temperature (SST) gradient, deepened thermocline and reduced upwelling in the eastern equatorial Pacific (EEP), to conditions similar to modern. This transition coincides with kilometer-scale uplift of the central Andes. To understand whether the rise of the Andes contributed to tropical Pacific climate evolution, we performed experiments with NCAR's Community Climate System Model version 4 to quantify changes in tropical Pacific climate and ENSO as a function of Andean elevations. Our results demonstrate that uplift increases the equatorial east-west SST gradient and Walker circulation. The rise of the Andes from 1 to 3 kms increases the SST gradient by 0.8 °C and Walker circulation by 60% due to strengthened radiative cooling by enhanced low cloud formation in the EEP. This cooling effect is largest in the southeastern tropical Pacific and accounts for about one-half of the reconstructed SST cooling along the Peru coast. The uplift also strengthens upwelling north of the EEP, consistent with documented increases in biological productivity in this region, and decreases the frequency of El Niño-Southern Oscillation and the number of strong El Niño events. Simulated responses to Andean uplift are generally consistent with Late Cenozoic proxy records, but too small in magnitude. Taken together, our results indicate that Andean uplift was likely one of multiple factors that contributed to the long-term evolution of both the mean climate state and interannual variability in the tropical Pacific.

5.2 Introduction

Geological evidence suggests that the tropical Pacific climate evolved through the Late Cenozoic from a mean state with a reduced zonal SST gradient across the equatorial Pacific to its current state (Wara et al., 2005; Fedorov et al., 2006; Zhang et al., 2014). In comparison to today, the western equatorial Pacific during the early Pliocene (~5 Ma) had similar SSTs (Wara et al., 2005); however, the eastern equatorial Pacific (EEP) was characterized by sea surface

temperatures (SST) that were ~2 to 6 °C warmer (Wara et al., 2005; Lawrence et al., 2006; Steph et al., 2010; Dekens et al., 2007), a deeper thermocline (Wara et al., 2005; Lawrence et al., 2006; Steph et al., 2010), and lower biologic productivity and richness (Wara, et al., 2005; Dekens et al., 2007; Lawrence et al., 2006; Kamikuri et al., 2009; Steph et al., 2010).

These proxy observations were originally used as evidence for a "permanent El Niño" state with a negligible zonal SST gradient across the equatorial Pacific (Wara et al., 2005; Fedorov et al., 2006), which was thought to have ended with intensification of the EEP cold tongue at ~3 Ma (Wara et al., 2005) or ~4 Ma (Lawrence et al., 2006; Steph et al., 2010). This argument is consistent with Early Pliocene terrestrial records of temperature and precipitation from around the world, which have been suggested to exhibit far-field patterns similar to those that occur during modern El Niño events (Molnar and Cane, 2007), although different causes such as changes in early Pliocene surface conditions and CO_2 levels could also produce these patterns (Bonham et al., 2009). More recent studies of marine sediment cores that extend into the Miocene challenge the suggested "permanent El Niño" state (Nathan and Leckie, 2009; Zhang et al., 2014). New SST estimates suggest that an SST zonal gradient of ~3 °C was sustained through the Late Miocene and increased during the Plio-Pleistocene (Zhang et al., 2014). And, records of marine productive indicate that upwelling in the northern EEP (6 °N, 86 °W) began to intensify in the Late Miocene (13 Ma), suggesting that the transition to modern conditions may have started much earlier than the Pliocene (Kamikuri et al., 2009; LaRiviere et al., 2012). Though late Cenozoic marine records differ in detail, they generally record a strengthening of the climate asymmetry in the tropical Pacific. The cause of this transition is crucial to understanding the formation and stability of modern climate variability.

The evolution of the tropical Pacific has been linked to both long-term changes in CO_2 levels and episodic gateway changes in the Late Cenozoic. However, none of these mechanisms can explain the changes documented in marine proxy records. CO_2-induced cooling has been found to have little direct effect on the SST gradient across the tropical Pacific (e.g. Lee and Poulsen, 2006; Haywood et al., 2007; Fedorov et al., 2013). The widening of the Indonesian seaway increases warm and fresh water flow to the central equatorial Pacific, which decreases the frequency of the El Niño-Southern Oscillation (ENSO), but has little influence on simulated SSTs in the eastern Pacific (Jochum et al., 2009). And, finally, the closing of the Panama Seaway raises the EEP thermocline by reducing flow of warm waters from the western Atlantic (Steph et

al., 2010; Zhang et al., 2010); however, the SST response is quite small in coupled experiments and has little effect on the zonal gradient across the equatorial Pacific (Zhang et al., 2010; Fedorov et al., 2013). Besides, when the Panama seaway closed remains controversial. Closure ages are proposed to between 4 and 5 Ma based on ocean drilling records (Haug and Tiedemann, 1998) or at ~15 Ma based on geological mapping and geo-chronological and -chemical data from the central Panama (Montes et al., 2012).

Other mechanisms have been proposed to explain the evolution of the tropical Pacific including an enhanced tropical-extratropical thermo-gradient (Fedorov et al., 2006; Brierley et al., 2009), expansion of Southern Ocean sea ice (Lee and Poulsen, 2006) and decrease in the frequency of tropical storms (Fedorov et al., 2010). Mechanisms such as dwindling CO_2 level, expansion of sea ice or decreasing albedo of the extratropical low clouds (Fedorov et al., 2013) are needed to explain the enhanced thermo-gradient. Therefore, unlike the other two, the thermo-gradient hypothesis by itself should not be considered as a direct forcing. Climate modeling studies of sea ice expansion and decreasing frequency of tropical storms show reasonable agreement with proxy observations. An increase in Southern Ocean sea ice from ice-free to modern extents in a coupled ocean-atmosphere model enhanced cold-water advection into the EEP through the meridional thermocline circulation, leading to a ~2 °C decrease in SSTs in the EEP. Similarly, a decrease in ocean diffusivity (by 10 times), representing weakened mixing due to reduced frequency of tropical storms, in another coupled model cooled SSTs in the EEP by 2.5 °C (Fedorov et al., 2010). Both mechanisms produce cooling that is consistent with proxy records, but until compelling geological evidence is found for either mechanism, both must be considered to be somewhat ad hoc.

Significant surface uplift of the Andes due to subduction of the Nazca plate beneath South America occurred since the Late Miocene (see summary by Insel et al., 2012). The possibility that Andean surface uplift influenced tropical Pacific climate draws support from dynamical studies. Notably, Rodwell and Hoskins (2001) found using a simplified atmospheric model that a high-elevation Andes strengthened the southeastern Pacific subtropical high-pressure system. Because the subtropical high is a dynamic response to subsidence of dry air, intensification of the high was speculated to coincide with evaporative cooling of the sea surface. Takahashi and Battisti (2007a) using a simplified atmospheric model with a mixed-layer ocean confirmed this linkage. In addition, they found that enhanced low cloud formation in the

southeastern tropical Pacific (SETP) contributed to SST cooling as well. Together these factors lead to a total cooling of up to 4 °C. The application of these studies to the late Cenozoic is limited, however, by their idealized nature and the absence of dynamic ocean-atmosphere interactions. In this study, we use an earth system model with coupled ocean-atmosphere dynamics to overcome this limitation.

The details and timing of Andean uplift are uncertain. Terrestrial proxy data from the Andean Altiplano have been argued to record rapid surface uplift of the central Andes by 2.5±1 km between 10 Ma and 6 Ma (Garzione et al., 2006; Ghosh et al., 2006; Leier et al., 2013) that proceeded from south to north (Gregory-Wodzicki, 2000). This interpretation of a rapid rise has been disputed in favor of more gradual uplift through the Cenozoic (e.g. Ehlers and Poulsen, 2009; Poulsen et al., 2010; Insel et al., 2012). Nonetheless, most geological studies support uplift of approximately 2 km since 15 Ma (see summary in Insel et al., 2012), which coincides with the long-term increase in upwelling documented in the northern EEP. Due to the uncertainties in both timing and distribution of surface uplift, we focus on the large-scale influence of the Andean range and do not assign any particular ages to our simulations.

In addition to the mean state, we also explore whether Andean uplift alters interannual variability (ENSO) in the tropical Pacific. High-resolution sedimentary records of late Miocene and early Pliocene age from the equatorial Pacific (Scroxton et al., 2011; Watanabe et al., 2012) and Mediterranean region (Galeotti et al., 2010) contain sedimentary features that are thought to represent ENSO variability, indicating that even under a climatological state with low equatorial SST gradient, the ENSO cycle was active in the early Pliocene. However, whether the strength and frequency of ENSO are different from modern is unclear, but crucial to understanding past climate variability. In this study, we show based on our modeling results a connection between ENSO and Andean uplift.

5.3 Methods

The Community Climate System Model version 4 (CCSM4) (Gent et al., 2011) is configured to include the Community Atmospheric Model version 4 (CAM4), dynamical ocean model of Parallel Ocean Program version 2 (POP2), Community Land Model version 4 (CLM4) and the Los Alamos Sea Ice model (CICE). All components are coupled through the version 7 coupler (CPL7). Both CAM4 and CLM4 are run at 1.9° × 2.5° horizontal resolution; CAM4 has 26 vertical levels. POP2 is configured with a 384 × 320 horizontal grid, 60 vertical layers and a

rotated north pole centered on Greenland. Pre-industrial boundary conditions are prescribed, including a CO_2 level of 287.4 ppm, a solar constant at 1360.9 W/m^2 and pre-industrial vegetation distribution and land surface types (see details in Gent et al., 2011).

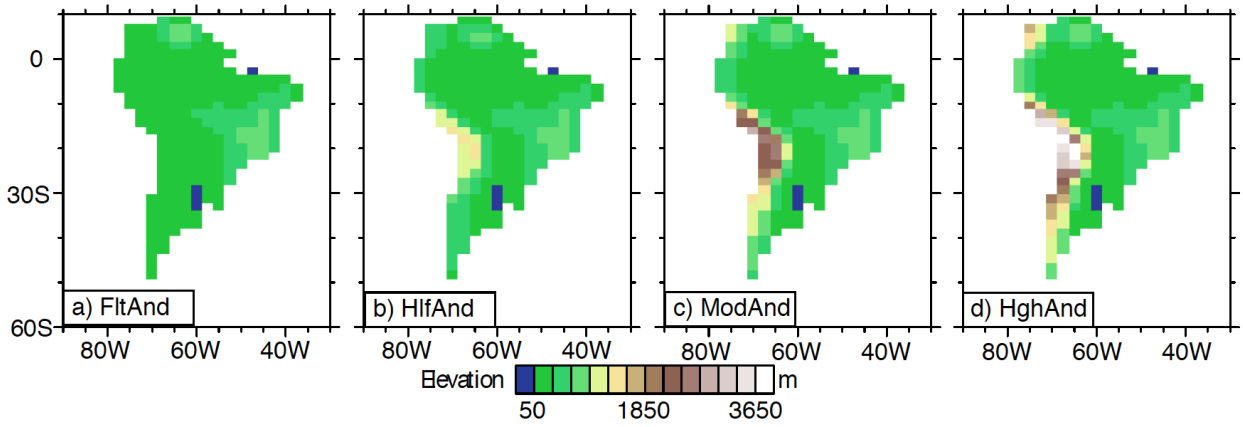

Figure 26 South American elevations specified in the a) FltAnd, b) HlfAnd, c) ModAnd, and d) HghAnd experiments.
The ModAnd features the standard topography of CCSM 4, in which the elevation is averaged within each 2 ° grid cell yielding average elevations in the central Andes of ~2 km. The elevations of central Andes are ~145 m and ~1 km in the FltAnd and HlfAnd and increase to ~3 km in the HghAnd.

Four topographic scenarios are prescribed in CAM4 (Figure 26a-d) with gradual rise of the entire South American coastal range, the elevation of which is adjusted proportionally to preserve its modern horizontal extent. The horizontal extent of the Andes, which has previously been shown to have no significant effect on the topography-induced dynamics (Takahashi and Battisti, 2007b), is kept the same for all experiments. The Altiplano region is raised incrementally from approximately sea-level (145 m, averaged across 16 – 23 °S, 70 – 65 °W) (referred to as "FltAnd") to a moderate height of 1059 m (referred to as "HlfAnd"), a standard height in CCSM4 of 2272 m (referred to as "ModAnd") and a higher elevation of 3184 m (referred to as "HghAnd") comparable to the averaged elevation across the entire modern Altiplano (3365 m calculated from GTOPO30 data (http://webgis.wr.usgs.gov/globalgis/gtopo30/gtopo30.html at 10-minute resolution). It should be noted that the default prescription of the Andes in a 2 × 2° CCSM4 modern simulation is lower than observation due to grid-scale averaging of topography (Figure 26c). Land surface boundary conditions are unchanged across experiments, eliminating the response of vegetation and land surface hydrology to elevation changes. All four experiments are branched from the end of a

1000-year pre-industrial control experiment and integrated for another 300 years. The diagnostics for the control experiment can be found at http://www.cesm.ucar.edu/experiments/cesm1.0/.

CCSM4 simulates SST in the EEP reasonably well. SSTs adjacent to the northern Chilean coast are too warm by 1 – 2°C due to coastal southerly winds that are too weak in the 2°-grid configuration. A 0.5°-grid simulation with the same physics packages but refined topography forces stronger southerly wind stress that eliminates this bias, indicating that the model physics is not the primary culprit (Gent et al., 2009). Higher resolution experiments may better constrain the exact magnitude of climate responses to the Andean uplift, but are not expected to change fundamentally with the same model physics. The simulated ENSO amplitude in CCSM4 is overestimated by 70% in a 2 × 2° modern simulation and has a stronger than normal 4-yr power spectrum peak (Deser et al., 2012). Nonetheless, CCSM4's ENSO simulation is among the best of the newest generation of coupled models and its 4-yr cycle falls within modern observations (Bellenger et al., 2013).

The Niño 3.4 index is used here to identify the frequency of ENSO. The index is defined as the 5-month running mean of the departure in monthly SST from its 30-year average across the central equatorial Pacific (170 ° – 120 °W, 5 °N – 5 °S). Modern El Niño events are identified as periods when the Niño 3.4 is equal to or greater than 0.4 °C for a minimum duration of 5 months (Trenberth, 1997). In modeling studies, the criteria for identifying El Niño events are somewhat different to account for systematic model biases. In CCSM, the standard deviation (σ) of the Niño 3.4 ($\sigma_{\text{Niño 3.4}}$) across climatological time scales has been used to identify El Niño and La Niña (Deser et al., 2012; Bellenger et al., 2013). In our experiments, the probability density functions of monthly Niño 3.4 of the last 230-yr experiments forms a single distribution that is close to normal, implying no systematic shifts of the Niño 3.4 statistics across different climatological time scales. Thus, following Bellenger et al. (2013), the $\sigma_{\text{Niño 3.4}}$ of the entire 230-yr time series is used to identify the El Niño and La Niña events. We define El Niño (La Niña) events as having a Niño 3.4 greater (smaller) than $0.5\sigma_{\text{Niño 3.4}}$ ($-0.5\sigma_{\text{Niño 3.4}}$) for at least 5 months. A value of $0.5\sigma_{\text{Niño 3.4}}$ is equivalent to a Niño 3.4 amplitude of 0.7 °C from modern SST observations, which is higher than the threshold of 0.4 °C used to identify El Niño and La Niña events from observations. This threshold choice minimizes the bias in CCSM 4 to overestimate Niño 3.4 variations.

The upper layer ocean equilibrates during the first 70 years in all four branched experiments. Upper layer (0 – 500 m) seawater trends in the following 230 yrs are less than 0.01 °C/century over the entire ocean and less than 0.06 °C/century in the EEP region (5 °S – 5 °N, 90 ° – 120 °W). The global mean upper layer seawater temperature is similar (~11.3 °C) in all four experiments. Climate responses are reported here as differences from the FltAnd case and are based on results from the last 230 yrs of simulation. In Section 5.4, we focus on comparisons between the ModAnd and FltAnd experiments for brevity; differences between the HghAnd and FltAnd experiments are similar though slightly larger in magnitude.

In order to retain the responses mostly due to changes in the mean state, we perform a consistency test when analyzing the climate responses to surface uplift (Figure 28, Figure 31 and Figure 32b). Consider a multi-decadal oscillation with the same period and average amplitude. A phase offset between experiments could result in net differences if the averaging time is not exactly one or a multiple of periods. Similar differences could also result from temporal variations in oscillation amplitudes. These differences, if measured at decadal time scales, may vary in sign, while differences in background states should be consistent. We compare the sign of differences between mean fields calculated on 30-yr time intervals (20-yrs for the final interval) at each grid point. Differences that vary in sign across these intervals are considered inconsistent and are not reported.

5.4 Results

5.4.1 La Niña-like SST response to the uplift of the Andes

The strongest SST responses to Andean uplift occur in the EEP and SETP. SST responses are small outside the tropical Pacific. Moderate warming in the northwestern Pacific and tropical Atlantic (Figure 27a) are reminiscent of extra-tropical SST responses to the La Niña-like tropical conditions (e.g., Alexander et al., 2002).

The responses of tropical climate to Andean uplift are nonlinear (Figure 28a, b) with notable changes in SST and zonal circulation occurring when the range exceeds the marine boundary layer of the eastern tropical Pacific, a height of more than 1100 m (Wood and Bretherton, 2004). This layer can be identified by the large vertical gradient of equivalent potential temperature (Xu et al., 2004), which separates the low-level mixed layer from the upper-level free troposphere. In our simulations, the top of the marine boundary layer occurs

between ~860 hPa and 700 hPa with much better defined boundaries in ModAnd and HghAnd as compared to the FltAnd and HlfAnd (Figure 28c-f).

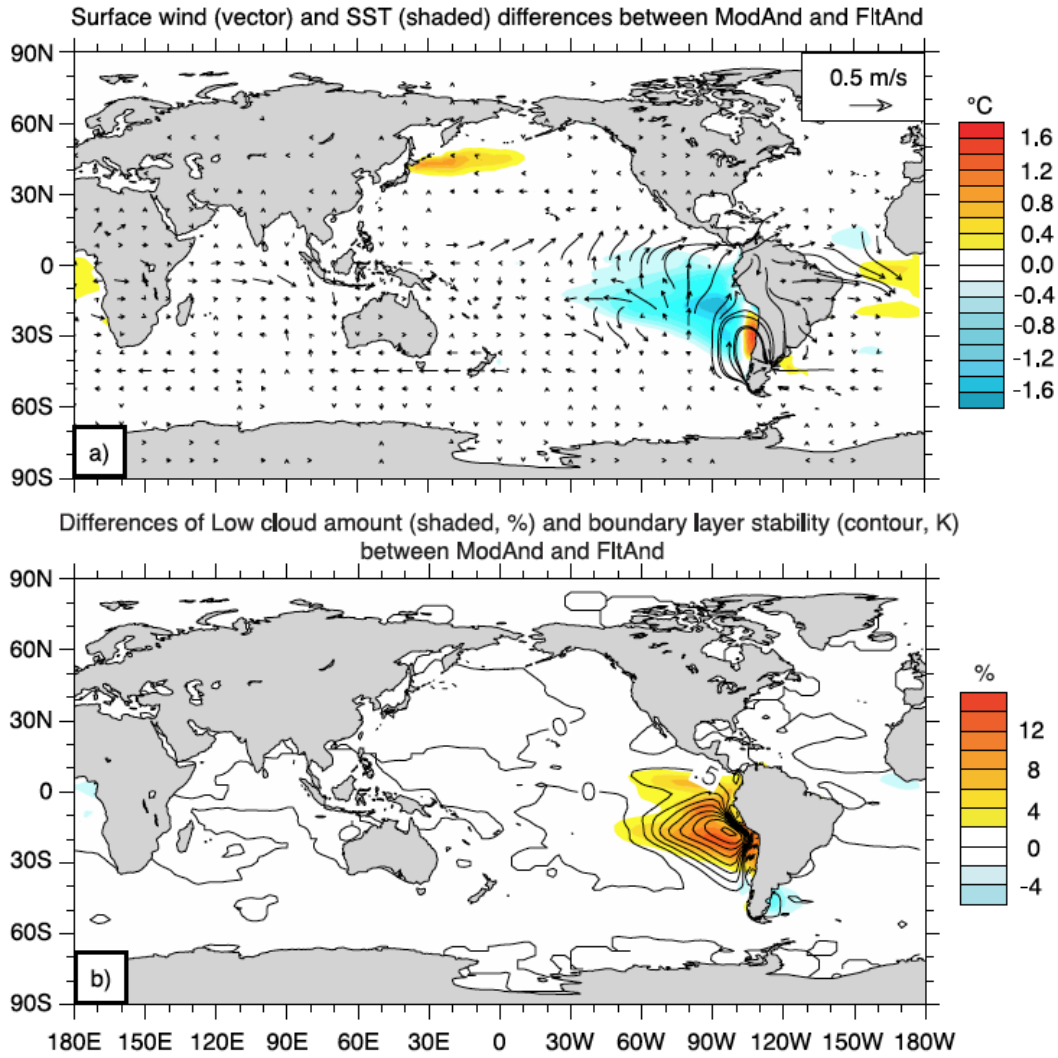

Figure 27 Global responses of SST and low-level atmosphere to the Andean uplift from FltAnd to ModAnd.
a) Mean SST (°C, shaded) and surface wind (m s^{-1}, vectors) differences. b) Differences of low cloud fraction (%, shaded) and marine boundary layer stability (K, contour). The marine boundary layer stability is measured by taking the difference of equivalent potential temperature between 700 hPa and 1000 hPa. Only responses that have passed consistency tests are shown.

In ModAnd and HghAnd, uplift of the Andes above the marine boundary layer leads to SST cooling of 0.4 °C and 0.8 °C in the EEP and 1.5 °C and 2.2 °C in the southeastern tropical Pacific (SETP, 15 ° – 20 °S, 80 ° – 100 °W) (Figure 28a). Within the equatorial zone, this non-linear SST response is coupled with strengthening of the Walker circulation, measured as the sea level pressure difference between the western (5 °S – 5 °N, 80 ° – 160 °E) and eastern (5 °S –

5 °N, 160 ° – 80 °W) equatorial Pacific (Vecchi and Soden, 2007). The strength of Walker circulation increases by 22 % in ModAnd and additional 28 % in HghAnd (Figure 28b). SST cooling is accompanied by anomalous surface wind divergence in the eastern tropical Pacific and strengthened easterlies at the western equatorial Pacific (120 °E – 180, Figure 27a). The coupling between SSTs, the Walker circulation, and equatorial easterlies comprises a Bjerknes feedback that strengthens the zonal SST gradient and enhances La Niña-like mean conditions.

5.4.2 Cooling due to increased low clouds

Increases in surface latent heat loss (Takahashi and Battisti, 2007a) and low cloud amounts by Andean uplift (Xu et al., 2004; Takahashi and Battisti, 2007a) have previously been suggested as mechanisms for SST cooling in the EEP and SETP. In our ModAnd experiment, radiative cooling due to enhanced shortwave reflection by low clouds contributes the largest forcing, which is locally as much as -8.5 W/m^2 (Table 5). Low clouds are enhanced year round by a strengthened marine boundary layer with a strong inversion cap (Figure 27b, Table 5), which is a result of uplift-induced circulation changes. A high Andes blocks northeasterly flow from northern South America and steers mid-latitude Westerlies in the southeastern Pacific towards the equator (Figure 27a). These changes in flow pattern induce advective cooling in the lower atmosphere (1000 – 900 hPa) of the EEP and SETP (Table 5). At the SETP, middle tropospheric subsidence is strengthened by Andean uplift, inducing anomalous subsidence warming on top of the boundary layer (Table 5). Both advective low-level cooling and higher level warming enhance the temperature difference across the boundary inversion, leading to a stronger moisture cap and greater low cloud amounts.

Surface cooling at the EEP and SETP is partially attenuated by subsurface warming in the southeastern Pacific. This warming is due to weakening of the Pacific Subtropical overturning Cell (STC), a wind-driven isopycnal flow that forms a meridional circulation in the upper (~200 m) tropical Pacific (Gu, 1997) and mixes tropical and subtropical waters through tropical thermocline upwelling of subtropical waters (Klinger et al., 2002). The STC consists of two meridional cells in the northern and southern tropical Pacific; however, only the southern STC is well defined in the eastern Pacific (Figure 29a). This southern STC extends from 150 °W to 85 °W at 9 °S with a core at ~50 m depth. We mainly focus here on the eastern portion of the southern STC (ESSTC) from 100 °W to 85 °W, which underlies uplift-induced SST cooling in the SETP.

Table 5 Differences (ModAnd − FltAnd) of individual forcing averaged over the eastern equatorial Pacific (EEP, 5 °S – 5 °N, 90 ° – 130 °W) and the southeastern tropical Pacific (SETP, 15 ° – 20 °S, 80 ° – 100 °W) due to surface uplift.

	Boundary layer stability	Latent heat flux	Temperature change (ΔT) due to low level horizontal advection	ΔT (700 hPa) due to vertical advection	Shortwave cloud forcing	Longwave cloud forcing
EEP	+0.7 °C	–0.1 W/m^2	–0.1 °C/yr	0 °C/yr	–8.5 W/m^2	–0.1 W/m^2
SETP	+3.5 °C	–0.2 W/m^2	–0.6 °C/yr	+0.8 °C/yr	–1.8 W/m^2	–1.3 W/m^2

In comparison to FltAnd, the ESSTC is slower in the ModAnd experiment with reduced upward transport in the extra-equatorial region (10 ° – 15 °S) and downwelling in the southern subtropics (17 ° – 25 °S) (Figure 29b). At 15 °S, the vertical velocity of water flow is 1.4×10^{-2} cm s^{-1} in FltAnd at 285 m depth, which decreases to zero in ModAnd. This decrease does not follow the isopycnal slant towards the equator, but mainly occurs at 15 – 16 °S as a result of anomalous Ekman downwelling (Figure 29c). The weakening of the ESSTC reduces equatorward transport of cooler waters from the middle latitudes, resulting in warming (up to 2 °C) of the subtropical ocean below the thermocline (20 °C isotherm) (Figure 29b and d). This anomaly propagates northward to warm the entire subsurface EEP (below 40 m). Thermocline upwelling of this anomalously warm water serves as a negative feedback that compensates surface cooling due to greater low cloud amounts. Consistent with this result, the cooling response to Andean uplift is larger (up to 4 °C compared to 2 °C in our simulations) in simulations using an atmospheric model coupled to a mixed-layer ocean model that does not allow for ocean dynamical adjustment (Takahashi and Battisti, 2007a).

5.4.3 ENSO response to Andean uplift

The ENSO response to Andean uplift is nonlinear. The ENSO response to uplift to HlfAnd is quite small. The spectral density of the Niño 3.4 index peaks at the same period as FltAnd with a slight increase in the peak density (not shown). These small responses are consistent with minimal changes in climate state of the tropical Pacific between FltAnd and HlfAnd. In contrast, in the ModAnd and HghAnd cases, the ENSO cycle lengthens in

comparison to FltAnd as shown by a systematic shift in the mean spectral density of the Niño 3.4 indices to longer periods (Figure 30a).

Kirtman (1997) suggests a link between anomalies of zonal wind stress curl and the length of the ENSO cycle, in which the former generates off-equatorial Rossby waves that weaken the strength of the reflected Kelvin wave at the western boundary. This weakening of the reflected Kelvin wave reduces damping of ENSO-related equatorial SST anomalies. Our experiments are consistent with this idea. The lengthening of the ENSO cycle is accompanied by greater variability of monthly zonal wind stress curl in the northern region of the western and central Pacific (4 ° – 10 °N, 120 °E – 180 °) in ModAnd and HghAnd (Figure 30b), which feasibly favors off-equatorial Rossby waves in the north. Although uplift leads to a reduction in the variability of wind stress curl in the southern region (4 ° – 10 °S, 120 °E – 180 °), the differences in magnitude are relatively small. As a result, the net changes of zonal wind stress curl favor weaker reflected Kelvin waves and more persistent SST anomalies. Lengthening of the ENSO cycle explains the slight decrease in the total number of El Niño events with Niño 3.4 $\geq$ $0.5\sigma_{\text{Niño 3.4}}$: there are 40 events in FltAnd, 36 and 39 events in ModAnd and HghAnd.

In addition to fewer events, Andean uplift also influences the magnitude distribution of El Niño events. The El Niño events shifted slightly towards weaker magnitude side in HlfAnd (not shown). Both ModAnd and HghAnd feature significant reduction in strong El Niño events (Figure 30c). There are fewer strong events with Niño 3.4 values between 1.0 and 2.5 $\sigma_{\text{Niño 3.4}}$ (9 fewer events in both cases) but more mild events with values between 0.5 to 1.0 $\sigma_{\text{Niño 3.4}}$ (4 more events in ModAnd, 5 more in HghAnd, Figure 30c). The number of extremely warm El Niño events with Niño 3.4 values between 2.5 to 3.5 $\sigma_{\text{Niño 3.4}}$ increases slightly in both experiments (1 more in ModAnd, 2 more in HghAnd), but the increase is rather small and might be a result of internal variability independent of the Andean uplift. The response of La Niña events to uplift is less clear; there are no systematic changes in the numbers of weak or strong events (Figure 30a).

The reduction in number of strong El Niño events (1.0 $\sigma_{\text{Niño 3.4}} \leq$ Niño 3.4 $\leq$ 2.5 $\sigma_{\text{Niño 3.4}}$) is associated with seasonal SST cooling (Figure 31a-h) and upwelling intensification (Figure 31i-p, indicated by the red shade) in the central and western equatorial Pacific from December to March. The emergence of SST and upwelling anomalies during the December is accompanied by stronger equatorial easterly wind stress (discussed in detail below) in the central equatorial Pacific (between ~130 °E and 160 °W, Figure 31l). These seasonal adjustments, which can be

viewed as a strengthened Bjerknes feedback, suppress SST warming and thermocline deepening in the central equatorial Pacific during the austral summer when the majority of El Niño events (> 60 % of all experiments) reach highest Niño 3.4 values.

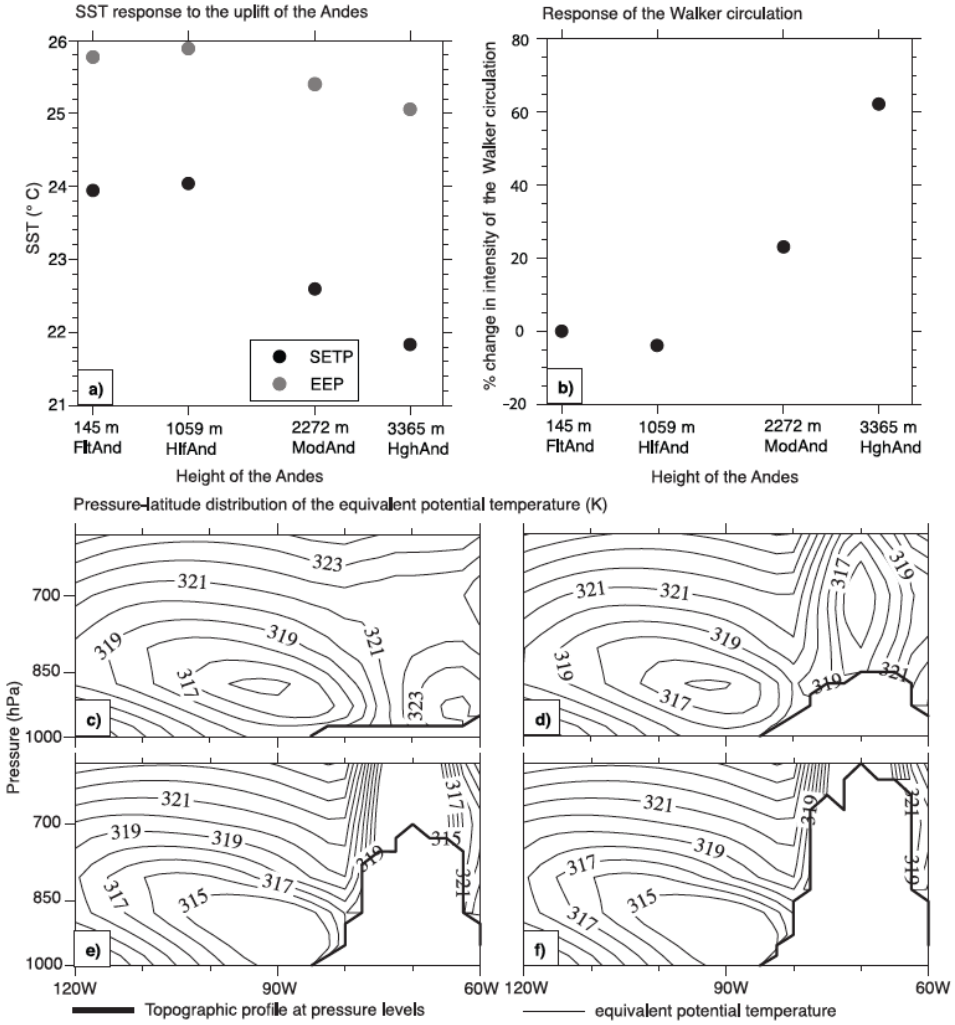

Figure 28 Climatological responses to the rise of Andes.
a) Mean SST in the southeastern tropical Pacific and the eastern equatorial Pacific. b) Changes in intensity (%) of the Walker circulation. c) - d) Zonal profile of equivalent potential temperature (K) averaged over 10 – 20 °S of different stages of Andean uplift. The strength of Walker circulation is measured by the sea level pressure difference between the western (5 °S – 5 °N, 80 ° − 160 °E) and eastern (5 °S – 5 °N, 160 ° − 80 °W) equatorial Pacific.

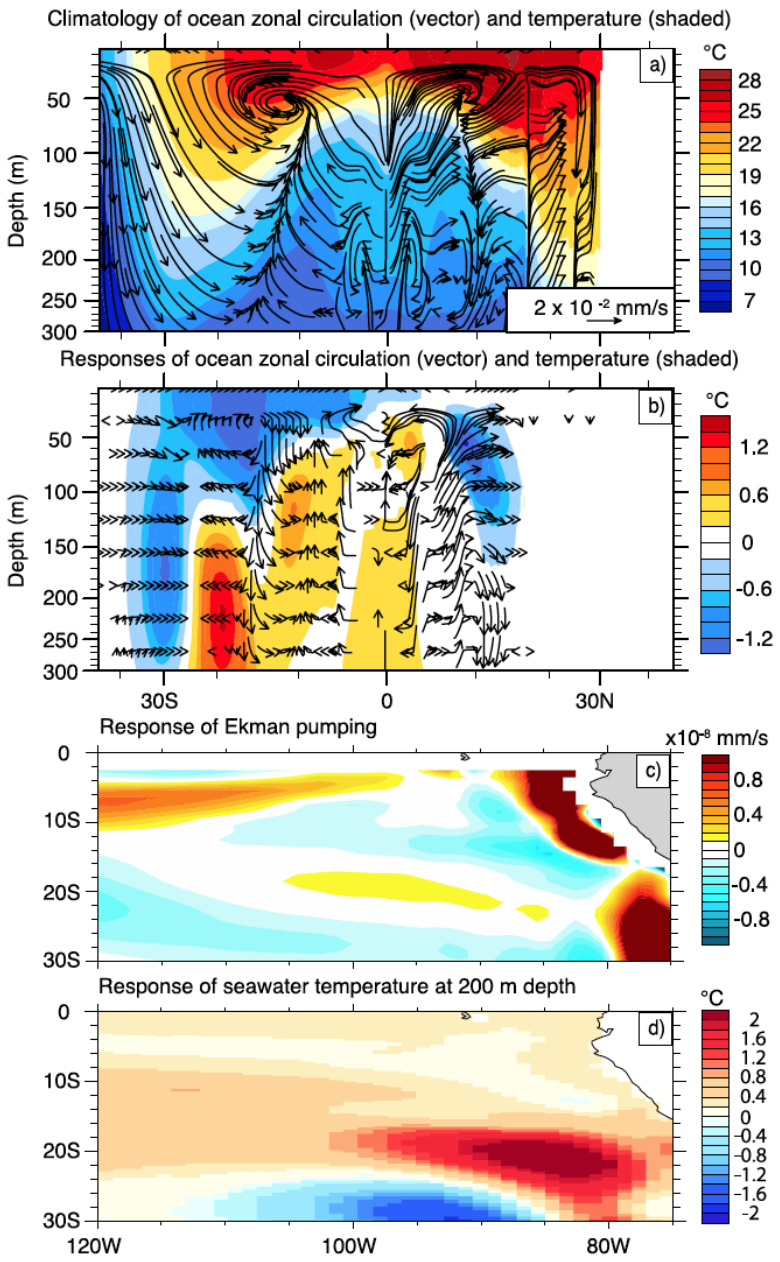

Figure 29 Ocean climatology and dynamical responses to Andean uplift in the eastern Pacific Ocean (100 ° − 80 °W).
a) Latitude-depth profile of the mean ocean circulation (vectors, 10^{-2} mm s^{-1}) and temperature (°C) of FltAnd. b-d) Horizontal climatological responses to Andean uplift: b) Subsurface temperature (°C) and circulation (10^{-2} mm s^{-1}); c) surface Ekman pumping speed (10^{-8} mm s^{-1}); and d) 200-m seawater temperature (°C) of the southern tropical Pacific (30 °S – 0 °). The vertical velocity of the ocean current is exaggerated by 10^5 times for visual purpose. The Ekman pumping speed within 2 °S – 0 ° is masked due to minimal Coriolis force around the equator.

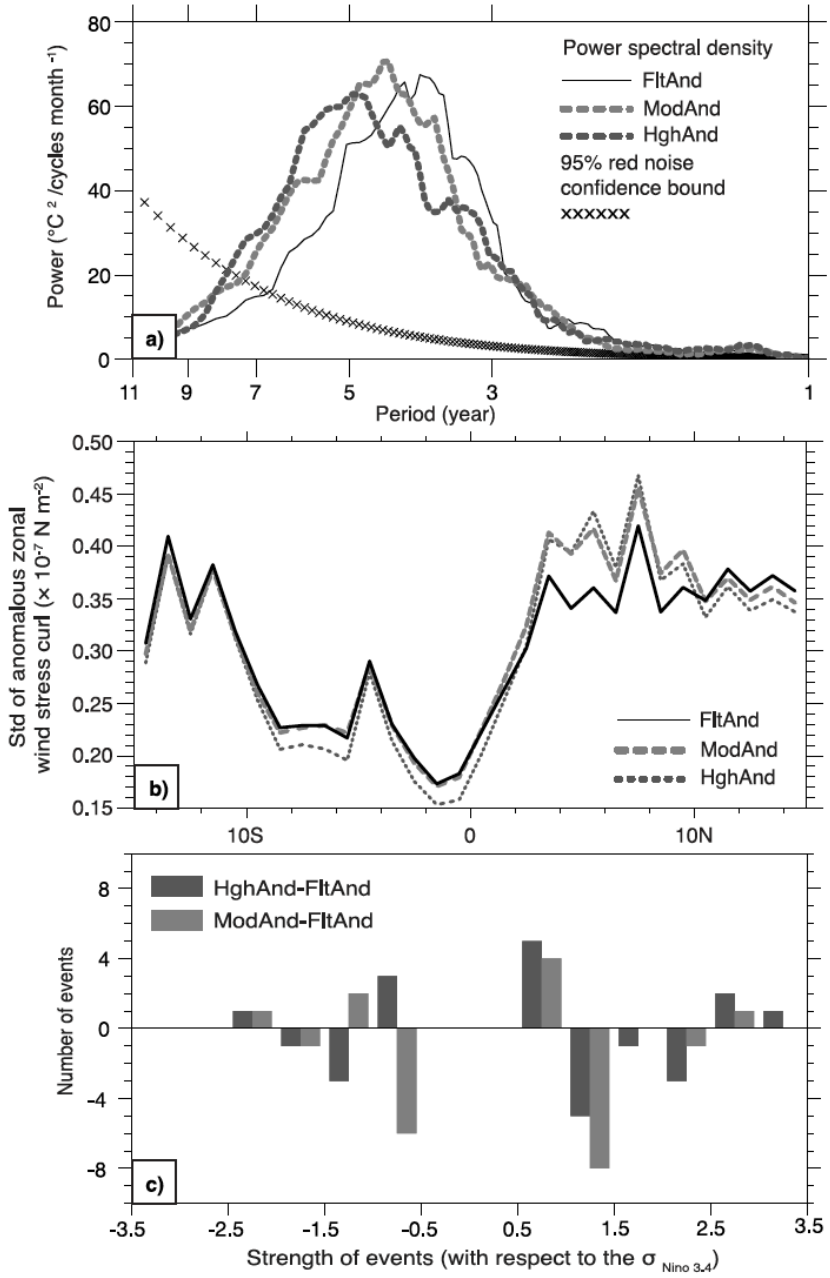

Figure 30 ENSO response to Andean uplift.
a) Spectral density of the Niño 3.4 index of the FltAnd, ModAnd and HghAnd; b) latitudinal distribution of standard deviation (Std) of anomalous monthly zonal wind stress curl averaged across the extra-equatorial western Pacific (120 °E - 180); c) difference from FltAnd in the number of El Niño and La Niña events in the ModAnd and HghAnd simulations. Magnitudes are binned in intervals of $0.5\sigma_{Niño3.4}$. In b), the seasonal cycle is removed from the time series of anomalous monthly zonal wind stress curl. The 9-yr high-pass Lanczos filter (Duchon et al., 1979) using 108 weights is applied to the Niño 3.4 index prior to the spectral analysis in a) to remove the decadal variation of the time series. The 95% red noise confidence bound is shown for FltAnd. Bounds are similar among experiments.

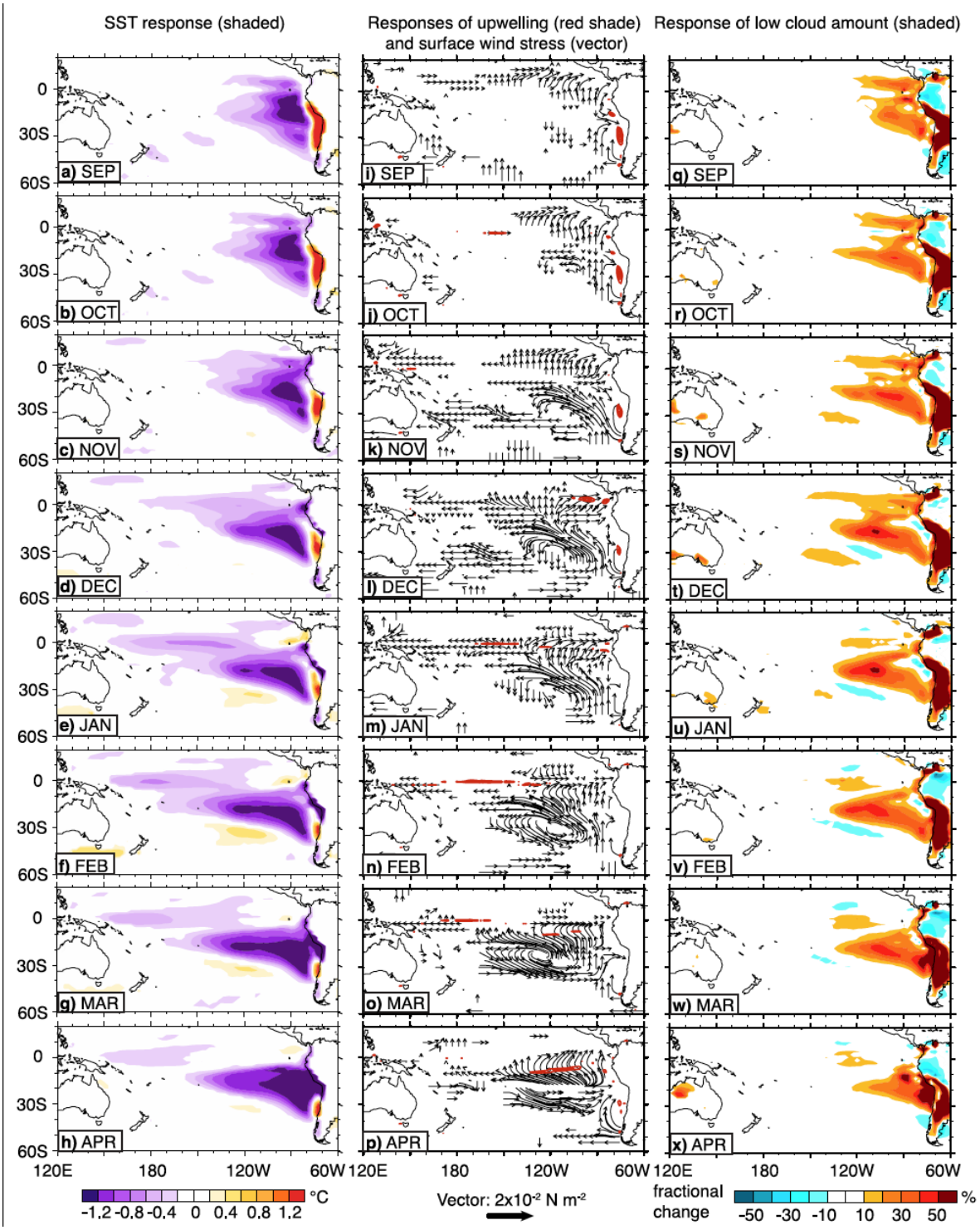

Figure 31 Austral warm season (September to April) monthly differences due to surface uplift (FltAnd – ModAnd).

a) - h) SST (°C, purple shading); i) - p) surface wind stress (vector) and upwelling (red shade: upwelling ≥ 0.2 mm s^{-1} averaged across the upper 50 m) (left column); and q) - x) percent change in low cloud cover (%, right column). Responses that passed consistency tests are shown.

5.4.4 Diabatic response of regional circulation

Strengthening of the Bjerknes feedback by uplift mainly occurs during the austral summer (Figure 31d-f and 6l-n) and coincides with enhanced SST cooling by low clouds (Figure 31t-v). This low cloud cooling effect persists throughout the year, but is greatest during the austral summer and extends further west (10 ° – 25 °S, 100 ° – 135 °W) from December to March (Figure 31t-w).

Enhanced low cloud formation in the summer is a result of uplift-induced diabatic circulation over the eastern central extra-equatorial Pacific. Andean uplift enhances the seasonal cycle of moist heating around the central Andes (600 hPa, 27.5 ° –10 °S, 83 ° – 58 °W) (Figure 32a). (Moist heating is calculated as the product of the rate of temperature changes due to moist processes and the specific heat capacity of the moist air, and includes both latent heat release during condensation and heat exchange during mixing processes associated with formation of clouds and precipitation.) The enhancement of moist heating, though persistent with elevation increase, is nonlinear and peaks between the HlfAnd and ModAnd runs. In ModAnd, the net moist heating in the summer is about twice the amount of that in FltAnd. This additional heating drives an anomalous zonal circulation centered at 450 hPa above the eastern extra-equatorial Pacific during the austral summer (Figure 32b), which is absent during the wintertime. Similar diabatic responses are reported from atmosphere-only simulations with simplified model physics (Rodwell and Hoskins, 2001; Takahashi and Battisti, 2007b).

The subsiding branch of the diabatic zonal circulation (shown by streamlines of anomalous flow in Figure 32b) overlies area of enhanced low cloud cover (Figure 31t-v) over the eastern extra-equatorial Pacific (10 ° – 20 °S, 90 ° – 135 °W). Subsidence increases the temperature and moisture contrast across the upper boundary layer, providing a stronger cap against deep moist convection. Stifling of cumulus convection is indicated by a reduction of high clouds between 120 ° – 135 °W (Figure 32c) and cooling and drying of the middle tropospheric column 700 – 250 hPa (Figure 32b). In turn, the reduction in moist convection leads to moisture trapping in the boundary layer and more low clouds (Figure 32c). The linkages between the diabatic circulation, low cloud cover and moist convection are summarized in Figure 32d.

SST cooling by changes in clouds and convection in the eastern central extra-equatorial Pacific (10 ° – 20 °S, 105 ° – 135 °W, Figure 31d-g) enhances the equatorial-extra-equatorial SST gradient during the summertime. This greater SST gradient drives southeasterly winds

towards the equator from the southern hemisphere (Figure 32d) (Lindzen and Nigam, 1987), strengthening the equatorial Easterlies.

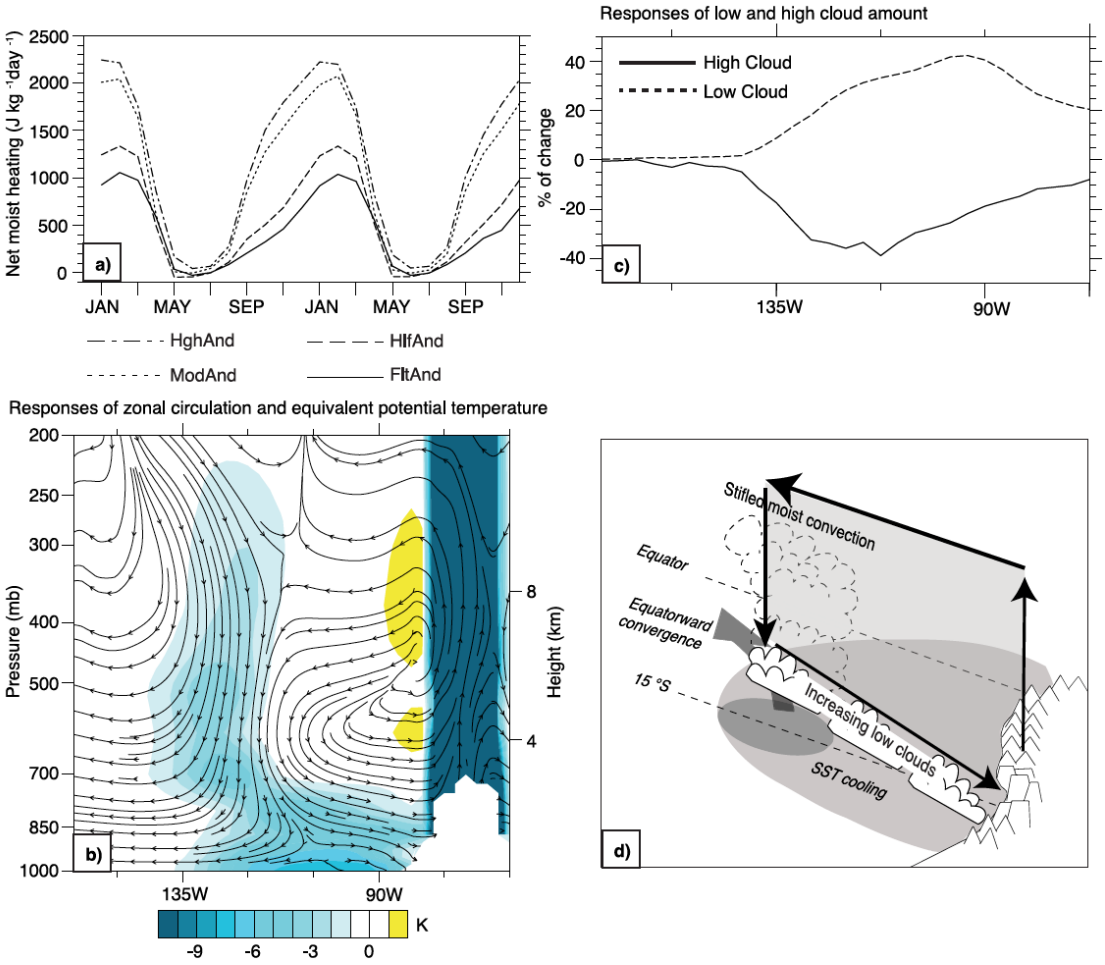

Figure 32 Moist heating and diabatic responses to Andean uplift.
a) Seasonal cycle of the net moist heating (J kg^{-1} day^{-1}) over the central Andes (700 hPa, 27.5 °–10.5 °S, 82.5 °–57.5 °W) for different stages of Andean uplift. b) Austral summer (December to February) zonal circulation (streamline) and equivalent potential temperature (K, shaded) differences (ModAnd – FltAnd) in the extra-equatorial (10 ° – 20 °S) eastern Pacific. c) Fractional change (%) in SETP (10 ° – 20 °S) low and high clouds due to uplift. d) Schematic diagram summarizing the atmospheric and oceanic responses to enhanced diabatic heating by Andean uplift during austral summer. Responses shown in b) have passed the consistency test.

5.5 Discussion

5.5.1 Comparison with paleoclimatic changes since the Late Miocene

Our simulated responses to Andean uplift are consistent with proxy observations from the Late Cenozoic. Here we compare in detail the climate response between our HghAnd and HlfAnd simulations, which represent ~2 km of surface uplift, with proxy records of late Miocene

(~13 Ma) and early Pliocene age (~ 5 Ma). These simulations were chosen for comparison because they best represent absolute estimates of paleo-elevations (Insel et al., 2012). Similar but slightly smaller responses are found by comparing our FltAnd and ModAnd simulations.

Surface uplift can partially explain SST and thermocline changes documented in proxy records from the northern EEP (6 °N, 86 °W) and Peruvian coast (16 °S, 80 °W) (Table 6). Northern EEP upwelling increases by 34% in HghAnd and is consistent with increasing radiolarian species richness since 13 Ma (LaRiviere et al., 2012). Along the northern Peruvian coast, simulated SSTs decrease by ~1.5 °C and upwelling increases by ~34%, which compares well with proxy records of cooling of 2.9 °C and increases in bio-productivity (Dekens et al., 2007). Andean uplift also produces a zonally asymmetric SST response of ~1°C in the equatorial Pacific, a feature observed in proxy records (Wara et al., 2005) but one that is not simulated by CCSM with many other mechanisms that have been hypothesized, including changes in greenhouse gas concentrations (Lee and Poulsen, 2006; Rosenbloom et al, 2013) and gateways (Jochum et al., 2011; Zhang et al., 2010). The equatorial SST asymmetry is crucial for development of a strong Walker circulation capable of sustaining the modern thermocline tilt and ENSO cycle. In this context, the uplift of the Andes may have been contributing to the triggering of the transition from an El Niño-like to modern climate.

The results of our simulations are also consistent with paleoclimate evidence of persistent ENSO activity through the Pliocene (Watanabe et al., 2012; Scroxton et al., 2011). Our simulations suggest the possibility that Andean uplift may have changed the frequency and magnitude of El Niño events. At the present time, marine proxy records do not have sufficient length or temporal resolution to evaluate this possibility.

Despite agreement between our simulations and proxy in several regions, the uplift induced responses are too small to completely explain past changes in the EEP. Uplift induced SST cooling, for example, only explains ~20 % of the reconstructed signal (Table 6). In addition, thermocline responses are an order of magnitude smaller than those documented by proxies. The major mismatch between proxy and model results occurs along the Central American coast (0 °, 82 °W). Foraminiferal records suggest strong sub-surface cooling and increase of biological productivity at this location (Table 6), which is not captured in our simulations. Uplift-induced responses are also too small to explain the oceanographic changes reported for the western cold tongue (3 °N, 118 °W) (Table 6), which are attributable to narrowing of the Indonesia (Rousselle

et al., 2013) and Central American seaways (Steph et al., 2010) through strengthening of the western Pacific warm pool (Nathan and Leckie, 2013) and the thermohaline overturning (Steph et al., 2010). Modeling of the climate response to changes in the Indonesia seaways (Jochum et al., 2009) and both climate modeling (Zhang et al., 2010) and tectonic reconstructions of Central American seaways (Monte et al., 2012), however, provide limited support for these hypotheses. Future studies are needed to explain these short-term developments of the Pacific cold tongue system.

5.5.2 Comparison with previous study

Previous studies indicate that uplift-induced surface cooling in the tropical southeastern Pacific is primarily caused by enhanced surface evaporation (Takahashi and Battisti, 2007a). In our experiments, stabilization of the boundary layer by subsidence and horizontal advection plays the dominant role in cooling. This difference likely emerges from different model treatments of boundary layer and low cloud formation. The intermediate complexity model used by Takahashi and Battisti (2007a) does not account for the environmental atmospheric responses to low cloud formation and boundary layer mixing, which are included in CCSM4 through parameterizations. The more detailed boundary layer representation in CCSM4 reduces drying of the boundary layer induced by large-scale entrainment of tropospheric subsidence, leading to moist conditions and less surface evaporation.

Uplift-induced SST cooling in the SETP is proposed to sustain the meridional and zonal asymmetry of the intertropical convergence zone (ITCZ) in the eastern Pacific (Takahashi and Battisti, 2007a, b). We observe a 10 – 20 % reduction in precipitation in the southern Pacific equatorial region (0 – 15 °S, 150 °E – 90 °W) under high Andes scenarios that is qualitatively consistent with Takahashi and Battisti (2007a, b) (> 50% reduction), but has a much smaller magnitude. Consequently, in our simulations, the Andean uplift only mildly affects the meridional asymmetry of the ITCZ and South Pacific Convergence zone (SPCZ). The uplift mainly affects the zonal asymmetry of the SPCZ during the austral summer through regional diabatic zonal circulation, which pushes the SPCZ westward ~15 ° (Figure 32b, as indicated by the stifled deep convection).

Table 6 Reconstructed* and simulated** SST and thermocline changes associated with the transition from El Niño-like to modern conditions at the eastern tropical Pacific since the Late Miocene.

		6 °N, 86 °W [a, b, c, d]		16 °S, 76 °W [c] (16 °S, 80 °W in the simulation***)	0°, 95 °W [e]	3 °S, 91 °W [f]	0 °, 82 °W [a]	1 °N, 111 °W [h]	3 °N, 118 °W [i]
Magn-itude of SST cooli-ng	Recons tructed	< 1 °C [a, b], 2 °C [d]		2.9 °C	~3.8 °C from Mg/Ca [e], 2.9 °C from U^{k7}_{37} [c]	~5 °C	~2 °C	5 – 6 °C	~4 °C
	Simulat ed	0.4 °C		2.2 °C	0.7 °C	1.2 °C	0.6 °C	0.7 °C	0.7 °C
Ther-mocli ne chan-ges	Recons tructed***	~6 °C subsurface cooling [a], increasing specie richness of radiolarian [d, g]		Increasing alkenone mass accumulation rate [c]	~ 5 °C increase of surface-subsurface ocean temperature contrast [e]	Increasing alkenone mass accumulation rate [f], deep water cooling [f]	~ 5 °C subsurface cooling [a]; increasing opal accumulati on rates [b]	NA	Episodic decrease of $\delta^{18}O_{seawater}$ may indicate shoaling of the thermocline at 10 – 11.5 Ma, 6 – 6.8 Ma and 4.6 – 3.6 Ma [h]
	Simu-lated	Thermo-cline depth****	-2.7 m	-11.3 m	-0.5 m	-0.9 m	+5 m	+0.4 m	+1.5 m
		Upwelli-ng*****	+36%	+32%	+1%	+2%	-19%	+2%	-5%

* Reconstructed SST and thermocline changes are summarized from a. Steph et al., (2010), b. Groeneveld et al. (2006), c. Dekens et al., (2007), d. LaRiviere et al., (2012), e. Wara et al, (2005), f. Lawrence et al., (2006), g. Kamikuri et al., (2009), h. Zhang et al., (2014), i. Rousselle et al., (2013).

** Simulated SST and thermocline changes are the consistent differences between HghAnd and HlfAnd averaged over 4 ° × 4 ° tile centered at the location of the proxy record.

*** The record at the Peru coast (16 °S, 76 °W) is moved 4 ° westward due to the under-representing of South American coastal line in the model (Figure 26).

**** Referring to Figure 27a, a 5 °C increase of surface-subsurface ocean temperature contrast indicates ~50 m decrease in thermocline depth.

***** The simulated thermocline depth is defined as the depth of the 20 °C isotherm.

****** The simulated responses of upwelling are reported with values just below the thermocline at 50 m for the first five locations, and at 80 m and 100 m for the last two locations due to westward deepening of the equatorial thermocline.

5.5.3 Model limitations

Our conclusions concerning the climate response to uplift of the Andes must be considered in the context of CCSM4's ability to realistically represent the Andean uplift and to reproduce the radiative effect of the tropical low clouds and ENSO cycle. Andean elevations are under-represented in our CCSM4 configuration. The highest elevation is 3903 m in the HghAnd,

which is lower by over 1000 m than the modern peaks surrounding the Bolivia Altiplano. In CCSM4, we find strengthened SST response to the Andean uplift from 1 km to 3 km. This SST response could be greater in a higher-resolution model with more detailed topographic changes. As a result, we consider our estimates to be conservative.

CCSM4 simulates low clouds and ENSO cycle reasonably well. However, low cloud coverage is still underestimated in subtropical regions worldwide. The net radiative effect of this bias is compensated through a model tuning process to strengthen the cloud radiative forcing (Nam et al., 2013). As a result, the low cloud bias may not substantially affect our simulated SST responses. The ENSO frequency is quite close to observations in a modern experiment with CCSM4 (Denser et al., 2012), and many atmosphere-ocean feedbacks crucial to ENSO dynamics are well represented by this model (Figure 13 in Bellenger et al., 2013). These results provide confidence that the simulated ENSO response to the Andean uplift is robust. However, CCSM4 still overestimates the overall strength of ENSO (Denser et al., 2012) and lacks triggering mechanisms for extremely strong El Niño events (McPhaden and Yu, 2012). Although these biases apply equally in all cases and, therefore, may not affect the simulated inter-experimental responses, it is likely that future advances in ENSO simulation may alter the details of our results.

5.6 Conclusions

Our simulations provide evidence that uplift of the Andes dissipates El Niño-like conditions in the eastern tropical Pacific through enhanced low cloud formation. An increase in low cloud amounts produces ~2 °C cooling in the SETP and ~0.8 °C cooling of the equatorial cold tongue region in response to 2 kms of uplift starting from a moderate Andean height (~ 1000 m). This cooling effect is partially attenuated by subthermocline warming due to spin-down of the shallow overturning cell at subtropical southeastern Pacific. Our simulations also provide support that Andean uplift may decrease ENSO frequency and the number of strong El Niño events. These changes result from the increasing variability of zonal wind stress curl north of the equator and the formation of diabatic zonal circulation in response to the Andean uplift during the austral summer.

The simulated response in CCSM 4 to Andean uplift can explain some, but not all, of the Late Cenozoic changes recorded by marine proxies. Uplift-induced climatic responses can account for ~50% of the reconstructed SST cooling along the Peru coast, strengthening of biological productivity in the northern EEP and increase in zonal SST and circulation asymmetry

across the equatorial Pacific. In sum, our study demonstrates that Andean uplift must be taken into account when considering the long-term evolution of the tropical Pacific.

5.7 Acknowledgements

This study was supported by NSF EAR grants 1019420 and 0907817 to C. Poulsen. We would like to acknowledge high-performance computing support from Yellowstone (ark:/85065/d7wd3xhc) provided by NCAR's Computational and Information Systems Laboratory, sponsored by the National Science Foundation. The Yellowstone mass storage system serves the data repository for simulation data used in this study. These data are available to readers upon request.

Bibliography

Alexander, M. A., Bladé, I., Newman, M., Lanzante, J. R., Lau, N. C., & Scott, J. D. (2002). The atmospheric bridge: The influence of ENSO teleconnections on air-sea interaction over the global oceans. J. Climate, 15(16), 2205-2231, doi: http://dx.doi.org/10.1175/1520-0442(2002)015<2205:TABTIO>2.0.CO;2.

Bellenger, H., E. Guilyardi, J. Leloup, M. Lengaigne, and J. Vialard (2013), ENSO representation in climate models: from CMIP3 to CMIP5, Clim Dyn, doi:10.1007/s00382-013-1783-z.

Brierley, C. M., A. V. Fedorov, Z. Liu, T. D. Herbert, K. T. Lawrence, and J. P. LaRiviere (2009), Greatly Expanded Tropical Warm Pool and Weakened Hadley Circulation in the Early Pliocene, Science, 323(5922), 1714–1718, doi:10.1126/science.1167625.

Bonham, S. G., Haywood, A. M., Lunt, D. J., Collins, M., & Salzmann, U. (2009). El Niño–Southern Oscillation, Pliocene climate and equifinality. Phil. Trans. R. Soc. A: Mathematical, Physical and Engineering Sciences, 367(1886), 127-156, doi: 10.1098/rsta.2008.0212.

Dekens, P. S., A. C. Ravelo, and M. D. McCarthy (2007), Warm upwelling regions in the Pliocene warm period, Paleoceanography, 22(3), PA3211, doi:10.1029/2006PA001394.

Deser, C., A. S. Phillips, R. A. Tomas, Y. M. Okumura, M. A. Alexander, A. Capotondi, J. D. Scott, Y.-O. Kwon, and M. OHBA (2012), ENSO and Pacific decadal variability in the community climate system model version 4, J. Climate, 25(8), 2622–2651, doi: http://dx.doi.org/10.1175/JCLI-D-11-00301.1.

Duchon, C. E. (1979), Lanczos Filtering in One and Two Dimensions, J. Appl. Meteor., 18(8), 1016–1022, doi:10.1175/1520-0450(1979)018<1016:LFIOAT>2.0.CO;2.

Ehlers, T. A., and C. J. Poulsen (2009), Influence of Andean uplift on climate and paleoaltimetry estimates, Earth Planet. Sci. Lett., 281(3), 238–248, doi: :10.1016/j.epsl.2009.02.026.

Fedorov, A. V. (2006), The Pliocene Paradox (Mechanisms for a Permanent El Nino), Science, 312(5779), 1485–1489, doi:10.1126/science.1122666.

Fedorov, A. V., C. M. Brierley, and K. Emanuel (2010), Tropical cyclones and permanent El Niño in the early Pliocene epoch, Nature, 463(7284), 1066–1070, doi:10.1038/nature08831.

Fedorov, A. V., C. M. Brierley, K. T. Lawrence, Z. Liu, P. S. Dekens, and A. C. Ravelo (2013), Patterns and mechanisms of early Pliocene warmth, Nature, 496(7443), 43–49, doi:10.1038/nature12003.

Galeotti, S., A. von der Heydt, M. Huber, D. Bice, H. Dijkstra, T. Jilbert, L. Lanci, and G. J. Reichart (2010), Evidence for active El Nino Southern Oscillation variability in the Late Miocene greenhouse climate, Geology, 38(5), 419–422, doi:10.1130/G30629.1.

Garzione, C. N., G. D. Hoke, J. C. Libarkin, S. Withers, B. MacFadden, J. Eiler, P. Ghosh, and A. Mulch (2008), Rise of the Andes, Science, 320(5881), 1304–1307, doi:10.1126/science.1148615.

Gent, P. R., G. Danabasoglu, L. J. Donner, M. M. Holland, E. C. Hunke, S. R. Jayne, D. M. Lawrence, R. B. Neale, P. J. Rasch, and M. Vertenstein (2011), The community climate system model version 4, J. Climate, 24(19), 4973–4991, doi:10.1175/2011JCLI4083.1.

Gent, P. R., S. G. Yeager, R. B. Neale, S. Levis, and D. A. Bailey (2009), Improvements in a half degree atmosphere/land version of the CCSM, Clim Dyn, 34(6), 819–833, doi:10.1007/s00382-009-0614-8.

Ghosh, P. (2006), Rapid Uplift of the Altiplano Revealed Through 13C-18O Bonds in Paleosol Carbonates, Science, 311(5760), 511–515, doi:10.1126/science.1119365.

Gregory-Wodzicki, K. M. (2000), Uplift history of the Central and Northern Andes: a review, Geol. Soc. Am. Bull., 112(7), 1091–1105, doi:10.1130/0016-7606(2000)112.

Gu, D. (1997), Interdecadal Climate Fluctuations That Depend on Exchanges Between the Tropics and Extratropics, Science, 275(5301), 805–807, doi:10.1126/science.275.5301.805.

Haywood, A. M., P. J. Valdes, and V. L. Peck (2007), A permanent El Niño-like state during the Pliocene? Paleoceanography, 22(1), PA1213, doi:10.1029/2006PA001323.

Insel, N., C. J. Poulsen, T. A. Ehlers, and C. Sturm (2012), Response of meteoric δ18O to surface uplift — Implications for Cenozoic Andean Plateau growth, Earth Planet. Sci. Lett., 317-318, 262–272, doi:10.1016/j.epsl.2011.11.039.

Jochum, M., B. Fox Kemper, P. H. Molnar, and C. Shields (2009), Differences in the Indonesian seaway in a coupled climate model and their relevance to Pliocene climate and El Niño, Paleoceanography, 24(1), PA1212, doi:10.1029/2008PA001678.

Kamikuri, S.-I., I. Motoyama, H. Nishi, and M. Iwai (2009), Evolution of Eastern Pacific Warm Pool and upwelling processes since the middle Miocene based on analysis of radiolarian assemblages: Response to Indonesian and Central American Seaways, Palaeogeogr. Palaeoclimatol. Palaeoecol., 280(3-4), 469–479, doi:10.1016/j.palaeo.2009.06.034.

Kirtman, B. P. (1997), Oceanic Rossby wave dynamics and the ENSO period in a coupled model,

J. Climate, 10(7), 1690–1704, doi: http://dx.doi.org/10.1175/1520-0442(1997)010<1690:ORWDAT>2.0.CO;2.

Klinger, B. A., J. P. McCreary Jr, and R. Kleeman (2002), The Relationship between Oscillating Subtropical Wind Stress and Equatorial Temperature*, J. Phys. Oceanogr., 32(5), 1507–1521, doi:10.1175/1520-0485(2002)032<1507:TRBOSW>2.0.CO;2.

LaRiviere, J. P., A. C. Ravelo, A. Crimmins, P. S. Dekens, H. L. Ford, M. Lyle, and M. W. Wara (2012), Late Miocene decoupling of oceanic warmth and atmospheric carbon dioxide forcing, Nature, 486(7401), 97–100, doi:10.1038/nature11200.

Lawrence, K. T., Z. Liu, and T. D. Herbert (2006), Evolution of the Eastern Tropical Pacific Through Plio-Pleistocene Glaciation, Science, 312(5770), 79–83, doi:10.1126/science.1120395.

Lee, S.-Y., and C. J. Poulsen (2006), Sea ice control of Plio–Pleistocene tropical Pacific climate evolution, Earth Planet. Sci. Lett., 248(1-2), 253–262, doi:10.1016/j.epsl.2006.05.030.

Leier, A., N., McQuarrie, C. Garzione, and J. Eiler (2013), Stable isotope evidence for multiple pulses of rapid surface uplift in the Central Andes, Bolivia, Earth Planet. Sci. Lett., 49–58, doi:10.1016/j.epsl.2013.04.025.

Lindzen, R. S., and S. Nigam (1987), On the Role of Sea Surface Temperature Gradients in Forcing Low-Level Winds and Convergence in the Tropics, J. Atmos. Sci., 44(17), 2418–2436, doi:10.1175/1520-0469(1987)044<2418:OTROSS>2.0.CO;2.

McPhaden, M. J., and X. Yu (2012), Equatorial waves and the 1997-98 El Niño, Geophys. Res. Lett., 26(19), 2961–2964, doi:10.1029/1999GL004901.

Molnar, P., and M. A. Cane (2007), Early Pliocene (pre–Ice Age) El Niño–like global climate: Which El Niño? Geosphere, 3(5), 337, doi:10.1130/GES00103.1.

Montes, C., G. Bayona, A. Cardona, D. M. Buchs, C. A. Silva, S. Morón, N. Hoyos, D. A. Ramírez, C. A. Jaramillo, and V. Valencia (2012), Arc-continent collision and orocline formation: Closing of the Central American seaway, J. Geophys. Res.: Solid Earth (1978–2012), 117(B4), B04105, doi:10.1029/2011JB008959.

Nam, C., S. Bony, J. L. Dufresne, and H. Chepfer (2012), The “too few, too bright”tropical low-cloud problem in CMIP5 models, Geophys. Res. Lett., 39, L21801, doi:10.1029/2012GL053421.

Nathan, S. A., and Leckie, R. M. (2009). Early history of the Western Pacific Warm Pool during

the middle to late Miocene (~ 13.2–5.8 Ma): Role of sea-level change and implications for equatorial circulation. Palaeogeogr. Palaeoclimatol. Palaeoecol., 274(3), 140-159, doi: 10.1016/j.palaeo.2009.01.007.

Poulsen, C. J., T. A. Ehlers, and N. Insel (2010), Onset of Convective Rainfall During Gradual Late Miocene Rise of the Central Andes, Science, 328(5977), 490–493, doi:10.1126/science.1185078.

Rodwell, M. J., and B. J. Hoskins (2001), Subtropical anticyclones and summer monsoons, J. Climate, 14(15), 3192–3211, doi: http://dx.doi.org/10.1175/1520-0442(2001)014<3192:SAASM>2.0.CO;2.

Rosenbloom, N. A., B. L. Otto-Bliesner, E. C. Brady, and P. J. Lawrence (2013), Simulating the mid-Pliocene Warm Period with the CCSM4 model, Geosci. Model Dev., 6(2), 549–561, doi:10.5194/gmd-6-549-2013.

Rousselle, G., Beltran, C., Sicre, M. A., Raffi, I., and De Rafelis, M. (2013), Changes in sea-surface conditions in the Equatorial Pacific during the middle Miocene–Pliocene as inferred from coccolith geochemistry. Earth Planet. Sci. Lett., 361, 412-421, doi:10.1016/j.epsl.2012.11.003.

Scroxton, N., S. G. Bonham, R. Rickaby, S. Lawrence, M. Hermoso, and A. M. Haywood (2011), Persistent El Niño–Southern Oscillation variation during the Pliocene Epoch, Paleoceanography, 26, PA2215, doi:10.1029/2010PA002097.

Steph, S., R. Tiedemann, M. Prange, J. Groeneveld, M. Schulz, A. Timmermann, D. Nürnberg, C. Rühlemann, C. Saukel, and G. H. Haug (2010), Early Pliocene increase in thermohaline overturning: A precondition for the development of the modern equatorial Pacific cold tongue, Paleoceanography, 25(2), PA2202, doi:10.1029/2008PA001645.

Takahashi, K., and D. S. Battisti (2007a), Processes Controlling the Mean Tropical Pacific Precipitation Pattern. Part I: The Andes and the Eastern Pacific ITCZ, J. Climate, 20(14), 3434–3451, doi:10.1175/JCLI4198.1.

Takahashi, K., and D. S. Battisti (2007b), Processes Controlling the Mean Tropical Pacific Precipitation Pattern. Part II: The SPCZ and the Southeast Pacific Dry Zone, J. Climate, 20(23), 5696–5706, doi:10.1175/2007JCLI1656.1.

Trenberth, K. E. (1997), The definition of El Niño, Bull. Amer. Meteor. Soc., 78(12), 2771–2777, doi: http://dx.doi.org/10.1175/1520-0477(1997)078<2771:TDOENO>2.0.CO;2.

Vecchi, G. A., and B. J. Soden (2007), Global warming and the weakening of the tropical circulation, J. Climate, 20(17), 4316–4340, doi:10.1175/JCLI4258.1.

Wara, M. W. (2005), Permanent El Nino-Like Conditions During the Pliocene Warm Period, Science, 309(5735), 758–761, doi:10.1126/science.1112596.

Watanabe, T. et al. (2012), Permanent El Niño during the Pliocene warm period not supported by coral evidence, Nature, 471(7337), 209–211, doi:10.1038/nature09777.

Wood, R., and C. S. Bretherton (2004), Boundary Layer Depth, Entrainment, and Decoupling in the Cloud-Capped Subtropical and Tropical Marine Boundary Layer, J. Climate, 17(18), 3576–3588, doi:10.1175/1520-0442(2004)017<3576:BLDEAD>2.0.CO;2.

Xu, H., Y. Wang, and S.-P. Xie (2004), Effects of the Andes on Eastern Pacific Climate: A Regional Atmospheric Model Study*, J. Climate, 17(3), 589–602, doi: http://dx.doi.org/10.1175/1520-0442(2004)017<0589:EOTAOE>2.0.CO;2.

Zhang, X. et al. (2010), Changes in equatorial Pacific thermocline depth in response to Panamanian seaway closure: Insights from a multi-model study, Earth Planet. Sci. Lett., 317-318, 76–84, doi:10.1016/j.epsl.2011.11.028.

Zhang, Y. G., Pagani, M., & Liu, Z. (2014). A 12-Million-Year Temperature History for the Tropical Pacific Ocean. Science, 344(6179), 84-87, doi: 10.1126/science.1246172.

Chapter 6
Conclusion and implications

This dissertation addresses three subjects regarding climate-topography interactions. First, I model regional climate and isotopic responses of precipitation ($\delta^{18}O_p$) to the uplift of the North American Cordillera during the early Cenozoic (55 – 40 Ma). Second, I explore isotopic and hydrological responses to large-scale changes in climate structure and surface boundary conditions during the Neogene (since ~23 Ma). Finally, I simulate tropical Pacific climate responses to late Cenozoic (since ~15 Ma) Andean uplift. Based on simulations with global climate models, this work provides new estimates for the Cenozoic climate history of the North and South American Cordilleras, and improves constraints on the elevation history of the North American Cordillera. This section summarizes major findings and highlights implications for future studies.

6.1 Summary of results

The following summary provides answers to the questions that have motivated this dissertation:

1) How does Eocene $\delta^{18}O_p$ respond to changes in regional atmospheric circulation and precipitation under different elevation scenarios of the North American Cordillera? What are the implications for $\delta^{18}O_p$ based paleoaltimetry?

Chapter 2 investigates these questions. A global climate model (GCM) with water isotopologue tracking functions (ECHAM5-wiso) is used to quantify climate and isotopic responses of precipitation ($\delta^{18}O_p$) to the proposed topographic hypothesis of Eocene north-to-south uplift of the western North American Cordillera. Model outputs show complex hydrological responses to the uplift, including changes in precipitation phase and type, vapor mixing and recycling, and variations in moisture sources. These responses vary between the windward (western) and leeward (eastern) sides of the Cordillera, (Figure 33).

On the windward side, the uplift leads to strong upslope flow and increases the amount of snowfall. $\delta^{18}O_p$ responses to individual changes are significant (up to 7 ‰), but responses to

upslope flow and snowfall counteract each other. On the leeward side, the moisture source switches from pre-uplift westerlies to continental inflow in the northern Cordillera and a mixture of continental and proto-Gulf of Mexico inflow in the central and southern Cordillera. Concurrently, recycling of water vapor and moist convection are enhanced on the leeward side. Changes in moisture source produce net $\delta^{18}O_p$ depletion of 3 – 6 ‰ compared to a uniform westerly source. This depletion is compensated by ^{18}O-enrichment due to increased vapor recycling and convective mixing, which brings up the lower level more ^{18}O-enriched water vapor to high-elevation flanks.

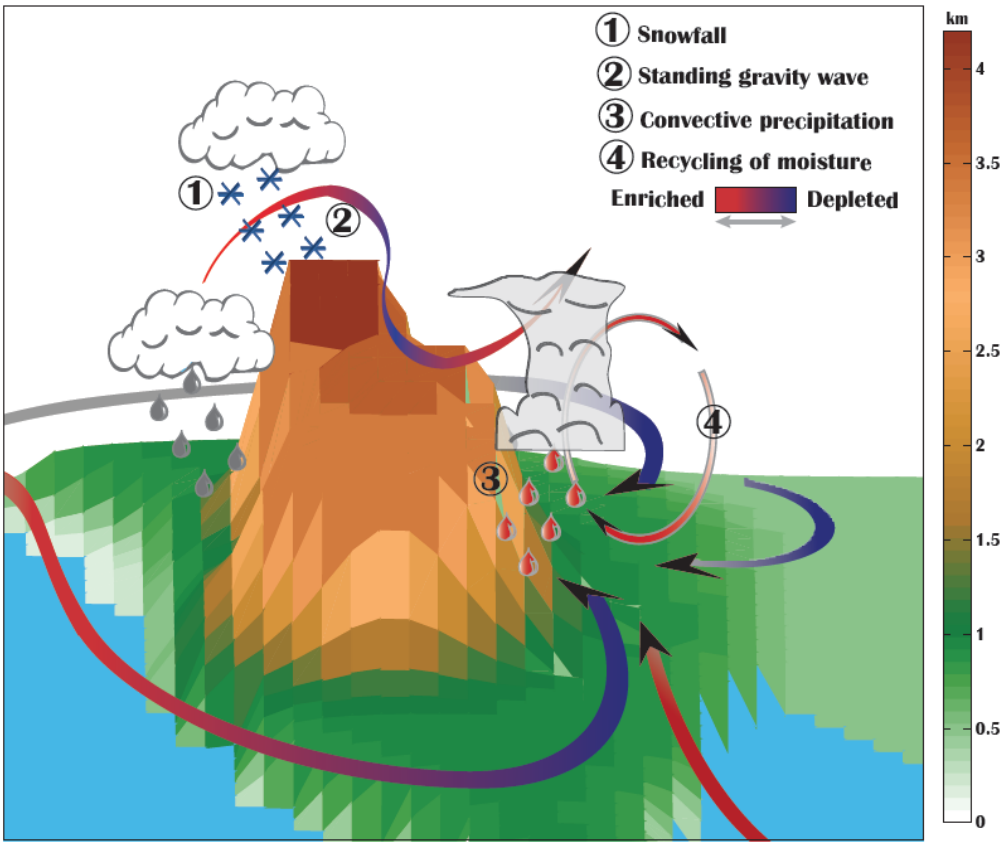

Figure 33 Diagram of precipitation and circulation responses to the Eocene uplift of the western North American Cordillera and their isotopic variations from expected values determined by a Rayleigh distillation model for moist adiabatic condensation.

Due to compensation of $\delta^{18}O_p$ variations among different hydrological responses, hypsometric estimates derived from GCM simulations of $\delta^{18}O_p$ suggest 3 – 4 km paleoelevations of the Cordilleran hinterland. The hypsometric estimates are similar to previous uplift estimates based on the Rayleigh distillation model (RDM). RDM assumes a one-dimensional rainout

process of ^{18}O during moist adiabatic lifting and condensation of an air parcel. Both previous and my estimates provide strong support for the early Cenozoic uplift of the North American Cordillera. However, consistent elevation estimates by the GCM and RDM are coincidental, which likely vary under different topographic and climate conditions. Thus the agreement between GCM and RDM results should not be considered as universal. The climate model simulates three-dimensional physical and dynamical responses to the uplift, while the one-dimensional RDM ignores most of these features and operates without a dynamical underpinning.

2) **How do changes in temperature and moist enthalpy between modern and Eocene climate states and amongst different uplift scenarios affect fossil leaf paleoaltimetry estimates of the North American Cordillera?**

Chapter 3 compares distributions of temperature and moist enthalpy between Early-to-Middle Eocene (55 – 40 Ma) simulations and modern distributions over the western U.S. The Eocene simulations are performed with a range of prescribed elevation scenarios. Simulation results suggest that Eocene lapse rates of temperature and moist enthalpy were similar to moist adiabatic rates (~5 °C km^{-1} and 9.8 kJ km^{-1}), i.e. rates determined by the conservation of moist static energy of an air parcel. In contrast, present-day rates (4.0 – 6.8 °C km^{-1} and 7.1 – 8.4 kJ km^{-1}) over the western U.S. are different due to the drying of the lower troposphere and the large-scale mixing with air masses from higher latitudes. The temperature and moist enthalpy variations due to these effects are small in the warm and moist Eocene climate of Western North America. Circulation responses to Cordilleran uplift include generation of mountain gravity waves and intensification of a leeward monsoonal circulation. These responses are non-linear and elevation dependent: small in low-to-moderate elevation cases (1 – 3-km case), but significant (up to 8 °C and 10 kJ) in high-elevation cases (peak elevations > 3 km). Ignoring these responses could result in kilometer-scale elevation misinterpretations by fossil leaf paleoaltimetry.

In order to overcome these uncertainties, paleoelevations of the North American Cordillera are estimated through direct comparison between proxy and simulated Eocene temperature and moist enthalpy. Simulations match proxy reconstructions at prescribed elevations of ~2 – 3 km for Cordilleran hinterland and ~1 – 2 km for the adjacent Laramide foreland basins. The new estimates of hinterland elevations by fossil leaf moist enthalpy (~3 km) and the elevation contrast between the hinterland and foreland basins by both fossil leaf moist

enthalpy and temperature are close to previous $\delta^{18}O$-based paleoelevation estimates (3 – 4 km of the hinterland and low-elevation foreland basins). Our findings support the hypothesis that the North American Cordillera is high during the Eocene, with a strong elevation gradient between the hinterland and Laramide foreland basins.

3) **How do large-scale changes in climate structure and surface conditions affect estimates of western U.S. elevation loss based on Neogene (since ~23 Ma) $\delta^{18}O$ records?**

Following early Cenozoic uplift of the western North American Cordillera, extension and subsidence occurred over this region during the Neogene (since ~23 Ma). **Chapter 4** investigates the history of elevation loss during this time based on proxy $\delta^{18}O$ records from the western U.S. These records display long-term $\delta^{18}O$ enrichment trends, which are often interpreted to reflect elevation loss through time. However, they may have also documented large-scale Neogene changes in climates, vegetation, and global geographical and topographical conditions outside of the North America.

Model simulations suggest that strengthening of the equator-to-pole temperature gradient during the Neogene leads to strong $\delta^{18}O$ enrichment (3 – 4 ‰) of soil water ($\delta^{18}O_{sw}$) in the Northern Sierra Nevada and central Rockies. A greater equator-to-pole temperature gradient induces a stronger (~20 %) Hadley circulation, resulting in enhanced evaporation of surface- and rain-water in the subsiding branch of the Hadley circulation. These enrichment responses are strongest across the subtropical ocean and continental areas proximal to the coast, including the northern Sierra Nevada and central Rockies.

The $\delta^{18}O$ enrichment response to Hadley circulation strengthening could explain 50 to 100% of proxy $\delta^{18}O$ enrichment in the Northern Sierra Nevada and Central Rockies. In contrast, the proxy enrichment over the northern Great Basin is less affected by Neogene environmental changes. The proxy enrichment over this region suggests ~1 – 1.4 km elevation loss of the northern Great Basin. By adding this amount to current Great Basin elevations, we estimate a pre-extension Cordilleran hinterland elevation of 3 – 4 km. This estimate is consistent with Eocene fossil leaf moist enthalpy and stable isotope-based estimates, suggesting localized Neogene extension across the early Cenozoic Cordilleran hinterland with muted elevation changes in the surrounding northern Sierra Nevada and central Rockies.

4) How does the Andean uplift influence the tropical ocean, and whether it has contributed to the development of the modern asymmetric tropical climate state?

Chapter 5 answers this question by quantifying the responses of tropical Pacific climate to surface uplift of the Andes. A series of coupled atmosphere-ocean simulations are conducted with peak Andean surface elevations increasing from ~0.1-km, to 1-km, 2-km, and 3-km, representing the flat Andes, half, and default model elevations (due to grid-scale averaging), and close-to-modern elevations of the Andean plateau, respectively.

Simulations suggest that Andean uplift from ~1 km to 3 km cools eastern tropical SSTs by ~0.8 – 2 °C and strengthens the Walker circulation by up to 60%. The western tropical Pacific climate, however, shows little change. SST cooling in the eastern tropical Pacific is primarily a response to increasing low-cloud coverage and the associated radiative cooling. This cooling response only occurs when peak Andean elevations exceed 2 km. However, the magnitude of the response is attenuated by sub-thermocline warming, resulting from weakening of the shallow meridional overturning cell between the tropics and subtropics. Additionally, simulations exhibit distinct El Niño responses to the Andean uplift. Specifically, mild El Niño events increase at the expense of anomalously strong events, which corresponds to a seasonal maximum of enhanced eastern tropical Pacific low-cloud formation during the austral summer. This summer low-cloud response damps the magnitude of El Niño events through seasonally enhanced SST cooling (60% of events reach mature phase during austral summer).

The SST cooling induced by Andean uplift can explain one-half of the Neogene SST cooling in the eastern tropical Pacific documented by proxies. Simulated responses of equatorial upwelling and thermocline depth to uplift are small, indicating that uplift alone can not fully explain ocean dynamical changes of the eastern tropical Pacific. Nonetheless, Andean uplift is one of the few mechanisms that can explain the long-term increase in zonal SST contrast between the eastern and western tropical Pacific. Therefore, the uplift must be taken into account when considering the late Cenozoic evolution of the tropical Pacific climates.

6.2 Implications

6.2.1 Implications to Cenozoic tectonic history of western North America

The work presented here supports the development and north-to-south migration of an early Cenozoic (49 to 28 Ma) Andean-type high plateau in western North America (Chamberlain et al., 2012; Mix et al., 2011). This wave of 3–4 km topography roughly coincides with Eocene north-to-south migration of volcanic front and core complex formation in the Cordilleran hinterland, but postdates Mesozoic shortening of the Cordilleran Orogenic wedge and the Late

Cretaceous-Paleogene Laramide orogeny. The timing and order of these events suggests that the driving forces of the Eocene uplift may have originated from mantle lithosphere instead of crust, which could be associated with roll-back of the Farallon plate (Humphreys, 1995; Smith et al., 2014) and/or thermal erosion of dense lower crustal root (Schmandt and Humphreys, 2010). This topographic scenario of the early Cenozoic high plateau indicates the lack of thick crust support for the high plateau, which rejects the hypothesis of Neogene (since ~23 Ma) extension driven by gravitational collapse of an overly thickened crust. Instead, thinning of the mantle lithosphere likely drives the extension. The pattern of elevation loss reconstructed from the Neogene $\delta^{18}O$ and δD records is consistent with this hypothesis. Maximal loss is found in the northern Great Basin with minimal (< 1 km) changes in the surrounding northern Sierra Nevada and Central Rockies. This pattern shows strong areal correspondence between the early Cenozoic hinterland uplift and Neogene extension, which could be explained as different phases of surface response to thinning of the mantle lithosphere and subsequent extension.

6.2.2 Implications for understanding the Cenozoic terrestrial $\delta^{18}O$ archive from the western U.S.

The presented work provides compelling evidence that Cenozoic terrestrial $\delta^{18}O$ archives have documented both climate variability and paleoelevations changes of western North America. Our model results provide general guidance for understanding the $\delta^{18}O$ archives over this region. The terrestrial $\delta^{18}O$ variations under early Cenozoic greenhouse climates are likely dominated by elevation changes. The simulated Eocene $\delta^{18}O$ shows clear stratification similar to RDM predictions along slopes of the North American Cordillera. However, this coincidence does not justify the use of RDM for paleoaltimetry. We have shown that during the early Cenozoic, lower tropospheric stratification is very different from that of the present-day. Atmospheric circulation and precipitation responses to the uplift of North American Cordillera are also complex, and promote significant isotopic variations. As a result, accurate paleoaltimetry estimates will require a quantification of these isotopic variations in response to changing climate state, atmospheric circulation pattern, and precipitation conditions, which can be provided by climate model simulations. In contrast to records from the early Cenozoic, Neogene terrestrial $\delta^{18}O$ records likely have documented changes in both elevation and large-scale climate conditions. Regional $\delta^{18}O$ responses to large-scale circulation changes are strong and heterogeneous. These responses must be removed from the $\delta^{18}O$ records prior to estimating paleoelevations. Therefore,

independent methods of constraining these responses, such as climate modeling, are needed for paleoaltimety studies.

6.3 Limitations and future work

6.3.1 Limitations

Results in this dissertation are derived from climate model simulations and comparisons with proxy records. The accuracy of our understanding is closely connected with current model resolution and paleoclimate simulation skills. The horizontal resolutions of our simulations (~1 ° and 2 °) are higher than in most previous studies. Yet, topographic height and steepness (at 2 ° resolution) as well as detailed topographic features, such as local basins and reliefs (at both 1 ° and 2 ° resolution) are still underrepresented. This underrepresentation could affect our results in two ways. Firstly, regional climate variability and responses to the uplift may be underestimated due to insufficient resolution. For the Andes, the 2° resolution model underestimates both areal elevations at the peak (by up to 1 km), and the topographic steepness between the western flank and eastern tropical Pacific. As a result, the climate forcings of uplift induced alpine diabatic heating and changes in low-level airflow path could be underestimated. For western North America, local hydrological responses to the uplift of the North American Cordillera may be underestimated because of the unresolved local topographic gradients between the high reliefs and intermountain basins.

Secondly, inclusion of paleo-reliefs, basins, and drainage networks in the model boundary conditions would provide more direct comparisons with terrestrial records from sedimentary basins, paleo-lakes, and riverbanks. These proxy records may have recorded distinct microenvironments rather than areal averaged conditions. Among Eocene records from the western U.S., lacustrine $\delta^{18}O$ records and fossil leaf temperatures from Laramide foreland basins show anomalously enriched $\delta^{18}O$ and warmer temperatures in comparison to the surroundings, suggesting distinct warm and evaporative conditions of these intermountain basins. Consequently, different climate-elevation relationships may be needed for paleoaltimetric studies that utilize these records. Future studies using high-resolution modeling tools, such as regional models, and detailed reconstructions of surface boundary conditions, are needed to improve paleoaltimetry estimates that are based upon records from these basins.

Further, simulation skill of past climates is determined by the ability of climate models to accurately represent atmospheric dynamics and physics, and by our understanding of

paleoclimate forcings. The skill of model to simulate clouds and moist convection, and their interactions with broader scale atmospheric circulation and temperature patterns, are a key to reported responses to surface uplift. Model biases in representing these processes likely affect results presented in this dissertation. For example, simulated Eocene climate is drier than indicated by proxy reconstructions; the precipitation amount is within 30% of the lower bound of reconstructions of the western U.S. Underestimates of precipitation may indicate an overall less energetic moist convection in the model. Simulated Eocene temperature stratification, circulation and precipitation responses that are closely linked to the moist convection, including alpine cooling rate, monsoonal circulation, leeside convective precipitation, and vapor recycling, may have been underestimated. Likewise, the current generation of coupled atmosphere-ocean models tends to underestimate tropical low cloud coverage (Nam et al., 2012). This may result in underestimates of low cloud responses and the associated SST cooling to the Andean uplift. Future improvements in model dynamics and physics will provide more accurate understanding of these circulation and hydrological changes in response to surface uplift.

Additionally, paleoclimate simulations are continuously being improved through our evolving understanding of past climate forcings. For example, studies have recently suggested that lower O_2 levels (Poulsen et al., 2015) and fewer aerosol nuclei in the cleaner atmosphere (Kump and Pollard, 2008) may be responsible for increasing precipitation in past greenhouse climates. The lower O_2 and aerosol levels were not included in our simulations.

6.3.2 Future work

We have provided reconstructions for two key snapshots of Cenozoic elevation and climates of the western North American Cordillera. There remain many unanswered questions. For example, it has been suggested, based upon the seasonally depleted $\delta^{18}O$ in the Laramide foreland province (Fricke et al., 2010; Sewall and Fricke, 2013) and surface temperature contrast between Nevada and Utah estimated with clumped isotope thermometry (Snell, et al., 2014), that the Western Cordillera had already reached 3-km during the late Cretaceous (~ 70 Ma). The suggested high elevation of the hinterland may indicate a different phase of surface uplift apart from the Eocene uplift tested in this dissertation. However, surface temperatures from the eastern central Nevada of Paleogene-Eocene age (~81 – 38 Ma) suggest a lack of temperature contrast with coastal temperatures from the Northern Sierra Nevada (Lechler et al, 2013). There are no direct late Cretaceous $\delta^{18}O$ records from the Cordillera hinterland. All the current Cretaceous

$\delta^{18}O$ records are from sites located within the Laramide foreland province. These sites could have received the majority of surface waters from the adjacent Sevier Fold and Thrust Belt, and high reliefs within the foreland province apart from the hinterland. Therefore, they may have recorded elevation signals of the Thrust belt and local reliefs, but not the broader scale hinterland to the west. Future $\delta^{18}O$ reconstructions and climate modeling work are needed to resolve this conflict.

Additionally, the mechanisms for climate drying in the Laramide foreland province and the associated influences on the paleoaltimetry estimates in the southern reach of the western Cordillera are not fully investigated in this dissertation. Proxy records suggest that the climate cools and dries during the late Eocene-early Oligocene (40 – 34 Ma) (Liu et al., 2009). While we demonstrate that drying in the southern side of the Laramide foreland province is unlikely due to Cordilleran uplift under Eocene climate conditions, the proxy identified climate shift is not directly considered in this dissertation. Including this climate trend in future studies may affect the climate and paleoelevation estimates in the southern reach of the Cordillera, and will help elucidate the contributions of uplift versus climate drying to recorded aridification in the Laramide foreland province.

The presented dissertation highlights the need to consider the co-evolution of climate and topography when reconstructing paleo-environments. This method differs from those used in the majority of previous studies, which often investigate either climate or tectonics while treating the other as roughly fixed. Incorporating climate simulations with climate and topographic reconstructions from geochemical proxies and fossil records allows for simultaneous consideration of climate and topographic evolution. Future studies should incorporate this powerful method in regions beyond the North American Cordillera and Andes.

References

Chamberlain, C.P., Mix, H.T., Mulch, A., Hren, M.T., Kent-Corson, M.L., Davis, S.J., Horton, T.W., Graham, S.A., 2012. The Cenozoic climatic and topographic evolution of the western North American Cordillera. American Journal of Science 312, 213–262. doi:10.2475/02.2012.05

Fricke, H.C., Foreman, B.Z., Sewall, J.O., 2010. Integrated climate model-oxygen isotope evidence for a North American monsoon during the Late Cretaceous. Earth and Planetary Science Letters 289, 11–21. doi:10.1016/j.epsl.2009.10.018

Humphreys, E.D., 1995. Post-Laramide removal of the Farallon slab, western United States. Geol 23, 987. doi:10.1130/0091-7613(1995)023<0987:PLROTF>2.3.CO;2

Kump, L.R., Pollard, D., 2008. Amplification of Cretaceous Warmth by Biological Cloud Feedbacks. Science 320, 195–195. doi:10.1126/science.1153883

Lechler, A. R., Niemi, N. A., Hren, M. T., & Lohmann, K. C., 2013. Paleoelevation estimates for the northern and central proto–Basin and Range from carbonate clumped isotope thermometry. Tectonics, 32(3), 295-316. doi: 10.1002/tect.20016

Liu, Z., Pagani, M., Zinniker, D., DeConto, R., Huber, M., Brinkhuis, H., Shah, S.R., Leckie, R.M., Pearson, A., 2009. Global Cooling During the Eocene-Oligocene Climate Transition. Science 323, 1187–1190. doi:10.1126/science.1166368

Mix, H.T., Mulch, A., Kent-Corson, M.L., Chamberlain, C.P., 2011. Cenozoic migration of topography in the North American Cordillera. Geol 39, 87–90. doi:10.1130/G31450.1

Nam, C., Bony, S., Dufresne, J.L., Chepfer, H., 2012. The "too few, too bright" tropical low-cloud problem in CMIP5 models. Geophys. Res. Lett. 39. doi:10.1029/2012GL053421

Poulsen, C.J., Tabor, C., White, J.D., 2015. Long-term climate forcing by atmospheric oxygen concentrations. Science 348, 1238–1241. doi:10.1126/science.1260670

Schmandt, B., Humphreys, E., 2010. Complex subduction and small-scale convection revealed by body-wave tomography of the western United States upper mantle. Earth and Planetary Science Letters 297, 435–445. doi:10.1016/j.epsl.2010.06.047

Sewall, J.O., Fricke, H.C., 2013. Andean-scale highlands in the Late Cretaceous Cordillera of the North American western margin. Earth and Planetary Science Letters 362, 88–98. doi:10.1016/j.epsl.2012.12.002

Snell, K. E., Koch, P. L., Druschke, P., et al. 2014. High elevation of the 'Nevadaplano'during

the Late Cretaceous. Earth and Planetary Science Letters, 386, 52-63. doi:10.1016/j.epsl.2013.10.046

Smith, M.E., Carroll, A.R., Jicha, B.R., Cassel, E.J., Scott, J.J., 2014. Paleogeographic record of Eocene Farallon slab rollback beneath western North America. Geol 42, 1039–1042. doi:10.1130/G36025.1